RADAR CROSS SECTION ENHANCEMENT
FOR RADAR NAVIGATION AND REMOTE SENSING

By

David George Michelson

B. A. Sc., The University of British Columbia, 1982

M. A. Sc., The University of British Columbia, 1986

A THESIS SUBMITTED IN PARTIAL FULFILLMENT OF

THE REQUIREMENTS FOR THE DEGREE OF

DOCTOR OF PHILOSOPHY

in

THE FACULTY OF GRADUATE STUDIES

DEPARTMENT OF ELECTRICAL ENGINEERING

We accept this thesis as conforming

to the required standard

....

....

THE UNIVERSITY OF BRITISH COLUMBIA

December 1993

In presenting this thesis in partial fulfilment of the requirements for an advanced degree at the University of British Columbia, I agree that the Library shall make it freely available for reference and study. I further agree that permission for extensive copying of this thesis for scholarly purposes may be granted by the head of my department or by his or her representatives. It is understood that copying or publication of this thesis for financial gain shall not be allowed without my written permission.

David G. Michelson

The University of British Columbia,

Department of Electrical Engineering,

2356 Main Mall,

Vancouver, B.C.

Canada

V6T 1Z4

Date: *29 December 1993*

Abstract

Research Supervisor: Prof. E.V. Jull

Recent developments in radar navigation and remote sensing have led to a requirement for rugged yet inexpensive location markers and calibration targets which present both a very large scattering cross section and a specified polarization response over a wide angular range. This study considers several problems related to the analysis and design of passive radar targets derived from corner reflectors.

Transformation of the polarization response of a target between global and local coordinate frames is shown to correspond to rotation of the polarization basis by a prescribed angle which is a function of both the coordinate transformation matrix and the direction of propagation. Once the angle of rotation has been determined using either spherical trigonometry or vector algebra, any polarization descriptor can be transformed between coordinate frames by application of a suitable rotation operator.

The scattering cross section and angular coverage of a conventional trihedral corner reflector can be altered by modifying the size and shape of its reflecting panels. A numerical algorithm based on physical optics is used to predict the contribution of triple-bounce reflections to the response of a reflector with polygonal panels of arbitrary shape. If three-fold symmetry is broken and the reflector is simply required to present bilateral symmetry, it is found that the scattering cross section, elevation beamwidth, and azimuthal beamwidth of the reflector can be chosen independently of each other.

A method for altering the polarization response of a conventional trihedral corner reflector by adding conducting fins or corrugations to one its interior surfaces is proposed. In calculating design curves for twist-polarizing or circularly polarizing reflectors by mode-matching, optimum accuracy and efficiency are obtained by setting the ratio of free space to groove modes equal to the ratio of groove width to the period. Methods for obtaining linear and circular

polarization selective responses are considered. The contribution of triple-bounce reflections to the response of such reflectors is a function of the direction of incidence, the orientation of the reflector, the dimensions of the corrugations, and the size and shape of the reflecting panels. Experimental results show that prototype twist-polarizing and circularly polarizing reflectors respond essentially as predicted.

Table of Contents

List of Tables

List of Figures

xiii

xiv

Acknowledgements

Chapter 1

INTRODUCTION

1.1 Background and Motivation

Radars function by radiating electromagnetic energy and detecting the presence and character of the echoes returned by reflecting objects or *targets*. If these echoes are correlated with the original transmitted signal, many of the characteristics of the targets can be estimated including their range, bearing, apparent size or reflectivity, and certain aspects of their physical geometry. If a series of radar measurements is processed over time, the original estimate of these characteristics can be refined and the future kinematic behaviour of the target can be predicted. Radar has traditionally been associated with the detection and navigation of ships and aircraft. More recently, it has become an important tool for remote sensing of the environment. The chief problem of radar is to detect targets of interest and estimate their position and physical characteristics in the presence of interference from clutter returns and noise [1], [2].

The scattering cross section σ of a target is defined as the area intercepting that amount of power which, when scattered isotropically, would produce an echo equal to that actually returned by the target. Thus,

$$\sigma = \lim_{r \to \infty} 4\pi r^2 \frac{|\mathbf{E}^s|^2}{|\mathbf{E}^i|^2} = \lim_{r \to \infty} 4\pi r^2 \frac{|\mathbf{H}^s|^2}{|\mathbf{H}^i|^2} \tag{1.1}$$

where $\mathbf{E}^i$ and $\mathbf{H}^i$ are the incident electric and magnetic fields, $\mathbf{E}^s$ and $\mathbf{H}^s$ are the scattered electric and magnetic fields, and r is the range at which the scattered field is measured. Radar cross section or RCS refers to that portion of the scattering cross section which is associated with a specified polarization component of the scattered wave and is a function of the size, shape, composition, and orientation of the target, the frequency of the incident wave, and the polarization state of the radar transmitting and receiving antennas [3], [4].

1

The tendency for both natural and man-made objects to depolarize radar echoes in characteristic ways has been recognized since the earliest days of radar. It is convenient to describe the relationship between the polarization states of the incident and scattered fields by a polarization scattering operator expressed in matrix form. Several representations are in common use. The polarization scattering matrix relates incident and scattered fields which have been expressed as complex polarization vectors while the Mueller matrix relates fields which have been expressed as Stokes vectors. Other forms, such as the Stokes scattering operator and the covariance matrix, are used in certain methods for synthesizing arbitrary polarization responses from sets of experimental data. Measurement of the complete polarization response of a target requires a radar which is capable of antenna polarization control or agility during transmission and polarization diversity on reception. Although such radars are considerably more complex than their conventional counterparts, polarimetric radar signal processing has become an important tool for target detection and classification in several fields including radar meteorology, geophysical remote sensing, and certain specialized forms of radar navigation [5]–[8].

It is often necessary to enhance the radar cross section of a cooperative target either to increase the maximum range at which the target can be reliably detected or to provide a target with a known response which may be used to assist in radar calibration and performance verification. Although it is sometimes possible to achieve the desired result simply by making minor modifications to the natural shape of the target or by disturbing the current distribution on the surface of the body with discrete impedance loading, it is usually more convenient to make use of auxiliary devices such as corner reflectors, dielectric lenses, and retrodirective antenna arrays which have been designed specifically to present a large radar cross section over wide angular ranges. The characteristics and relative merits of the various types of RCS enhancement devices have been widely discussed in the literature [9]–[12]. The response characteristics which are required of such devices are determined by several factors including the distance between the radar and the target, the reflectivity of the surrounding clutter, the resolution of the radar in range and azimuth, the combination of transmit and receive polarizations employed by the radar, and the nature of the target detection or radar calibration algorithm. Beamwidth

and pulse width limited radar resolution cells are shown in Figure 1.1. The probabilities of detection P_D and false alarm P_{FA} are determined by the value of the detection threshold and the probability distribution functions of the target and clutter returns as suggested by the example presented in Figure 1.2.
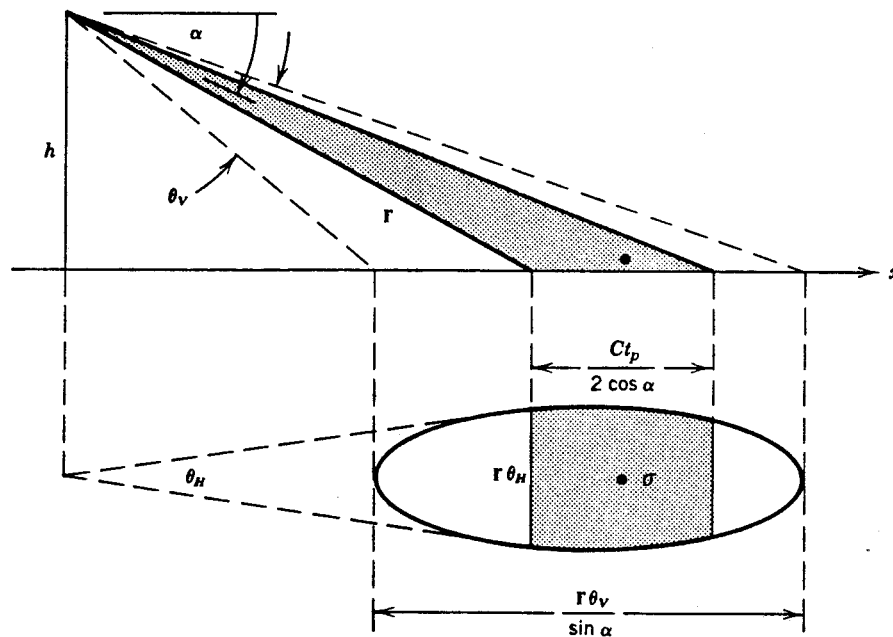
Figure 1.1: Detection of a point target in ground clutter where the radar resolution cell is either beamwidth limited (entire ellipse) or pulse width limited (shaded portion of ellipse). σ is the radar cross section of the target, r is the range to the target, h is the height of the radar, θ_H and θ_V are the half-power beamwidths of the radar antenna in azimuth and elevation, t_p is the pulse duration, C is the speed of light, and α is the depression angle. (after [2, p. 84])
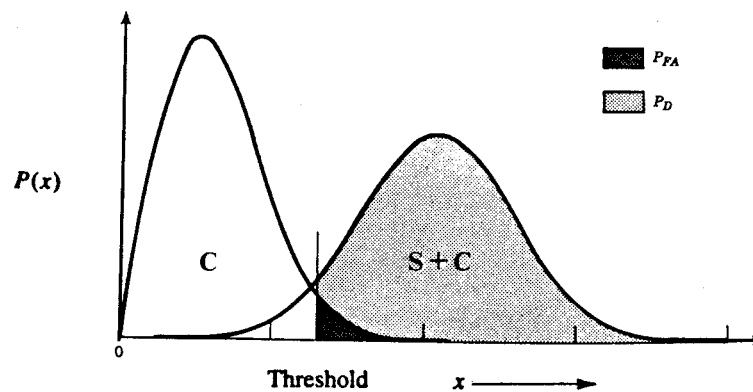
Figure 1.2: Probability distribution functions of clutter C and a signal embedded in clutter $S + C$ and the corresponding probabilities of detection P_D and false alarm P_{FA} for a given detection threshold. (after [2, p. 42])

In recent years, the development of airborne and spaceborne imaging radar systems for geophysical remote sensing and radar-assisted positioning systems for marine navigation has led to a requirement for rugged yet inexpensive calibration targets and location markers which present both a very large scattering cross section and a specified polarization response over a wide angular range. The NASA/JPL synthetic aperture radar (SAR) calibration site shown in Figure 1.3 is similar to the calibration ranges which have been established by several other research organizations to assist in the geometric, radiometric, and polarimetric calibration of SAR imagery [13], [14]. The experimental radar-assisted positioning system depicted in Figures 1.4 and 1.5 is being developed by Transport Canada as a method for allowing large vessels navigating in inland waterways, harbours, and harbour approaches to accurately determine their position with respect to cooperative shore-based targets in real time [15]–[19]. While the requirements for targets used in the calibration of airborne radars can be estimated with a fair degree of confidence [12]–[14], scattering by terrain at grazing incidence has not been well characterized [20]–[22] and it is not yet possible to give reliable estimates of the size of targets required to achieve specified probabilities of detection and false alarm in applications such as radar-assisted positioning.

Although active targets are physically compact and their scattering cross section, angular coverage, and polarization response can be modified with relative ease, their usefulness is limited by several factors including their requirement for an external power source, interaction between their transmitting and receiving antennas which may lead to regenerative feedback and distortion of their response patterns, and the limited reliability and stability of active components. Despite their greater physical size and finer mechanical tolerances, passive targets provide a better and more reliable alternative when it is necessary to install devices in remote locations for extended periods of time. In Figure 1.6, the relative sizes of corner reflectors which present the same maximum radar cross section (4500 m^2) at a frequency of 10 GHz are compared. In the face of conflicting requirements for a target which presents a large response and wide angular coverage while retaining mechanical ruggedness and ease of manufacture, trihedral corner reflectors frequently represent the best compromise.
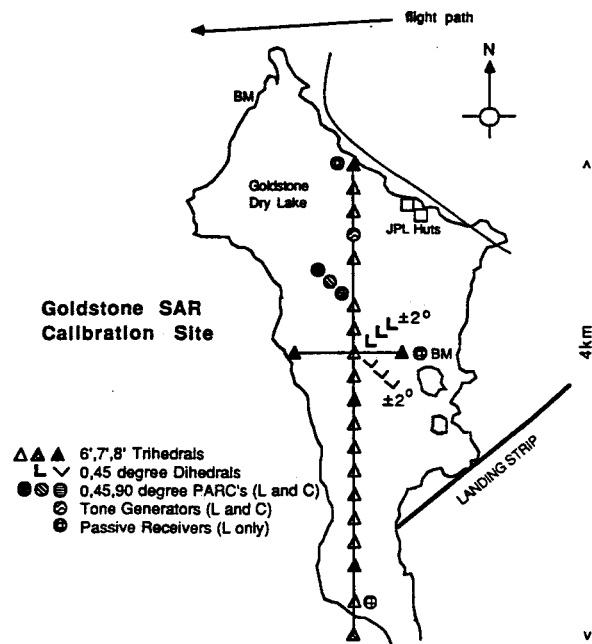
Figure 1.3: NASA/JPL synthetic aperture radar calibration site at Goldstone, California. (from [14, p. 227])
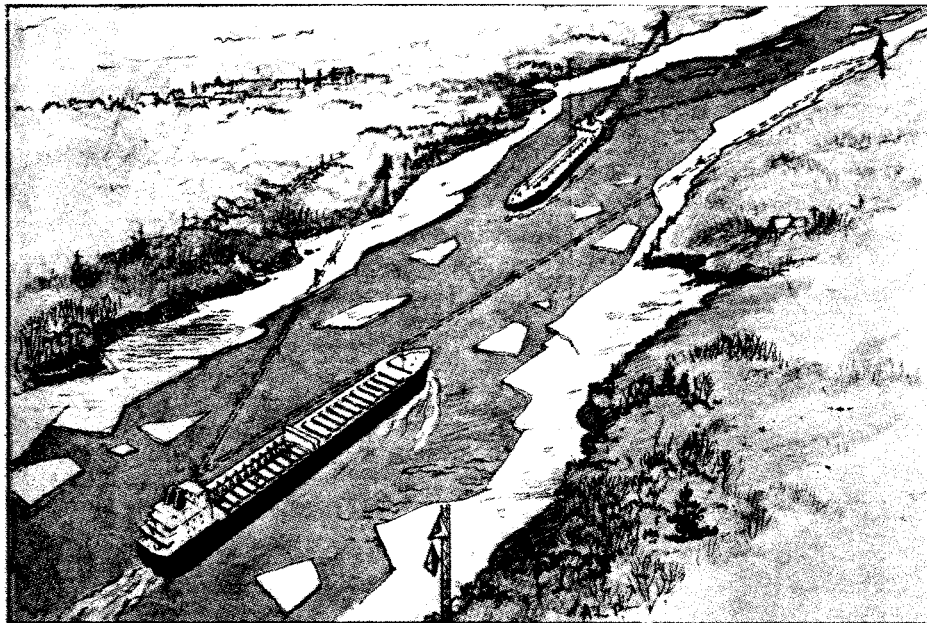
Figure 1.4: Radar-assisted positioning with respect to cooperative shore-based targets. (from [15, front cover])
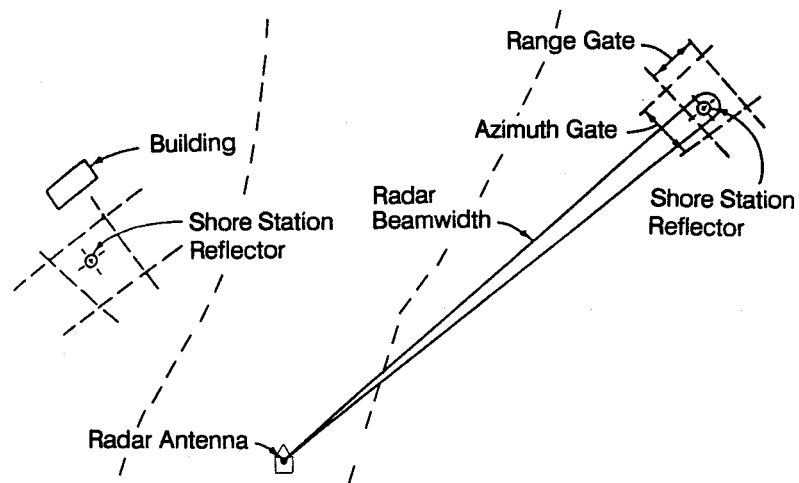
Figure 1.5: Use of range and azimuth gates to isolate shore station reflectors from surrounding clutter.
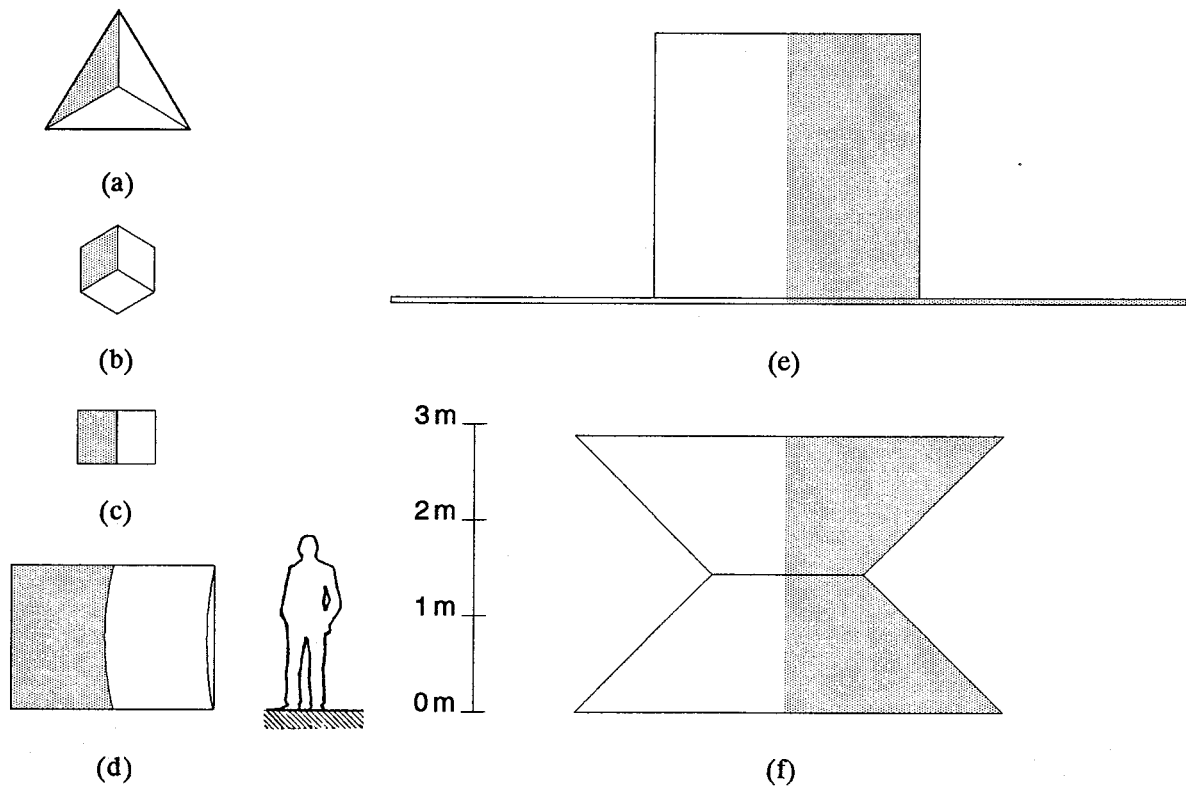
Figure 1.6: Relative size of corner reflectors which present the same maximum radar cross section (4500 m²) at $f = 10$ GHz. A spherical target which presents an equivalent response would have a diameter of over 75 metres. (a) Trihedral corner reflector with triangular panels, (b) Trihedral corner reflector with square panels. (c) Dihedral corner reflector. (d) Bruderhedral (a cylindrical sector attached to a flat plate). (e) Top hat reflector. (f) Biconical reflector.

1.2 Outline

This study considers several problems related to the analysis, design, and implementation of passive targets including transformation of polarization descriptors between coordinate frames, modification of the angular coverage and polarization response of conventional trihedral corner reflectors, design of top hat reflectors with specified response characteristics, and design of reflection polarizers derived from conducting gratings with rectangular grooves.

In Chapter 2, the problem of transforming representations of polarization state and polarization scattering operators between coordinate frames is considered. It is shown that such transformations correspond to rotation of the polarization basis by a prescribed angle which is a function of both the transformation matrix which relates the two coordinate frames and the direction of propagation. Two methods for determining the angle of rotation are derived for the case in which the local vertical is defined by the $\hat{z}$ direction in each frame. Algorithms for transforming common polarization descriptors are presented.

In Chapter 3, the problem of predicting the response and angular coverage of a trihedral corner reflector with panels of completely arbitrary shape is considered. For most purposes, only triple-bounce reflections from the interior of the reflector need be accounted for since they completely dominate the response for most directions of incidence. A simple yet robust RCS prediction algorithm which overcomes many of the limitations of previous work is described. The response patterns of three-fold symmetric and bilaterally symmetric trihedral corner reflectors with panels of various shapes are compared and design curves for realizing bilaterally symmetric trihedral corners with specified response characteristics are given.

In Chapter 4, a method for altering the polarization response of a conventional trihedral corner reflector by adding conducting fins or corrugations of appropriate dimensions and orientation to one of its interior surfaces is proposed. Design curves for twist-polarizing and circularly polarizing trihedral corner reflectors are given. Methods for realizing linear polarization selective trihedral corner reflectors using similar techniques are proposed. An algorithm for predicting the contribution of triple-bounce reflections to the response of a depolarizing trihedral corner reflector as a function of the direction of incidence and the orientation of the

reflector is derived. Experimental results are presented which show that prototype depolarizing reflectors respond essentially as predicted.

In Chapter 5, the results of this study are summarized and recommendations for further work are offered.

In Appendix A, the problem of designing top hat reflectors with specified response characteristics is considered. Expressions for the elevation response pattern, maximum scattering cross section, angle of maximum response, 1 and 3 dB beamwidths, and angle of median response for 1 and 3 dB beamwidths are derived and used to generate design curves. The results are used to solve a sample design problem.

In Appendix B, the problem of scattering by a conducting grating with rectangular grooves is considered. Analytical solutions are derived for the cases of TM- and TE-polarized incident waves by mode-matching between the free space and groove regions. Procedures for determining the validity of numerical results are described and the problem of determining the minimum number of modes required to accurately represent the fields in each region is studied. An implementation of the analytical solutions as a pair of subroutines coded in Fortran 77 is presented.

In Appendix C, the problem of modifying a conventional trihedral corner reflector to present a circular polarization selective response is considered. It is shown that such a response cannot be realized simply by using the techniques of Chapter 4 because the corresponding polarization scattering matrix cannot be diagonalized. Alternative methods for obtaining such a response based on the addition of a suitable transmission polarizer to reflectors which present either a linear polarization selective or a twist polarizing response are proposed.

In Appendix D, the experimental facility which was developed to measure the response of prototype trihedral corner reflectors is briefly described. Details of its physical layout, the design and implementation of the CW radar apparatus and digital pattern recorder, and the results of tests used to verify its suitability for use in the measurement program are given. Recommendations for future modifications and improvements are offered.

References

[1] F.E. Nathanson, *Radar Design Principles: Signal Processing and the Environment,* 2nd ed. New York: McGraw-Hill, 1991, pp. 1–48.

[2] N. Levanon, *Radar Principles.* New York, Wiley, 1988, pp. 1–97.

[3] E.F. Knott, J.F. Shaeffer, and M.T. Tuley, *Radar Cross Section: Its Prediction, Measurement, and Reduction.* Norwood, MA: Artech House, 1985, pp. 47–83.

[4] A.K. Bhattacharyya and D.L. Sengupta, *Radar Cross Section Analysis and Control.* Norwood, MA: Artech House, 1991, pp. 10–32.

[5] D. Giuli, "Polarization diversity in radars," *Proc. IEEE,* vol. 74, pp. 245–269, Feb. 1986.

[6] A. Macikunas and S. Haykin, "Polarization as a Radar Discriminant," in *Selected Topics in Signal Processing,* S. Haykin, Ed. Englewood Cliffs, NJ: Prentice-Hall, 1989, pp. 251–286.

[7] D. Atlas, Ed., *Radar in Meteorology.* Boston, MA: American Meteorology Society, 1990.

[8] F. T. Ulaby and C. Elachi, Eds., *Radar Polarimetry for Geoscience Applications.* Norwood, MA: Artech House, 1990.

[9] D. R. Brown, R. J. Newman, and J. W. Crispin, Jr., "RCS Enhancement Devices," in *Methods of Radar Cross Section Analysis,* J. W. Crispin, Jr. and K. M. Siegel, Eds. New York: Academic Press, 1969, pp. 237–280.

[10] G. T. Ruck, "Radar Cross Section Enhancement," in *Radar Cross Section Handbook,* G.T. Ruck, Ed. New York: Plenum Press, 1970, pp. 585–601.

[11] F. T. Ulaby, R. K. Moore, and A. K. Fung, *Microwave Remote Sensing: Active and Passive,* vol. 2. Norwood, MA: Artech House, 1982, pp. 766–779.

[12] D. R. Brunfeldt and F. T. Ulaby, "Active reflector for radar calibration," *IEEE Trans. Geosci. Remote Sensing,* vol. GE-22, pp. 165–169, Mar. 1984.

[13] S. H. Yueh, J. A. Kong, R. M. Barnes, and R. T. Shin, "Calibration of polarimetric radars using in-scene reflectors," *J. Electromagn. Waves Appl.,* vol. 4, pp. 27–48, Jan. 1990.

[14] A. Freeman, Y. Shen, and C.L. Warner, "Polarimetric SAR calibration experiment using active radar reflectors," *IEEE Trans. Geosci. Remote Sensing,* vol. GE-28, pp. 224–240, Mar. 1990.

[15] G. Stiles, R.O. Hewitt, and C.O. McHale, "PRANS Trials: Evaluation of a Precise Radar Navigation System." Transport Canada Publ. No. TP 2800E. Montreal: Transportation Development Centre, Aug. 1981.

[16] D. Kalnicki and R. Harrs, "Performance Evaluation and Demonstration of the RANAV (Radar-Assisted Precise Navigation) System in the St. Lawrence River." Transport Canada Publ. No. TP 11326E. Montreal: Transportation Development Centre, April 1992.

[17] S. Haykin, "Polarimetric radar for accurate navigation," *Can. J. Elect. Comp. Eng.,* vol. 17, pp. 130–135, July 1992.

[18] H. Lanziner, D. Michelson, S. Lachance, and D. Williams, "Experiences with a commercial ECDIS," *Int. Hydrogr. Rev.,* vol. 67, no. 2, pp. 69–86, July 1990.

[19] D.G. Michelson *et al.,* "Use of circular polarization in a marine radar positioning system," *Proc. IGARSS'89,* (Vancouver, B.C.), July 1989.

[20] M.W. Long, *Radar Reflectivity of Land and Sea.* Norwood, MA: Artech House, 1983.

[21] D.K. Barton, "Land clutter models for radar design and analysis," *Proc. IEEE,* vol. 73, pp. 198–204, Feb. 1985.

[22] F.T. Ulaby and M.C. Dobson, *Handbook of Radar Scattering Statistics for Terrain.* Norwood, MA: Artech House, 1989.

Chapter 2

TRANSFORMATION OF POLARIZATION DESCRIPTORS
BETWEEN COORDINATE FRAMES

2.1 Introduction

The polarization state of an electromagnetic wave is a vector quantity which refers to the behaviour with time of the electric field as observed at a fixed point in space. If the wave is monochromatic, the tip of the electric field vector will trace an ellipse in the plane orthogonal to the direction of propagation. Such a wave is said to be *completely polarized*. If the wave contains a random component in amplitude or phase, it will occupy a finite bandwidth and the polarization ellipse will tend to change shape and orientation with time. Such a wave is said to be *partially polarized*. In the extreme case, the tip of the electric field vector will trace out a figure which is totally random in shape and the wave is said to be *randomly polarized* (or *unpolarized*). The fundamental aspects of wave polarization have been reviewed by several authors, e.g., [1]–[6].
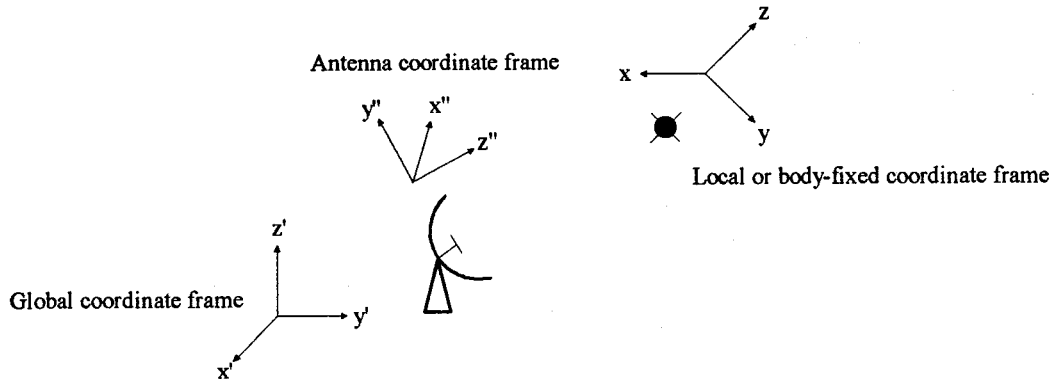
Figure 2.1: Coordinate frames used to define polarization state in radar scattering problems.

Since polarization is a vector quantity, its description must be referred to a particular coordinate frame. When problems involving propagation or scattering in the vicinity of the earth's surface are considered, it is often convenient to describe the polarization state of an antenna or the polarization response of a target with respect to a global coordinate frame in which the earth's surface is coincident with the x-y plane and the local vertical is parallel to the z axis. If the radiation or scattering characteristics of an object can be determined more efficiently in a different frame or if the object is free to rotate about one or more axes as in the case of airborne or spaceborne platforms, it may be preferable to define the polarization characteristics of the object with respect to a local or body-fixed coordinate frame instead, as suggested by Figure 2.1. In turn, the response of the device is measured in yet another coordinate frame which is defined by the antenna. However, with the exception of the special cases considered by Mott [6] and Krichbaum [7], the problem of transforming polarization descriptors between coordinate frames has received little attention in the literature.

In section 2.2, the concept of polarization state is briefly reviewed. In section 2.3, it is shown that transformation of a polarization descriptor between coordinate frames corresponds to rotation of its basis by a prescribed angle which is a function of both the transformation matrix which relates the two coordinate frames and the direction of propagation. Two methods for determining the angle of rotation for the case in which the local vertical is defined by the $\hat{z}$ direction in each frame are derived using spherical trigonometry and vector algebra, respectively. In section 2.3, methods for determining the elements of the coordinate transformation matrix are reviewed. Although the matrix can be determined from either the relative directions of the three principal axes in each coordinate frame or the Euler angles which define a series of rotations which will transform one coordinate frame into the other, in practice it may be difficult to obtain these parameters. A third method is derived which permits the elements of the transformation matrix to be determined from any pair of arbitrary directions which have been expressed in terms of both coordinate frames. In section 2.4, algorithms for rotating the basis of several common polarization descriptors are presented.

2.2 Wave Polarization

The electric field vector $\mathbf{E}$ of a plane wave travelling in the direction $\hat{k}$ may be characterized in terms of a horizontally polarized component $E_H \hat{h}$ and a vertically polarized component $E_V \hat{v}$. Thus,

$$\mathbf{E} = (E_H \hat{h} + E_V \hat{v}) \, e^{-j\mathbf{k}\cdot\mathbf{r}} \,, \tag{2.1}$$

where $k = 2\pi/\lambda$ is the propagation constant in free space and the time dependence $e^{j\omega t}$ has been suppressed. The amplitudes E_H and E_V are complex quantities given by

$$E_H = a_H \, e^{j\delta_H} \,, \tag{2.2}$$

$$E_V = a_V \, e^{j\delta_V} \,, \tag{2.3}$$

where a_H and a_V are the magnitudes of E_H and E_V, respectively, and δ_H and δ_V are their phase angles. The coordinate frame $(\hat{h}, \hat{v}, \hat{k})$ can be specified in terms of the triad $(\hat{r}, \hat{\theta}, \hat{\phi})$ defined by a spherical coordinate system such that

$$\hat{k} = \frac{\mathbf{k}}{k} \equiv \hat{r} = \cos\phi\sin\theta \, \hat{x} + \sin\phi\sin\theta \, \hat{y} + \cos\theta \, \hat{z} \,, \tag{2.4}$$

$$\hat{h} = \frac{\hat{z} \times \hat{k}}{|\hat{z} \times \hat{k}|} \equiv \hat{\phi} = -\sin\phi \, \hat{x} + \cos\phi \, \hat{y} \,, \tag{2.5}$$

$$\hat{v} = \hat{k} \times \hat{h} \equiv -\hat{\theta} = -\cos\phi\cos\theta \, \hat{x} - \sin\phi\cos\theta \, \hat{y} + \sin\theta \, \hat{z} \,, \tag{2.6}$$

as depicted in Figure 2.2. The definitions of $\hat{h}$ and $\hat{v}$ given by (2.5) and (2.6) are somewhat arbitrary and any pair of orthogonal directions which form a right hand triad with $\hat{k}$ may be substituted. In cases where the direction of propagation coincides with the z axis, e.g., the antenna coordinate frame of Figure 2.1, the definitions of $\hat{h}$ and $\hat{v}$ given by (2.5) and (2.6) are ambiguous. If

$$\hat{k} = \pm\hat{z} \,, \tag{2.7}$$

it is common to define $\hat{h}$ and $\hat{v}$ such that

$$\hat{h} = \hat{y} \times \hat{k} = \pm\hat{x} \,, \tag{2.8}$$

$$\hat{v} = \hat{k} \times \hat{h} = \pm\hat{y} \,. \tag{2.9}$$

When propagation occurs mainly in the vicinity of the z axis, it is often more convenient to simply redefine polarization in terms of a new coordinate frame in which $\hat{x}', \hat{y}',$ and $\hat{z}'$ correspond to $\hat{z}, \hat{x},$ and $\hat{y}$, respectively, in the original frame and z' defines the new local vertical.
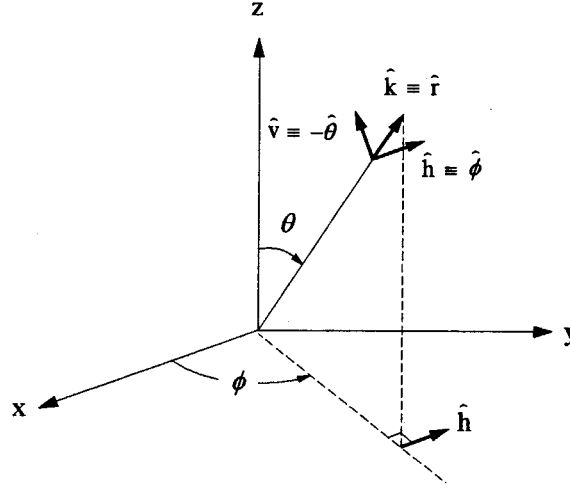
Figure 2.2: Coordinate system for a plane wave propagating in the direction $\hat{k}$.

If the wave is monochromatic, the tip of the electric field vector will trace an ellipse in the plane orthogonal to the direction of propagation. The shape, sense of rotation, and orientation of the ellipse are sufficient to specify the polarization state of the wave. Consider a polarization ellipse with semi-major axis OA and semi-minor axis OB, as depicted in Figure 2.3. The magnitude of the axial ratio R is given by

$$|R| = \frac{OA}{OB}, \qquad (1 \leq |R| \leq \infty),$$ (2.10)

while the ellipticity angle ϵ is defined as

$$\epsilon = -\cot^{-1} R, \qquad (-45° \leq \epsilon \leq +45°).$$ (2.11)

According to the IEEE convention, the axial ratio is positive for right-hand polarized waves and negative for left-hand polarized waves while the reverse is true for the ellipticity angle. The tilt angle τ is defined as the angle between the horizontal and the semi-major axis of the polarization ellipse and is valid over the range $-90° \leq \tau \leq +90°$. The entire range of possible polarization states can be mapped onto the surface of a Poincaré sphere as shown in Figure 2.4.

A polarization state with ellipticity angle ϵ and tilt angle τ corresponds to a point having longitude 2τ and latitude 2ϵ. Linear and circular polarization states map onto the equator and poles, respectively, while left and right elliptical polarization states map onto the upper and lower hemispheres.
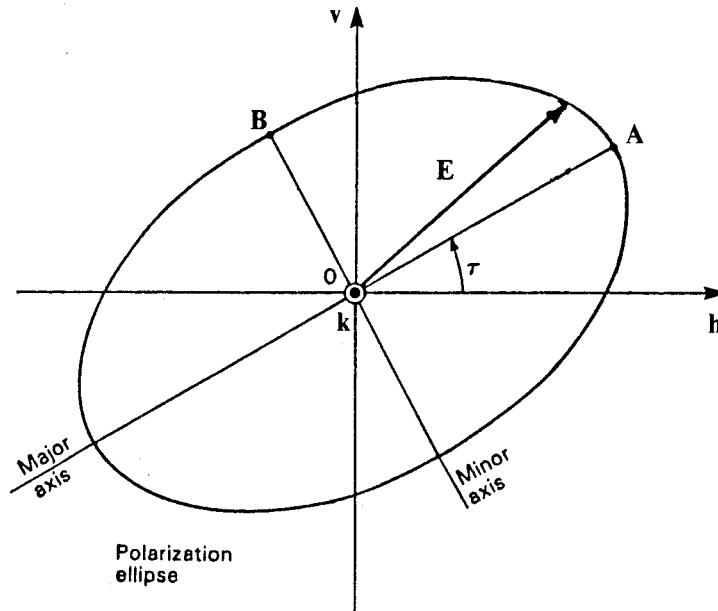
Figure 2.3: A polarization ellipse with semi-major axis OA, semi-minor axis OB, and tilt angle τ.
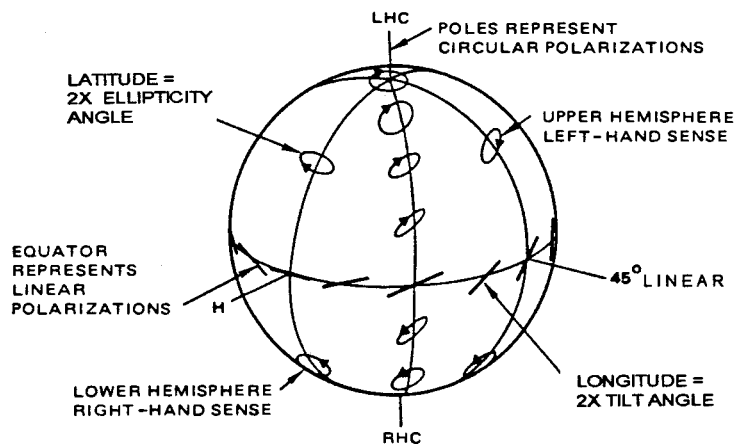
Figure 2.4: Mapping of polarization states onto a Poincaré sphere. (from [8], p. 82)

2.3 Transformation of Coordinates

Consider two coordinate frames which are related by a combination of translation and rotation and let the directions $\hat{z}$ and $\hat{Z}$ define the local vertical in each frame. In cartesian coordinates, the position vectors $\mathbf{r'}$ and $\mathbf{R}$ in the two frames are related by a coordinate transformation matrix $[T]$ such that

$$\begin{bmatrix} x' \\ y' \\ z' \end{bmatrix} = \begin{bmatrix} \ell_1 & m_1 & n_1 \\ \ell_2 & m_2 & n_2 \\ \ell_3 & m_3 & n_3 \end{bmatrix} \begin{bmatrix} X - X_0 \\ Y - Y_0 \\ Z - Z_0 \end{bmatrix}, \tag{2.12}$$

where the origin O' of the $x'y'z'$ coordinate frame is located at (X_0, Y_0, Z_0) relative to the XYZ coordinate frame and $l_1, m_1, n_1;\ l_2, m_2, n_2;$ and l_3, m_3, n_3 are the direction cosines of the x', y', z' axes relative to the X, Y, Z axes, respectively. Since the coordinate transformation matrix is a unitary matrix, its inverse is identical to its transpose and the reverse transformation is simply given by

$$\begin{bmatrix} X \\ Y \\ Z \end{bmatrix} = \begin{bmatrix} \ell_1 & \ell_2 & \ell_3 \\ m_1 & m_2 & m_3 \\ n_1 & n_2 & n_3 \end{bmatrix} \begin{bmatrix} x' \\ y' \\ z' \end{bmatrix} + \begin{bmatrix} X_0 \\ Y_0 \\ Z_0 \end{bmatrix}. \tag{2.13}$$

The polarization state of a propagating wave can be transformed from one coordinate frame to another by direct application of either (2.12) or (2.13) to the components of the electric field vector as described by Mott [6, pp. 212–219]. However, this technique is cumbersome and cannot be easily generalized to the many different methods which are used to represent the polarization state of a wave or the polarization response of a scatterer. The limitations are particularly apparent in cases where polarization state is described with respect to an elliptically or circularly polarized basis or where the wave is partially polarized. A more general approach is suggested by considering transformation of the corresponding polarization ellipse between coordinate frames. The ellipticity angle ϵ is invariant under either translation or rotation since it depends only on the magnitude of the axial ratio and the polarization sense of the wave. Although the tilt angle τ is invariant under translation, it will not be preserved under rotation

unless the horizontal planes in both coordinate frames are parallel to each other. This condition will be satisfied only if the coordinate transformation matrix is of the form

$$[T] = \begin{bmatrix} \cos\psi & \sin\psi & 0 \\ -\sin\psi & \cos\psi & 0 \\ 0 & 0 & 1 \end{bmatrix}, \tag{2.14}$$

which corresponds to rotation about the z axis by an angle ψ. Otherwise, the difference between the tilt angles of the polarization ellipse in the two coordinate frames is given by

$$\alpha = \tau - \tau', \qquad (-90° \le \alpha \le +90°), \tag{2.15}$$

where α corresponds to the angle between the unit vectors $\hat{\phi}$ and $\hat{\phi}'$ which define the horizontal plane in each coordinate frame with respect to the direction of propagation, as depicted in Figure 2.5. In general, it can be shown that transformation of any polarization descriptor between coordinate frames may be regarded as a change of basis transformation corresponding to rotation of the polarization basis by an angle α about the direction of propagation.
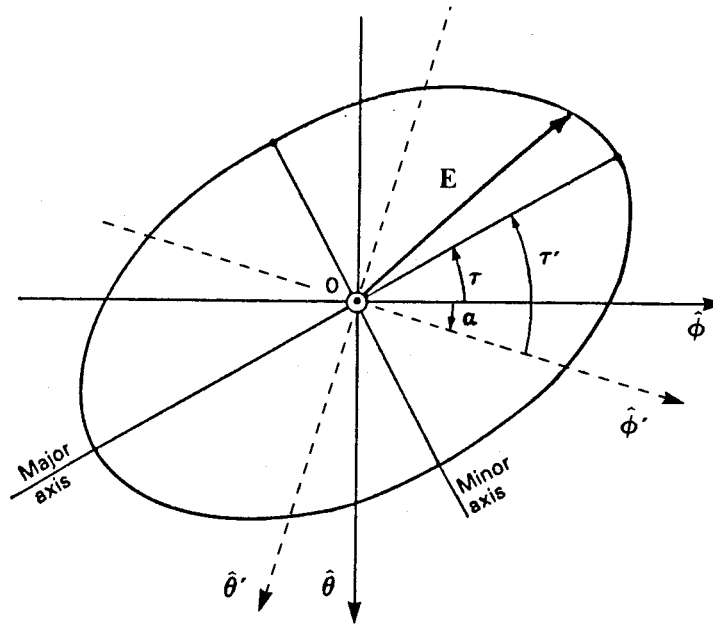
Figure 2.5: A polarization ellipse showing the relationship between the tilt angles τ and τ' in the xyz and $x'y'z'$ coordinate frames.

The angle α between the unit vectors $\hat{\phi}$ and $\hat{\phi}'$ is a function of both the direction of propagation and the coordinate transformation matrix which relates the two coordinate frames. This variation is apparent in Figures 2.6 and 2.7 where the parallels of two coordinate frames which are related by pure rotation are plotted on perspective and Mercator projections, respectively. Since the Mercator projection is conformal, the angles between the parallels are accurately depicted at all points on the grid and the variation in the angle α with the direction of propagation can be easily visualized. In the context of radar cross section measurement, Krichbaum [7] has derived an expression for this angle [1] for the special case in which the direction of propagation is coincident with the z axis and the coordinate transformation corresponds to rotation about the x and y axes. Here, two methods for determining the angle α for any direction of propagation and coordinate transformation are derived using spherical trigonometry and vector algebra, respectively. Since translation between the coordinate frames can be neglected, it is convenient to define

$$x = X - X_0, \quad y = Y - Y_0, \quad z = Z - Z_0, \qquad (2.16)$$

and reduce (2.9) and (2.10) to

$$\begin{bmatrix} x' \\ y' \\ z' \end{bmatrix} = \begin{bmatrix} \ell_1 & m_1 & n_1 \\ \ell_2 & m_2 & n_2 \\ \ell_3 & m_3 & n_3 \end{bmatrix} \begin{bmatrix} x \\ y \\ z \end{bmatrix}, \qquad (2.17)$$

and

$$\begin{bmatrix} x \\ y \\ z \end{bmatrix} = \begin{bmatrix} \ell_1 & \ell_2 & \ell_3 \\ m_1 & m_2 & m_3 \\ n_1 & n_2 & n_3 \end{bmatrix} \begin{bmatrix} x' \\ y' \\ z' \end{bmatrix}, \qquad (2.18)$$

where the origins of the xyz and $x'y'z'$ coordinate frames are coincident and $\ell_1, m_1, n_1; \ell_2, m_2, n_2;$ and ℓ_3, m_3, n_3 are the direction cosines of the x', y', z' axes relative to the x, y, z axes, respectively. Expressions for transforming direction expressed in terms of the elevation angle θ and azimuth angle ϕ between coordinate frames can be derived from the coordinate transformations

---

[1] which he refers to as the *polarization angle* Υ.
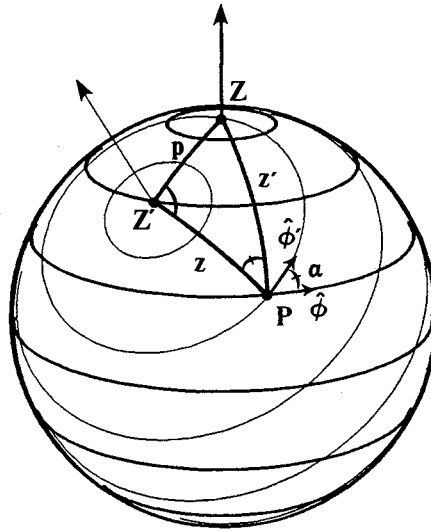
Figure 2.6: A perspective projection of the parallels of two coordinate frames which are related by pure rotation.
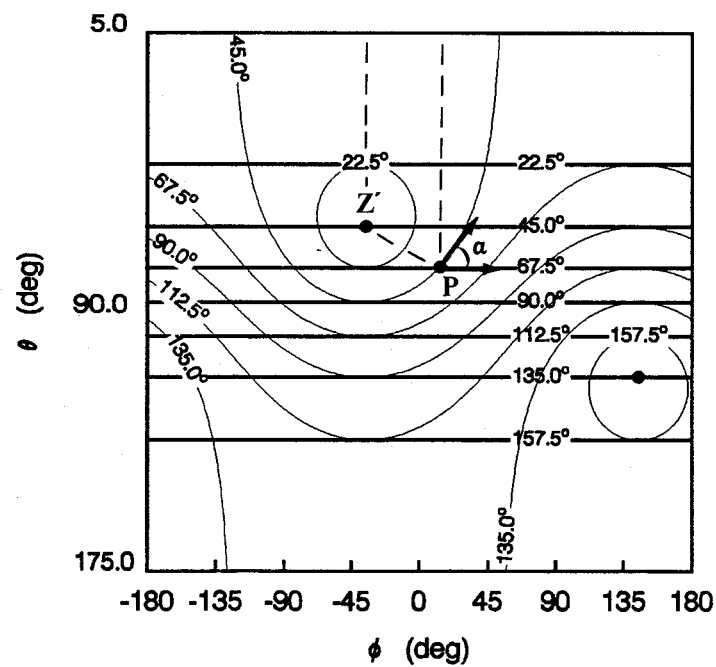
Figure 2.7: A Mercator projection of the parallels of two coordinate frames which are related by pure rotation. Since the projection is conformal, the angles between the parallels are accurately depicted at all points on the grid.

(2.17) and (2.18) and the relations

$$r = 1 \,, \qquad \theta = \cos^{-1} z \,, \qquad \phi = \tan^{-1}(y/x) \,,$$

$$x = \sin\theta\cos\phi \,, \qquad y = \sin\theta\sin\phi \,, \qquad z = \cos\theta \,. \qquad (2.19)$$

The forward transformation is given by

$$\theta' = \cos^{-1}\left[\ell_3 \sin\theta\cos\phi + m_3 \sin\theta\sin\phi + n_3 \cos\theta\right] \,, \qquad (2.20)$$

$$\phi' = \tan^{-1}\left[\frac{\ell_2 \sin\theta\cos\phi + m_2 \sin\theta\sin\phi + n_2 \cos\theta}{\ell_1 \sin\theta\cos\phi + m_1 \sin\theta\sin\phi + n_1 \cos\theta}\right] \,, \qquad (2.21)$$

while the reverse transformation is given by

$$\theta = \cos^{-1}\left[n_1 \sin\theta'\cos\phi' + n_2 \sin\theta'\sin\phi' + n_3 \cos\theta'\right] \,, \qquad (2.22)$$

$$\phi = \tan^{-1}\left[\frac{m_1 \sin\theta'\cos\phi' + m_2 \sin\theta'\sin\phi' + m_3 \cos\theta'}{\ell_1 \sin\theta'\cos\phi' + \ell_2 \sin\theta'\sin\phi' + \ell_3 \cos\theta'}\right] \,. \qquad (2.23)$$

Method I

A general expression for the angle α may be derived using spherical trigonometry. Consider two coordinate frames which are related by pure rotation as shown in Figure 2.6. Let the point O be the common origin of the coordinate frames and let the points Z, Z', and P be the intersection of the z axis, the z' axis, and the direction of propagation with a unit sphere centered about the origin. The points Z, Z', and P define the spherical triangle $ZZ'P$. The great circle angles defined by the arcs $\overgroup{Z'P}$, $\overgroup{ZP}$, and $\overgroup{ZZ'}$ are designated by z, z', and p. The angles defined by the vertices of the triangle opposite to arcs z, z', and p, are designated by Z, Z', and P. Since the vectors which are tangential to $\overline{PZ}$ and $\overline{PZ'}$ at P correspond to the directions $\hat{\theta}$ and $\hat{\theta}'$ and the vectors $\hat{\theta}_p$ and $\hat{\phi}_p$ are orthogonal in both the $x'y'z'$ and xyz coordinate frames, it can be shown that the angle P between the unit vectors $\hat{\theta}$ and $\hat{\theta}'$ is congruent to the angle α between the unit vectors $\hat{\phi}$ and $\hat{\phi}'$.

In terms of spherical coordinates, the great circle angles z, z', and p are given by

$$z = \theta'_P , \tag{2.24}$$

$$z' = \theta_P , \tag{2.25}$$

$$p = \theta'_Z = \theta_{Z'} , \tag{2.26}$$

while the vertex angles Z and Z' are given by

$$Z = \phi_P - \phi_{Z'} , \tag{2.27}$$

$$Z' = \phi'_Z - \phi'_P . \tag{2.28}$$

If the point P lies on the great circle defined by the arc ZZ', the vertex angles Z and Z' vanish and α is given by

$$
\begin{aligned}
\alpha &= \quad 0° , \qquad 0° < (\theta_P - \theta'_Z) < 180° , \\
&= \pm 180° , \qquad -180° < (\theta_P - \theta'_Z) < \quad 0° .
\end{aligned}
\tag{2.29}
$$

However, if the point P is coincident with either the point Z or its antipode, the local horizontal in the xyz coordinate frame will be undefined and the angle α cannot be determined. Similar considerations apply if the point P is coincident with either the point Z' or its antipode. In all other cases, an expression for the angle α is obtained by applying the laws of sines to the spherical triangle $ZZ'P$ to give either

$$
\begin{aligned}
\sin \alpha &= \frac{\sin p \, \sin Z}{\sin z} , \\
&= \frac{\sin \theta'_Z \, \sin(\phi_P - \phi_{Z'})}{\sin \theta'_P} ,
\end{aligned}
\tag{2.30}
$$

or

$$
\begin{aligned}
\sin \alpha &= \frac{\sin p \, \sin Z'}{\sin z'} , \\
&= \frac{\sin \theta'_Z \, \sin(\phi'_Z - \phi'_P)}{\sin \theta_P} ,
\end{aligned}
\tag{2.31}
$$

then applying the law of cosines to give

$$\cos \alpha = -\cos Z \cos Z' + \sin Z \sin Z' \cos p , \qquad (2.32)$$

$$= -\cos(\phi_P - \phi_Z') \cos(\phi_Z' - \phi_P') + \sin(\phi_P - \phi_Z') \sin(\phi_Z' - \phi_P') \cos \theta_Z' .$$

Since both the sine and cosine of the angle are known, it is a simple matter to determine the angle α using a four-quadrant arctangent function, e.g.,

$$\alpha = \tan^{-1} \left(\frac{\sin p \, \sin Z / \sin z}{-\cos Z \cos Z' + \sin Z \sin Z' \cos p} \right) , \qquad (2.33)$$

$$= \tan^{-1} \left(\frac{\sin \theta_Z' \, \sin(\phi_P - \phi_Z') / \sin \theta_P'}{-\cos(\phi_P - \phi_Z') \cos(\phi_Z' - \phi_P') + \sin(\phi_P - \phi_Z') \sin(\phi_Z' - \phi_P') \cos \theta_Z'} \right)$$

Method II

An alternative expression for the angle α may be derived using vector algebra. Let $\hat{\phi}_P$ define the horizontal plane of the xyz coordinate frame with respect to the direction of propagation and be given by

$$\hat{\phi}_P = -\sin \phi \, \hat{x} + \cos \phi \, \hat{y} , \qquad (2.34)$$

and let $\hat{\phi}_P'$ similarly define the horizontal plane of the $x'y'z'$ coordinate frame and be given by

$$\hat{\phi}_P' = -\sin \phi' \, \hat{x}' + \cos \phi' \, \hat{y}' . \qquad (2.35)$$

Let $\hat{r}_P$ be the outward normal to the unit sphere at the point P in the xyz coordinate frame and be given by

$$\hat{r}_P = -\sin \theta \cos \phi \, \hat{x} + \sin \theta \sin \phi \, \hat{y} + \cos \theta \, \hat{z} . \qquad (2.36)$$

The expression for the unit vector $\hat{\phi}_P'$ in the $x'y'z'$ coordinate frame given by (2.35) must be transformed to the xyz coordinate frame. This can be accomplished by determining ϕ' in terms of θ and ϕ using (2.21) and converting the basis of the vector using (2.18). The scalar triple product of the unit vectors $\hat{\phi}_P$, $\hat{\phi}_P'$, and $\hat{r}_P$ gives

$$\sin \alpha = \hat{r}_P \cdot (\hat{\phi}_P \times \hat{\phi}_P') , \qquad (2.37)$$

while the dot product of the unit vectors $\hat{\phi}_P$ with $\hat{\phi}'_P$ gives

$$\cos\alpha = \hat{\phi}_P \cdot \hat{\phi}'_P \, . \tag{2.38}$$

Since both the sine and cosine of the angle are known, α can be determined using a four-quadrant arctangent function, i.e.,

$$\alpha = \tan^{-1}\left(\frac{\hat{r}_P \cdot (\hat{\phi}_P \times \hat{\phi}'_P)}{\hat{\phi}_P \cdot \hat{\phi}'_P}\right) \, . \tag{2.39}$$

If $\hat{r}_P$ is coincident with z axis then the definition of $\hat{\phi}_P$ given by (2.34) is ambiguous. In such cases, the direction of the horizontal plane with respect to the direction of propagation must be defined arbitrarily. If $\hat{r}_P$ is coincident with the z' axis, similar considerations apply to the definition of $\hat{\phi}'_P$ given by (2.35).

2.4 Evaluation of the Coordinate Transformation Matrix

In order to apply the results presented in the previous section, it is necessary to determine the elements of the coordinate transformation matrix which relates the xyz and $x'y'z'$ coordinate frames according to (2.17) and (2.18). This can be accomplished if either the relative directions of the basis vectors defined by the three principal axes in each coordinate frame or a series of Euler angle rotations which will transform one coordinate frame into the other are known [9], [10]. In the first case, the coordinate transformation matrix is given by

$$[T] = \begin{bmatrix} \ell_1 & m_1 & n_1 \\ \ell_2 & m_2 & n_2 \\ \ell_3 & m_3 & n_3 \end{bmatrix} = \begin{bmatrix} \hat{x}' \cdot \hat{x} & \hat{x}' \cdot \hat{y} & \hat{x}' \cdot \hat{z} \\ \hat{y}' \cdot \hat{x} & \hat{y}' \cdot \hat{y} & \hat{y}' \cdot \hat{z} \\ \hat{z}' \cdot \hat{x} & \hat{z}' \cdot \hat{y} & \hat{z}' \cdot \hat{z} \end{bmatrix} \, , \tag{2.40}$$

where the two sets of basis vectors $(\hat{x}', \hat{y}', \hat{z}')$ and $(\hat{x}, \hat{y}, \hat{z})$ have been expressed with respect to a common coordinate frame. In the second case, the transformation is described in terms a series of angles through which the first frame can be rotated in order to bring it into coincidence with the second. A maximum of three Euler angle rotations is sufficient to bring any two frames

into coincidence. One possibility is to begin the sequence with rotation about the y axis by an angle ξ,

$$\begin{bmatrix} x'' \\ y'' \\ z'' \end{bmatrix} = \begin{bmatrix} \cos\xi & 0 & \sin\xi \\ 0 & 1 & 0 \\ -\sin\xi & 0 & \cos\xi \end{bmatrix} \begin{bmatrix} x \\ y \\ z \end{bmatrix}, \qquad (2.41)$$

follow by rotation about the x'' axis by an angle η,

$$\begin{bmatrix} x''' \\ y''' \\ z''' \end{bmatrix} = \begin{bmatrix} 1 & 0 & 0 \\ 0 & \cos\eta & \sin\eta \\ 0 & -\sin\eta & \cos\eta \end{bmatrix} \begin{bmatrix} x'' \\ y'' \\ z'' \end{bmatrix}, \qquad (2.42)$$

and conclude with rotation about the z axis by angle ζ,

$$\begin{bmatrix} x' \\ y' \\ z' \end{bmatrix} = \begin{bmatrix} \cos\zeta & \sin\zeta & 0 \\ -\sin\zeta & \cos\zeta & 0 \\ 0 & 0 & 1 \end{bmatrix} \begin{bmatrix} x''' \\ y''' \\ z''' \end{bmatrix}, \qquad (2.43)$$

as suggested by Krichbaum [7]. The product of the three rotation matrices given in (2.41), (2.42), and (2.43) yields the transformation matrix which relates the xyz and $x'y'z'$ coordinate frames,

$$[T] = \begin{bmatrix} \cos\zeta\cos\xi - \sin\zeta\sin\eta\sin\xi & \sin\zeta\cos\eta & \cos\zeta\sin\xi + \sin\zeta\sin\eta\cos\xi \\ -\sin\zeta\cos\xi - \cos\zeta\sin\eta\sin\xi & \cos\zeta\cos\eta & -\sin\zeta\sin\xi + \cos\zeta\sin\eta\cos\xi \\ -\cos\eta\sin\xi & -\sin\eta & \cos\eta\cos\xi \end{bmatrix}. \qquad (2.44)$$

Since rotation is not commutative, this formulation is not unique and there are several other combinations of Euler angle rotations which will yield an equivalent coordinate transformation, e.g., [6], [9], [10].

In practice, it may be difficult to obtain the parameters required by the basis vector and Euler angle methods for determining the elements of the coordinate transformation matrix. An alternative method is derived here which allows the matrix to be determined from two arbitrary directions (θ_1, ϕ_1) and (θ_2, ϕ_2) which have been expressed in terms of both coordinate frames.

The unit vectors which correspond to these two directions can be determined by applying (2.19) to the ordered pairs (θ_1, ϕ_1), (θ'_1, ϕ'_1), (θ_2, ϕ_2), and (θ'_2, ϕ'_2) to yield

$$\hat{r}_1 = (x_1, y_1, z_1) \quad \equiv \quad \hat{r}'_1 = (x'_1, y'_1, z'_1) \,, \tag{2.45}$$

$$\hat{r}_2 = (x_2, y_2, z_2) \quad \equiv \quad \hat{r}'_2 = (x'_2, y'_2, z'_2) \,. \tag{2.46}$$

A third direction, $\hat{r}_3$, can be determined from the normalized cross products,

$$\hat{r}_3 = \frac{\hat{r}_1 \times \hat{r}_2}{|\hat{r}_1 \times \hat{r}_2|} \,, \qquad \hat{r}'_3 = \frac{\hat{r}'_1 \times \hat{r}'_2}{|\hat{r}'_1 \times \hat{r}'_2|} \,, \tag{2.47}$$

in order to obtain two sets of vectors $(\hat{r}_1, \hat{r}_2, \hat{r}_3)$ and $(\hat{r}'_1, \hat{r}'_2, \hat{r}'_3)$ which form a linearly independent set in their respective coordinate frames, i.e.,

$$\begin{vmatrix} x_1 & x_2 & x_3 \\ y_1 & y_2 & y_3 \\ z_1 & z_2 & z_3 \end{vmatrix} \neq 0 \,, \qquad \begin{vmatrix} x'_1 & x'_2 & x'_3 \\ y'_1 & y'_2 & y'_3 \\ z'_1 & z'_2 & z'_3 \end{vmatrix} \neq 0 \,. \tag{2.48}$$

From (2.17), it can be shown that

$$\begin{bmatrix} x'_1 & x'_2 & x'_3 \\ y'_1 & y'_2 & y'_3 \\ z'_1 & z'_2 & z'_3 \end{bmatrix} = \begin{bmatrix} \ell_1 & m_1 & n_1 \\ \ell_2 & m_2 & n_2 \\ \ell_3 & m_3 & n_3 \end{bmatrix} \begin{bmatrix} x_1 & x_2 & x_3 \\ y_1 & y_2 & y_3 \\ z_1 & z_2 & z_3 \end{bmatrix} \,. \tag{2.49}$$

Solving for the coordinate transformation matrix gives

$$\begin{bmatrix} \ell_1 & m_1 & n_1 \\ \ell_2 & m_2 & n_2 \\ \ell_3 & m_3 & n_3 \end{bmatrix} = \begin{bmatrix} x'_1 & x'_2 & x'_3 \\ y'_1 & y'_2 & y'_3 \\ z'_1 & z'_2 & z'_3 \end{bmatrix} \begin{bmatrix} x_1 & x_2 & x_3 \\ y_1 & y_2 & y_3 \\ z_1 & z_2 & z_3 \end{bmatrix}^{-1} \,. \tag{2.50}$$

Since the coordinate matrices satisfy (2.48), they will always have an inverse and (2.50) will always have a valid solution.

2.5 Rotation of the Basis of Common Polarization Descriptors

In this section, methods for rotating the basis of polarization coordinates and the complex polarization vector e.g., [1], [3], [11], are extended to more general cases. Methods for rotating the basis of the Stokes vector and the coherency basis are derived. Some of the results presented here have recently been confirmed using a different approach by Mott [6].

Polarization Coordinates and Complex Polarization Ratios

The entire range of possible polarization states of a completely polarized wave can be mapped onto the surface of a Poincaré sphere so that each polarization state is represented by its coordinates in either latitude and longitude or elevation and azimuth. For example, a spherical coordinate system can be devised in which a polarization state W with ellipticity angle ϵ and tilt angle τ is represented by a point having longitude 2τ and latitude 2ϵ, as shown in Figure 2.8. If the basis vectors $\hat{h}$ and $\hat{v}$ of (2.5) and (2.6) are rotated about the propagation vector $\hat{k}$ by an angle α, the coordinates of the polarization state W' in the new frame are given by

$$\epsilon' = \epsilon, \tag{2.51}$$

$$\tau' = \tau - \alpha. \tag{2.52}$$

Alternatively, the coordinates of the polarization state W may be described in terms of the polarization angle γ and phase angle δ which are derived from the expression of the corresponding plane wave as the weighted sum of orthogonally polarized basis states. For example, the electric field vector $\mathbf{E}$ may be characterized in terms of horizontally and vertically polarized components with

$$\mathbf{E} = \left(E_H \hat{h} + E_V \hat{v} \right) e^{-j\mathbf{k} \cdot \mathbf{r}}, \tag{2.53}$$

where the time dependence $e^{j\omega t}$ has been suppressed and E_H and E_V are complex amplitudes given by

$$E_H = a_H\, e^{j\delta_H}, \tag{2.54}$$

$$E_V = a_V\, e^{j\delta_V}, \tag{2.55}$$
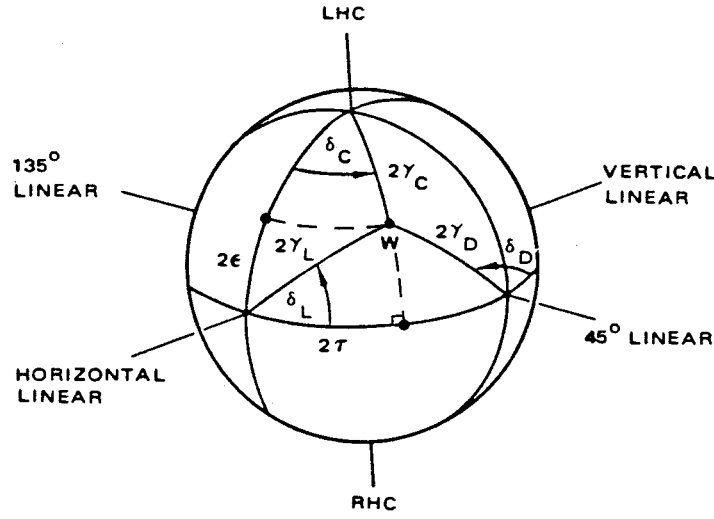
Figure 2.8: Poincaré sphere representation of the polarization state W of a plane wave. (after [8], p. 81)

as described in section 2.2. The quantities a_H and a_V are the magnitudes of E_H and E_V, respectively, and δ_H and δ_V are their phase angles. The polarization angle γ_L and phase angle δ_L are given by

$$\gamma_L = \tan^{-1}(a_V/a_H), \qquad (-90° \le \gamma_L \le +90°), \tag{2.56}$$

$$\delta_L = \delta_V - \delta_H, \qquad (-90° \le \delta_L \le +90°). \tag{2.57}$$

Although any pair of orthogonally polarized basis states may be employed, the most common are horizontal and vertical, 45° and 135° linear, and left and right circular. In the latter cases, the polarization angle and phase angle are defined in a similar manner to γ_L and δ_L with

$$\gamma_D = \tan^{-1}(a_{135}/a_{45}), \qquad (-90° \le \gamma_D \le +90°), \tag{2.58}$$

$$\delta_D = \delta_{135} - \delta_{45}, \qquad (-90° \le \delta_D \le +90°), \tag{2.59}$$

and

$$\gamma_C = \tan^{-1}(a_R/a_L), \qquad (-90° \le \gamma_C \le +90°), \tag{2.60}$$

$$\delta_C = \delta_R - \delta_L, \qquad (-90° \le \delta_C \le +90°). \tag{2.61}$$

In each case, a polarization state W with polarization angle γ and phase angle δ is represented by a point having elevation 2γ and azimuth δ. The orientation of the axes from which γ and δ are measured is shown in Figure 2.8. The phase reference for orthogonal circular components is defined in Figure 2.9.
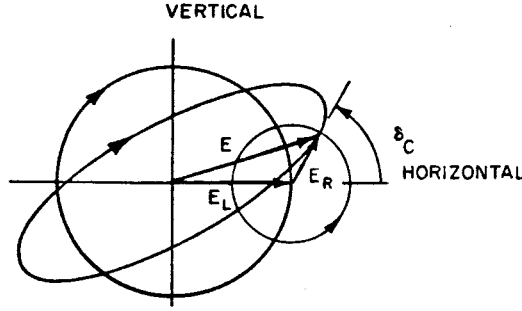
Figure 2.9: Definition of the phase reference for orthogonal circular components. (from [8], p. 82)

Rotation of the basis of polarization coordinates is easily accomplished if they are expressed in terms of the ellipticity angle ϵ and tilt angle τ of the corresponding polarization elllipse. Expressions for transforming the polarization coordinates (γ_L, δ_L), (γ_D, δ_D), or (γ_C, δ_C) into the polarization coordinates (ϵ, τ) and back can be derived using spherical trigonometry. Consider the right spherical triangle defined by the points corresponding to horizontal polarization, the polarization state W, and the polarization state $(0, \tau)$. For polarization coordinates expressed with respect to a horizontally and vertically polarized basis, the forward transformation is given by

$$\epsilon = \frac{1}{2}\sin^{-1}\left(\sin 2\gamma_L \, \sin \delta_L\right) , \tag{2.62}$$

$$\tau = \frac{1}{2}\tan^{-1}\left(\tan 2\gamma_L \, \cos \delta_L\right) , \tag{2.63}$$

while the reverse transformation is given by

$$\gamma_L = \frac{1}{2}\cos^{-1}\left(\cos 2\epsilon \, \cos 2\tau\right) , \tag{2.64}$$

$$\delta_L = \tan^{-1}\left(\tan 2\epsilon \, \csc 2\tau\right) . \tag{2.65}$$

Next, consider the right spherical triangle defined by the points corresponding to 45° linear polarization, the polarization state $W(\epsilon, \tau)$, and the polarization state $(0, \tau)$. For polarization coordinates expressed with respect to a 45° and 135° linearly polarized basis, the forward transformation is given by

$$\epsilon = \frac{1}{2} \sin^{-1} (\sin 2\gamma_D \, \sin \delta_D) \, , \tag{2.66}$$

$$\tau = -\frac{1}{2} \tan^{-1} (\cot 2\gamma_D \, \sec \delta_D) \, , \tag{2.67}$$

while the reverse transformation is given by

$$\gamma_D = \frac{1}{2} \cos^{-1} (\cos 2\epsilon \, \sin 2\tau) \, , \tag{2.68}$$

$$\delta_D = \tan^{-1} (\tan 2\epsilon \, \sec 2\tau) \, . \tag{2.69}$$

Finally, consider the right spherical triangle defined by the points corresponding to left circular polarization $(45°, 0)$, the polarization state $W(\epsilon, \tau)$, and the polarization state $(\epsilon, 0)$. For polarization coordinates expressed with respect to a left and right circularly polarized basis, the forward transformation is given by

$$\epsilon = \tan^{-1}(1) - \gamma_C \, , \tag{2.70}$$

$$\tau = \delta_C / 2 \, , \tag{2.71}$$

while the reverse transformation is given by

$$\gamma_C = \tan^{-1}(1) - \epsilon \, , \tag{2.72}$$

$$\delta_C = 2\tau \, . \tag{2.73}$$

The surface of the Poincaré sphere can be mapped onto the entire complex plane by a stereographic projection. Each polarization state is represented by a complex number which is referred to as the complex polarization ratio ρ. Rotation of the basis of the complex polarization ratio is easily accomplished if the ellipticity angle ϵ and tilt angle τ of the corresponding

polarization ellipse are known. The complex polarization ratio is related to the polarization coordinates (γ_L, δ_L), (γ_D, δ_D), and (γ_C, δ_C) by

$$\boldsymbol{\rho}_L = \rho_L\, e^{j\delta_L}\, , \tag{2.74}$$

$$\boldsymbol{\rho}_D = \rho_D\, e^{j\delta_D}\, , \tag{2.75}$$

$$\boldsymbol{\rho}_C = \rho_C\, e^{j\delta_C}\, , \tag{2.76}$$

where the polarization ratio ρ is defined by

$$\rho_L = \tan\gamma_L = a_V/a_H\, , \tag{2.77}$$

$$\rho_D = \tan\gamma_D = a_{135}/a_{45}\, , \tag{2.78}$$

$$\rho_C = \tan\gamma_C = a_R/a_L\, , \tag{2.79}$$

and the phase angle δ is defined by (2.57), (2.59), and (2.61). Together with (2.62)–(2.73), this is sufficient to define the transformation of the complex polarization ratios $\boldsymbol{\rho}_L$, $\boldsymbol{\rho}_D$, $\boldsymbol{\rho}_C$ to the polarization coordinates (ϵ, τ) and back.

Complex Polarization Vectors

The pair of complex amplitudes which arise from the representation of a plane wave as the weighted sum of orthogonally polarized basis states may be arranged to yield a complex polarization vector, e.g.,

$$\mathbf{E} = \begin{bmatrix} E_H \\ E_V \end{bmatrix}\, , \tag{2.80}$$

where E_H and E_V are the complex amplitudes which correspond to a horizontally and vertically polarized basis. Rotation of the polarization basis about the propagation vector $\hat{k}$ by an angle α is accomplished by application of a rotation operator $[R]$ to the complex polarization vector $\mathbf{E}$ to yield

$$\mathbf{E}' = [R]\,\mathbf{E}\, . \tag{2.81}$$

If the basis of the complex polarization vector is linear, the corresponding rotation operator $[R_L]$ is simply given by

$$[R_L] = \begin{bmatrix} \cos\alpha & -\sin\alpha \\ \sin\alpha & \cos\alpha \end{bmatrix}. \tag{2.82}$$

Thus,

$$\begin{bmatrix} E'_H \\ E'_V \end{bmatrix} = \begin{bmatrix} \cos\alpha & -\sin\alpha \\ \sin\alpha & \cos\alpha \end{bmatrix} \begin{bmatrix} E_H \\ E_V \end{bmatrix}, \tag{2.83}$$

and

$$\begin{bmatrix} E'_{45} \\ E'_{135} \end{bmatrix} = \begin{bmatrix} \cos\alpha & -\sin\alpha \\ \sin\alpha & \cos\alpha \end{bmatrix} \begin{bmatrix} E_{45} \\ E_{135} \end{bmatrix}. \tag{2.84}$$

If the basis of the complex polarization vector is either elliptical or circular, it must be transformed to linear before the rotation operator given by (2.82) is applied. After it has been rotated, the polarization basis can be restored to its original ellipticity by the reverse transformation. This transformation can be performed by an ellipticity operator,

$$[H] = \begin{bmatrix} \cos\epsilon & j\sin\epsilon \\ j\sin\epsilon & \cos\epsilon \end{bmatrix}, \tag{2.85}$$

which will modify the ellipticity angle of the polarization basis states which define the upper and lower element in the polarization vector by ϵ and -ϵ, respectively, without affecting their respective tilt angles [11]. Let ϵ be the ellipticity angle of the polarization basis state which defines the first element in the polarization vector. Since the basis states are orthogonal, the ellipticity angle of the polarization basis state which defines the second element in the polarization vector is given by -ϵ. Thus, the general rotation operator $[R]$ for the complex polarization vector is given by

$$[R] = [H(\epsilon)] [R_L(\alpha)] [H(-\epsilon)] \tag{2.86}$$

$$= \begin{bmatrix} \cos\epsilon & j\sin\epsilon \\ j\sin\epsilon & \cos\epsilon \end{bmatrix} \begin{bmatrix} \cos\alpha & -\sin\alpha \\ \sin\alpha & \cos\alpha \end{bmatrix} \begin{bmatrix} \cos\epsilon & -j\sin\epsilon \\ -j\sin\epsilon & \cos\epsilon \end{bmatrix}.$$

If the basis is circularly polarized, $\epsilon = \pi/4$ and the corresponding rotation operator $[R_C]$ is given by

$$[R_C] = \begin{bmatrix} e^{-j\alpha} & 0 \\ 0 & e^{j\alpha} \end{bmatrix} . \tag{2.87}$$

Thus,

$$\begin{bmatrix} E'_L \\ E'_R \end{bmatrix} = \begin{bmatrix} e^{-j\alpha} & 0 \\ 0 & e^{j\alpha} \end{bmatrix} \begin{bmatrix} E_L \\ E_R \end{bmatrix} . \tag{2.88}$$

The Stokes Vector

The Stokes vector representation of a completely polarized wave is given by

$$\mathbf{S} = \begin{bmatrix} S_0 \\ S_1 \\ S_2 \\ S_3 \end{bmatrix} = \begin{bmatrix} I \\ Q \\ U \\ V \end{bmatrix} = \begin{bmatrix} \frac{1}{2\eta}(|E_V|^2 + |E_H|^2) \\ \frac{1}{2\eta}(|E_V|^2 - |E_H|^2) \\ \frac{1}{\eta}|E_V||E_H|\cos\delta_L \\ \frac{1}{\eta}|E_V||E_H|\sin\delta_L \end{bmatrix} = I_0 \begin{bmatrix} 1 \\ \cos 2\epsilon \cos 2\tau \\ \cos 2\epsilon \sin 2\tau \\ \sin 2\epsilon \end{bmatrix} \tag{2.89}$$

where E_H, E_V, and δ_L are defined in (2.54), (2.55), and (2.57), η is the impedance of free space, I_0 is the total power carried by the wave, and ϵ and τ are the ellipticity and tilt angles of the corresponding polarization ellipse. For a completely polarized wave,

$$S_0^2 = S_1^2 + S_2^2 + S_3^2 . \tag{2.90}$$

The normalized Stokes vector is given by

$$\mathbf{s} = \begin{bmatrix} s_0 \\ s_1 \\ s_2 \\ s_3 \end{bmatrix} = \begin{bmatrix} 1 \\ \cos 2\epsilon \cos 2\tau \\ \cos 2\epsilon \sin 2\tau \\ \sin 2\epsilon \end{bmatrix} , \tag{2.91}$$

where

$$1 = s_1^2 + s_2^2 + s_3^2 . \tag{2.92}$$

Since all the elements of the Stokes vector are expressed in units of power, polarimetric data which are expressed in Stokes format can be spatially and temporally averaged with relative ease. Also, the elements of the Stokes vector are always expressed in real numbers so recourse to complex arithmetic is not required. Unlike the complex polarization vector, the Stokes vector can also represent the polarization state of quasi-monochromatic or partially polarized wave. In such cases, the Stokes vector can be resolved into a completely polarized component $\mathbf{S}_p$ and an unpolarized component $\mathbf{S}_u$ such that

$$\mathbf{S} = \mathbf{S}_p + \mathbf{S}_u \ . \tag{2.93}$$

Then,

$$\mathbf{S} = \begin{bmatrix} S_0 \\ S_1 \\ S_2 \\ S_3 \end{bmatrix} = I_0 \left(\begin{bmatrix} 1-d \\ 0 \\ 0 \\ 0 \end{bmatrix} + d \begin{bmatrix} 1 \\ \cos 2\epsilon \cos 2\tau \\ \cos 2\epsilon \sin 2\tau \\ \sin 2\epsilon \end{bmatrix} \right) = I_0 \begin{bmatrix} 1 \\ d \cos 2\epsilon \cos 2\tau \\ d \cos 2\epsilon \sin 2\tau \\ d \sin 2\epsilon \end{bmatrix} , \tag{2.94}$$

where d is the ratio of the power carried by the polarized component of wave $\mathbf{S}_p$ to the total power carried by the wave and is given by

$$d = \frac{\sqrt{S_1^2 + S_2^2 + S_3^2}}{S_0} \ , \qquad 0 \le d \le 1 \ . \tag{2.95}$$

The equivalent normalized Stokes vector is given by

$$\mathbf{s} = \begin{bmatrix} s_0 \\ s_1 \\ s_2 \\ s_3 \end{bmatrix} = \begin{bmatrix} 1-d \\ 0 \\ 0 \\ 0 \end{bmatrix} + d \begin{bmatrix} 1 \\ \cos 2\epsilon \cos 2\tau \\ \cos 2\epsilon \sin 2\tau \\ \sin 2\epsilon \end{bmatrix} = \begin{bmatrix} 1 \\ d \cos 2\epsilon \cos 2\tau \\ d \cos 2\epsilon \sin 2\tau \\ d \sin 2\epsilon \end{bmatrix} , \tag{2.96}$$

where the depolarization ratio d is given by

$$d = \sqrt{s_1^2 + s_2^2 + s_3^2} \ , \qquad 0 \le d \le 1 \ . \tag{2.97}$$

Consider rotation of the polarization basis about the propagation vector $\hat{k}$ by an angle α. Let **S** represent the Stokes vector in the original coordinate frame and let **S'** represent the Stokes vector in the new coordinate frame. From (2.94), **S'** is given by

$$
\begin{bmatrix} S_0' \\ S_1' \\ S_2' \\ S_3' \end{bmatrix} = I_0 \begin{bmatrix} 1 \\ d\cos 2\epsilon \cos 2\tau' \\ d\cos 2\epsilon \sin 2\tau' \\ d\sin 2\epsilon \end{bmatrix} . \tag{2.98}
$$

From (2.15), $\tau' = \tau - \alpha$, and

$$
\begin{bmatrix} S_0' \\ S_1' \\ S_2' \\ S_3' \end{bmatrix} = I_0 \begin{bmatrix} 1 \\ d\cos 2\epsilon \cos 2(\tau - \alpha) \\ d\cos 2\epsilon \sin 2(\tau - \alpha) \\ d\sin 2\epsilon \end{bmatrix} , \tag{2.99}
$$

$$
= I_0 \begin{bmatrix} 1 \\ d\cos 2\epsilon(\cos 2\tau \cos 2\alpha + \sin 2\tau \sin 2\alpha) \\ d\cos 2\epsilon(\sin 2\tau \cos 2\alpha - \cos 2\tau \sin 2\alpha) \\ d\sin 2\epsilon \end{bmatrix} .
$$

By inspection, (2.99) can be factored to yield

$$
\begin{bmatrix} S_0' \\ S_1' \\ S_2' \\ S_3' \end{bmatrix} = I_0 \begin{bmatrix} 1 & 0 & 0 & 0 \\ 0 & \cos 2\alpha & \sin 2\alpha & 0 \\ 0 & -\sin 2\alpha & \cos 2\alpha & 0 \\ 0 & 0 & 0 & 1 \end{bmatrix} \begin{bmatrix} 1 \\ d\cos 2\epsilon \cos 2\tau \\ d\cos 2\epsilon \sin 2\tau \\ d\sin 2\epsilon \end{bmatrix} . \tag{2.100}
$$

Thus, **S'** is related to **S** by

$$
\begin{bmatrix} S_0' \\ S_1' \\ S_2' \\ S_3' \end{bmatrix} = \begin{bmatrix} 1 & 0 & 0 & 0 \\ 0 & \cos 2\alpha & \sin 2\alpha & 0 \\ 0 & -\sin 2\alpha & \cos 2\alpha & 0 \\ 0 & 0 & 0 & 1 \end{bmatrix} \begin{bmatrix} S_0 \\ S_1 \\ S_2 \\ S_3 \end{bmatrix} . \tag{2.101}
$$

It is convenient to express (2.101) in the form

$$[S'] = [R_S] [S] ,$$
(2.102)

where $[R_S]$ is a rotation operator given by

$$[R_S] = \begin{bmatrix} 1 & 0 & 0 & 0 \\ 0 & \cos 2\alpha & \sin 2\alpha & 0 \\ 0 & -\sin 2\alpha & \cos 2\alpha & 0 \\ 0 & 0 & 0 & 1 \end{bmatrix} .$$
(2.103)

A modified form of the Stokes vector is sometimes used to simplify the formulation of radiative transfer problems, e.g., [4], [12]. From (2.89), expressions for the vertically and horizontally polarized intensity,

$$I_H = \frac{1}{2\eta}|E_V|^2 = (I + Q)/2 ,$$
(2.104)

$$I_V = \frac{1}{2\eta}|E_H|^2 = (I - Q)/2 ,$$
(2.105)

are obtained. These expressions are substituted for the first two elements of the Stokes vector to yield the modified Stokes vector $\mathbf{S}_m$,

$$\begin{bmatrix} S_{m0} \\ S_{m1} \\ S_{m2} \\ S_{m3} \end{bmatrix} = \begin{bmatrix} I_H \\ I_V \\ U \\ V \end{bmatrix} = \begin{bmatrix} \frac{1}{2\eta}(|E_V|^2) \\ \frac{1}{2\eta}(|E_H|^2) \\ \frac{1}{\eta}|E_V||E_H|\cos\delta_L \\ \frac{1}{\eta}|E_V||E_H|\sin\delta_L \end{bmatrix} = I_0 \begin{bmatrix} \frac{1}{2}(1 + d\cos 2\epsilon \cos 2\tau) \\ \frac{1}{2}(1 - d\cos 2\epsilon \cos 2\tau) \\ d\cos 2\epsilon \cos 2\tau \\ d\sin 2\epsilon \end{bmatrix} ,$$
(2.106)

which is related to the conventional Stokes vector $\mathbf{S}$ by

$$\begin{bmatrix} S_{m0} \\ S_{m1} \\ S_{m2} \\ S_{m3} \end{bmatrix} = \begin{bmatrix} \frac{1}{2} & \frac{1}{2} & 0 & 0 \\ \frac{1}{2} & -\frac{1}{2} & 0 & 0 \\ 0 & 0 & 1 & 0 \\ 0 & 0 & 0 & 1 \end{bmatrix} \begin{bmatrix} S_0 \\ S_1 \\ S_2 \\ S_3 \end{bmatrix} .$$
(2.107)

Consider rotation of the polarization basis about the propagation vector $\hat{k}$ by an angle α. Let $\mathbf{S}_m$ represent the modified Stokes vector in the original coordinate frame and let $\mathbf{S}'_m$ represent

the modified Stokes vector in the new coordinate frame. From (2.101) and (2.107), it can be shown that the rotation operator $[R_m]$ is given by

$$
[R_m] =
\begin{bmatrix}
\frac{1}{2} & \frac{1}{2} & 0 & 0 \\
\frac{1}{2} & -\frac{1}{2} & 0 & 0 \\
0 & 0 & 1 & 0 \\
0 & 0 & 0 & 1
\end{bmatrix}
\begin{bmatrix}
1 & 0 & 0 & 0 \\
0 & \cos 2\alpha & \sin 2\alpha & 0 \\
0 & -\sin 2\alpha & \cos 2\alpha & 0 \\
0 & 0 & 0 & 1
\end{bmatrix}
\begin{bmatrix}
\frac{1}{2} & \frac{1}{2} & 0 & 0 \\
\frac{1}{2} & -\frac{1}{2} & 0 & 0 \\
0 & 0 & 1 & 0 \\
0 & 0 & 0 & 1
\end{bmatrix}^{-1},
$$

$$
=
\begin{bmatrix}
\cos^2 \alpha & \sin^2 \alpha & \frac{1}{2}\sin 2\alpha & 0 \\
\sin^2 \alpha & \cos^2 \alpha & -\frac{1}{2}\sin 2\alpha & 0 \\
-\sin 2\alpha & \sin 2\alpha & \cos 2\alpha & 0 \\
0 & 0 & 0 & 1
\end{bmatrix}.
\tag{2.108}
$$

Thus, $\mathbf{S}'_m$ is related to $\mathbf{S}$ by

$$
\begin{bmatrix}
S'_{m0} \\
S'_{m1} \\
S'_{m2} \\
S'_{m3}
\end{bmatrix}
=
\begin{bmatrix}
\cos^2 \alpha & \sin^2 \alpha & \frac{1}{2}\sin 2\alpha & 0 \\
\sin^2 \alpha & \cos^2 \alpha & -\frac{1}{2}\sin 2\alpha & 0 \\
-\sin 2\alpha & \sin 2\alpha & \cos 2\alpha & 0 \\
0 & 0 & 0 & 1
\end{bmatrix}
\begin{bmatrix}
S_{m0} \\
S_{m1} \\
S_{m2} \\
S_{m3}
\end{bmatrix}.
\tag{2.109}
$$

A third variant of the Stokes vector is used to define the data format employed by the JPL polarimetric imager [4]. The JPL Stokes vector $\mathbf{S}_j$ is given by

$$
\begin{bmatrix}
S_{j0} \\
S_{j1} \\
S_{j2} \\
S_{j3}
\end{bmatrix}
=
\begin{bmatrix}
\frac{1}{2\eta}(|E_H|^2 + |E_V|^2) \\
\frac{1}{2\eta}(|E_H|^2 - |E_V|^2) \\
-\frac{1}{\eta}|E_V||E_H|\cos \delta_L \\
\frac{1}{\eta}|E_V||E_H|\sin \delta_L
\end{bmatrix}
= I_0
\begin{bmatrix}
1 \\
-d\cos 2\epsilon \cos 2\tau \\
-d\cos 2\epsilon \sin 2\tau \\
d\sin 2\epsilon
\end{bmatrix},
\tag{2.110}
$$

and is related to the conventional Stokes vector $\mathbf{S}$ by

$$
\begin{bmatrix}
S_{j0} \\
S_{j1} \\
S_{j2} \\
S_{j3}
\end{bmatrix}
=
\begin{bmatrix}
1 & 0 & 0 & 0 \\
0 & -1 & 0 & 0 \\
0 & 0 & -1 & 0 \\
0 & 0 & 0 & 1
\end{bmatrix}
\begin{bmatrix}
S_0 \\
S_1 \\
S_2 \\
S_3
\end{bmatrix}.
\tag{2.111}
$$

Consider rotation of the polarization basis about the propagation vector $\hat{k}$ by an angle α. Let $\mathbf{S}_j$ represent the JPL Stokes vector in the original coordinate frame and let $\mathbf{S}'_j$ represent the JPL Stokes vector in the new coordinate frame. From (2.103) and (2.111), it can be shown that the rotation operator $[R_j]$ is given by

$$[R_j] = \begin{bmatrix} 1 & 0 & 0 & 0 \\ 0 & -1 & 0 & 0 \\ 0 & 0 & -1 & 0 \\ 0 & 0 & 0 & 1 \end{bmatrix} \begin{bmatrix} 1 & 0 & 0 & 0 \\ 0 & \cos 2\alpha & \sin 2\alpha & 0 \\ 0 & -\sin 2\alpha & \cos 2\alpha & 0 \\ 0 & 0 & 0 & 1 \end{bmatrix} \begin{bmatrix} 1 & 0 & 0 & 0 \\ 0 & -1 & 0 & 0 \\ 0 & 0 & -1 & 0 \\ 0 & 0 & 0 & 1 \end{bmatrix}^{-1},$$

$$= \begin{bmatrix} 1 & 0 & 0 & 0 \\ 0 & \cos 2\alpha & \sin 2\alpha & 0 \\ 0 & -\sin 2\alpha & \cos 2\alpha & 0 \\ 0 & 0 & 0 & 1 \end{bmatrix}. \tag{2.112}$$

Thus, $\mathbf{S}'_j$ is related to $\mathbf{S}_j$ by

$$\begin{bmatrix} S'_{j0} \\ S'_{j1} \\ S'_{j2} \\ S'_{j3} \end{bmatrix} = \begin{bmatrix} 1 & 0 & 0 & 0 \\ 0 & \cos 2\alpha & \sin 2\alpha & 0 \\ 0 & -\sin 2\alpha & \cos 2\alpha & 0 \\ 0 & 0 & 0 & 1 \end{bmatrix} \begin{bmatrix} S_{j0} \\ S_{j1} \\ S_{j2} \\ S_{j3} \end{bmatrix}. \tag{2.113}$$

The Coherency Matrix

The coherency matrix is another method for representing the polarization state of a partially polarized wave which is sometimes used [5], [6], [13]. In terms of the Stokes vector, the elements of the coherency matrix are given by

$$[J] = \begin{bmatrix} J_{11} & J_{12} \\ J_{21} & J_{22} \end{bmatrix} = \begin{bmatrix} \frac{1}{2}(S_0 + S_1) & \frac{1}{2}(S_2 + jS_3) \\ \frac{1}{2}(S_2 - jS_3) & \frac{1}{2}(S_0 - S_1) \end{bmatrix}. \tag{2.114}$$

Substitution of the expressions for S_0, S_1, S_2, and S_3 given in (2.94) into (2.114) yields an expression for the coherency matrix in terms of the wave intensity I_0, the ellipticity angle ϵ and

tilt angle τ of the polarized component of the wave and the depolarization ratio d,

$$[J] = I_0 \begin{bmatrix} \frac{1}{2}(1 + d\cos 2\epsilon \cos 2\tau) & \frac{1}{2}d(\cos 2\epsilon \sin 2\tau + j\sin 2\epsilon) \\ \frac{1}{2}d(\cos 2\epsilon \sin 2\tau - j\sin 2\epsilon) & \frac{1}{2}(1 - d\cos 2\epsilon \cos 2\tau) \end{bmatrix}. \qquad (2.115)$$

The coherency matrix can be resolved into polarized and unpolarized components,

$$[J] = [J_u] + [J_p], \qquad (2.116)$$

to give

$$[J] = I_0 \begin{bmatrix} 0 & 1-d \\ 1-d & 0 \end{bmatrix} + I_0 d \begin{bmatrix} \frac{1}{2}(1 + \cos 2\epsilon \cos 2\tau) & \frac{1}{2}(\cos 2\epsilon \sin 2\tau + j\sin 2\epsilon) \\ \frac{1}{2}(\cos 2\epsilon \sin 2\tau - j\sin 2\epsilon) & \frac{1}{2}(1 - \cos 2\epsilon \cos 2\tau) \end{bmatrix}. \qquad (2.117)$$

Consider rotation of the polarization basis about the propagation vector $\hat{k}$ by an angle α. Let $[J]$ represent the coherency matrix in the original coordinate frame and let $[J']$ represent the coherency matrix in the new coordinate frame. Since the unpolarized component $[J_u]$ is invariant under rotation of the polarization basis,

$$\begin{bmatrix} J'_{u11} & J'_{u12} \\ J'_{u21} & J'_{u22} \end{bmatrix} = \begin{bmatrix} J_{u11} & J_{u12} \\ J_{u21} & J_{u22} \end{bmatrix}, \qquad (2.118)$$

and only transformation of the polarized component $[J_p]$ need be considered. In the new coordinate frame, $[J'_p]$ is given by

$$\begin{bmatrix} J'_{p11} & J'_{p12} \\ J'_{p21} & J'_{p22} \end{bmatrix} = I_0 d \begin{bmatrix} \frac{1}{2}(1 + \cos 2\epsilon \cos 2\tau') & \frac{1}{2}(\cos 2\epsilon \sin 2\tau' + j\sin 2\epsilon) \\ \frac{1}{2}(\cos 2\epsilon \sin 2\tau' - j\sin 2\epsilon) & \frac{1}{2}(1 - d\cos 2\epsilon \cos 2\tau') \end{bmatrix}. \qquad (2.119)$$

From (2.15), $\tau' = \tau - \alpha$ and

$$\begin{bmatrix} J'_{p11} & J'_{p12} \\ J'_{p21} & J'_{p22} \end{bmatrix} = I_0 d \begin{bmatrix} \frac{1}{2}(1 + \cos 2\epsilon \cos 2(\tau - \alpha)) & \frac{1}{2}(\cos 2\epsilon \sin 2(\tau - \alpha) + j\sin 2\epsilon) \\ \frac{1}{2}(\cos 2\epsilon \sin 2(\tau - \alpha) - j\sin 2\epsilon) & \frac{1}{2}(1 - \cos 2\epsilon \cos 2(\tau - \alpha)) \end{bmatrix}, \qquad (2.120)$$

With a little effort, (2.120) can be factored to yield

$$\begin{bmatrix} J'_{p11} & J'_{p12} \\ J'_{p21} & J'_{p22} \end{bmatrix} = \begin{bmatrix} \cos \alpha & \sin \alpha \\ -\sin \alpha & \cos \alpha \end{bmatrix} \begin{bmatrix} J_{p11} & J_{p12} \\ J_{p21} & J_{p22} \end{bmatrix} \begin{bmatrix} \cos \alpha & -\sin \alpha \\ \sin \alpha & \cos \alpha \end{bmatrix}. \qquad (2.121)$$

Thus, from (2.118) and (2.121), it can be shown that $[J']$ is related to $[J]$ by

$$
\begin{bmatrix} J'_{11} & J'_{12} \\ J'_{21} & J'_{22} \end{bmatrix} = \begin{bmatrix} \cos\alpha & \sin\alpha \\ -\sin\alpha & \cos\alpha \end{bmatrix} \begin{bmatrix} J_{11} & J_{12} \\ J_{21} & J_{22} \end{bmatrix} \begin{bmatrix} \cos\alpha & -\sin\alpha \\ \sin\alpha & \cos\alpha \end{bmatrix} . \tag{2.122}
$$

Polarization Scattering Operators

The scattering cross section σ of a target is defined as the area intercepting that amount of power which, when scattered isotropically, would produce an echo equal to that actually returned by the target. Thus,

$$
\sigma = \lim_{r \to \infty} 4\pi r^2 \frac{|\mathbf{E}^s|^2}{|\mathbf{E}^i|^2} , \tag{2.123}
$$

where $\mathbf{E}^i$ is the incident electric field, $\mathbf{E}^s$ is the scattered electric field, and r is the range at which the scattered field is measured. Radar cross section refers to that portion of the scattering cross section which is associated with a specified polarization component of the scattered wave and is a function of the size, shape, composition, and orientation of the target, the frequency of the incident wave, and the polarization state of the radar transmitting and receiving antennas.

The relationship between the polarization states of the incident and scattered fields can be described by a polarization scattering operator expressed in matrix form. Following the definition of scattering cross section presented in (2.123), the polarization scattering matrix $[S]$ relates incident and scattered fields which have been expressed as complex polarization vectors, i.e.,

$$
\begin{bmatrix} E_1^s \\ E_2^s \end{bmatrix} = \frac{e^{-jkr}}{\sqrt{4\pi r}} \begin{bmatrix} S_{11} & S_{12} \\ S_{21} & S_{22} \end{bmatrix} \begin{bmatrix} E_1^i \\ E_2^i \end{bmatrix} . \tag{2.124}
$$

When defined with respect to a horizontally and vertically polarized basis, the polarization scattering matrix can also be used to relate incident and scattered fields which have been expressed as coherency matrices, i.e.,

$$
\begin{bmatrix} J_{11}^s & J_{12}^s \\ J_{21}^s & J_{22}^s \end{bmatrix} = \frac{1}{4\pi r^2} \begin{bmatrix} S_{HH} & S_{HV} \\ S_{VH} & S_{VV} \end{bmatrix} \begin{bmatrix} J_{11}^i & J_{12}^i \\ J_{21}^i & J_{22}^i \end{bmatrix} \begin{bmatrix} S_{HH}^* & S_{HV}^* \\ S_{VH}^* & S_{VV}^* \end{bmatrix}^T . \tag{2.125}
$$

The Mueller matrix $[L]$ relates incident and scattered fields which have been expressed as Stokes vectors, i.e.,

$$
\begin{bmatrix} S_0^s \\ S_1^s \\ S_2^s \\ S_3^s \end{bmatrix} = \frac{1}{4\pi r^2} \begin{bmatrix} L_{11} & L_{12} & L_{13} & L_{14} \\ L_{21} & L_{22} & L_{23} & L_{24} \\ L_{31} & L_{32} & L_{33} & L_{34} \\ L_{41} & L_{42} & L_{43} & L_{44} \end{bmatrix} \begin{bmatrix} S_0^i \\ S_1^i \\ S_2^i \\ S_3^i \end{bmatrix} . \tag{2.126}
$$

There are three principal variants of the Mueller matrix which correspond to the conventional, modified, and JPL Stokes vectors, respectively. In practice, polarization scattering matrices and Mueller matrices are often normalized by factoring out the scattering cross section of the target and the range dependence of the response. Other polarization scattering operators which are derived from the polarization scattering matrix and the Mueller matrix, such as the covariance matrix and the Stokes scattering operator, are used in computationally efficient methods for synthesizing arbitrary polarization responses from experimental data [4].

It is convenient to describe scattering problems with respect to a coordinate frame which is centered on the scatterer. The local coordinate systems used to define the polarization state of the incident and scattered fields are specified in a manner similar to that presented in section 2.2 for the case of a single propagating wave. However, it is also necessary to specify the relationship between the local coordinate systems. According to the *forward scatter alignment* (FSA) convention, the propagation vectors of the incident and scattered fields are aligned with the direction of propagation while according to *backscatter alignment* (BSA) convention, they always point towards the scatterer. While the expressions for the incident field are identical under both conventions, the expressions for the scattered field and, by extension, the corresponding polarization scattering operator, are not. The coordinate systems and scattering geometries corresponding to the FSA and BSA conventions are depicted in Figures 2.10 and 2.11, respectively. The subscripts i and s refer to fields expressed with respect to the FSA convention while the subscripts t and r refer to fields expressed with respect to the BSA convention. The unit
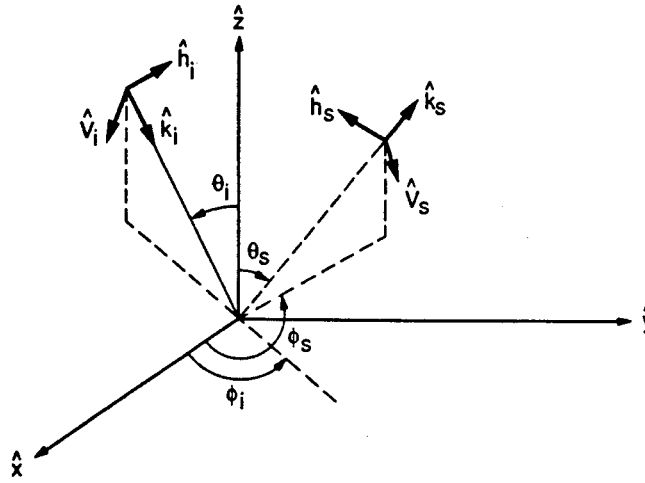
Figure 2.10: Coordinate systems and scattering geometry for the forward scattering alignment (FSA) convention. (after [4], p. 18])
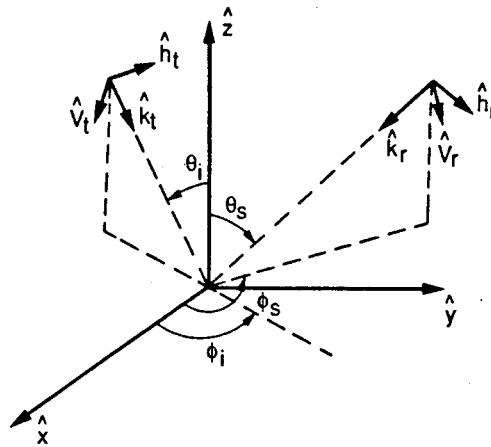
Figure 2.11: Coordinate systems and scattering geometry for the backscatter alignment (BSA) convention. (after [4], p. 18])

vectors in the local coordinate system for the incident (or transmitted) field are given by

$$\hat{k}_t = \hat{k}_i = \frac{\mathbf{k}}{k} \equiv -\hat{r} = -\cos\phi_i\sin\theta_i\,\hat{x} - \sin\phi_i\sin\theta_i\,\hat{y} - \cos\theta_i\,\hat{z}\,, \quad (2.127)$$

$$\hat{h}_t = \hat{h}_i = -\frac{\hat{z}\times\hat{k}}{|\hat{z}\times\hat{k}|} \equiv \hat{\phi} = -\sin\phi_i\,\hat{x} + \cos\phi_i\,\hat{y}\,, \quad (2.128)$$

$$\hat{v}_t = \hat{v}_i = \hat{k}\times\hat{h} \equiv -\hat{\theta} = -\cos\phi\cos\theta\,\hat{x} - \sin\phi\cos\theta\,\hat{y} + \sin\theta\,\hat{z}\,, \quad (2.129)$$

while the corresponding unit vectors for the scattered (or received) field are given by

$$\hat{k}_r = -\hat{k}_s = \frac{\mathbf{k}}{k} \equiv -\hat{r} = -\cos\phi_s\sin\theta_s\,\hat{x} - \sin\phi_s\sin\theta_s\,\hat{y} - \cos\theta_s\,\hat{z}\,, \quad (2.130)$$

$$\hat{h}_r = -\hat{h}_s = \frac{\hat{z}\times\hat{k}}{|\hat{z}\times\hat{k}|} \equiv -\hat{\phi} = \sin\phi_s\,\hat{x} - \cos\phi_s\,\hat{y}\,, \quad (2.131)$$

$$\hat{v}_r = \hat{v}_s = \hat{k}\times\hat{h} \equiv -\hat{\theta} = -\cos\phi_s\cos\theta_s\,\hat{x} - \sin\phi_s\cos\theta_s\,\hat{y} + \sin\theta_s\,\hat{z}\,. \quad (2.132)$$

Since the coordinate systems $(\hat{k}_t, \hat{h}_t, \hat{v}_t)$ and $(\hat{k}_r, \hat{h}_r, \hat{v}_r)$ are coincident when the transmitting and receiving antennas are collocated, the BSA convention is a particularly convenient choice for use in radar scattering problems. Unless otherwise stated, the BSA convention will be the convention used in the remainder of this study.

Once the local coordinate systems for the incident and scattered fields have been defined, it is a simple matter to apply the results derived earlier in this section to the problem of rotating the basis of either the polarization scattering matrix or the Mueller matrix about the radial vector $\hat{r}$ by an angle α. Since the propagation vector $\hat{k} = -\hat{r}$, this transformation is equivalent to rotating the polarization basis about $\hat{k}$ by an angle $-\alpha$. Let $[S]$ represent the normalized polarization scattering matrix in the original coordinate frame and let $[S']$ represent the normalized polarization scattering matrix in the new coordinate frame. The corresponding scattering equations are given by

$$\mathbf{E}^s = [S]\,\mathbf{E}^i\,, \quad (2.133)$$

$$\mathbf{E}^{s'} = [S']\,\mathbf{E}^{i'}\,. \quad (2.134)$$

Since the rotation operator $[R]$ is a unitary matrix,

$$R[(\alpha)]^{-1} = [R(-\alpha)] \tag{2.135}$$

and

$$\mathbf{E}^{s'} = [R]^{-1} \mathbf{E}^s , \tag{2.136}$$

$$\mathbf{E}^{i'} = [R]^{-1} \mathbf{E}^i , \tag{2.137}$$

where expressions for the rotation operator $[R]$ which are appropriate for use with complex polarization vectors having linearly polarized, circularly polarized, or arbitrarily polarized basis states are given by (2.82), (2.87), and (2.86), respectively. Multiplying both sides of (2.136) and (2.137) by $[R]$ yields

$$\mathbf{E}^s = [R] \mathbf{E}^{s'} , \tag{2.138}$$

$$\mathbf{E}^i = [R] \mathbf{E}^{i'} . \tag{2.139}$$

Substituting (2.138) and 2.(139) into (2.133) gives

$$[R] \mathbf{E}^{s'} = [S] [R] \mathbf{E}^{i'} . \tag{2.140}$$

Multiplying both sides by $[R]^{-1}$ gives

$$[R]^{-1} [R] \mathbf{E}^{s'} = [R]^{-1} [S] [R] \mathbf{E}^{i'} , \tag{2.141}$$

which simplifies to

$$\mathbf{E}^{s'} = [R]^{-1} [S] [R] \mathbf{E}^{i'} . \tag{2.142}$$

Thus, by equating (2.134) and (2.142), it can be shown that $[S']$ and $[S]$ are related by

$$[S'] = [R]^{-1} [S] [R] . \tag{2.143}$$

In a similar fashion, it can be be shown that a Mueller matrix $[L']$ in the new coordinate frame is related to the Mueller matrix $[L]$ in the original coordinate frame by

$$[L'] = [R_S]^{-1} [L] [R_S] , \tag{2.144}$$

where expressions for the rotation operator $[R_S]$ which are appropriate for use with conventional, modified, and JPL Stokes vectors are given by (2.94), (2.106), and (2.110), respectively.

2.6 Conclusions

It has been shown that transformation of a polarization descriptor between coordinate frames corresponds to rotation of its polarization basis by a prescribed angle which is a function of both the transformation matrix that relates the two coordinate frames and the direction of propagation. Two methods for determining the angle of rotation for the case in which the local vertical is defined by the $\hat{z}$ direction in each frame have been derived using spherical trigonometry and vector algebra, respectively. Both methods are robust and will yield the correct result but the method based on vector algebra is more compact and would be easier to implement in software. Although the elements of the coordinate transformation matrix can be determined from either the relative directions of the three principal axes in each coordinate frame or the Euler angles which define a series of rotations which will transform one coordinate frame into the other, in practice it may be difficult to obtain these parameters. A third method has been derived which overcomes this limitation by allowing the elements of the coordinate transformation matrix to be determined from any pair of directions which have been expressed in terms of both coordinate frames. Algorithms for rotating the basis of several commonly used polarization descriptors, including polarization coordinates, the complex polarization ratio, the complex polarization vector, the Stokes vector and several of its variants, the coherency matrix, the polarization scattering matrix, and the Mueller matrix have been derived.

References

[1] R.M.A. Azzam and N.M. Bashara, *Ellipsometry and Polarized Light.* Amsterdam: North-Holland, 1977.

[2] S.R. Cloude, "Polarimetric techniques in radar signal processing," *Microwave J.*, vol. 26, no. 7, pp. 119–127, July 1983.

[3] J.D. Kraus, *Antennas,* 2nd ed. New York: McGraw-Hill, 1988, pp. 70–81.

[4] F.T. Ulaby and C. Elachi, Eds., *Radar Polarimetry for Geoscience Applications.* Norwood, MA: Artech House, 1990, pp. 1–52.

[5] W.L. Stutzman, *Polarization in Electromagnetic Systems.* Norwood, MA: Artech House, 1992.

[6] H.A. Mott, *Antennas for Radar and Communications: A Polarimetric Approach.* New York: Wiley, 1992.

[7] C.K. Krichbaum, "Radar cross-section measurements," in *Radar Cross Section Handbook.* (G.T. Ruck *et al.*, Eds.) vol. 2, New York: Plenum, 1970, pp. 893–896.

[8] *IEEE Standard Test Procedures for Antennas.* (ANSI/IEEE Std 149–1979.) New York: IEEE, 1979.

[9] W.T. Thomson, *Introduction to Space Dynamics.* New York: Wylie, 1961, pp. 33–37.

[10] R.R. Bate, D.D. Mueller, and J.E. White, *Fundamentals of Astrodynamics.* New York: Dover, 1971, pp. 74–83.

[11] S.H. Bickel, "Some invariant properties of the polarization scattering matrix," *Proc. IEEE,* vol. 53, pp. 1070–1072, Aug. 1965.

[12] S. Chandrasekhar, *Radiative Transfer.* New York: Dover, 1960, pp. 24–35.

[13] M. Born and E. Wolf, *Principles of Optics.* New York: Pergamon, 1965, pp. 545–553.

Chapter 3

TRUNCATION AND COMPENSATION OF
TRIHEDRAL CORNER REFLECTORS

3.1 Introduction

A trihedral corner reflector is a reentrant structure formed by the intersection of three mutually orthogonal reflecting panels. In general, a ray incident upon one of its interior surfaces will undergo reflection from each of the others in succession and will be returned to the source. Although other scattering mechanisms contribute to the response, triple-bounce reflections from the interior of the reflector dominate over most directions of incidence. Since trihedral corner reflectors present a large scattering cross section over a wide angular range, are mechanically rugged, and can be manufactured with relative ease, they are widely used in radar navigation and remote sensing as location markers and calibration targets. The relative sizes of trihedral corner reflectors in common use are compared in Figure 3.1.
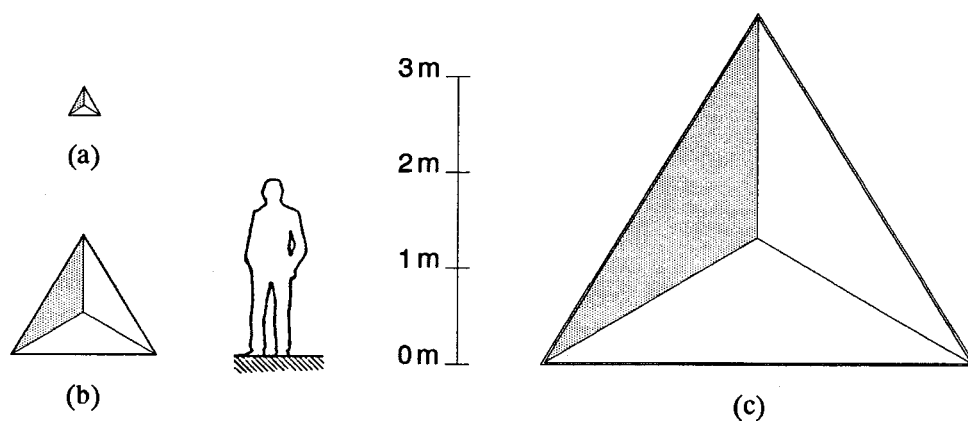
Figure 3.1: Relative sizes of trihedral corner reflectors used as location markers and calibration targets in (a) radar navigation, (b) radar-assisted positioning, and (b/c) radar remote sensing.

The dependence of the scattering cross section and angular coverage of a trihedral corner reflector on the size and shape of its reflecting panels has been recognized since the advent of radar. In the 1940's and 50's, closed-form expressions for the contribution of triple-bounce reflections to the response of trihedral corner reflectors with triangular, elliptical or rectangular panels with corners of arbitrary length were derived [1]–[3]. Although it was apparent that a wide variety of response characteristics could be obtained by appropriate shaping of the reflecting panels, a procedure which Robertson [4], [5] referred to as *truncation and compensation*, work in this area was not pursued due to the lack of either suitable methods for determining the response of a trihedral corner reflector with panels of completely arbitrary shape or a need for physically large targets which would benefit from such modifications. In recent years, interest in altering the response of trihedral corner reflectors in this manner has been renewed by a requirement for physically large targets to serve as location markers and calibration targets in radar navigation and remote sensing [6]–[9]. However, very little design data and related material to guide the development of such reflectors are available in the literature.

In section 3.2, the problem of predicting the response of a trihedral corner reflector with panels of completely arbitrary shape is considered and an efficient and robust numerical method for solving Robertson's model for the equivalent flat plate area of a trihedral corner reflector is proposed. In section 3.3, the response characteristics of a selected set of trihedral corner reflectors which present three-fold symmetry are compared. In section 3.4, the response characteristics of trihedral corner reflectors which present bilateral symmetry are considered and the possibility of increasing the beamwidth of the response of such reflectors in one principal plane relative to the beamwidth in the orthogonal plane by modifying the size and shape of the reflecting panels in a suitable manner is examined. Design curves for bilaterally symmetric reflectors which are composed solely of triangular, elliptical, or rectangular reflecting panels are given. The response characteristics of a selected set of bilaterally symmetric reflectors which are composed of combinations of panels with various shapes including triangular, circular, and square are compared. A related problem, the design of top hat reflectors with specified response characteristics, is considered in Appendix A.

3.2 Analysis

A rigorous solution for the scattering cross section of a trihedral corner reflector must account for the contributions of single, double, and triple-bounce reflections from the interior of the reflector, deviations of the reflecting panels from perfect flatness and mutual orthogonality, and diffraction by the panel edges. Numerical techniques such as the finite-difference time-domain (FD-TD) and the shooting and bouncing ray (SBR) methods have been successfully applied to the problem and can account for most contributions to the response. However, calculating the response of a large target is extremely demanding and access to some type of supercomputer or massively parallel processor is generally required [10], [11]. In the case of an ideal reflector with reflecting panels which are perfectly flat and mutually orthogonal, the problem can be simplified considerably. A reasonably complete solution can be obtained by using physical optics (PO) to account for the contribution of reflections from the interior of the reflector while using the method of equivalent currents (MEC) to account for first order diffraction from the edges [12]. Alternatively, a hybrid approach which permits application of the Uniform Theory of Diffraction (UTD) to the problem can be employed [13]. However, neither of these techniques can be easily applied to reflectors with panels of completely arbitrary shape.

For the purposes of designing trihedral corner reflectors with specified response characteristics, it is usually sufficient to account for the contribution of triple-bounce reflections from the interior since they completely dominate the response for most directions of incidence. If the reflector is ideal, a ray which is incident upon one of the interior surfaces will generally undergo reflection from each of the others in succession and will be returned to the source. However, the reflecting panels are of finite extent and some rays will fail to intercept one or more of the panels and will be lost. The equivalent flat plate area A of the reflector can be determined by launching a set of parallel rays towards the target, tracing each ray as it is reflected by each of the interior surfaces, and projecting that portion of the reflector which contributes to the backscatter response onto a view plane which is normal to the direction of incidence, as suggested by Figure 3.2. The scattering cross section σ of the reflector is related to its equivalent

(a)   (b)   (c)
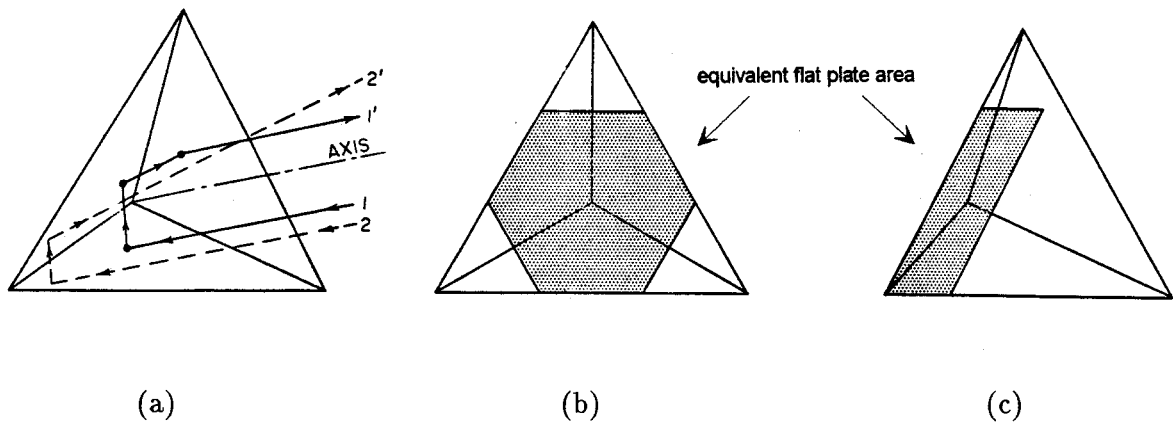
Figure 3.2: Scattering by a trihedral corner reflector with triangular panels. (a) Alternative ray paths. Path 1-1' represents a ray which has undergone triple-bounce reflection back to the source while path 2-2' represents a ray which has undergone double-bounce reflection and been scattered in a different direction. (b) The equivalent flat plat area of the reflector for incidence along the symmetry axis. (c) The equivalent flat plat area for incidence off the symmetry axis. (from [5], p. 13-11)
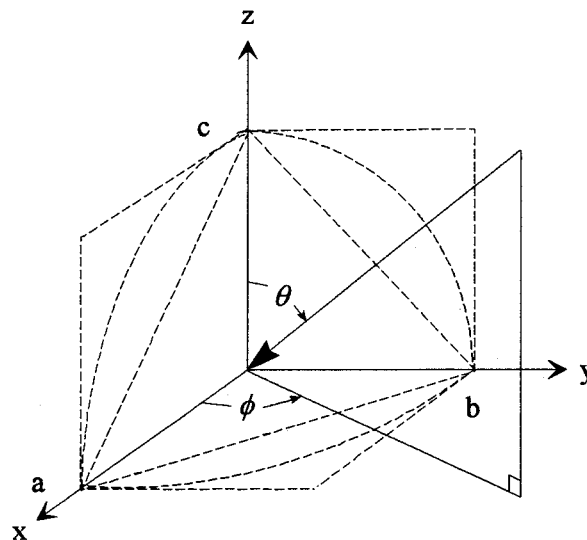
Figure 3.3: Problem geometry and coordinate system for scattering by a trihedral corner reflector composed of triangular, elliptical, or rectangular panels with corners of arbitrary length.
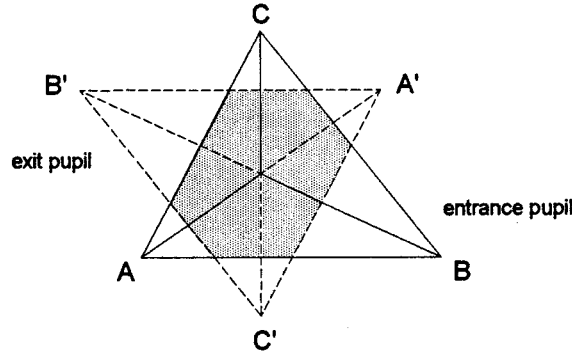
Figure 3.4: Spencer's model for the equivalent flat plate area of a trihedral corner reflector. In this example, the intersection of the entrance pupil ABC and exit pupil $A'B'C'$ gives the equivalent flat plat area of a trihedral corner reflector with triangular panels for incidence off the symmetry axis.

flat plate area A by the physical optics relation,

$$\sigma = 4\pi \frac{A^2}{\lambda^2} , \tag{3.1}$$

where λ is the wavelength of the incident wave.

It is convenient to describe scattering by a trihedral corner reflector with respect to the coordinate frame shown in Figure 3.3. Spencer [1] empirically derived a simple geometric model for predicting the equivalent flat plate area of an ideal trihedral corner reflector based on experiments that he conducted with reflectors fabricated from optical mirrors. In the model, the polygon which defines the outside edges of the reflecting panels and its inverted image are projected onto a view plane which is normal to the direction of incidence. The inverted image is obtained by projecting the original polygon through the apex of the reflector. The projection and its inverted image are referred to as the *entrance pupil* and *exit pupil* of the reflector, respectively. An example for the case of a reflector with triangular panels is shown in Figure 3.4. According to the model, the equivalent flat plate area of the reflector is the area common to the two pupils. Using this model, Spencer derived closed-form expressions for the response of trihedral corner reflectors composed of triangular and square panels with equal corner lengths.

Later, these were extended to the case of trihedral corner reflectors composed of triangular, elliptical, or rectangular panels with unequal corner lengths by Siegel *et al.* [2], [3]. In their formulation, the procedure for calculating the equivalent flat plate area of a reflector begins with determination of the intermediate quantities p, q, and r from the relations

$$p = \frac{\sin\theta\sin\phi}{a}, \tag{3.2}$$

$$q = \frac{\sin\theta\cos\phi}{b}, \tag{3.3}$$

$$r = \frac{\sin\theta\sin\phi}{c}, \tag{3.4}$$

where a, b, and c are the corner lengths of the reflector along the x, y, and z axes, respectively, and the direction of incidence is given by the angles θ and ϕ as depicted in Figure 3.3. The values given to p, q, and r are then reassigned in order of increasing magnitude such that $|p| \leq |q| \leq |r|$. For a reflector with triangular panels, the equivalent flat plate area is given by

$$A = \begin{cases} abc\left[p + q + r - 2\dfrac{p^2 + q^2 + r^2}{p + q + r}\right], & p + q \geq r, \\[4mm] 4abc\left[\dfrac{pq}{p + q + r}\right], & p + q \leq r, \end{cases} \tag{3.5}$$

while for a reflector with elliptical panels, the area is given by

$$A = \begin{cases} abc\left[\sqrt{L}\tan^{-1}\left(\dfrac{(M+N)^2 - L^2}{4L\sqrt{MN}}\right) + \sqrt{L}\tan^{-1}\left(\dfrac{(M+N)^2 - L^2}{4L\sqrt{MN}}\right) \right. \\[4mm] \qquad\qquad \left. + \sqrt{L}\tan^{-1}\left(\dfrac{(M+N)^2 - L^2}{4L\sqrt{MN}}\right)\right], & L + M \geq N, \\[4mm] abc\left[\sqrt{M}\tan^{-1}\left(\dfrac{2\sqrt{LN}}{M+N-L}\right) + \sqrt{L}\tan^{-1}\left(\dfrac{2\sqrt{MN}}{L-M+N}\right)\right], & L + M \leq N, \end{cases} \tag{3.6}$$

where $L = p^2$, $M = q^2$, and $N = r^2$. For a reflector with rectangular panels, the equivalent flat plate area is simply given by

$$A = \begin{cases} abc\,p\,(4 - r/q), & q \geq r/2, \\[2mm] 4abc\,(pq/r), & q \leq r/2. \end{cases} \tag{3.7}$$

These closed-form expressions permit rapid and efficient computation of the equivalent flat plate area of trihedral corner reflectors with panels having certain specific shapes. In order to apply Spencer's model to trihedral corner reflectors with panels having more general shapes Keen [14], [15] devised a numerical method for determining the size and shape of the polygon defined by the intersection of the entrance and exit pupils.

Although Spencer's model accurately predicts the equivalent flat plate area of trihedral corner reflectors with many different panel geometries, it may fail without indication when applied to reflectors with panels of completely arbitrary shape. This was first noticed by Robertson [4] who proposed an alternative geometric model which will always yield the correct solution. Robertson's model is based on the observation that the absolute values of the coordinates at which a ray incident from a given direction intersects the three planes defined by the trihedral axes are identical to the coordinates which define the points of reflection of the ray when it is incident upon one of the interior surfaces of a trihedral corner reflector. A physical implementation of Robertson's model is presented in Figure 3.5. Consider the trihedral corner reflector with panels of arbitrary shape which is shown in Figure 3.5(a). First, the panels of the reflector are replaced by complementary apertures which are derived from each reflecting panel by reflection about the trihedral axes as shown in Figure 3.5(b). The optical model which results is shown in Figure 3.5(c). To the observer, the polygons defined by the three complementary apertures are projected onto a view plane which is normal to the direction of incidence. The area common to all three polygons is the equivalent flat plate area of the reflector.

Examples of trihedral corner reflectors for which Spencer's model gives accurate predictions of the equivalent flat plate area are shown in Figure 3.6 while examples for which the predictions are erroneous are shown in Figure 3.7. From these cases, it appears that Spencer's model will give the correct result if the projections of all three complementary apertures in Robertson's model are convex polygons. However, if one or more of the aperture polygons is concave, it is possible that Spencer's model will fail without indication and give an incorrect result which will be larger than the actual value. Although a more formal study of the conditions under which Spencer's model fails was not pursued, it is clear that Keen's numerical implementation is *not* suitable for use with trihedral corner reflectors with panels of completely arbitrary shape.

(a)

(b)

(c)
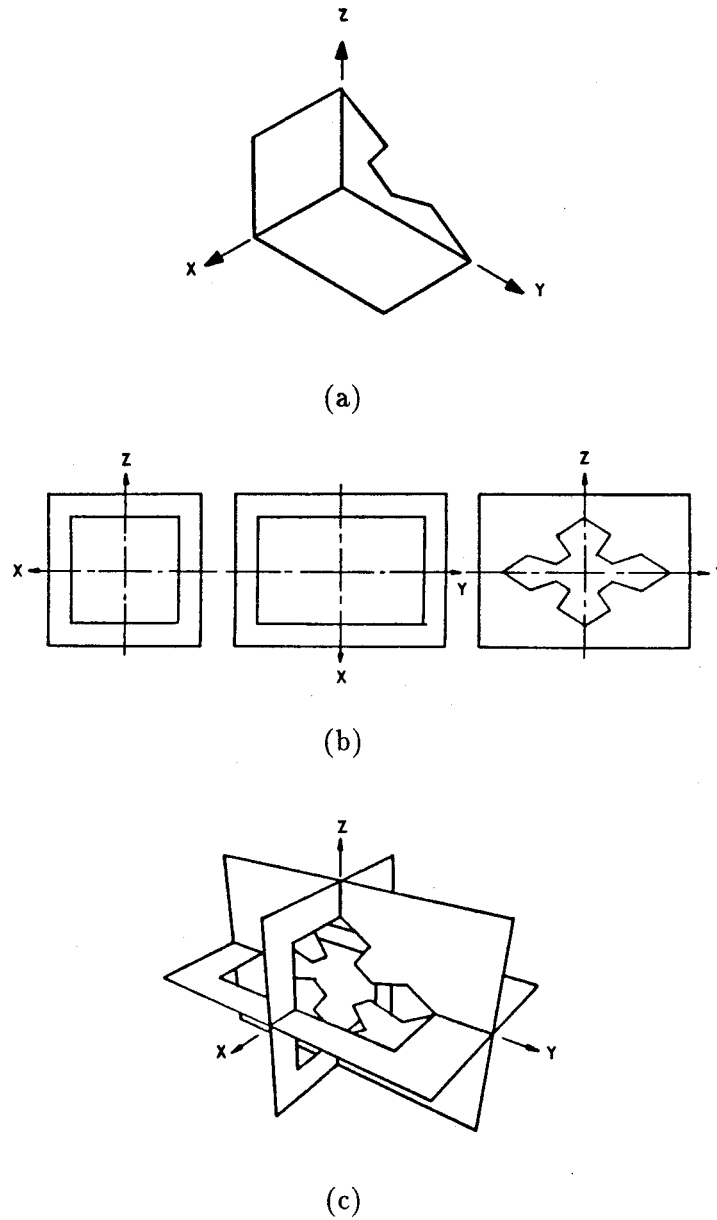
Figure 3.5: A physical implementation of Robertson's model for the contribution of triple-bounce reflections to the response of a trihedral corner reflector. (a) A trihedral corner reflector with panels of arbitrary shape. (b) Aperture planes derived from each panel by reflection about the trihedral axes. (c) An optical model for the equivalent flat plate area of a trihedral corner reflector. (from [16, p. 240])

(a)   (b)   (c)
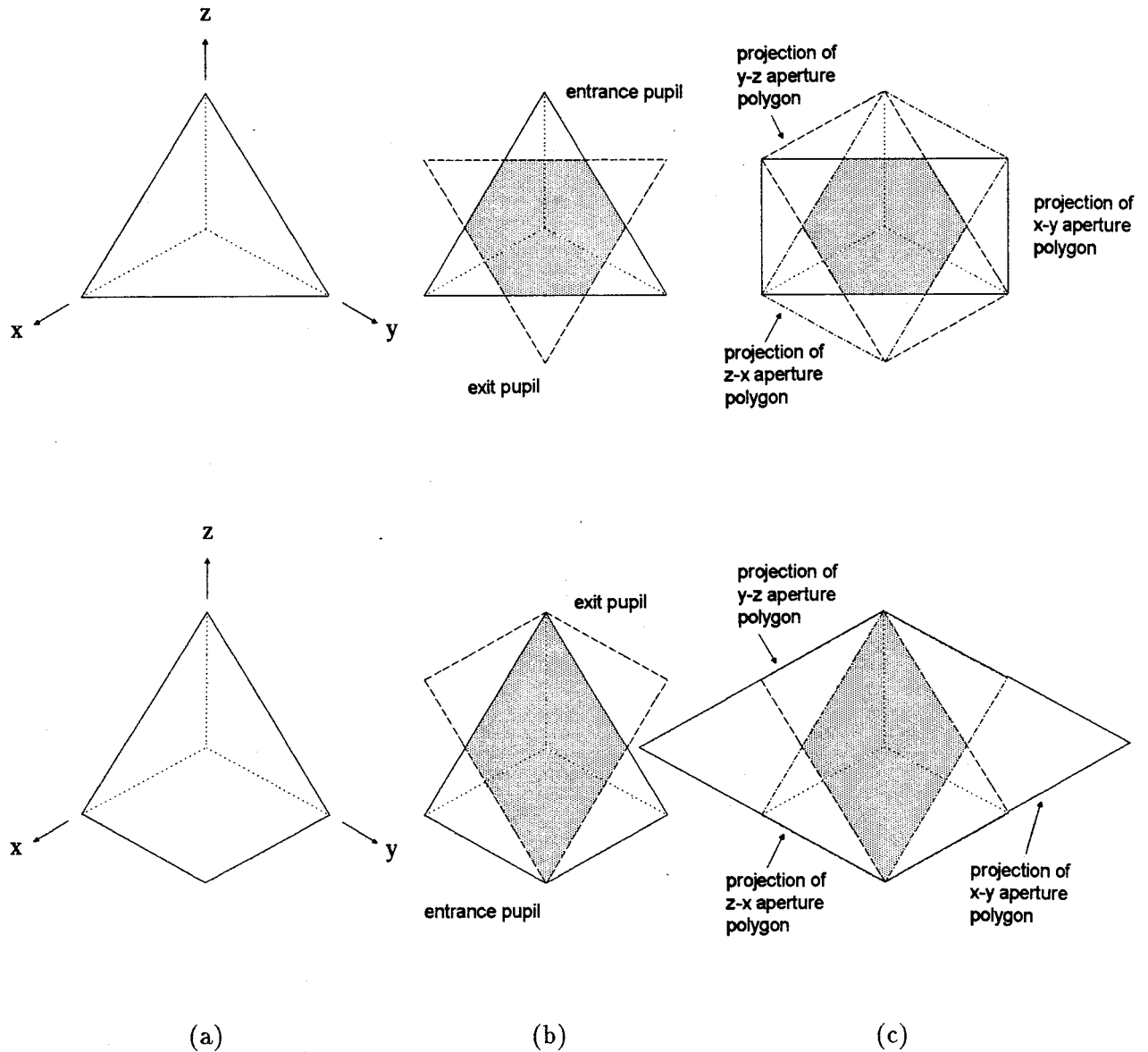
Figure 3.6: Examples of trihedral corner reflectors for which Spencer's model gives accurate predictions of the equivalent flat plate area. (a) Reflector geometry. (b) Spencer's model: projection of the entrance and exit pupils of the reflector onto the view plane and determination of their intersection. (c) Robertson's model: projection of the aperture planes onto the view plane and determination of their intersection.

(a) (b) (c)
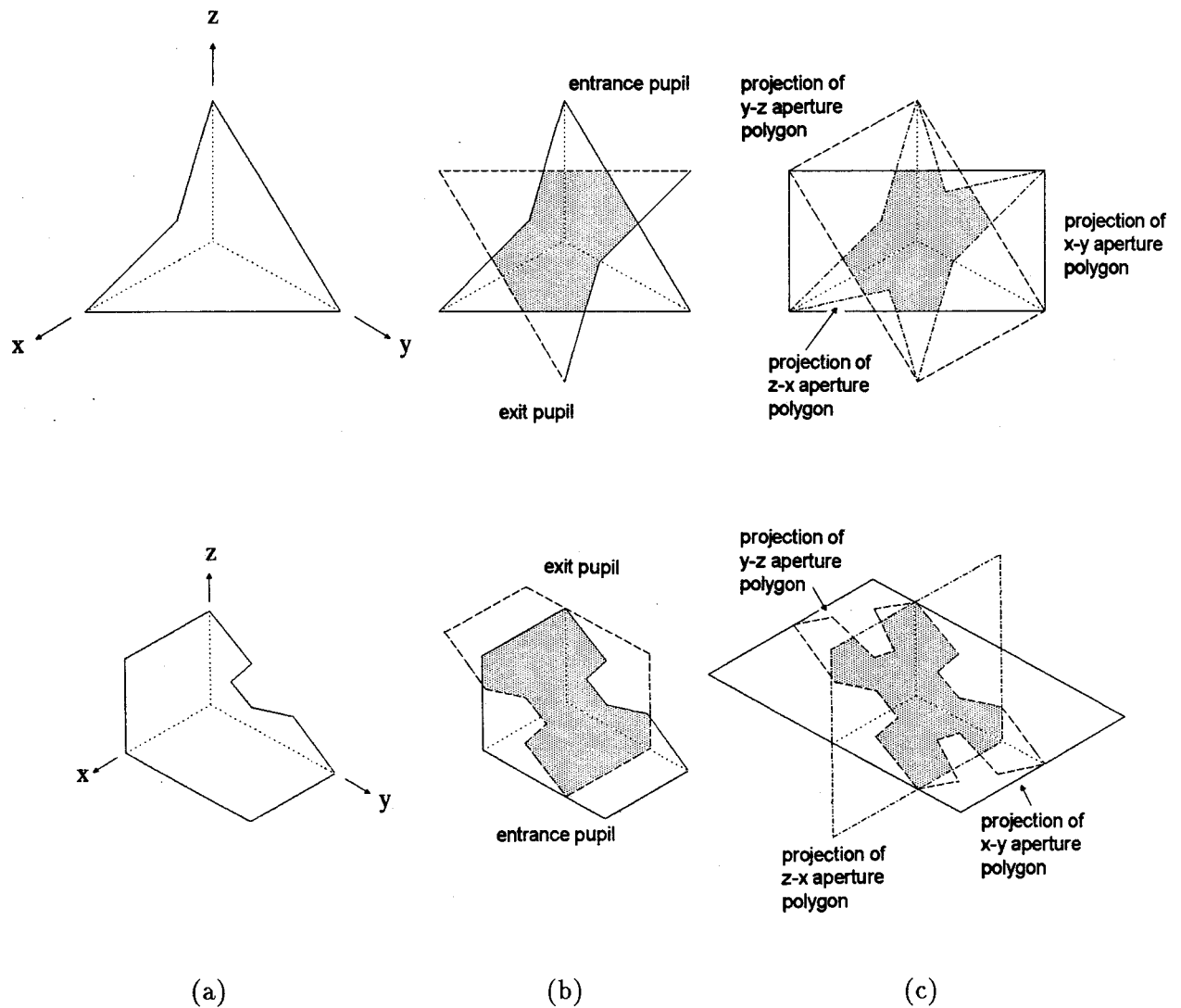
Figure 3.7: Examples of trihedral corner reflectors for which Spencer's model gives erroneous predictions of the equivalent flat plate area. (a) Reflector geometry. (b) Spencer's model: projection of the entrance and exit pupils of the reflector onto the view plane and determination of their intersection. (c) Robertson's model: projection of the aperture planes onto the view plane and determination of their intersection.

An algorithm for solving Robertson's model for the contribution of triple-bounce reflections to the equivalent flat plate area of an ideal trihedral corner reflector can be devised using an approach similar to the one followed by Keen [14], [15] in his solution of Spencer's model. The four geometric primitives used in this algorithm are defined as follows [17]–[19]: A *point* is specified by its coordinates $P(x, y, z)$. A *line segment* is specified by giving its end points $P_1(x_1, y_1, z_1)$ and $P_2(x_2, y_2, z_2)$. A *polyline* is a chain of connected line segments which is specified by giving a list of the vertices $P_1, \ldots, P_N$ that define the line segments. The first vertex is called the initial or starting point while the last vertex is called the final or terminal point. A *polygon* is a closed polyline in which the initial and terminal points coincide. The line segments $\overline{P_1 P_2}, \overline{P_2 P_3}, \ldots, \overline{P_N P_1}$ are called the edges of the polygon. The vertex list for the exterior boundary of the polygon is traversed in a counterclockwise direction and the enclosed region has a positive vector area. If the polygon contains interior boundaries (or holes), the corresponding vertex lists are traversed in a clockwise direction and the enclosed regions have a negative vector area. Once the polygons which represent the panels of the reflector and the direction of incidence have been specified, the prediction algorithm is executed in four steps:

1. The polygons which represent the x-y, y-z, and z-x reflecting panels are converted into corresponding aperture polygons by reflection about the principal axes of the trihedral.

2. The x-y, y-z, and z-x aperture polygons are projected onto a view plane which contains the origin and is normal to the direction of incidence.

3. The polygon which represents the region that is common to the projection of all three aperture polygons is determined. This is accomplished by calculating the intersection of the projection of the x-y aperture polygon and the projection of the y-z aperture polygon then calculating the intersection of the result and the projection of the z-x polygon.

4. The area of the polygon which represents the region that is common to the projection of all three aperture polygons is calculated.

The first step in the prediction algorithm, conversion of the polygons which represent the reflecting panels into aperture polygons by reflection about the principal axes of the trihedral, can be performed by inspection. The second step, projection of the aperture polygons onto a view plane which contains the origin and is normal to the direction of incidence, may be accomplished by a transformation of coordinates through pure rotation. If the reflector frame is defined by x, y, and z axes of the trihedral corner reflector, let the x'-y' plane define the view plane and let the z' axis be coincident with the direction of propagation of the reflected wave, as suggested by Figure 3.8. If the direction of propagation is given by the elevation and azimuth angles θ and ϕ, the view plane is defined by

$$\frac{x}{\alpha} + \frac{y}{\beta} + \frac{z}{\gamma} = 0 \, , \tag{3.8}$$

and the vector $\hat{z}'$ is given by

$$\hat{z}' = \alpha\,\hat{x} + \beta\,\hat{y} + \gamma\,\hat{z} \, , \tag{3.9}$$

where the direction cosines α, β, and γ are given by

$$\alpha = \sin\theta\sin\phi \, , \tag{3.10}$$

$$\beta = \sin\theta\cos\phi \, , \tag{3.11}$$

$$\gamma = \cos\theta \, . \tag{3.12}$$
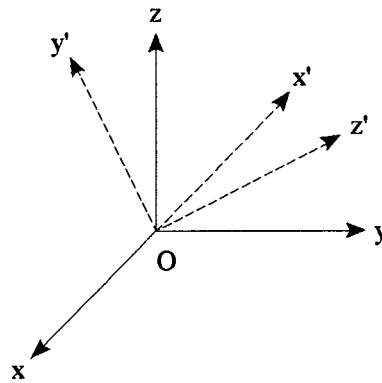
Figure 3.8: Transformation of coordinates by pure rotation.

From (3.9), it can be shown that the view plane and reflector coordinate systems are related by a transformation matrix of the form

$$
\begin{bmatrix} x' \\ y' \\ z' \end{bmatrix} = \begin{bmatrix} t_{11} & t_{12} & t_{13} \\ t_{21} & t_{22} & t_{23} \\ \cos\alpha & \cos\beta & \cos\gamma \end{bmatrix} \begin{bmatrix} x \\ y \\ z \end{bmatrix} , \tag{3.13}
$$

where t_{ij} corresponds to elements of the coordinate transformation matrix with unknown values. Since the angle of rotation of the x'-y' plane with respect to the z' axes can be defined arbitrarily, it is convenient to set t_{13} to zero so that a vector parallel to the z axis will have only a y' component in the view plane. Then, from the unitary property of the transformation matrix, it can be shown that $t_{23} = \sin\gamma$. Thus,

$$
\begin{bmatrix} x' \\ y' \\ z' \end{bmatrix} = \begin{bmatrix} t_{11} & t_{12} & 0 \\ t_{21} & t_{22} & \sin\gamma \\ \cos\alpha & \cos\beta & \cos\gamma \end{bmatrix} \begin{bmatrix} x \\ y \\ z \end{bmatrix} . \tag{3.14}
$$

In order to determine the values of the remaining elements, the coordinate transformation matrix may be compared to a prototype transformation matrix which corresponds to rotation about the z-axis through angle ψ followed by rotation about the x'-axis through angle ζ which gives

$$
\begin{bmatrix} x' \\ y' \\ z' \end{bmatrix} = \begin{bmatrix} \cos\psi & \sin\psi & 0 \\ -\cos\zeta\sin\psi & -\cos\zeta\cos\psi & \sin\zeta \\ \sin\zeta\sin\psi & -\sin\zeta\cos\psi & \cos\zeta \end{bmatrix} \begin{bmatrix} x \\ y \\ z \end{bmatrix} . \tag{3.15}
$$

By inspection of (3.14) and (3.15), it can be shown that

$$
\sin\zeta \equiv \sin\gamma , \tag{3.16}
$$

$$
\cos\zeta \equiv \cos\gamma , \tag{3.17}
$$

$$
\sin\psi \equiv \cos\alpha / \sin\zeta , \tag{3.18}
$$

$$
\cos\psi \equiv -\cos\beta / \sin\zeta . \tag{3.19}
$$

From (3.16)–(3.19), it can be shown that the view plane coordinate frame is related to the reflector coordinate frame by

$$
\begin{bmatrix} x' \\ y' \\ z' \end{bmatrix} = \begin{bmatrix} -\cos\beta/\sin\gamma & \cos\alpha/\sin\gamma & 0 \\ -\cos\alpha/\tan\gamma & -\cos\beta/\tan\gamma & \sin\gamma \\ \cos\alpha & \cos\beta & \cos\gamma \end{bmatrix} \begin{bmatrix} x \\ y \\ z \end{bmatrix}.
\tag{3.20}
$$

where α, β, and γ are given by (3.10)–(3.12). The projection of each of the aperture polygons onto the view plane can be determined by transforming the coordinates of each vertex from the reflector frame into the view plane frame using (3.20) and setting their z' coordinates to zero.

The third step in the prediction algorithm, determining the region of the view plane which is common to the projection of all three aperture polygons, is more difficult. A variety of algorithms for determining the intersection of overlapping polygons have been developed for use in computer graphics applications and are widely used. Most of these, including the Sutherland-Hodgman and Liang-Barskey polygon-clipping algorithms, are unsuitable for use in prediction algorithm derived from Robertson's model because they require at least one of the polygons to be convex. However, the Weiler-Atherton polygon-clipping algorithm overcomes this limitation and is capable of clipping a concave polygon with interior holes to the boundaries of another concave polygon with interior holes [18]–[21].

In the Weiler-Atherton polygon-clipping algorithm, the subject and clip polygons are described by circular lists of vertices $S_1, S_2, \ldots, S_M$ and $C_1, C_2, \ldots, C_N$, respectively. Before the actual clipping is performed, the points at which the subject and clip polygons intersect are determined. The coordinates of the intersection points are inserted into both the subject and clip polygon vertex lists in the appropriate sequence. In order to establish a bidirectional link between the vertex lists, each intersection point in the subject polygon vertex list is given a pointer to the location of the same intersection point in the clip polygon list and vice versa. The actual clipping is performed as follows: The subject polygon is traversed in a counterclockwise direction until an intersection is reached. If this series of points lies in the interior of the clip polygon, they are added to the result list. If the next vertex of the subject polygon lies inside

the clip polygon, the subject polygon vertex list is followed. Otherwise, the algorithm jumps to the clip polygon vertex list and follows it to the next intersection. This process continues until all the intersections have been traversed and the algorithm has returned to the first point in the result polygon. Methods for implementing the algorithm and enhancing its efficiency and robustness have been discussed in the literature [18]–[21].

Application of the Weiler-Atherton polygon-clipping algorithm to the problem of determining the equivalent flat plate area of a trihedral corner reflector with triangular panels of equal corner length for incidence along the symmetry axis is demonstrated in Figure 3.9. The projections of the *x-y*, *y-z*, and *z-x* aperture polygons onto the view plane are shown in Figure 3.9(a). The shaded region represents the area which is common to the projections of all three aperture polygons. Symbolically, this area may be described by

$$A = ((Z \cap X) \cap Y) \,, \tag{3.21}$$

where Z, X, and Y are the projections of the *x-y*, *y-z*, and *z-x* aperture polygons, respectively. In Figure 3.9(b), polygon Z is clipped against polygon Y to yield a first result. In Figure 3.9(c), the first result is clipped against polygon X to yield the final result. The polygon which defines the region common to the projection of all three aperture polygons is shown in Figure 3.9(d).

The last step in the prediction algorithm is calculation of the area of the polygon which defines the region common to the projection of all three aperture polygons. If the vertices of the polygon are given by $\{S_n\}$, the *z*-directed vector area of the polygon is simply given by

$$\mathbf{A} \;=\; \frac{1}{2} \sum_{i=1}^{n-1} \mathbf{S}_i \times \mathbf{S}_{i+1} \,. \tag{3.22}$$

Once the equivalent flat plate area has been calculated from (3.22), the scattering cross section of the reflector can be determined from (3.1).
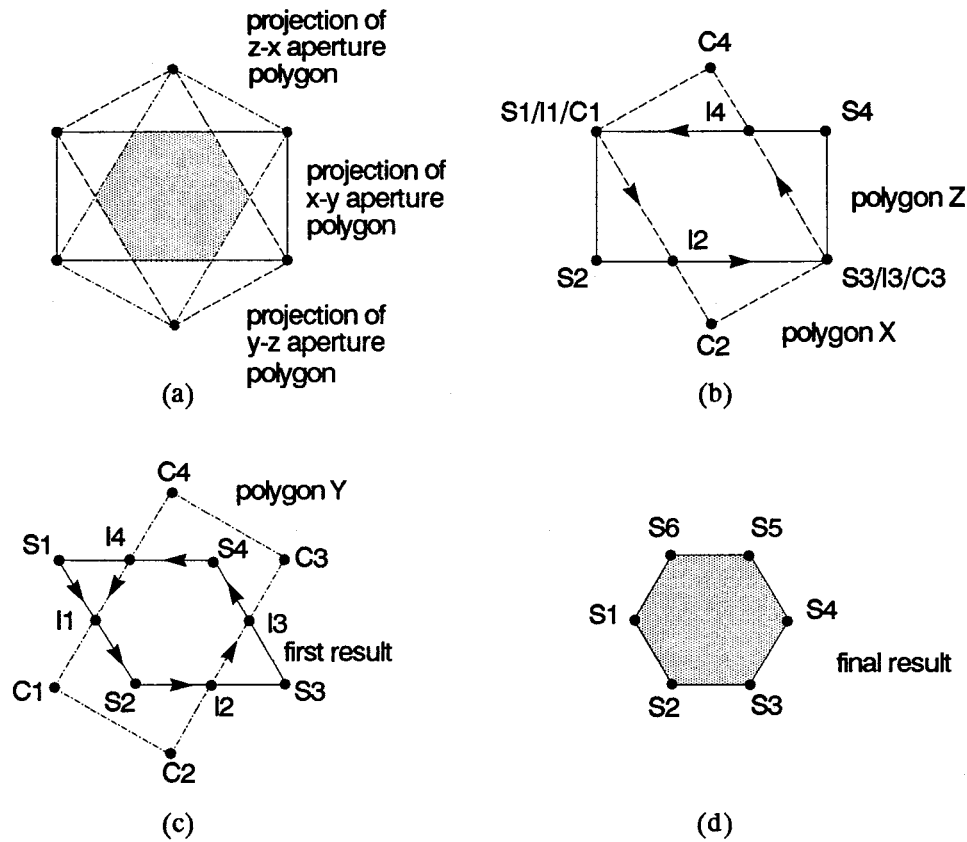
First Clipping Sequence

Second Clipping Sequence

Z polygon list	X polygon list
$S_1/I_1/(C_1)$	$C_1/I_1/(S_1)$
S_2	I_2
I_2	C_2
$S_3/I_3/(C_3)$	$C_3/I_3/(S_3)$
S_4	I_4
I_4	C_4

First result list	Y polygon list
S_1	C_1
I_1	C_2
S_2	I_2
I_2	I_3
S_3	C_3
I_3	C_4
S_4	I_4
I_4	I_1

Figure 3.9: Execution of the Weiler-Atherton polygon clipping algorithm. (a) The x-y, y-z, and z-x apertures are projected onto the view plane to yield polygons Z, X, and Y, respectively. (b) Polygon Z is clipped against polygon X to yield the first result list. (c) The polygon defined by the first result list is clipped against polygon Y to yield the final result list. (d) The final result list defines the polygon A which contains the area common to polygons Z, X, and Y. In each case, S_n refers to points in the subject polygon, C_n refers to points in the clip polygon, and I_n refers to the points at which the polygons intersect.

3.3 Reflectors with Three-Fold Symmetry

In this section, the extent to which the response characteristics of trihedral corner reflectors which present three-fold symmetry can be altered by appropriate shaping of their reflecting panels is considered. In each case, the contribution of triple-bounce reflections to the scattering cross section of the reflector was calculated over the entire quadrant defined by the axes of the trihedral. The resulting array of values in θ and ϕ were then converted to contours expressed in decibels with respect to the maximum response of the reflector. Although the reflector coordinate frame of Figure 3.10(a) is a convenient choice for analyzing the response of a trihedral corner reflector, it is not the most natural choice for presenting response patterns. Instead, the results were transformed to the global coordinate frame of Figure 3.10(b) in which the z' axis is aligned with the local vertical and the direction of maximum response (or the *boresight* of the reflector) lies in the horizontal plane and is aligned with the x' axis.
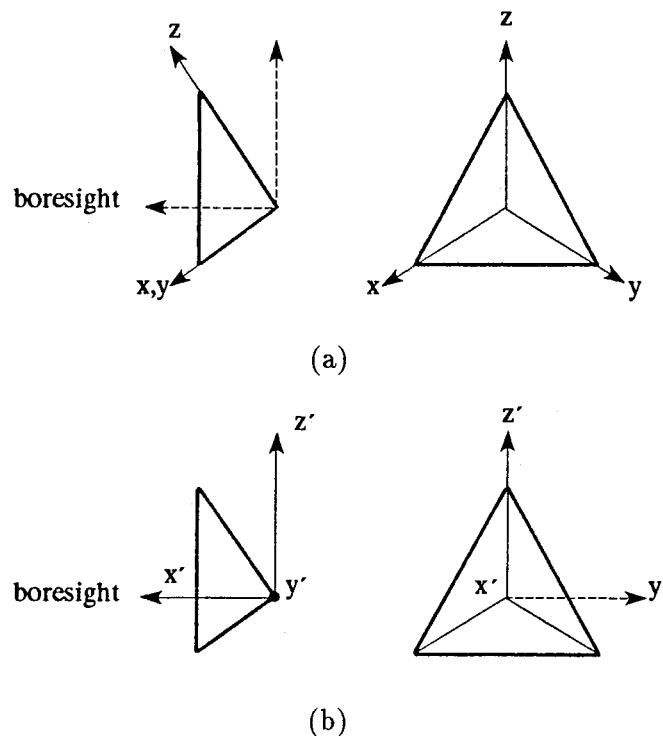
Figure 3.10: (a) Reflector coordinate frame and (b) global coordinate frame.

The boresight of a trihedral corner reflector which presents three-fold symmetry is usually coincident with the symmetry axis defined by $\theta = 54.74°$ and $\phi = 45°$. Using the method of evaluating coordinate transformation matrices that was derived in section 2.4, it can be shown that the global coordinate frame is related to the reflector coordinate frame by

$$
\begin{bmatrix} x' \\ y' \\ z' \end{bmatrix} = \begin{bmatrix} \frac{1}{\sqrt{3}} & -\frac{1}{\sqrt{2}} & -\frac{1}{\sqrt{6}} \\ \frac{1}{\sqrt{3}} & \frac{1}{\sqrt{2}} & -\frac{1}{\sqrt{6}} \\ \frac{1}{\sqrt{3}} & 0 & \sqrt{\frac{2}{3}} \end{bmatrix} \begin{bmatrix} x \\ y \\ z \end{bmatrix} .
\tag{3.23}
$$

Thus, direction expressed in terms of the angles θ' and ϕ' in the global coordinate frame is related to direction expressed in terms of the angles θ and ϕ in the reflector coordinate frame by

$$
\theta' = \cos^{-1}\left[\frac{1}{\sqrt{3}} \sin\theta \cos\phi + \sqrt{\frac{2}{3}} \cos\theta \right] ,
\tag{3.24}
$$

$$
\phi' = \tan^{-1}\left[\frac{\frac{1}{\sqrt{3}} \sin\theta \cos\phi + \frac{1}{\sqrt{2}} \sin\theta \sin\phi - \frac{1}{\sqrt{6}} \cos\theta}{\frac{1}{\sqrt{3}} \sin\theta \cos\phi - \frac{1}{\sqrt{2}} \sin\theta \sin\phi - \frac{1}{\sqrt{6}} \cos\theta} \right] .
\tag{3.25}
$$

while the reverse transformation is given by

$$
\theta = \cos^{-1}\left[-\frac{1}{\sqrt{6}} \sin\theta' \cos\phi' - \frac{1}{\sqrt{6}} \sin\theta' \sin\phi' + \sqrt{\frac{2}{3}} \cos\theta' \right] ,
\tag{3.26}
$$

$$
\phi = \tan^{-1}\left[\frac{-\frac{1}{\sqrt{2}} \sin\theta' \cos\phi' + \frac{1}{\sqrt{2}} \sin\theta' \sin\phi'}{\frac{1}{\sqrt{3}} \sin\theta' \cos\phi' + \frac{1}{\sqrt{3}} \sin\theta' \sin\phi' + \frac{1}{\sqrt{3}} \cos\theta'} \right] ,
\tag{3.27}
$$

Although the response contours could be plotted on a conventional rectangular grid, distortion of the pattern can be minimized by using a grid derived from an equal area projection of the type used in geodesy and cartography [22], [23]. Several common projections are suitable, but the sinusoidal projection is the easiest to implement and was selected for use here. While the horizontal axis of the response patterns is expressed in terms of the azimuth angle ϕ', the vertical axis is expressed in terms of the co-elevation or altitude angle $\overline{\theta}'$ given by

$$
\overline{\theta}' = 90 - \theta
\tag{3.28}
$$

in order to simplify interpretation of the results.

The angular coverage of symmetrical trihedral corner reflectors with triangular, circular, and square panels were predicted using the algorithm described in the previous section. The circular panels were represented by a twenty-sided polygon of equivalent area. The results are presented in Figures 3.11, 3.12, and 3.13 and summarized in Table 3.1. It is generally found that attempts to increase the angular coverage of a symmetrical trihedral corner reflector with a fixed corner length by modifying the shape of its reflecting panels are generally accompanied by a corresponding decrease in the ratio of the scattering cross section to the physical size of the reflector, as previously noted by Robertson [5].

Robertson [4] proposed a method for altering the angular coverage of a symmetrical reflector with triangular panels by removing notches of prescribed width and depth from the outside edge of each panel, as shown in Figure 3.14. The depth of the notch can be expressed by a parameter d_n/d_p which is the ratio of the depth of the notch to the length of the median to the outside edge of the panel. The angular coverage of a Robertson reflector with shallow notches ($d_n/d_p = 0.25$) is depicted in Figure 3.15. After notching the panels, three equal maxima appear at about 12 degrees off the symmetry axis. Although the angular coverage of the reflectors increases dramatically, the maximum response is correspondingly smaller. The angular coverage of a reflector with notches of intermediate depth ($d_n/d_p = 0.50$) is depicted in Figure 3.16. The three maxima are more pronounced and have shifted outward to about 21 degrees off the symmetry axis. The angular coverage of a reflector with deep notches ($d_n/d_p = 0.75$) is depicted in Figure 3.17. The null in the response which has formed along the symmetry axis is -25 dB with respect to the maximum response. The results are summarized in Table 3.1.

The cumulative probability distribution of the response of symmetrical trihedral corner reflectors with triangular, circular, and square panels, and Robertson panels with shallow notches (where $d_n/d_p = 0.25$) over the quadrant defined by the axes of the trihedral is shown in Figure 3.18. Of the four targets, Robertson's reflector with shallow notches presents the most uniform response. Siegel *et al.* [2] claimed that the cumulative distribution of a trihedral corner reflector with circular panels exceeds that of reflectors with either triangular or square panels. In fact, the results presented here show that its cumulative distribution is only intermediate.
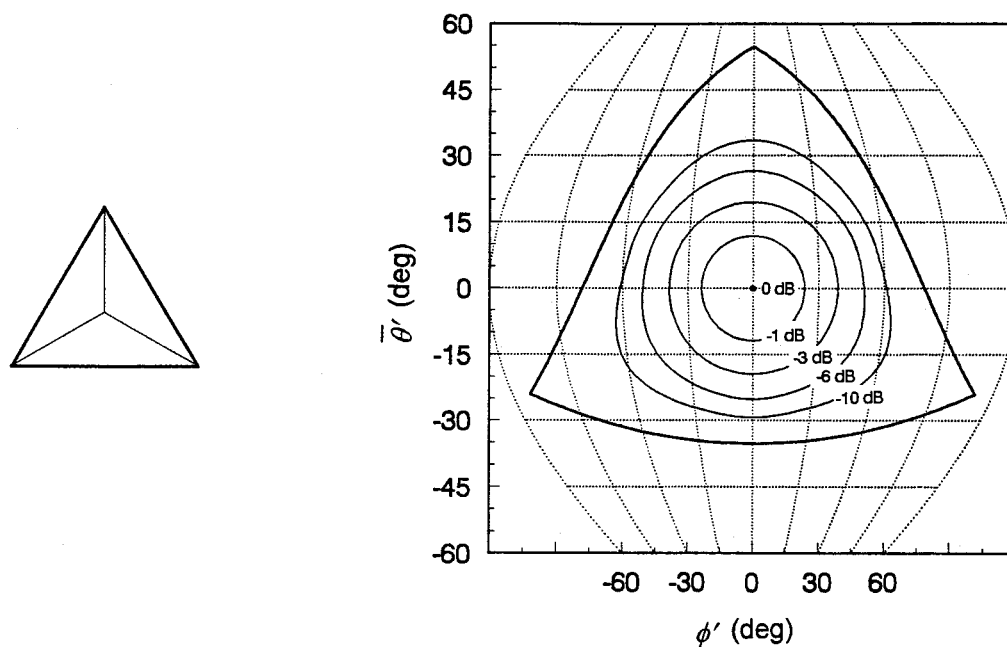
Figure 3.11: Angular coverage of a trihedral corner reflector with triangular panels.
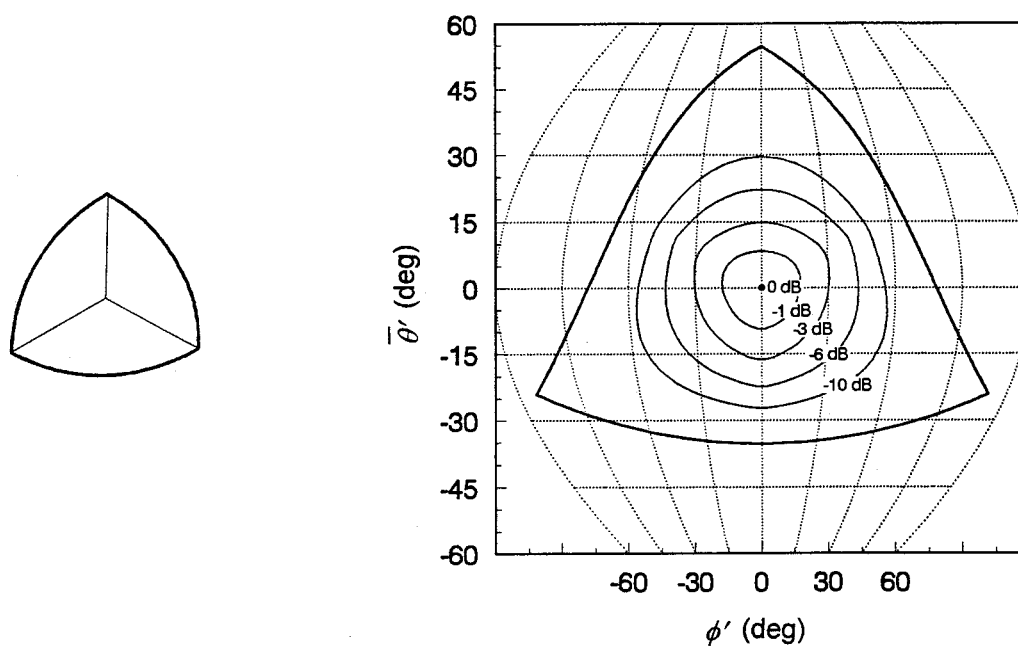
Figure 3.12: Angular coverage of a trihedral corner reflector with circular panels.
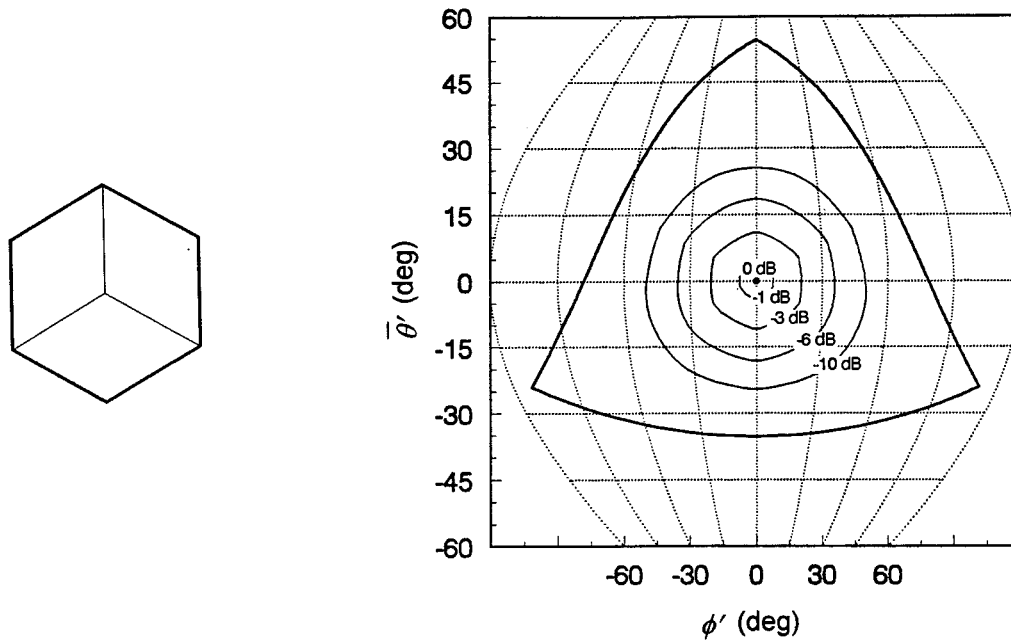
Figure 3.13: Angular coverage of a trihedral corner reflector with square panels.
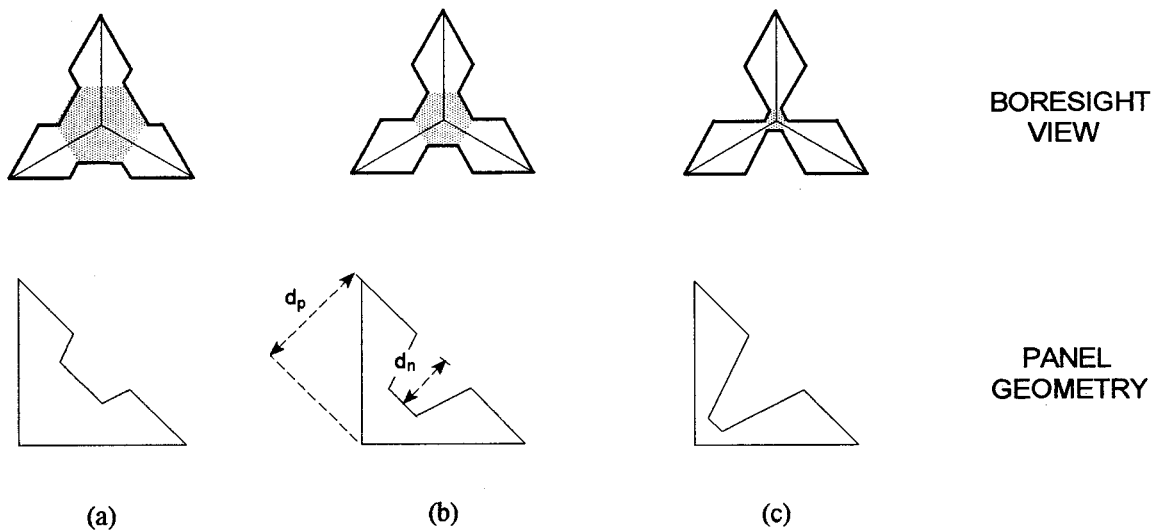
Figure 3.14: Boresight view and panel geometry of trihedral corner reflectors with Robertson panels where the ratio of notch depth to panel depth, d_n/d_p, is (a) 0.25, (b) 0.50, and (c) 0.75. The shaded portion indicates the equivalent flat plate area of the reflector for incidence along the boresight.
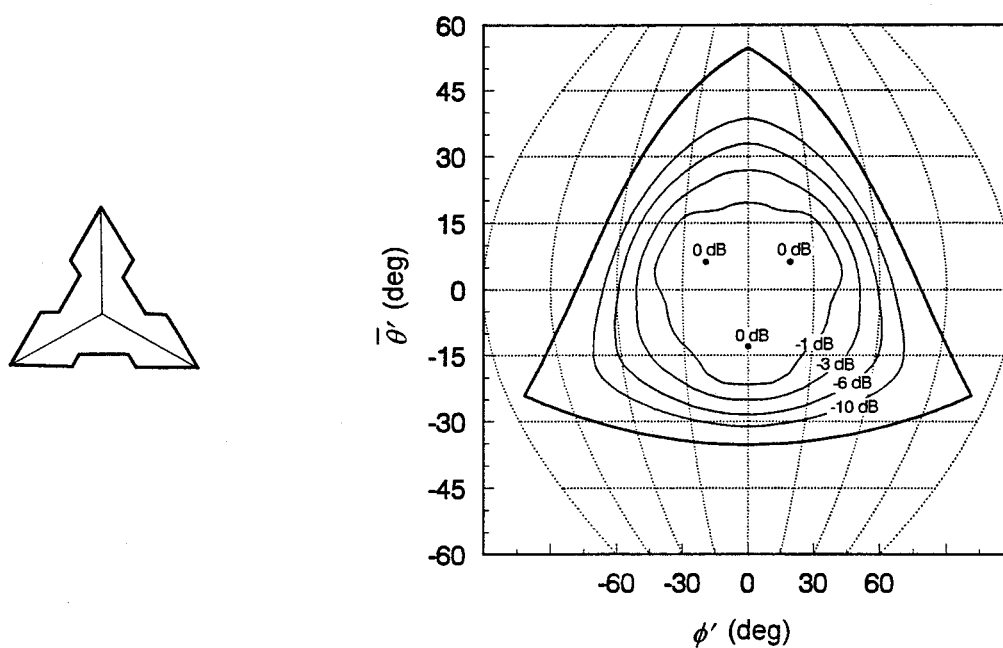
Figure 3.15: Angular coverage of a trihedral corner reflector with Robertson panels where $d_n/d_p = 0.25$.
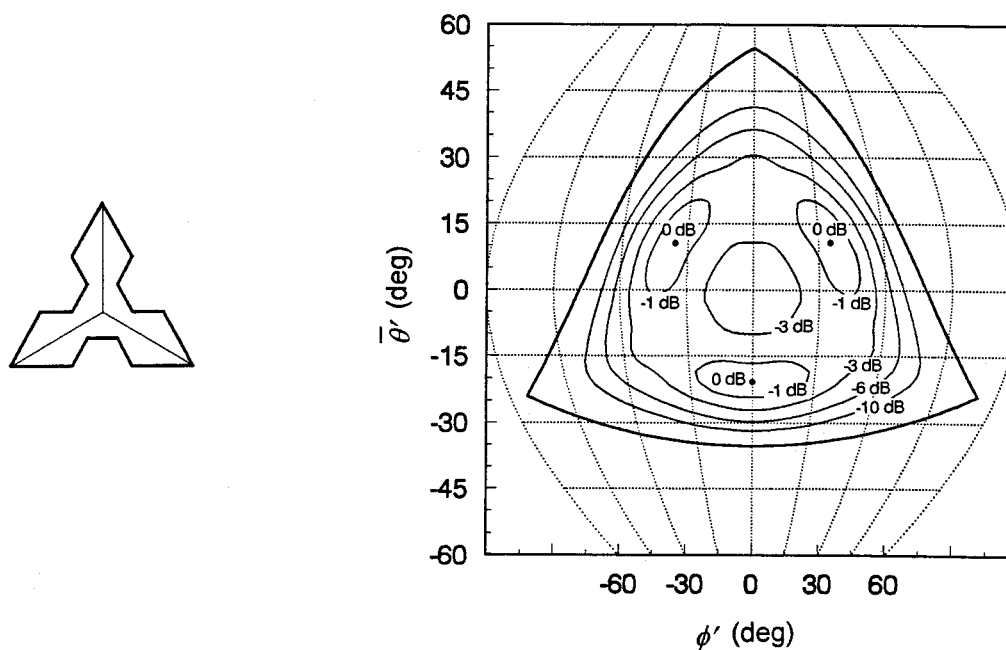
Figure 3.16: Angular coverage of a trihedral corner reflector with Robertson panels where $d_n/d_p = 0.50$.
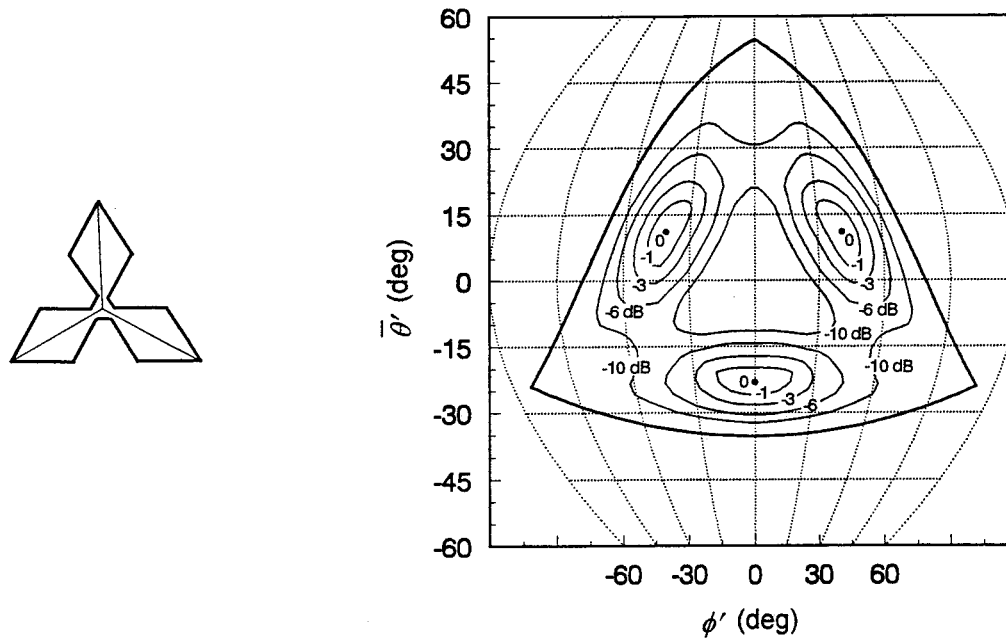
Figure 3.17: Angular coverage of a trihedral corner reflector with Robertson panels where $d_n/d_p = 0.75$.
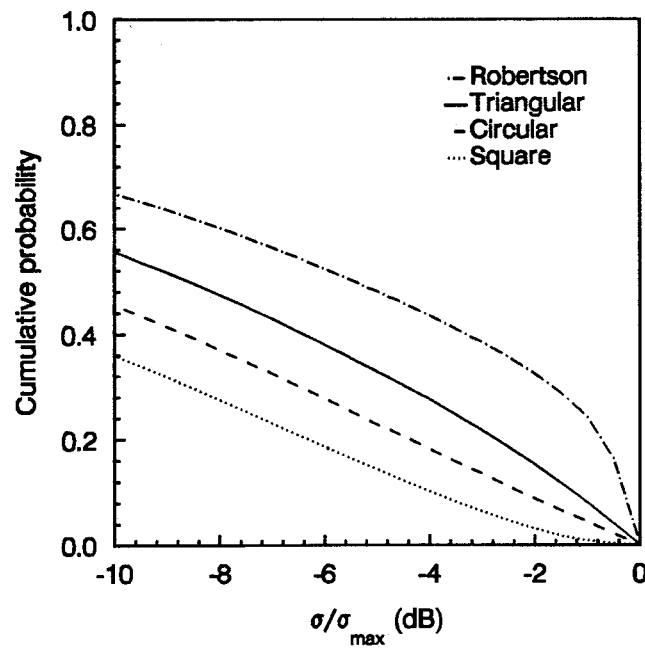
Figure 3.18: Cumulative probability distribution of the response of trihedral corner reflectors with triangular, circular, square, and Robertson panels (where $d_n/d_p = 0.25$) over the quadrant defined by the axes of the trihedral.

Table 3.1:

Response Characteristics of Selected Trihedral Corner Reflectors with Three-fold Symmetry

Maximum Response

Figure	Panel Geometry	σ_{max} [1]	σ_{max} [2]
3.11	Triangular	$(4\pi/3)\,a^4/\lambda^2$	0.0 dB
3.12	Circular	$15.6\,a^4/\lambda^2$	5.7 dB
3.13	Square	$12\pi\,a^4/\lambda^2$	9.5 dB
3.15	Robertson[3]	$0.39\,a^4/\lambda^2$	-4.1 dB
3.16	Robertson[4]	$0.18\,a^4/\lambda^2$	-7.0 dB
3.17	Robertson[5]	$0.12\,a^4/\lambda^2$	-9.4 dB

1 and 3 dB Elevation and Azimuthal Beamwidths of the Main Response Lobe

Figure	Panel Geometry	Θ_{1dB}	Φ_{1dB}	Θ_{3dB}	Φ_{3dB}
3.11	Triangular	24°	24°	39°	39°
3.12	Circular	18°	17°	31°	30°
3.13	Square	8°	8°	22°	20°
3.15	Robertson[3]	41°	40°	52°	50°
3.16	Robertson[4]	n/a	n/a	n/a	n/a
3.17	Robertson[5]	n/a	n/a	n/a	n/a

6 and 10 dB Elevation and Azimuthal Beamwidths of the Main Response Lobe

Figure	Panel Geometry	Θ_{6dB}	Φ_{6dB}	Θ_{10dB}	Φ_{10dB}
3.11	Triangular	52°	51°	63°	61°
3.12	Circular	44°	43°	57°	55°
3.13	Square	36°	35°	50°	50°
3.15	Robertson[3]	61°	59°	70°	66°
3.16	Robertson[4]	65°	64°	73°	68°
3.17	Robertson[5]	n/a	n/a	n/a	n/a

Notes: (1) where a is the corner length of the reflector.

(2) relative to σ_{max} of a trihedral corner reflector with triangular panels of the same corner length.

(3) where the ratio of notch depth to panel depth, d_n/d_p, is 0.25.

(4) where $d_n/d_p = 0.50$.

(5) where $d_n/d_p = 0.75$.

3.4 Reflectors with Bilateral Symmetry

The response characteristics of bilaterally symmetric trihedral corner reflectors with triangular, elliptical, and rectangular panels can be predicted using the closed-form expressions for their equivalent flat plate area which are given by (3.5), (3.6), and (3.7), respectively. Although the form of the expressions makes it difficult to derive closed-form solutions for either the size and direction of the maximum response or the azimuthal and elevation beamwidths of the main response lobe, it is a relatively simple matter to determine these quantities using a numerical approach. The problem geometry and the reflector coordinate system are shown in Figure 3.3. It is convenient to define bilateral symmetry by a mirror plane which contains the z axis and bisects the x-y plane at an azimuthal angle of 45 degrees. If the length of the corner along the z axis is given by c and the length of the corners along the x and y axes are given by a, then the reflector aspect ratio is defined as c/a.

If a reflector presents a single main response lobe and is bilaterally symmetric, the direction of its maximum response must lie in its mirror plane. While the azimuthal angle ϕ_{max} of the direction of maximum response is a fixed quantity, the corresponding elevation angle θ_{max} is a function of the reflector aspect ratio c/a. A golden section search [24] was used to determine the elevation angle of maximum response of bilaterally symmetric trihedral corner reflectors with triangular, elliptical, and rectangular panels. The results are presented in Figure 3.19. Although the directions of maximum response are coincident when the reflector aspect ratio is unity, they diverge as the reflector becomes increasingly asymmetric. Trihedral corner reflectors with triangular panels are of special interest since they present a planar aperture which facilitates the attachment of either a transmission polarizer or a protective dielectric cover. Since the intercepts of the plane which defines the reflector aperture are given by the corner lengths of the reflector, it can be shown that the elevation angle of the normal to the reflector aperture is given by

$$\theta_{\mathrm{n}} = \cos^{-1}\left(\frac{c}{\sqrt{2a^2 + c^2}}\right) . \tag{3.29}$$

The angle of maximum response $\theta_{\max}$ and the angle of the normal aperture θ_n of bilaterally symmetric trihedral corner reflectors with triangular panels are plotted as a function of the reflector aspect ratio c/a in Figure 3.20. Although the direction of maximum response and the normal to the reflector aperture are coincident if the reflector aspect ratio is unity, they diverge as the reflector becomes increasing asymmetric. If the reflector aspect ratio is less than unity, the normal to the aperture is lower than the direction of maximum response. If the ratio is greater than unity, the reverse is true.

If a trihedral corner reflector has corners of equal length ℓ, it is convenient to express its scattering cross section in the form

$$\sigma_{\max} = K \frac{\ell^4}{\lambda^2} \, . \tag{3.30}$$

The parameter K is a figure of merit which can be used to compare the maximum response of trihedral corner reflectors with similar dimensions but different panel shapes. Although it is desirable to employ a similar scheme to express the scattering cross section of a bilaterally symmetric reflector, the equivalent corner length of such a reflector must be defined. Although the equivalent corner length could be defined in several different ways, it is convenient to simply take the arithmetic mean of the three corner lengths, i.e.,

$$\ell = \frac{a + 2c}{3} \, . \tag{3.31}$$

Using this definition, the parameter K for bilaterally symmetric trihedral corner reflectors with triangular, elliptical, and rectangular panels is plotted as a function of the reflector aspect ratio in Figure 3.21.

The azimuthal and elevation beamwidths of bilaterally symmetric trihedral corner reflectors with triangular, elliptical, and rectangular panels were determined by applying a bracketing and bisection algorithm [24] to (3.5), (3.6), and (3.7) in a global coordinate frame similar to that defined in Figure 3.10(b) where the z' axis is aligned with the local vertical and the x' axis is aligned with the direction of maximum response. The results are presented as a function of the reflector aspect ratio c/a in Figures 3.22, 3.23, and 3.24, respectively. The increase in

and the converse for large reflector aspect ratios is evident. The angular coverage of bilaterally symmetric trihedral corner reflectors with triangular panels and reflector aspect ratios of 4.0 and 0.25 are presented in Figures 3.25 and 3.26, respectively.

In certain cases, it has been found useful to realize bilaterally symmetric trihedral corner reflectors which are composed of combinations of triangular, elliptical, and rectangular panels. For example, the trihedral corner reflector developed by the European Space Agency for use as a calibration target in the SAR-580 program is composed of triangular side panels and a square center panel [8]. The angular coverage of the SAR-580 calibration target and five other reflectors which have been realized in a similar manner are presented in Figures 3.27 through 3.32. The results are summarized in Table 3.2.

During the course of this study, an alternative approach to the design of bilaterally symmetric trihedral corner reflectors for use in radar-assisted positioning systems was suggested by Helmut Lanziner of Offshore Systems Ltd. [25]. The primary design objective was to produce a set of reflectors which would support themselves on a horizontal surface with their direction of maximum response in the horizontal plane. A secondary objective was to provide most of the reflectors with a planar aperture in order to facilitate the attachment of a protective cover or a transmission polarizer. Three variations were devised as shown in Figure 3.33. The truncated reflector of Figure 3.33(a) is simply a symmetrical trihedral corner reflector with triangular panels which has been inverted and had its side panels truncated in such a way that structure is self supporting when placed on a horizontal surface but the effective flat plate area for incidence along the boresight is unaffected. The compensated reflector of Figure 3.33(b) is developed from the truncated reflector by increasing the size of the side panels until maximum aperture efficiency is obtained. The extended reflector of Figure 3.33(c) is developed from the compensated reflector by extending the side panels further still. While the aperture of the reflector is no longer planar, the result is a large increase in the azimuthal beamwidth. The angular coverage of the truncated, compensated, and extended reflectors is presented in Figures 3.34, 3.35, and 3.36, respectively. The results are summarized in Table 3.2.
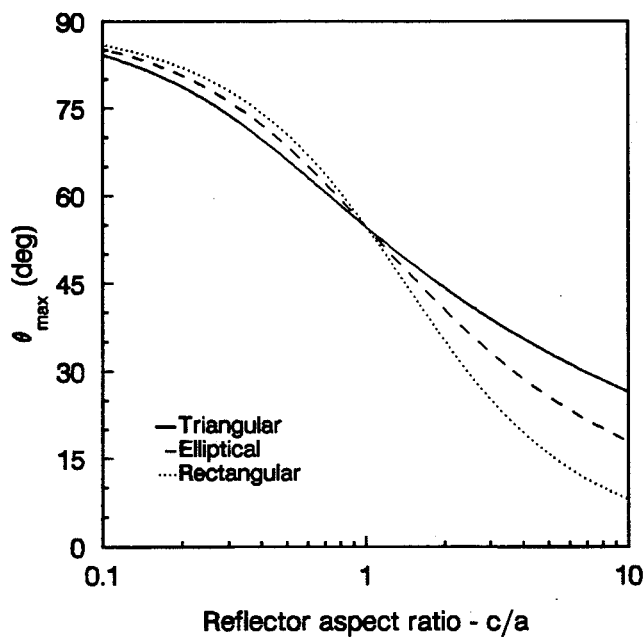
Figure 3.19: Angle of maximum response θ_{max} of bilaterally symmetric trihedral corner reflectors with triangular, elliptical, and rectangular panels vs. the reflector aspect ratio c/a.
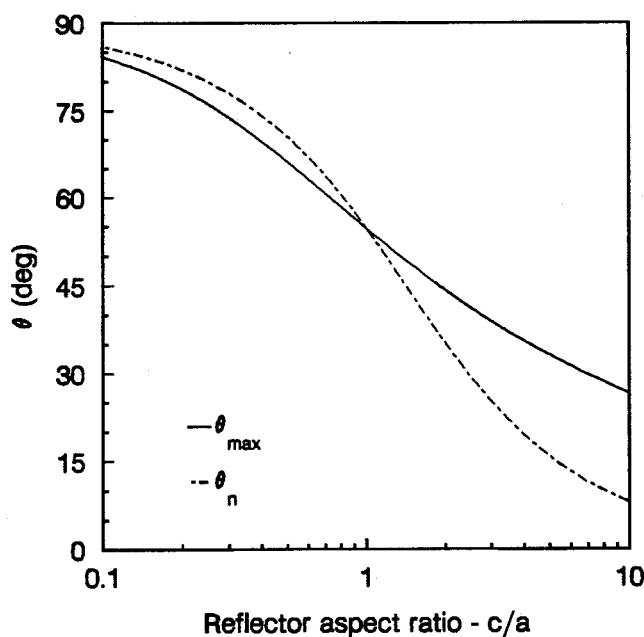
Figure 3.20: Angle of maximum response θ_{max} and angle of the normal to the aperture θ_n of bilaterally symmetric trihedral corner reflectors with triangular panels vs. the reflector aspect ratio c/a.
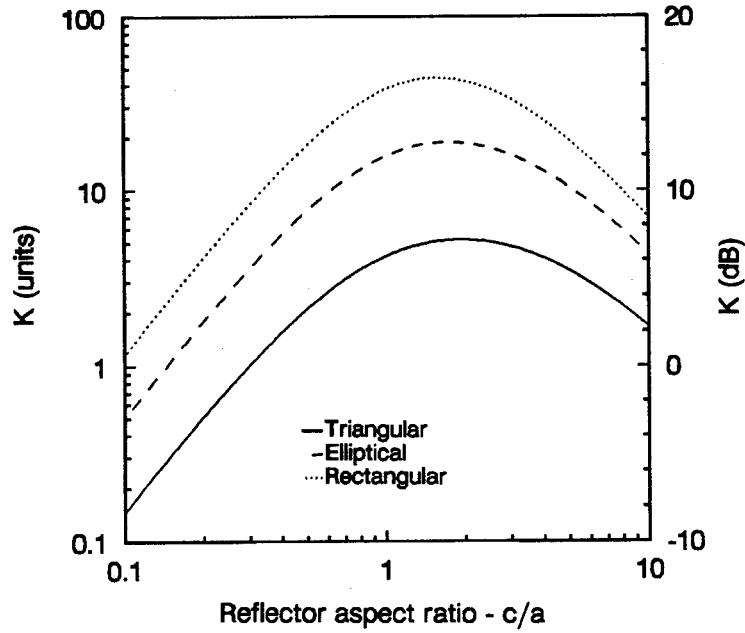
Figure 3.21: Maximum response of a bilaterally symmetric trihedral corner reflectors with triangular, elliptical, and rectangular panels vs. the reflector aspect ratio c/a where $\sigma_{\text{max}} = K\,\ell^4\,/\lambda^2$ and $\ell = (a + 2c)/3$.
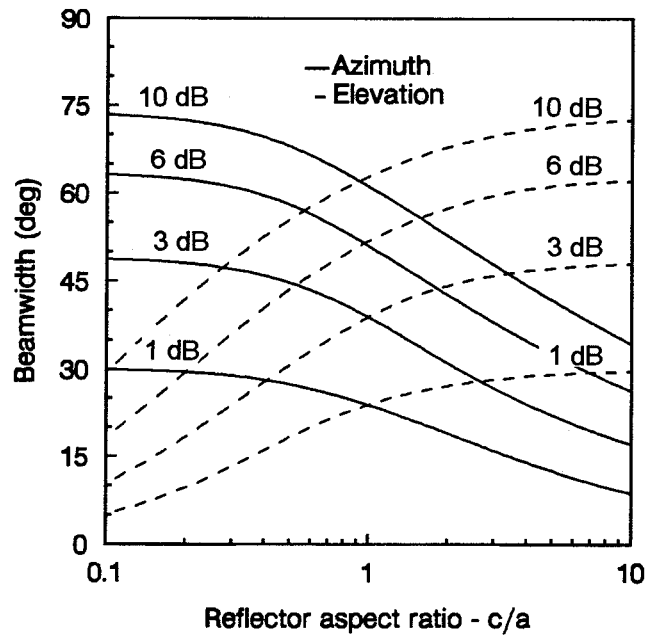
Figure 3.22: Azimuthal and elevation beamwidths of a bilaterally symmetric trihedral corner reflector with triangular panels vs. the reflector aspect ratio c/a.
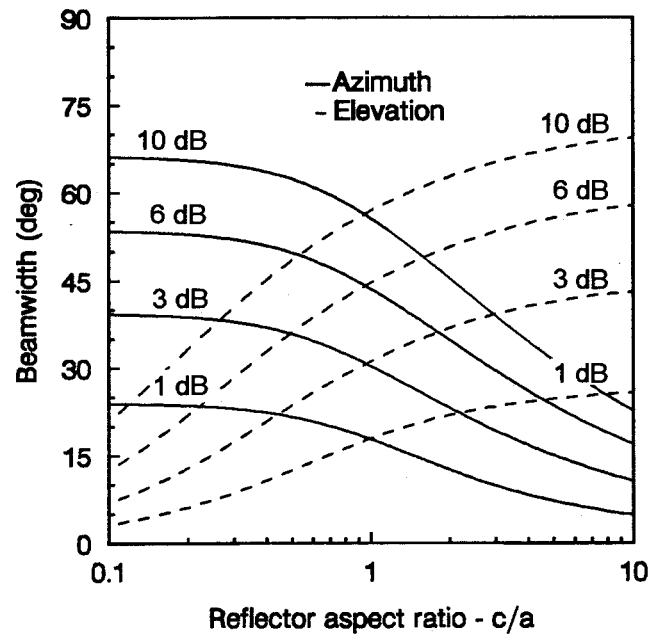
Figure 3.23: Azimuthal and elevation beamwidths of a bilaterally symmetric trihedral corner reflector with elliptical panels vs. the reflector aspect ratio c/a.
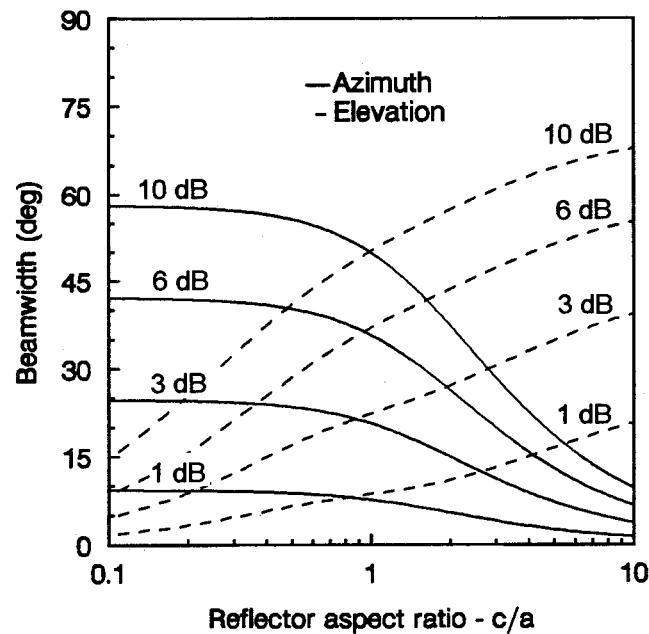
Figure 3.24: Azimuthal and elevation beamwidths of a bilaterally symmetric trihedral corner reflector with rectangular panels vs. the reflector aspect ratio c/a.
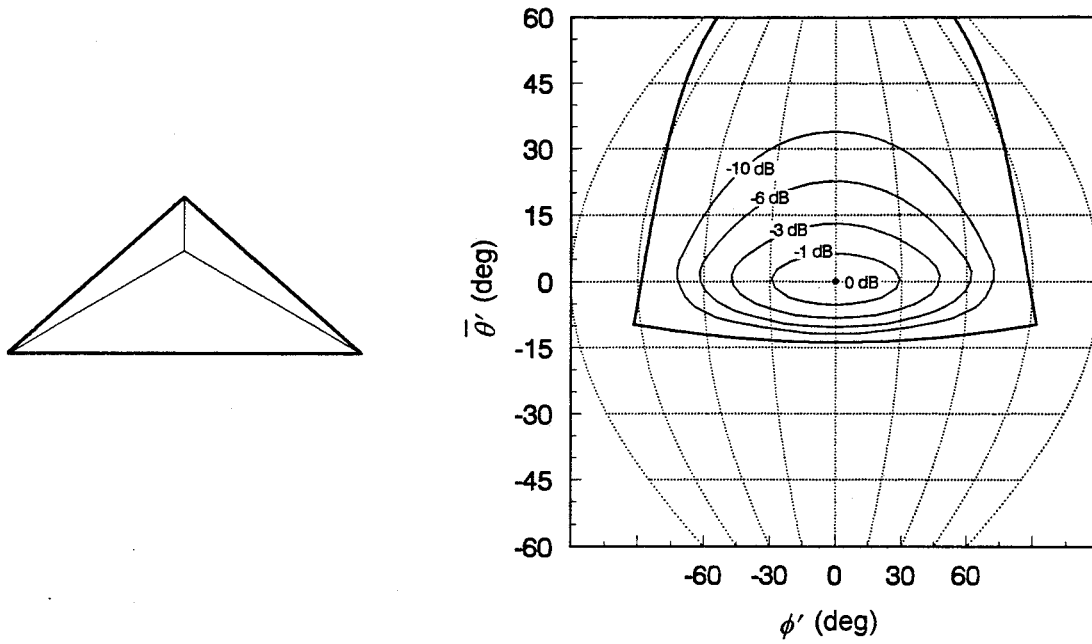
Figure 3.25: Angular coverage of a bilaterally symmetric trihedral corner reflector with triangular panels and reflector aspect ratio $c/a = 0.25$.
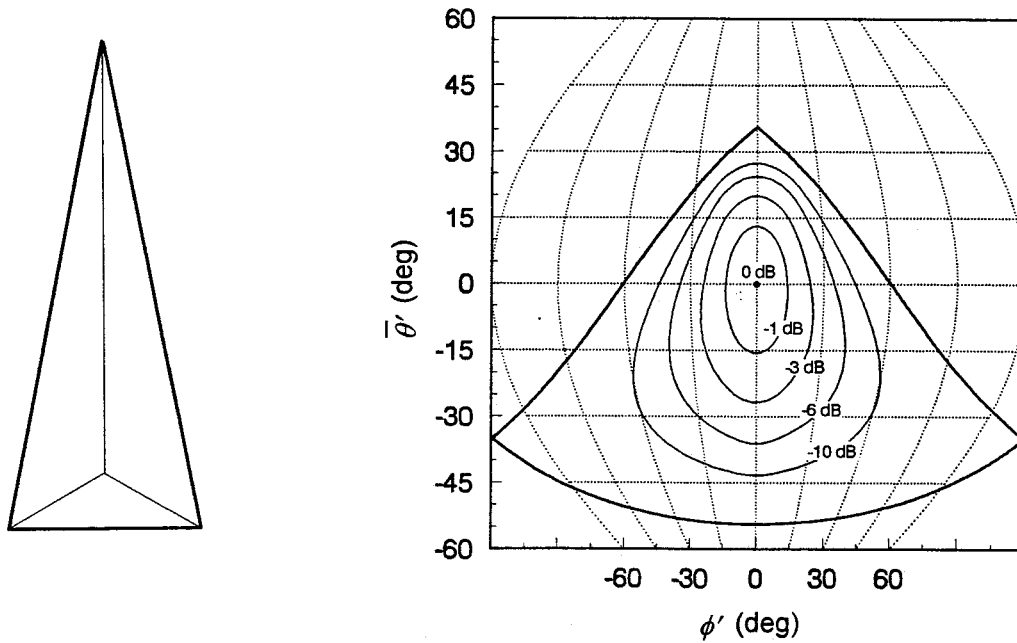
Figure 3.26: Angular coverage of a bilaterally symmetric trihedral corner reflector with triangular panels and reflector aspect ratio $c/a = 4.0$.
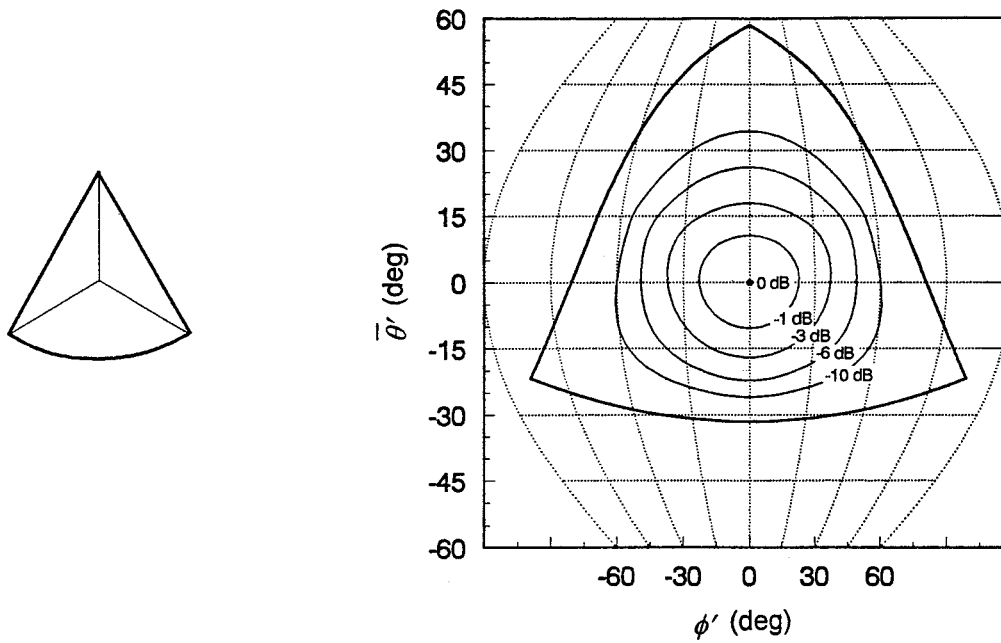
Figure 3.27: Angular coverage of a bilaterally symmetric trihedral corner reflector with triangular side panels and a circular center panel.
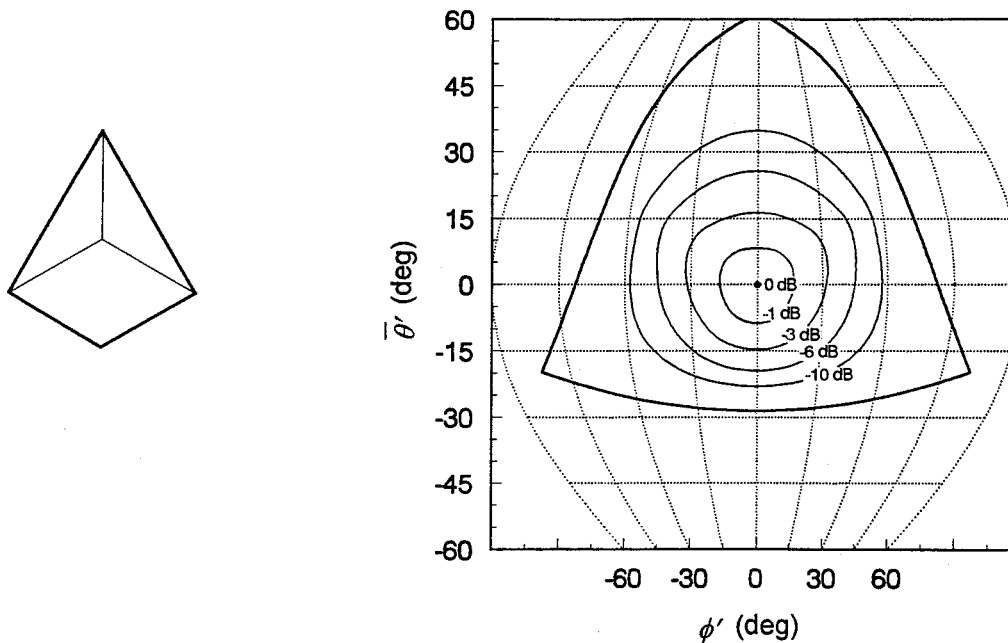
Figure 3.28: Angular coverage of a bilaterally symmetric trihedral corner reflector with triangular side panels and a square center panel.
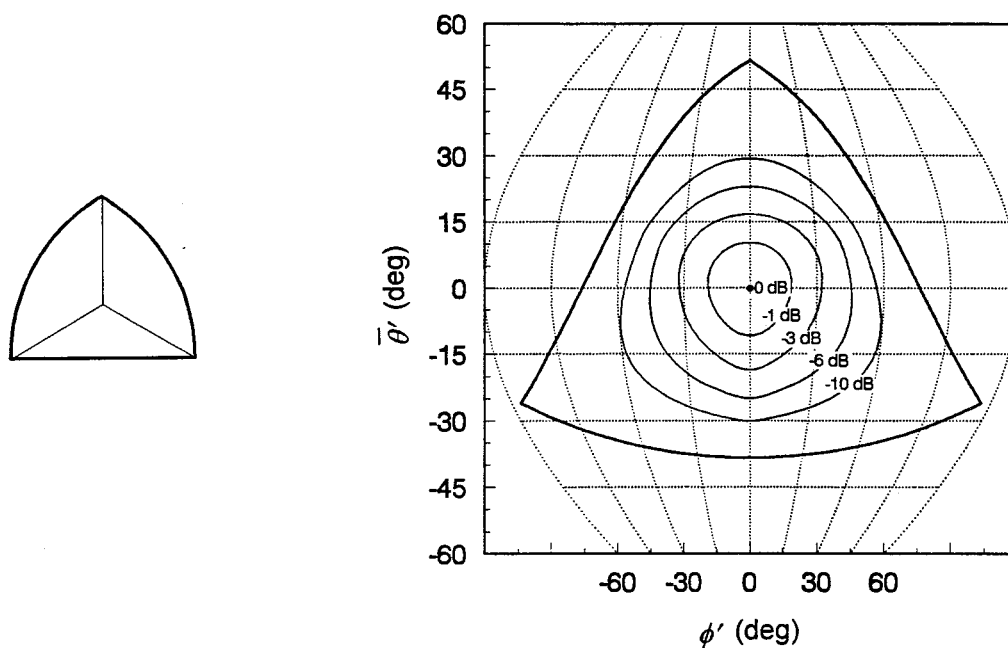
Figure 3.29: Angular coverage of a bilaterally symmetric trihedral corner reflector with circular side panels and a triangular center panel.
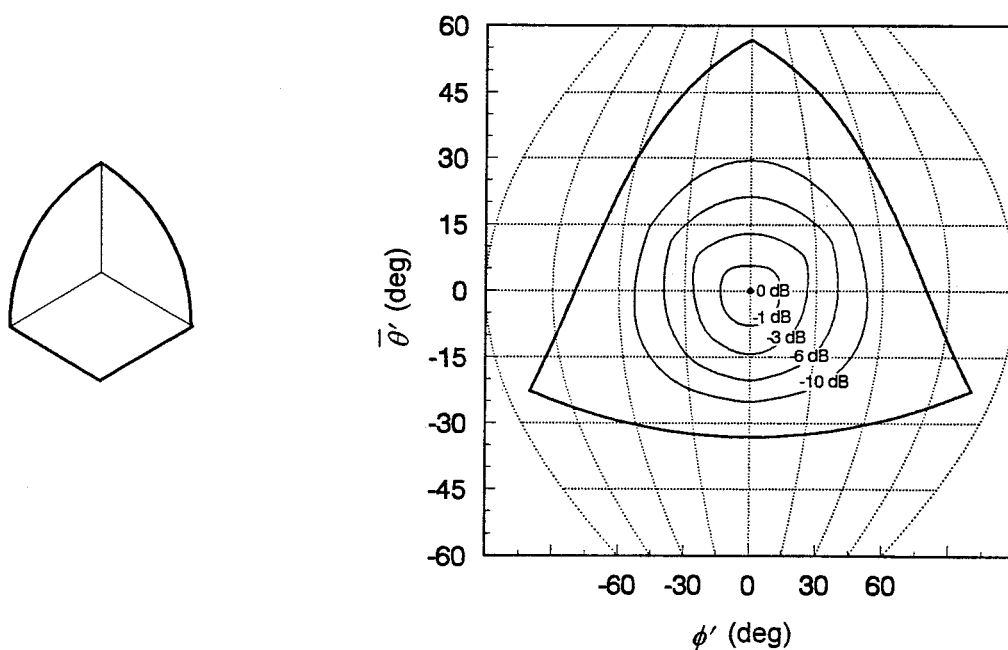
Figure 3.30: Angular coverage of a bilaterally symmetric trihedral corner reflector with circular side panels and a square center panel.
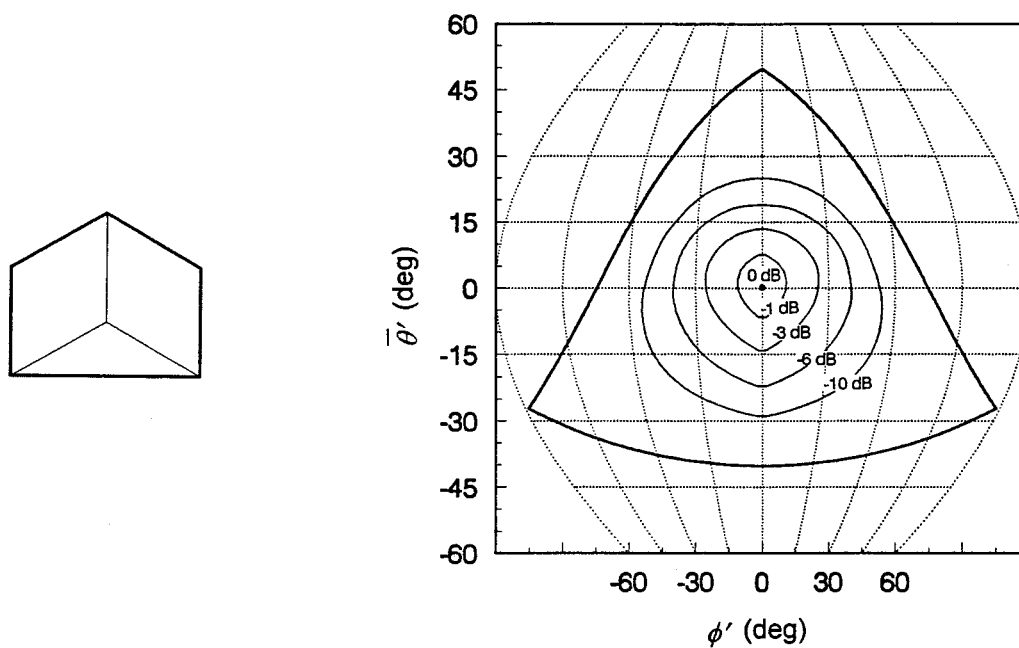
Figure 3.31: Angular coverage of a bilaterally symmetric trihedral corner reflector with square side panels and a triangular center panel.
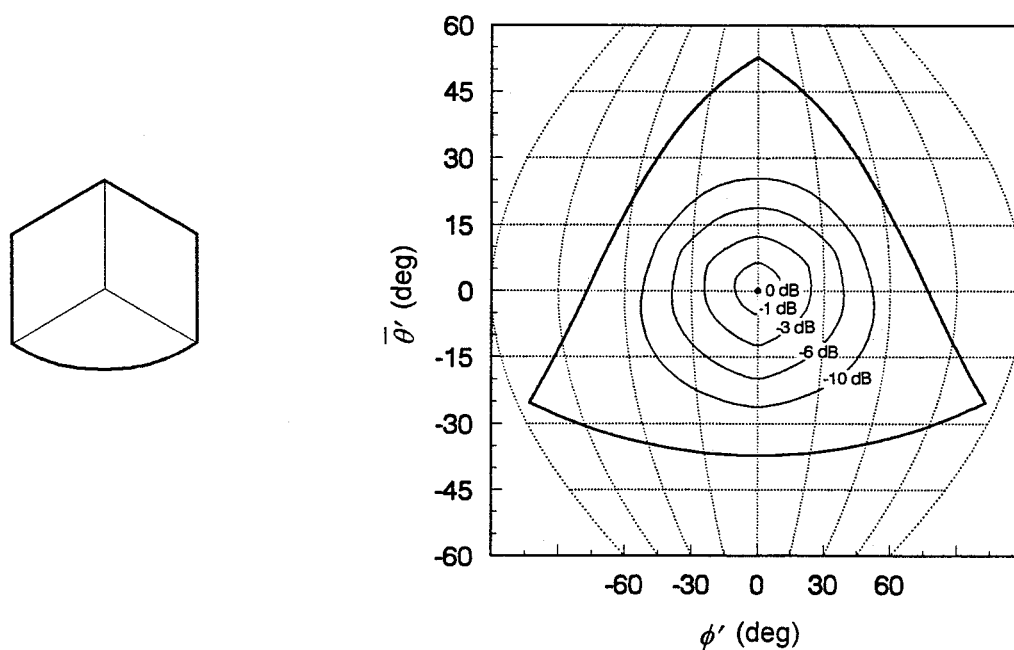
Figure 3.32: Angular coverage of a bilaterally symmetric trihedral corner reflector with square side panels and a circular center panel.
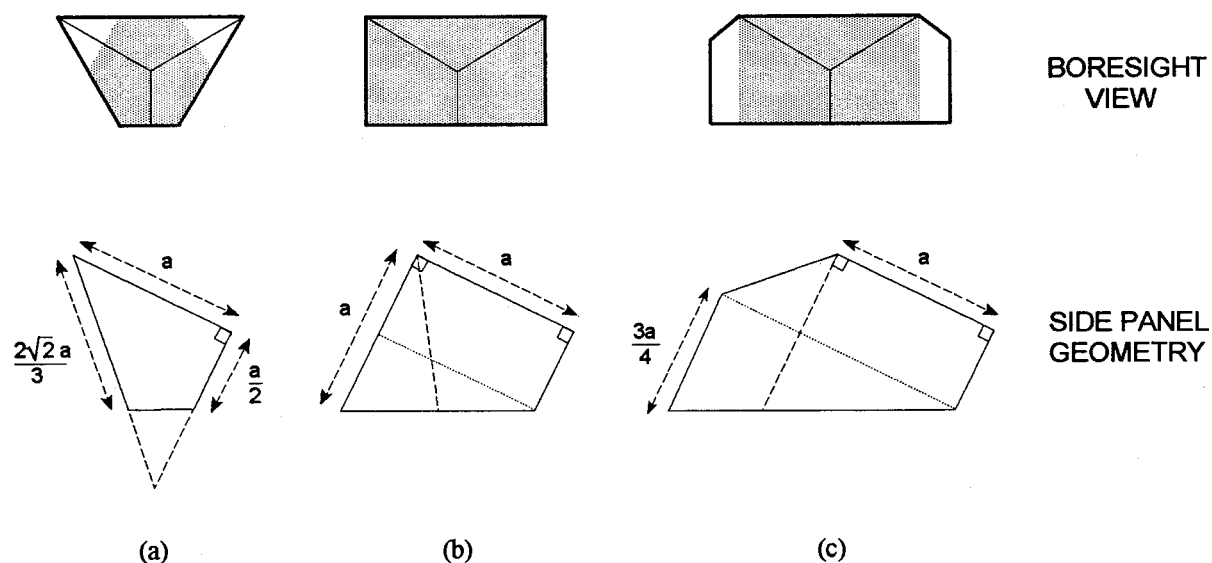
Figure 3.33: Evolution of Lanziner's bilaterally symmetric trihedral corner reflector through (a) truncation, (b) compensation, and (c) extension of the triangular side panels. The shaded portion indicates the equivalent flat plate area of the reflector for incidence along the boresight.
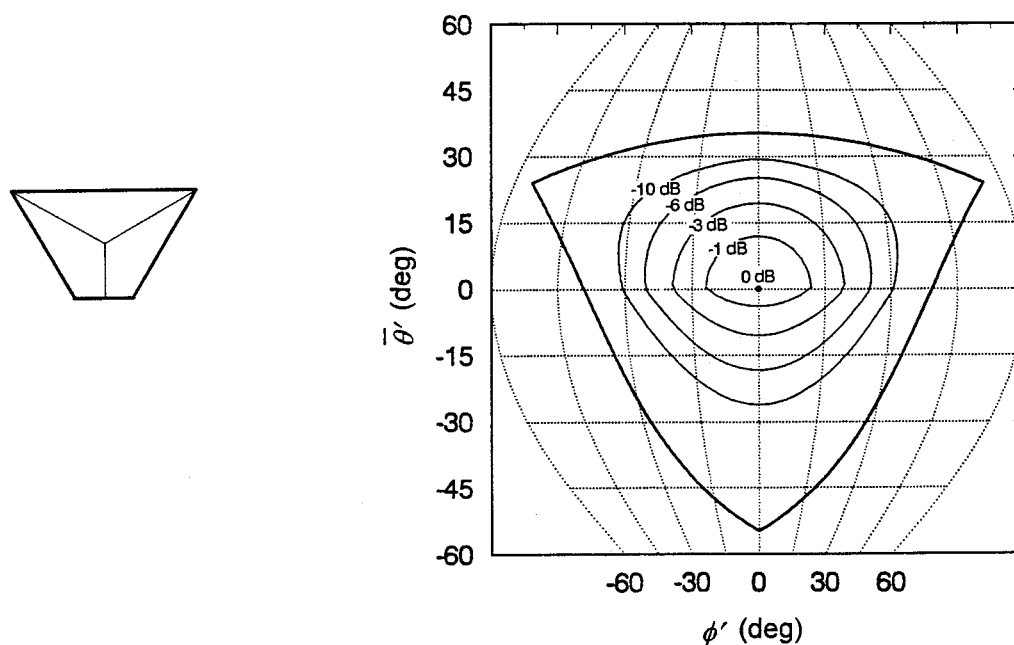
Figure 3.34: Angular coverage of a bilaterally symmetric trihedral corner reflector with truncated triangular side panels and a triangular center panel.
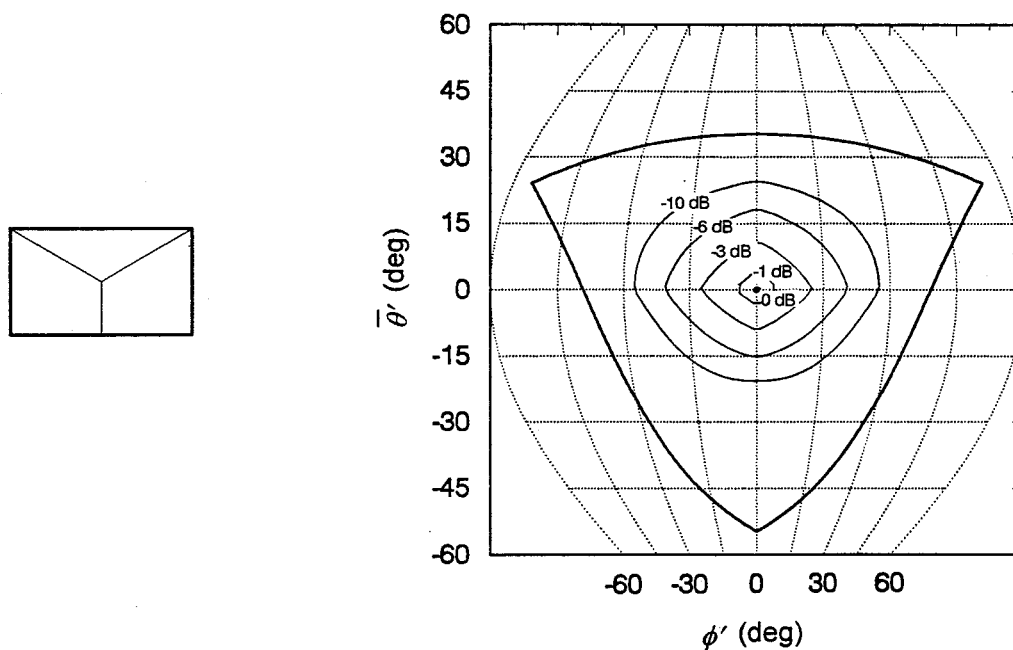
Figure 3.35: Angular coverage of a bilaterally symmetric trihedral corner reflector with truncated and compensated triangular side panels and a triangular center panel.
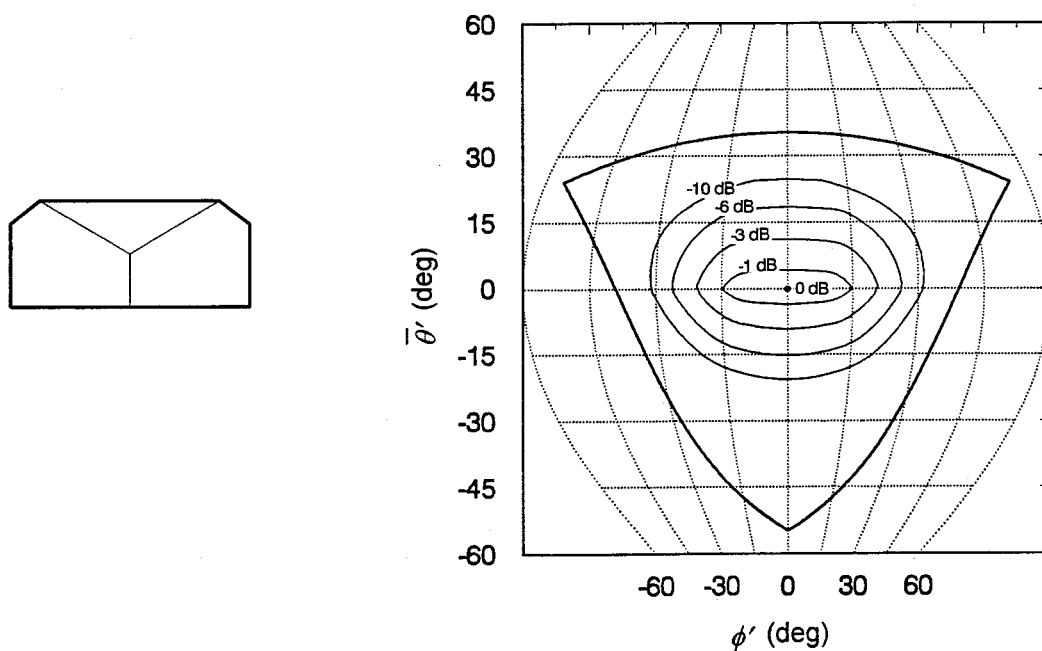
Figure 3.36: Angular coverage of a bilaterally symmetric trihedral corner reflector with truncated, compensated, and extended side panels and a triangular center panel.

Table 3.2:
Response Characteristics of Selected Trihedral Corner Reflectors with Bilateral Symmetry

Maximum Response

Figure	Side Panels	Center Panel	σ_{max} [1]	σ_{max} [2]	θ_{max}
3.27	Triangular	Circular	$6.4\,a^4/\lambda^2$	1.8 dB	58.5°
3.28	Triangular	Square	$8.7\,a^4/\lambda^2$	3.2 dB	61.4°
3.29	Circular	Triangular	$10.0\,a^4/\lambda^2$	3.8 dB	51.6°
3.30	Circular	Square	$21.3\,a^4/\lambda^2$	7.1 dB	56.9°
3.31	Square	Triangular	$18.8\,a^4/\lambda^2$	6.5 dB	49.8°
3.32	Square	Circular	$28.6\,a^4/\lambda^2$	8.3 dB	52.8°
3.34	Truncated	Triangular	$(4\pi/3)\,a^4/\lambda^2$	0.0 dB	54.7°
3.35	Compensated	Triangular	$(16\pi/3)\,a^4/\lambda^2$	6.0 dB	54.7°
3.36	Extended	Triangular	$(16\pi/3)\,a^4/\lambda^2$	6.0 dB	54.7°

1 and 3 dB Elevation and Azimuthal Beamwidths of the Main Response Lobe

Figure	Side Panels	Center Panel	Θ_{1dB}	Φ_{1dB}	Θ_{3dB}	Φ_{3dB}
3.27	Triangular	Circular	21°	22°	35°	37°
3.28	Triangular	Square	17°	17°	31°	31°
3.29	Circular	Triangular	21°	19°	35°	32°
3.30	Circular	Square	13°	14°	27°	26°
3.31	Square	Triangular	14°	11°	28°	25°
3.32	Square	Circular	11°	10°	25°	24°
3.34	Truncated	Triangular	16°	23°	30°	38°
3.35	Compensated	Triangular	8°	8°	20°	24°
3.36	Extended	Triangular	8°	29°	20°	41°

6 and 10 dB Elevation and Azimuthal Beamwidths of the Main Response Lobe

Figure	Side Panels	Center Panel	Θ_{6dB}	Φ_{6dB}	Θ_{10dB}	Φ_{10dB}
3.27	Triangular	Circular	48°	49°	60°	60°
3.28	Triangular	Square	45°	45°	58°	57°
3.29	Circular	Triangular	48°	45°	60°	57°
3.30	Circular	Square	41°	39°	55°	53°
3.31	Square	Triangular	41°	40°	54°	53°
3.32	Square	Circular	38°	39°	52°	52°
3.34	Truncated	Triangular	43°	51°	56°	61°
3.35	Compensated	Triangular	33°	40°	45°	55°
3.36	Extended	Triangular	33°	52°	45°	62°

Notes: (1) where a is the corner length of the center panel of the reflector.
(2) relative to σ_{max} of a trihedral corner reflector with triangular panels of the same corner length.

3.5 Effect of Errors in Construction on Reflector Performance

A trihedral corner reflector will present an optimum response if its three reflecting panels are perfectly flat and its corner angles are exactly 90 degrees. Approximate methods for determining the extent to which the response degrades as the reflecting panels deviate from perfect flatness and mutual orthogonality have been presented by Spencer [1], Keen [26], and Trebits [27]. The reduction in the scattering cross section of a symmetrical trihedral corner reflector with triangular panels due to errors in all three corner angles is presented in Figure 3.37. In general, the tolerances on the corner angles generally decrease as the size of the reflector increases. It has also been found that the tolerances on the corner angles depend on the shape of the reflecting panels and the size of the equivalent flat plate area. Although the approximate methods described by Spencer, Keen, and Trebits may be used to determine the effect of panel deviations on the response of trihedral corner reflectors with modified panel geometries, numerical techniques such as the finite-difference time-domain (FD-TD) and the shooting and bouncing ray (SBR) methods could also be used to perform the necessary calculations if sufficient computational resources are available [10], [11]. Alternatively, experimental techniques may be used to assess the effect of construction errors on the response of trihedral corner reflectors [28].
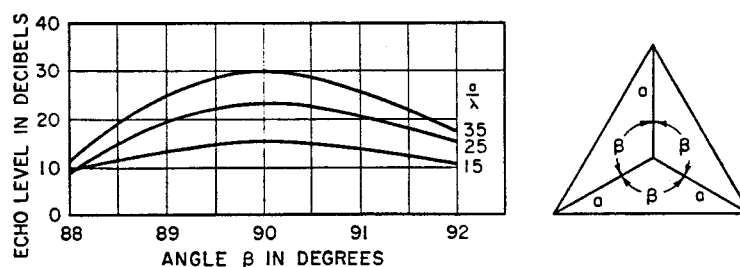
Figure 3.37: Effect of errors in all three corner angles on the response of a trihedral corner reflector with triangular panels for incidence along the the symmetry axis. (from [5, p. 13-12])

3.6 Conclusions

Methods for predicting the scattering cross section and angular coverage of a conventional trihedral corner reflector with panels of completely arbitrary shape have been considered. Although numerical techniques such as the finite-difference time-domain (FD-TD) and the shooting and bouncing ray (SBR) methods can predict both the contributions of single, double, and triple-bounce reflections from the interior and the effect of deviations of the reflecting panels from perfect flatness or mutual orthogonality, they are extremely demanding computationally. If the reflector is sufficiently large, it is usually sufficient to account for the contribution of triple-bounce reflections from the interior since they completely dominate the response for most directions of incidence. Spencer's model [1] for the contribution of triple-bounce reflections to the equivalent flat plate area of an ideal trihedral corner reflector with either triangular or square panels, and the prediction algorithm subsequently derived from it by Keen [14], [15], may fail when applied to reflectors with panels of completely arbitrary shape but an alternative model proposed by Robertson [4] will always provide the correct solution. An efficient and robust numerical method for solving Robertson's model has been presented.

The response patterns of ideal trihedral corner reflectors which present three-fold symmetry have been plotted on grids derived from equal area projections and compared. If the corner length of the reflector is fixed, it is generally found that attempts to increase the beamwidth of the response by modifying the shape of the panels are accompanied by a reduction in the amplitude of the maximum response. If three-fold symmetry is broken so that the reflector simply presents bilateral symmetry about a mirror plane which contains one of the trihedral axes and bisects the opposite panel, the beamwidth of the response in one principal plane can be increased relative to the beamwidth in the orthogonal plane by modifying the shape of the reflecting panels in a suitable manner. The additional degree of freedom may also prove useful when a reflector must be designed subject to a constraint such as a requirement that the modified reflector present a planar aperture in order to facilitate the attachment of either a transmission polarizer or a protective cover. A set of design curves for bilaterally symmetric

reflectors which are composed solely of triangular, elliptical, or rectangular reflecting panels has been presented. The curves present the elevation angle of the direction of maximum response, the amplitude of the maximum response, and the elevation and azimuthal beamwidths as a function of the reflector aspect ratio. For the case of a bilaterally symmetric trihedral corner reflector with triangular panels, the elevation angles of the direction of maximum response and the normal to the reflector aperture have been compared as a function of the reflector aspect ratio. The response patterns of selected bilaterally symmetric reflectors which are composed of combinations of panels with various shapes including triangular, circular, and square have also been presented and compared. The European Space Agency's SAR-580 calibration target is included in this set. A related problem, the design of top hat reflectors with specified response characteristics, is considered in Appendix A.

Degradation of the response of a trihedral corner reflector caused by deviation of its reflecting panels from perfect flatness or orthogonality is an important consideration in the design and fabrication of calibration targets and location markers. Although the approximate methods presented by Spencer [1], Keen [26], and Trebits [27] may be used to determine the effect of panel deviations on the response of trihedral corner reflectors with modified panel geometries, numerical techniques such as the finite-difference time-domain and the shooting and bouncing ray methods mentioned above can also be used to perform such calculations if sufficient computing resources are available.

References

[1] R. C. Spencer, *Optical Theory of the Corner Reflector*. Cambridge, MA: MIT Rad. Lab. Tech. Rep. 433, 2 Mar. 1944.

[2] K.M. Siegel *et al.*, *Studies in Radar Cross Sections XVIII - Airborne Passive Measures and Countermeasures*. Ann Arbor, MI: Univ. Michgan, Jan. 1956. (cited in C.G. Bachman, *Radar Targets*. Lexington, MA: Heath, 1982, p. 71–101.)

[3] A.L. Maffett, *Topics for a Statistical Description of Radar Cross Section*. New York: Wiley, 1989, pp. 190–201.

[4] S. D. Robertson, "Targets for microwave radar navigation," *Bell Syst. Tech. J.*, vol. 26, pp. 852–869, 1947.

[5] W. C. Jakes, Jr., and S. D. Robertson, "Passive Reflectors," in *Antenna Engineering Handbook*, H. Jasik, Ed. New York: McGraw-Hill, 1961, chap. 13.

[6] P. O. Gillard and K. B. Whiting, *Ground Plane Corner Reflectors for Navigation and Remote Indication*. U.S. Patent No. 4,104,634, dated Aug. 1, 1978.

[7] S. Haykin, "Polarimetric radar for accurate navigation," *Can. J. Elect. Comp. Eng.*, vol. 17, pp. 130–135, July 1992.

[8] D.G. Corr, A.D. Woode, and S. Bruzzi, "The SAR-580 calibration site at RAE, Bedford," *Int. J. Remote Sensing*, vol. 3, pp. 223-227, 1982.

[9] A. Freeman, Y. Shen, and C. L. Werner, "Polarimetric SAR calibration experiment using active radar reflectors," *IEEE Trans. Geosci. Remote Sensing*, vol. GE-28, pp. 224–240, Mar. 1990.

[10] A. Taflove and K.R. Umashankar, "Review of FD-TD numerical modelling of electromagnetic wave scattering and radar cross section," *Proc. IEEE,* vol. 77, pp. 682–699, May 1989.

[11] J. Baldauf, S-W Lee, L. Lin, S-K Jeng, S.M. Scarborough, and C.L. Yu, "High frequency scattering from trihedral corner reflectors and other benchmark targets: SBR versus experiment," *IEEE Trans. Antennas Propagat.,* vol. 39, pp. 1345–1351, Sept. 1991.

[12] A.C. Polycarpou, C.A. Balanis, and P.A. Tirkis, "Radar cross section evaluation of the square trihedral corner reflector using PO and MEC," in *IEEE/AP-S Symp. Dig.* (Ann Arbor, MI), June 1993, pp. 1428–1431.

[13] Z.O. Al-hekail and W.D. Burnside, "Scattering from corner reflectors: a hybrid approach," in *IEEE/AP-S Symp. Dig.* (Ann Arbor, MI), June 1993, pp. 1432–1435.

[14] K. M. Keen, "New technique for the evaluation of the scattering cross-sections of radar corner reflectors," *IEE Proc. H,* vol. 130, pp. 322–326, Aug. 1983.

[15] K. M. Keen, "Fast algorithm for the exact determination of the mapped effective areas of trihedral radar reflectors," *Electron. Lett.,* vol. 19, pp. 1014–1015, Nov. 24, 1983.

[16] D.R. Brown, R.J. Newman, and J.W. Crispin, Jr., "RCS Enhancement Devices," in *Methods of Radar Cross Section Analysis,* J.W. Crispin, Jr. and K.M. Siegel, Eds. New York: Academic Press, 1969, pp. 237–280.

[17] R. Sedgewick, *Algorithms,* 2nd ed. Reading, MA: Addison-Wesley, 1988, pp. 347–356.

[18] D.F. Rogers, *Procedural Elements for Computer Graphics.* New York: McGraw-Hill, 1985, pp. 111–188.

[19] J.D. Foley, A. van Dam, S.K. Feiner, and J.F. Hughes, *Computer Graphics: Principles and Practice,* 2nd ed. Reading, MA: Addison-Wesley, 1990, pp. 124–127,

[20] K. Weiler and P. Atherton, "Hidden surface removal using polygon area sorting," *Computer Graphics*, vol. 11, pp. 214–222, Summer 1977.

[21] K. Weiler, "Polygon comparison using a graph representation," *Computer Graphics*, vol. 14, pp. 10–18, Spring 1980.

[22] P. Richardus and R.K. Adler, *Map Projections for Geodesists, Cartographers, and Geographers.* Amsterdam: North-Holland, 1972.

[23] J.P. Snyder and P.M. Voxland, *An Album of Map Projections.* U.S. Geol. Surv. Prof. Pap., no. 1453, 1989.

[24] W. H. Press, B. P. Flannery, S. A. Teukolsky, and W. T. Vetterling, *Numerical Recipes*, 2nd ed. Cambridge Univ. Press: Cambridge, 1992.

[25] D. G. Michelson and H. H. Lanziner, *Radar Reflector to Enhance Detection.* U.S. Patent No. 4,990,918, dated Feb. 5, 1991.

[26] K. M. Keen, "Prediction of scattering cross-section reductions due to plate orthogonality errors in trihedral radar reflectors," *Electron. Lett.*, vol. 19, pp. 115–117, Feb. 3, 1983.

[27] R.N. Trebits, "Radar Cross Section," in *Radar Reflectivity Measurement: Techniques and Applications,* N.C. Currie, Ed. Norwood, MA: Artech House, 1989, pp. 46–49.

[28] D. Kähny and J. van Zyl, "How does corner reflector construction affect polarimetric SAR calibration?" in *Proc. IGARSS'90* (College Park, MD), May 1990, pp. 1093–1096.

Chapter 4

DEPOLARIZING TRIHEDRAL CORNER REFLECTORS

4.1 Introduction

A conventional trihedral corner reflector returns linearly polarized incident waves without modification but reverses the sense of elliptically or circularly polarized waves. This is often referred to as a *regular* polarization response since it is also characteristic of spheres and flat plates. Although this is an ideal response for targets intended for use with conventional radars which employ either horizontally or vertically polarized antennas for both transmission and reception, radars which employ same-sense circular polarization to assist in rain clutter suppression or, more recently, various forms of polarization diversity to assist in target classification and identification often require calibration targets and location markers with twist-polarizing, circularly polarizing, or linear polarization selective responses [1], [2]. Several methods for altering the polarization response of conventional trihedral corner reflectors have been developed over the years [3]–[12]. The three basic approaches are shown in Figure 4.1.
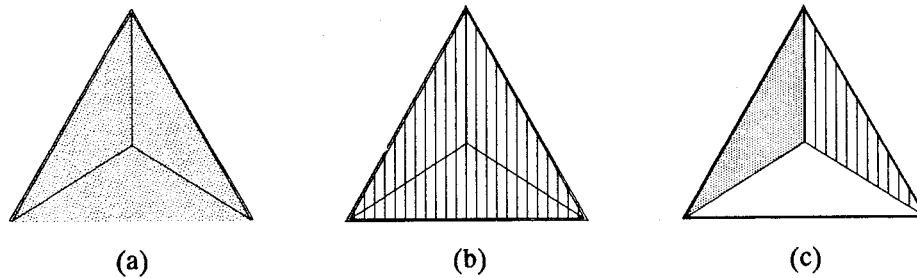
Figure 4.1: Methods for altering the polarization response of a conventional trihedral corner reflector. (a) Removal of one reflecting panel and loading of the interior of the reflector with a low-loss dielectric material ($2.3 \leq \epsilon_r \leq 4$). (b) Installation of a transmission polarizer across the reflector aperture. (c) Replacement of one of the reflecting panels by a reflection polarizer.

Since it is often necessary to deploy large numbers of calibration targets and location markers in the field for extended periods of time where they are exposed the effects of sun, wind, and rain, the mechanical ruggedness of trihedral corner reflectors which incorporate depolarizing elements and the ease with which such reflectors can be manufactured are important considerations. Schemes which require that a transmission polarizer be installed across the reflector aperture become increasingly difficult to implement as the reflector grows larger and cannot be applied at all if the reflector doesn't present a planar aperture [4]-[6]. Schemes which involve replacing or augmenting one of the reflecting panels with a reflection polarizer oriented such that the axis of the grating is parallel to one of the principal axes of the trihedral have attracted considerable interest, particularly in recent years, because they avoid many of the mechanical problems associated with the use of transmission polarizers and can easily be applied to reflectors with panels of arbitrary size and shape [7]-[12]. However, trihedral corner reflectors which incorporate reflection polarizers that make substantial use of wire grids and dielectric materials in their construction are relatively fragile [13]-[14]. Although mechanical and environmental damage can be prevented through the use of protective covers and weatherproof seals, such measures substantially increase manufacturing costs and are not always effective.

Many of the limitations of previous schemes for altering the polarization response of trihedral corner reflectors can be overcome [15]-[16] by utilizing a reflection polarizer derived from conducting fins or corrugations [17]-[22]. In section 4.2, the scattering properties of conducting gratings with rectangular grooves are reviewed and design curves for twist polarizing and circularly polarizing trihedral corner reflectors are presented. Methods for realizing conducting gratings with linear polarization selective responses are proposed. In section 4.3, an algorithm for predicting the contribution of triple-bounce reflections to the polarization scattering matrix of a trihedral corner reflector which has been modified by the addition of conducting fins or corrugations to one of its interior surfaces as a function of the direction of incidence and orientation of the reflector is described. In section 4.4, the response patterns of prototype reflectors with regular, twist-polarizing, and circularly polarizing responses are compared to theoretical predictions. The results show that the prototype reflectors respond essentially as expected.

4.2 Scattering by a Conducting Grating with Rectangular Grooves

Consider a plane wave incident on a conducting grating with rectangular grooves as shown in Figure 4.2. Let the direction of the grooves define the grating axis. If the grating is of infinite extent, the scattered field will consist of a finite number of propagating plane waves or *diffracted orders* and an infinite number of nonpropagating or *evanescent* waves. If the plane of incidence is perpendicular to the grating axis, the direction in which the mth diffracted order propagates is given by the grating equation,

$$\sin\phi_m = \sin\phi_i + m\frac{\lambda}{d} \,, \qquad m = \dots, -1, 0, 1, 2, \dots \,, \tag{4.1}$$

where ϕ_m is the angle of reflection of the mth diffracted order, ϕ_i is the angle of incidence, λ is the wavelength of the incident wave, and d is the period of the grating. If $|\sin\phi_m| \leq 1$, the mth diffracted order will propagate away from the surface at angle ϕ_m with respect to the x axis. If $|\sin\phi_m| > 1$, the mth diffracted order takes the form of an evanescent field which decays exponentially with increasing distance from the surface of the grating.

The number of diffracted orders which are visible is dependent on the period of the grating and the angle of incidence. The chart shown in Figure 4.3 is derived by solving the grating equation at each angle of incidence for the point at which each diffracted order becomes visible as the period of the grating is gradually increased. Diffracted orders with negative indices will appear at $\phi_m = -90°$ while those with positive indices will appear at $\phi_m = 90°$. If the grating period and the angle of incidence are chosen such that

$$\sin\phi_i - \frac{\lambda}{d} < -1 \,, \tag{4.2}$$

then only the specularly reflected order will propagate. However, if the grating period and the angle of incidence are chosen such that the following conditions are satisfied simultaneously,

$$\sin\phi_i - \frac{\lambda}{d} > -1 \,, \tag{4.3}$$

$$\sin\phi_i - 2\frac{\lambda}{d} < -1 \,, \tag{4.4}$$

$$\sin\phi_i + \frac{\lambda}{d} > +1 \,, \tag{4.5}$$
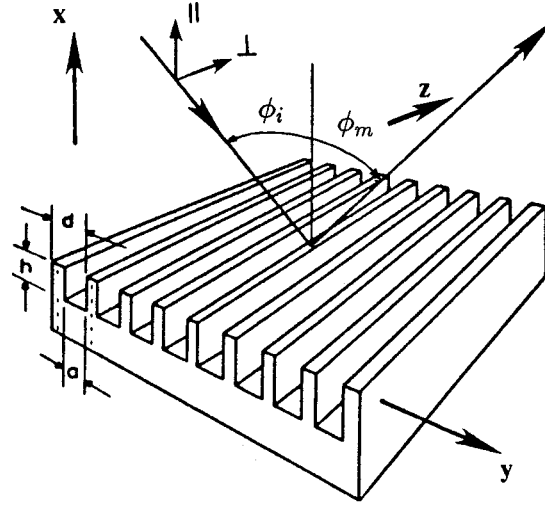
Figure 4.2: Problem geometry for scattering by a conducting grating with rectangular grooves where d, a, and h are the period of the grating and the width and depth of the grooves, respectively, ϕ_i is the angle of incidence, and ϕ_m is the angle of reflection of the mth diffracted order.
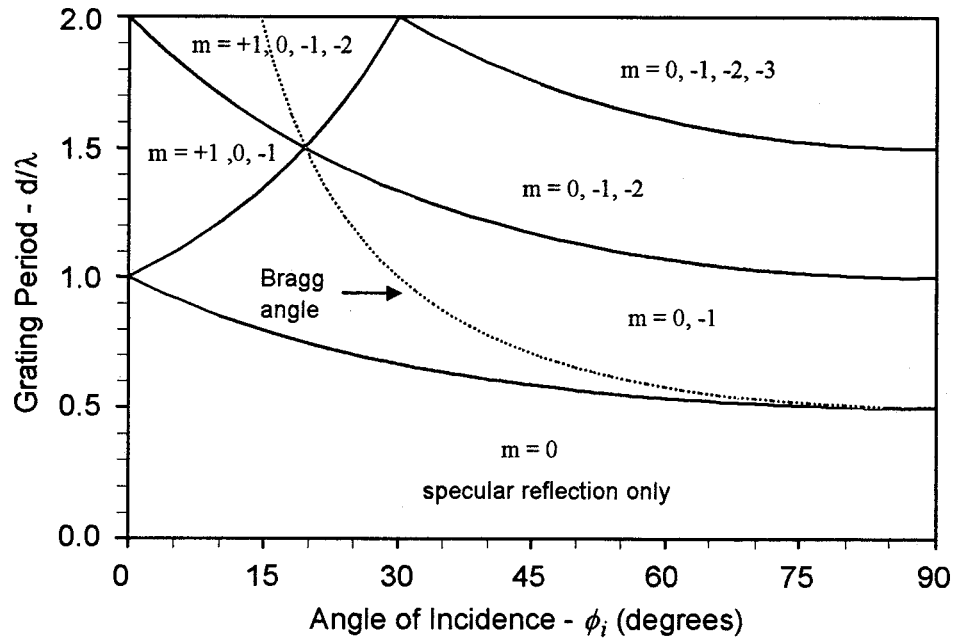
Figure 4.3: Visible diffracted orders as a function of the grating period d/λ and the angle of incidence ϕ_i where the plane of incidence is normal to the grating axis.

then both the $m = 0$ and the $m = -1$ diffracted orders will propagate. The Bragg angle condition corresponds to propagation of the $m = -1$ diffracted order back towards the source and is given by

$$d = \frac{\lambda}{2 \sin \phi_i} \, . \tag{4.6}$$

It has been found that a grating which satisfies this condition can be made to diffract all the power in an incident wave into the $m = -1$ diffracted order by appropriate shaping of its profile.

Since the grating is uniform in the z-direction, the spatial derivatives associated with the incident and scattered fields vanish in z and Maxwell's equations divide into two independent sets,

$$\frac{\partial H_z}{\partial y} = j\omega\epsilon_o E_x, \qquad \frac{\partial H_z}{\partial x} = -j\omega\epsilon_o E_y, \qquad \frac{\partial E_y}{\partial x} - \frac{\partial E_x}{\partial y} = -j\omega\mu_o H_x \, , \tag{4.7}$$

$$\frac{\partial E_z}{\partial y} = -j\omega\mu_o H_x, \qquad \frac{\partial E_z}{\partial x} = j\omega\mu_o H_y, \qquad \frac{\partial H_y}{\partial x} - \frac{\partial H_x}{\partial y} = j\omega\epsilon_o E_z \, . \tag{4.8}$$

The first, which consists of H_z, E_x, and E_y components, is called a transverse magnetic (TM) or E-polarized field while the second, which consists of E_z, H_x, and H_y components, is called a transverse electric (TE) or H-polarized field. Let $[S_m]$ be the normalized polarization scattering matrix which is associated with diffraction into the mth order. Since the TM- and TE-polarized fields are decoupled, the off diagonal elements of the matrix vanish and $[S_m]$ reduces to

$$[S_m] = \begin{bmatrix} S_{EE,m} & S_{EH,m} \\ S_{HE,m} & S_{HH,m} \end{bmatrix} = \begin{bmatrix} \Gamma_m^{EE} & 0 \\ 0 & \Gamma_m^{HH} \end{bmatrix} , \tag{4.9}$$

where Γ_m^{HE} represents the complex reflection coefficient for diffraction of a TM-polarized incident wave into the TE-polarized component of the mth diffracted order and $[S_m]$ is expressed according to the forward scattering alignment (FSA) convention. If the amplitude of the complex reflection coefficients $|\Gamma_0^{EE}| = |\Gamma_0^{HH}| = 1$, then the total power in the specular reflected order will be independent of the polarization state of the incident wave. Such a response is said to be *polarization-operative*. However, if the amplitude $|\Gamma_0^{EE}| \neq |\Gamma_0^{HH}|$, then the total power in the specular reflected order will be dependent on the polarization state of the incident wave. Such a response is said to be *polarization-selective*.

The complex reflection coefficients Γ_m^{EE} and Γ_m^{HH} are functions of both the dimensions of the grating and the direction and wavelength of the incident wave. Since the free space and groove regions are defined by separable coordinate systems, a rigorous solution to the problem can be obtained by representing the fields in each region as the weighted sum of orthonormal basis functions and determining the relative amplitude and phase of the propagating diffracted orders by mode-matching at the boundary between the regions. A complete derivation of the solution and procedures for determining the validity of numerical results obtained by this method are presented in Appendix B. Although the solution will invariably converge to an essentially constant result as the number of modes used in the field expansions are systematically and gradually increased, it is shown that the manner in which the solution converges and the value of the final result will depend on both the number of modes used to represent the fields in each region and their ratio. This phenomenon is commonly referred to as relative convergence. Numerical results are presented which suggest that the optimum ratio of groove modes to free space modes is similar in value to the aspect ratio of the grating, a/d. An implementation of the solution as a pair of subroutines coded in Fortran 77 is also presented.

For the purpose of defining the polarization states of the incident and reflected waves, let the z axis define the local vertical. If period of the grating is less than one-half wavelength, only the specular order will propagate. In such cases, the phase difference δ between the TE and TM reflection coefficients can be exploited to yield a depolarizing response of the form,

$$[S] = \begin{bmatrix} S_{HH} & S_{HV} \\ S_{VH} & S_{VV} \end{bmatrix} = \begin{bmatrix} \Gamma_0^{EE} & 0 \\ 0 & \Gamma_0^{HH} \end{bmatrix} = \begin{bmatrix} 1 & 0 \\ 0 & e^{j\delta} \end{bmatrix}. \tag{4.10}$$

A phase difference of 0 will yield a regular polarization response while phase differences of 180 and 90 degrees will yield twist-polarizing and circularly polarizing responses, respectively. The co-polar and cross-polar response of regular, twist, and circular polarizers with polarization responses defined by (4.10) are plotted as a function of the polarization state of the incident wave in Figures 4.4, 4.5, and 4.6. If the grating is modified in such a way that $\Gamma_0^{EE} \to 0$, the linear polarization selective response of Figure 4.7 will be obtained.
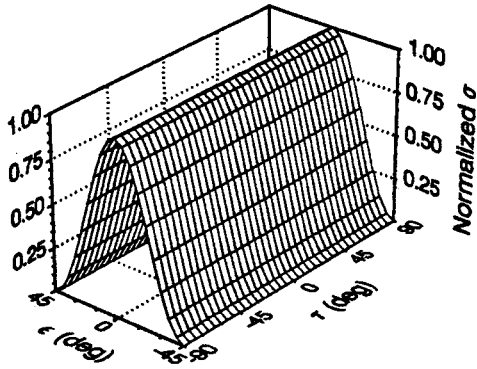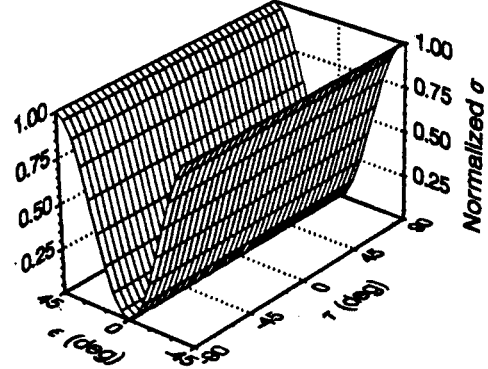
(a)   (b)

Figure 4.4: Normalized response of a regular reflector as a function of the polarization state of the incident wave. (a) Co-polar response. (b) Cross-polar response.
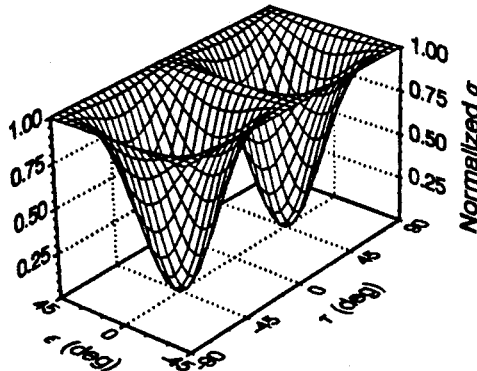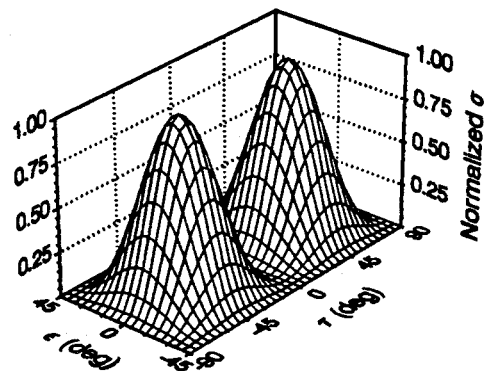
(a)   (b)

Figure 4.5: Normalized response of a twist-polarizing reflector as a function of the polarization state of the incident wave. (a) Co-polar response. (b) Cross-polar response.

(a)　　　　　　　　　　　　　　(b)
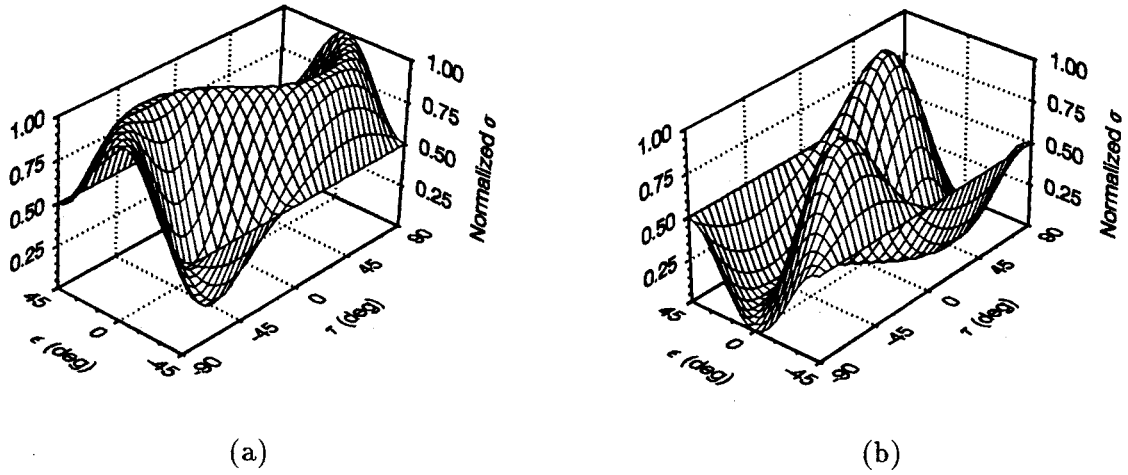
Figure 4.6: Normalized response of a circularly polarizing reflector as a function of the polarization state of the incident wave. (a) Co-polar response. (b) Cross-polar response.

(a)　　　　　　　　　　　　　　(b)
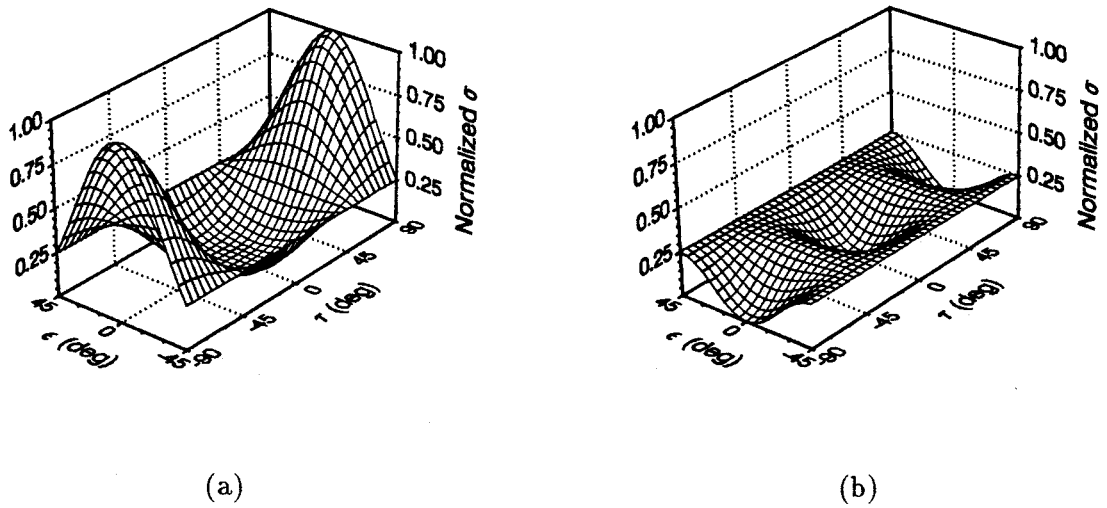
Figure 4.7: Normalized response of a vertical polarization selective reflector as a function of the polarization state of the incident wave. (a) Co-polar response. (b) Cross-polar response.

For a grating with a vanishingly small period and arbitrarily thin fins, the groove depths required to realize twist and circularly polarizing responses for normal incidence are simply $\lambda/4$ and $\lambda/8$, respectively. In practice, however, account must be taken of both the finite dimensions of the grating and the angle of incidence. The groove depths required to realize twist and circularly polarizing responses were determined as a function of the period and aspect ratio of the grating and the direction and wavelength of the incident wave by applying a bracketing and bisection algorithm to a subroutine which calculates the phase difference between the TE and TM specular reflection coefficients. The calculations were performed using the mode-matching formulation presented in Appendix B. Twist polarizer design curves for essentially normal incidence and 45 degree incidence are presented in Figures 4.8 and 4.9, respectively. (The response of the grating could not be calculated for incidence at $\phi_i = 0°$ due to the nature of the analytical formulation so the design curves for normal incidence were calculated at $\phi_i = 1°$ instead.) As the grating period approaches zero, the groove depth required to yield a twist-polarizing response converges to $\lambda/4$ for all aspect ratios and angles of incidence. As the period of the grating increases, the required groove depth increases for large aspect ratios and decreases for small aspect ratios. Circular polarizer design curves for essentially normal incidence and 45 degree incidence are presented in Figures 4.10 and 4.11. In this case, the ideal groove depth is satisfactory only for very thin fins and at normal incidence. The difference between the groove depths required to realize twist polarizers and circular polarizers with identical aspect ratios is nearly constant as a function of the grating period. A large difference between the required groove depths implies that the grating will present the desired polarization response over a wide operating bandwidth while a small difference implies that the grating will present the desired response over a relatively narrow operating bandwidth. For normal incidence, the differences between the required groove depths for gratings with aspect ratios a/d of 0.3333, 0.7500, and 0.9999, are approximately $0.05\,\lambda$, $0.10\,\lambda$, and $0.13\,\lambda$, respectively. Similar results are obtained for 45 degree incidence. This suggests that twist and circular polarizers derived from corrugated surfaces should be designed with the largest possible aspect ratios in order to obtain optimum performance.

Three methods for realizing a grating which presents a linear polarization selective response are depicted in Figure 4.12. A grating with a small period and large aspect ratio which has been loaded with lossy media, as shown in Figure 4.12(a), will present a TE-polarization selective response since the groove region functions as a resonant absorber for TM-polarized incident waves [23], [24]. This approach has several disadvantages including the limitations on the minimum value of the TM reflection coefficient that can be obtained, the frequency selective nature of the response, and the vulnerability of the lossy groove media to mechanical or environmental damage. Alternatively, a conventional grating which satisfies the Bragg condition can be made to diffract the TM-polarized component of an incident wave into the $m = -1$ diffracted order while it specularly reflects the TE-polarized component by appropriate shaping of its profile [25]. Although such a grating will act as a retro-reflector for TM-polarized waves and cannot be used to realize a linear polarization selective trihedral corner reflector, it has been shown that gratings can be perfectly blazed for other angles of incidence as well, as suggested by Figure 4.12(b) [26]. The phenomena of perfect blazing for non-Bragg angle incidence is not well understood and relatively few examples are known. Also, the direction of the higher diffracted order is a function of both the wavelength and direction of the incident wave and must be accounted for when designing an apparatus which incorporates such a polarizer. A third approach is shown in Figure 4.12(c). A grating with a small period, large aspect ratio, and a sloped profile which subtends an angle β, will reflect TM-polarized incident from the bottom of the groove region at an angle ϕ_0 with respect to the grating normal but will reflect TE-polarized incident waves from the top of the corrugations at an angle $\phi_0 - 2\beta$. Since the response is independent of the wavelength of the incident wave and the structure is inherently rugged, this approach overcomes many of the limitations of the other two schemes. Although the angle β should be as large as possible so that the directions of the TM and TE polarized reflected waves are separated by a wide angle, the maximum height of the fins is given by $h_{\max} = r \sin \beta$ where r is the maximum dimension of the polarizer in the plane perpendicular to the grating axis. Thus, a practical limit on the slope angle which can be accomodated is imposed when a physically large polarizer of this type is required.
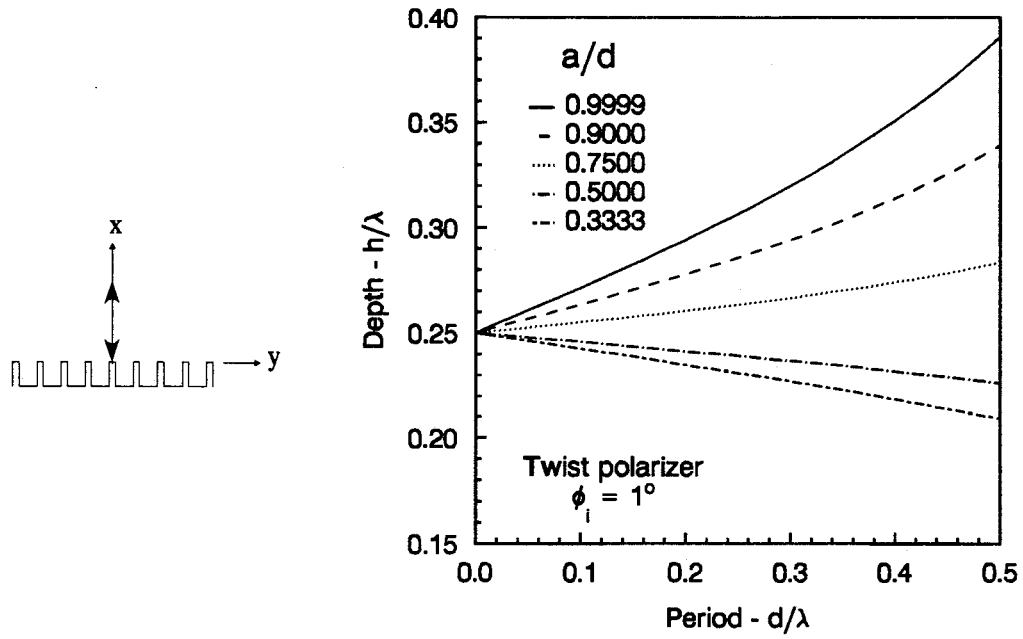
Figure 4.8: Twist polarizer design curves for normal incidence.
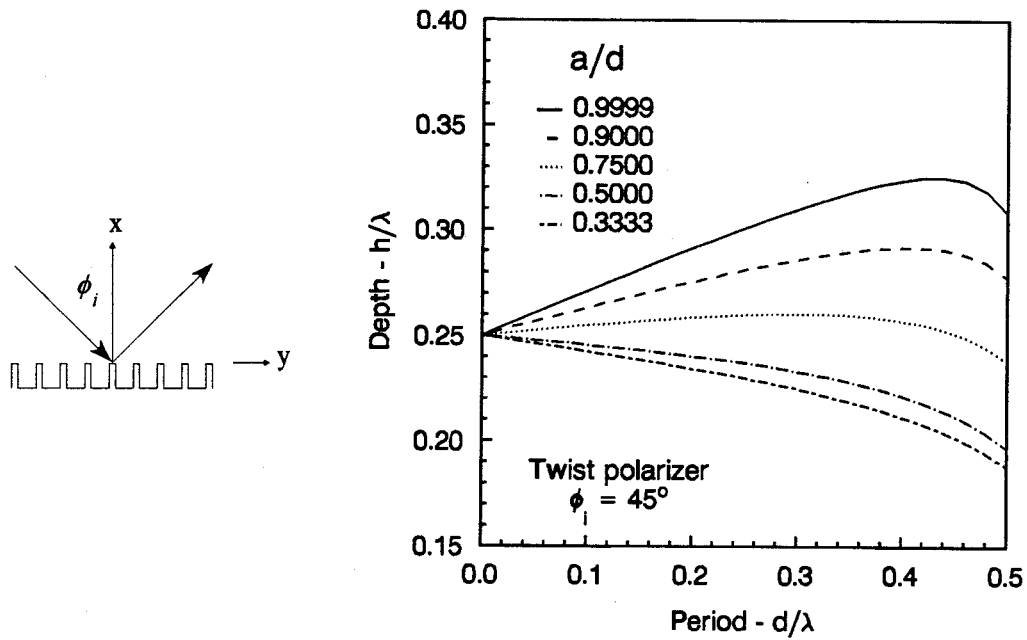
Figure 4.9: Twist polarizer design curves for 45 degree incidence.
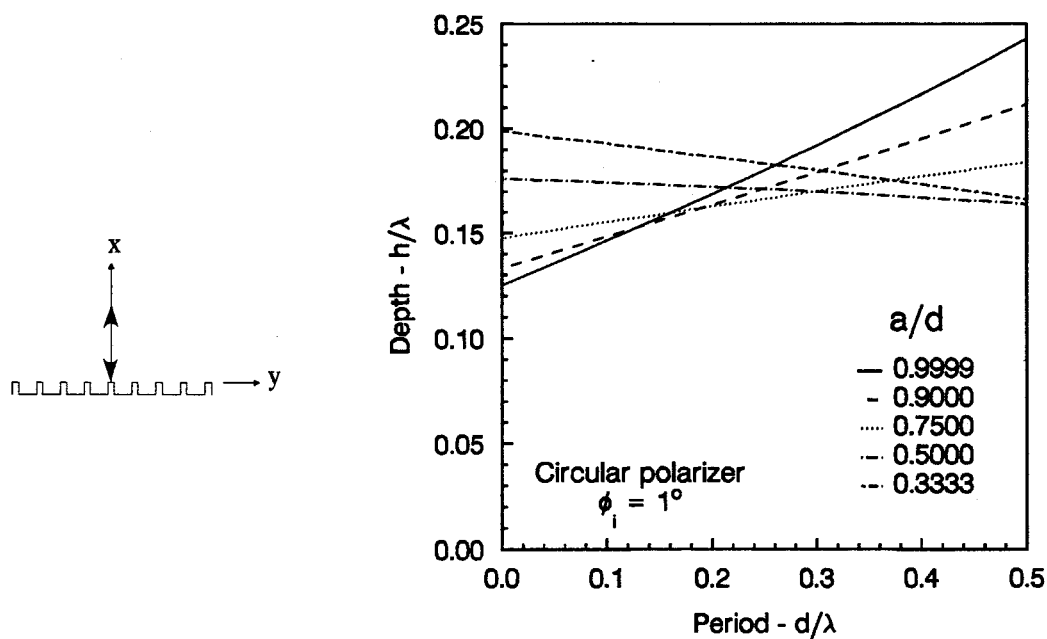
Figure 4.10: Circular polarizer design curves for normal incidence.
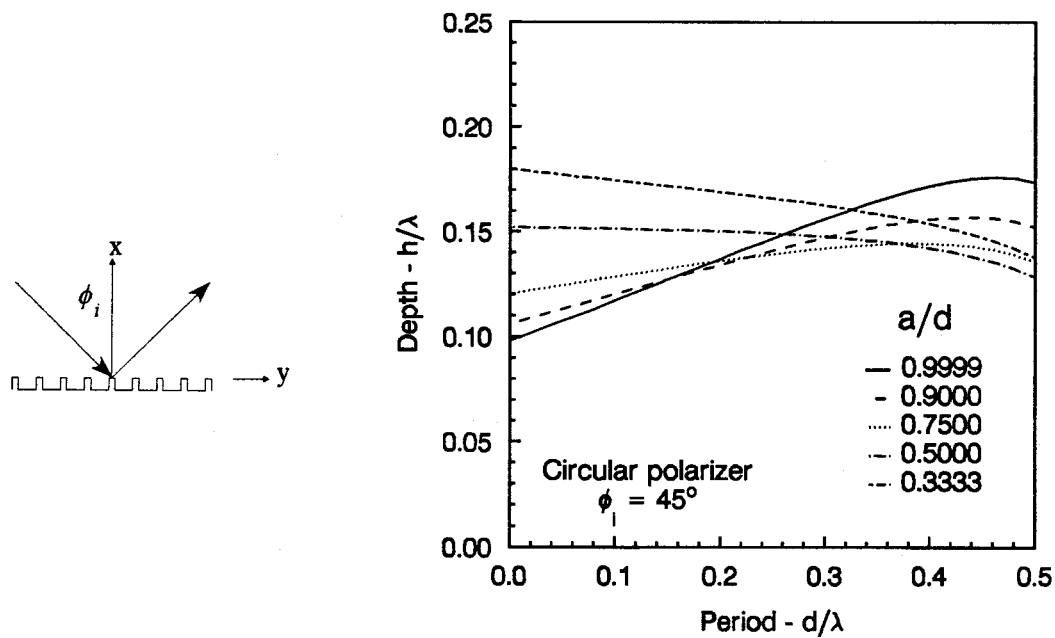
Figure 4.11: Circular polarizer design curves for 45 degree incidence.
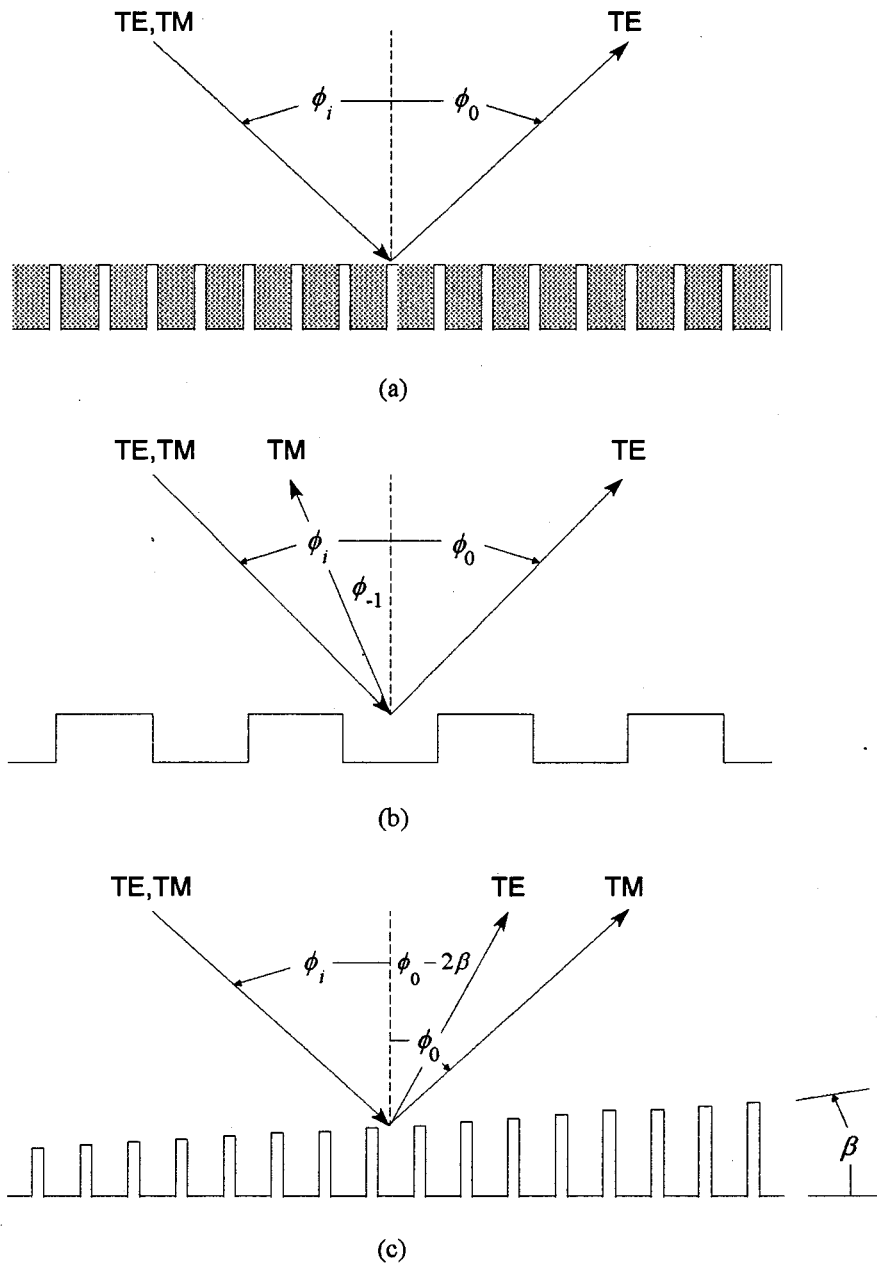
Figure 4.12: Linear polarization selective reflectors derived from corrugated surfaces. (a) Specular reflection of TE-polarized incident waves and dissipation of TM-polarized incident waves in lossy groove media. (b) Specular reflection of TE-polarized incident waves and diffraction of TM-polarized incident waves into the $m = -1$ order. (c) Specular reflection of TM-polarized incident waves with respect to the base of a polarizer with a sloped profile and specular reflection of TE-polarized incident waves with respect to the upper surface.

Thus far, it has been assumed that the plane of incidence is perpendicular to the grating axis with the phase of the incident wave given by

$$\exp(jk\zeta_i) = \exp[jk(x\cos\phi_i - y\sin\phi_i)] . \tag{4.11}$$

Since the grating is uniform along its axis, the results are easily extended to the case of oblique incidence [27]. In this case, the phase of the incident wave is given by

$$\exp(jk\zeta_i) = \exp[jk(x\sin\theta_i\cos\phi_i - y\sin\theta_i\sin\phi_i + z\cos\theta_i)] , \tag{4.12}$$

which is obtained from (4.11) by replacing k by $k\sin\theta_i$ and multiplying by $\exp(jkz\cos\theta_i)$. Since the scattered field also varies with z as $\exp(jkz\cos\theta_i)$, the spatial derivative $\partial/\partial z$ in Maxwell's equations may simply be replaced with $jk\cos\theta_i$. As in the case of perpendicular incidence, the equations divide into TM-polarized and TE-polarized sets. In the TM-polarized case, $E_z = 0$ and the field components are expressed in terms of H_z where

$$\frac{\partial^2 H_z}{\partial x^2} + \frac{\partial^2 H_z}{\partial y^2} + k^2\sin^2\theta_i\,H_z = 0 , \tag{4.13}$$

$$E_x\,\hat{x} + E_y\,\hat{y} = j\frac{Z_o}{k\sin^2\theta_i}\left(\frac{\partial H_z}{\partial y}\,\hat{x} - \frac{\partial H_z}{\partial x}\,\hat{y}\right) , \tag{4.14}$$

$$H_x\,\hat{x} + H_y\,\hat{y} = j\frac{\cos\theta}{k\sin^2\theta_i}\left(\frac{\partial H_z}{\partial y}\,\hat{x} + \frac{\partial H_z}{\partial x}\,\hat{y}\right) , \tag{4.15}$$

while in the TE-polarized case, $H_z = 0$ and the field components are expressed in terms of E_z where

$$\frac{\partial^2 E_z}{\partial x^2} + \frac{\partial^2 E_z}{\partial y^2} + k^2\sin^2\theta_i\,E_z = 0 , \tag{4.16}$$

$$E_x\,\hat{x} + E_y\,\hat{y} = j\frac{\cos\theta_i}{k\sin^2\theta_i}\left(\frac{\partial E_z}{\partial y}\,\hat{x} + \frac{\partial E_z}{\partial x}\,\hat{y}\right) , \tag{4.17}$$

$$H_x\,\hat{x} + H_y\,\hat{y} = j\frac{1}{kZ_o\sin^2\theta_i}\left(\frac{\partial E_z}{\partial y}\,\hat{x} - \frac{\partial E_z}{\partial x}\,\hat{y}\right) . \tag{4.18}$$

Since the boundary conditions are identical, the solution to the problem of scattering by a conducting grating at oblique incidence to the grating axis is identical to the solution for perpendicular incidence if k is replaced by $k\sin\theta_i$ and all fields are multiplied by $\exp(jkz\cos\theta_i)$.

4.3 Scattering by a Depolarizing Trihedral Corner Reflector

The polarization response of a trihedral corner reflector can be modified by replacing one of its panels by a reflection polarizer derived from a conducting grating with rectangular grooves, as depicted in Figure 4.13. Projections of a typical ray path in the x-y, z-x, and y-z planes are also shown. The coordinate frame is identical to that used in the previous section to describe scattering by a free-standing grating. In order for this type of depolarizing trihedral corner reflector to function correctly, the grating must be oriented in such a way that all of the rays which are incident from a given direction undergo identical polarization transformations regardless of the sequence in which they are reflected by each of the interior surfaces. It can be shown that this condition will be satisfied if the grating axis is parallel to one of the principal axes of the trihedral. If the incident field is resolved into orthogonal components which are TM- and TE-polarized with respect to the grating axis, the components will not be coupled due to reflection from either the grating or any of the three dihedral corners which comprise the trihedral corner reflector. As a result, reflection from each interior surface can be represented by a diagonal polarization scattering matrix and the cumulative transformation due to the three reflections necessary to return a incident ray to the source will be independent of the sequence in which the reflections occur. Furthermore, it can be shown that the angles of incidence of the rays with respect to both the grating normal and the grating axis will be equivalent regardless of the sequence in which the rays are reflected by the interior surfaces of the reflector. Thus, all of the rays which are incident on the reflector will undergo identical polarization transformations on reflection from the grating and the required condition will be met.

For the purpose of defining the polarization states of incident and reflected waves, hence the polarization response of the reflector, let the z axis define the local vertical in the reflector coordinate frame. For an arbitrary direction of incidence, it is convenient to specify horizontal and vertical in terms of the triad $(\hat{r}, \hat{\theta}, \hat{\phi})$ associated with a conventional spherical coordinate
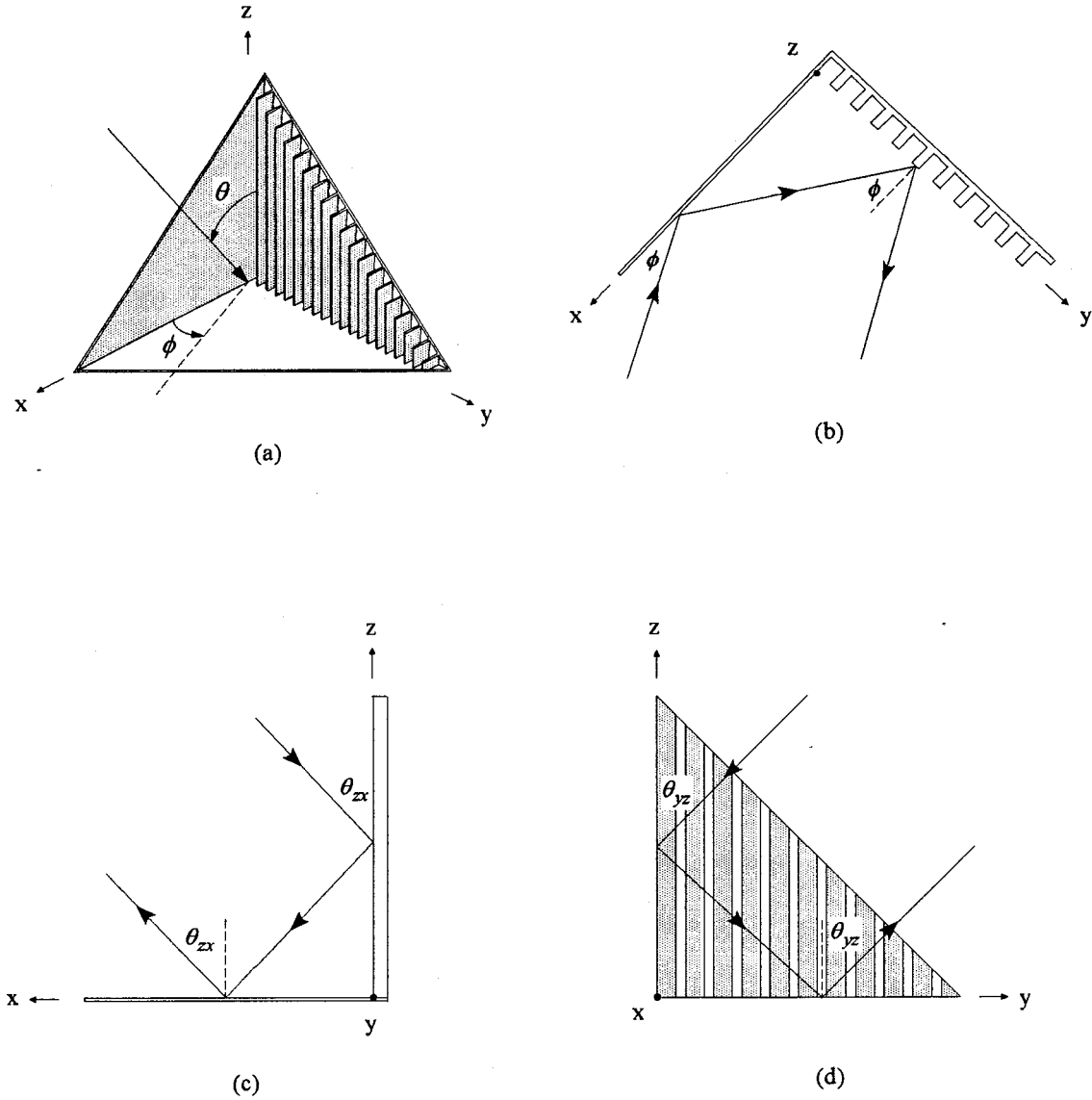
Figure 4.13: Replacement of one panel of a trihedral corner reflector by a reflection polarizer derived from a corrugated surface. (a) View along the symmetry axis. (b) Projection of a typical ray path in the x-y plane. (c) Projection of a typical ray path in the z-x plane. (d) Projection of a typical ray path in the y-z plane. If the direction of incidence is (θ, ϕ), the angle θ_{zx} is given by $\cos^{-1}(\cos\theta\cos\phi)$ and the angle θ_{yz} is given by $\cos^{-1}(\cos\theta\sin\phi)$.
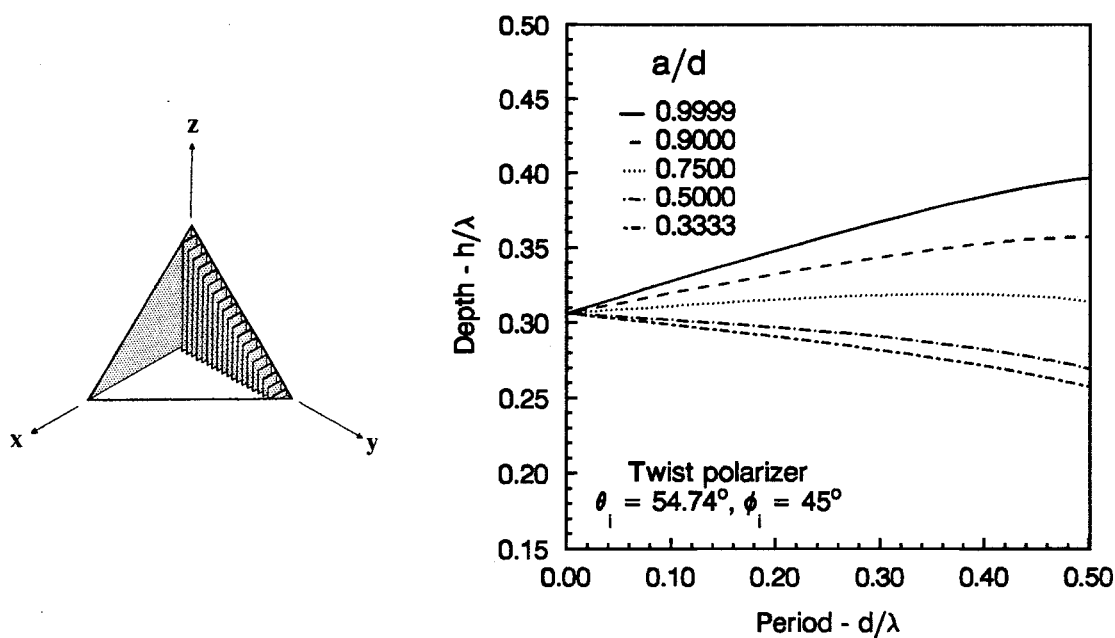
Figure 4.14: Twist polarizer design curves for incidence along the symmetry axis of a trihedral corner reflector.
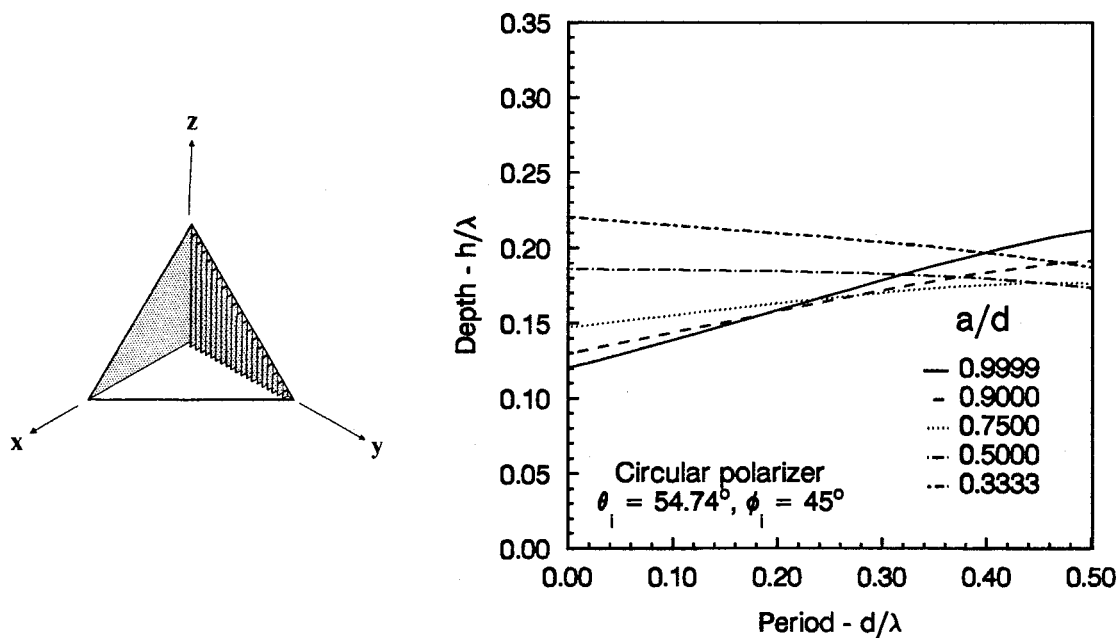
Figure 4.15: Circular polarizer design curves for incidence along the symmetry axis of a trihedral corner reflector.

system where

$$\hat{k} = \frac{\mathbf{k}}{k} \equiv \hat{r} = \cos\phi\sin\theta\,\hat{x} + \sin\phi\sin\theta\,\hat{y} + \cos\theta\,\hat{z}, \qquad (4.19)$$

$$\hat{h} = \frac{\hat{z}\times\hat{k}}{|\hat{z}\times\hat{k}|} \equiv \hat{\phi} = -\sin\phi\,\hat{x} + \cos\phi\,\hat{y}, \qquad (4.20)$$

$$\hat{v} = \hat{k}\times\hat{h} \equiv -\hat{\theta} = -\cos\phi\cos\theta\,\hat{x} - \sin\phi\cos\theta\,\hat{y} + \sin\theta\,\hat{z}, \qquad (4.21)$$

as described in section 2.2. Here, the component of an incident wave which is TM-polarized with respect to z corresponds to horizontal polarization while the component which is TE-polarized with respect to z corresponds to vertical polarization.

The polarization scattering matrix of a depolarizing trihedral corner reflector according to the backscatter alignment (BSA) convention is identical to that of a free-standing grating according to the forward scatter alignment (FSA) convention for the same direction of incidence. If only the specular reflected order propagates, the polarization response of the reflector is of the form

$$[S] = \begin{bmatrix} S_{HH} & S_{HV} \\ S_{VH} & S_{VV} \end{bmatrix} = \begin{bmatrix} \Gamma_0^{EE} & 0 \\ 0 & \Gamma_0^{HH} \end{bmatrix} = \begin{bmatrix} 1 & 0 \\ 0 & e^{j\delta} \end{bmatrix}. \qquad (4.22)$$

Since TM- and TE-polarized waves are decoupled upon reflection from the grating even if the plane of incidence makes an oblique angle with the grating axis, the off diagonal elements of the polarization scattering matrix given by (4.19) will always vanish in the reflector coordinate frame of Figure 4.13. The polarization scattering matrix of a target relates the scattered field $\mathbf{E}^s$ at the receiver to the incident field $\mathbf{E}^i$ at the target according to

$$\begin{bmatrix} E_1^s \\ E_2^s \end{bmatrix} = \frac{e^{-jkr}}{\sqrt{4\pi}r} \begin{bmatrix} S_{11} & S_{12} \\ S_{21} & S_{22} \end{bmatrix} \begin{bmatrix} E_1^i \\ E_2^i \end{bmatrix}, \qquad (4.23)$$

where both the fields and the polarization scattering matrix have been expressed with respect to an arbitrarily polarized basis. Often, this expression is normalized by factoring out the scattering cross section of the target and the range dependence of the response. The *polarization match factor* or *polarization efficiency* between the scattered field and a receiving antenna of

(a)

(b)
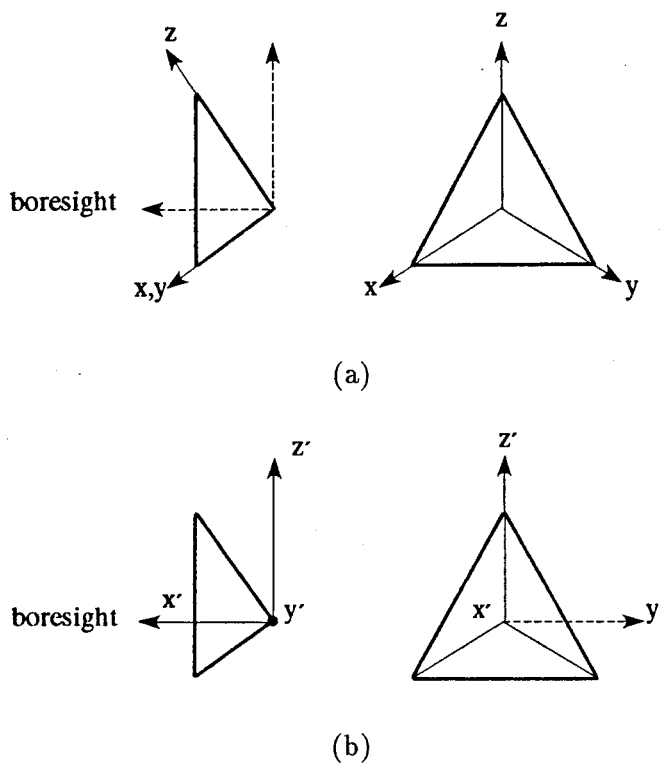
Figure 4.16: (a) Reflector coordinate frame and (b) global coordinate frame.

(a)   (b)
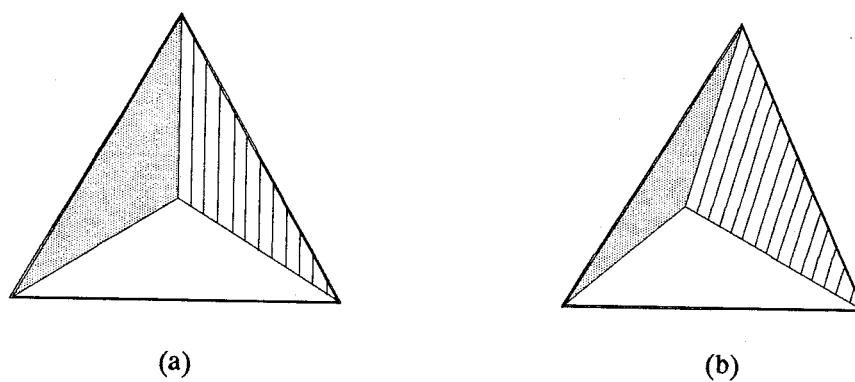
Figure 4.17: Angle of rotation of the projection of the grating axis onto the view plane for incidence (a) along the symmetry axis and (b) 30 degrees off the symmetry axis.

polarization state **h** is given by

$$\rho = \frac{|\mathbf{E}^s \cdot \mathbf{h}|^2}{|\mathbf{E}^s|^2 \, |\mathbf{h}|^2} \,, \qquad 0 \leq \rho \leq 1. \tag{4.24}$$

A reflection polarizer designed for incorporation into a trihedral corner reflector should present the desired polarization response along the same direction of incidence that the reflector presents its maximum scattering cross section. For reflectors composed of triangular, circular, or square panels with equal corner lengths, this direction falls along the symmetry axis of the reflector. In the reflector coordinate frame of Figure 4.13, this direction is given in spherical coordinates by $\theta = 54.74°$, $\phi = 45°$. Design curves for twist polarizers and circular polarizers for incidence along this direction are presented in Figures 4.14 and 4.15, respectively. In the previous section, it was shown that the response of a grating for oblique incidence to the grating axis is identical to its response for perpendicular incidence to the grating axis if k is replaced by $k \sin \theta$ and all fields are multiplied by $\exp(jkz \cos \theta)$. In this case, $\sin \theta$ is given by $\sqrt{2/3}$ and $\cos \theta$ is given by $1/\sqrt{3}$. This transformation may also be applied in the design of linear polarization selective reflectors which are based on the concepts described in the previous section.

The response of the target can be altered to suit a particular application by rotating the target about its symmetry axis [28]. After the target has been rotated by an angle α from the vertical, as shown in Figure 4.19, its polarization scattering matrix is given by

$$[S'] = [R]^{-1} \, [S] \, [R] \,. \tag{4.25}$$

If the response is expressed with respect to a linearly polarized basis, the rotation operator $[R]$ is given by

$$[R_L] = \begin{bmatrix} \cos \alpha & -\sin \alpha \\ \sin \alpha & \cos \alpha \end{bmatrix}, \tag{4.26}$$

while if the response is expressed with respect to a circularly polarized basis, the operator is given by

$$[R_C] = \begin{bmatrix} e^{-j\alpha} & 0 \\ 0 & e^{j\alpha} \end{bmatrix}. \tag{4.27}$$

For example, if a twist-polarizing target is rotated about its symmetry axis to $\alpha = 0°$, $\pm 90°$, or $180°$ degrees, it will present a maximum co-polar response for horizontally, vertically, and circularly polarized incident waves. If the target is rotated to $\alpha = \pm 45°$ or $\pm 135°$, it will still present a maximum co-polar response to circularly polarized incident waves but will present a maximum cross-polar response to horizontally and vertically polarized incident waves.

In practice, it is often necessary to describe the polarization response of a depolarizing trihedral corner reflector with respect to a global coordinate frame in which the horizontal plane contains the boresight of the reflector and the vertical plane is parallel to the axis of the grating, as suggested by Figure 4.16. By the methods described in section 2.4, it can be shown that the global coordinate frame $x'y'z'$ is related to the reflector coordinate frame xyz by

$$
\begin{bmatrix} x' \\ y' \\ z' \end{bmatrix} = \begin{bmatrix} \frac{1}{\sqrt{3}} & -\frac{1}{\sqrt{2}} & -\frac{1}{\sqrt{6}} \\ \frac{1}{\sqrt{3}} & \frac{1}{\sqrt{2}} & -\frac{1}{\sqrt{6}} \\ \frac{1}{\sqrt{3}} & 0 & \sqrt{\frac{2}{3}} \end{bmatrix} \begin{bmatrix} x \\ y \\ z \end{bmatrix} ,
\tag{4.28}
$$

where the x' axis in the global coordinate frame corresponds to the symmetry axis of the reflector and the z' axis is parallel to vertical. Transformation of the polarization scattering matrix of a depolarizing trihedral corner from the reflector coordinate frame to the global coordinate frame corresponds to rotation of its basis by a prescribed angle which is a function of both the transformation matrix which relates the two coordinate frames and the direction of propagation, as described in Chapter 2. Let $\hat{\phi}_P$ define the horizontal plane of the xyz coordinate frame with respect to the direction of propagation and be given by

$$
\hat{\phi}_P = -\sin\phi\,\hat{x} + \cos\phi\,\hat{y} ,
\tag{4.29}
$$

and let $\hat{\phi}'_P$ similarly define the horizontal plane of the $x'y'z'$ coordinate frame and be given by

$$
\hat{\phi}'_P = -\sin\phi'\,\hat{x}' + \cos\phi'\,\hat{y}' .
\tag{4.30}
$$

Let $\hat{r}_P$ be the outward normal to the unit sphere at the point P in the xyz coordinate frame and be given by

$$
\hat{r}_P = -\sin\theta\cos\phi\,\hat{x} + \sin\theta\sin\phi\,\hat{y} + \cos\theta\,\hat{z} .
\tag{4.31}
$$

The expression for the unit vector $\hat{\phi}'_P$ in the $x'y'z'$ coordinate frame given by (4.30) must be transformed to the xyz coordinate frame. This can be accomplished by determining ϕ' in terms of θ and ϕ according to the relation

$$\phi' = \tan^{-1}\left[\frac{\frac{1}{\sqrt{3}}\sin\theta\cos\phi + \frac{1}{\sqrt{2}}\sin\theta\sin\phi - \frac{1}{\sqrt{6}}\cos\theta}{\frac{1}{\sqrt{3}}\sin\theta\cos\phi - \frac{1}{\sqrt{2}}\sin\theta\sin\phi - \frac{1}{\sqrt{6}}\cos\theta}\right], \tag{4.32}$$

and converting the basis of the unit vector $\hat{\phi}'_P$ according to the relation given by (4.28). Then, the angle of rotation can be determined from

$$\alpha = \tan^{-1}\left(\frac{\hat{r}_P \cdot (\hat{\phi}_P \times \hat{\phi}'_P)}{\hat{\phi}_P \cdot \hat{\phi}'_P}\right). \tag{4.33}$$

If $\hat{r}_P$ is coincident with z axis then the definition of $\hat{\phi}_P$ given by (4.29) is ambiguous. In such cases, the direction of the horizontal plane with respect to the direction of propagation must be defined arbitrarily, as noted in section 2.2. If $\hat{r}_P$ is coincident with the z' axis, similar considerations apply to the definition of $\hat{\phi}'_P$ given by (4.30). Although several factors cause the polarization response of a depolarizing trihedral corner reflector to degrade as the direction of incidence shifts away from the boresight, rotation of the projection of the grating axis in the aperture plane with respect to the local vertical is the most important since it results in an effective rotation of the corresponding polarization scattering matrix, as suggested by Figure 4.17.

The polarization scattering matrix corresponding to a circular polarization selective response cannot be diagonalized when expressed with respect to a linearly polarized basis. As a result, it is not possible to modify a conventional trihedral corner reflector to present a circular polarization selective response simply by adding conducting fins or corrugations of appropriate dimensions and orientation to one of its interior surfaces. Alternative methods for obtaining such a response based on the addition of a transmission circular polarizer to a linear polarization selective reflector or a circular polarization selective surface to a twist-polarizing reflector are proposed in Appendix C.

4.4 Numerical and Experimental Results

In this section, the results of a test program that was conducted in order to evaluate the response characteristics of depolarizing trihedral corner reflectors which incorporate a reflection polarizer derived from a corrugated surface are given. Prototype trihedral corner reflectors which present regular, twist-polarizing, and circularly polarizing responses were designed for use at the standard marine radar frequency of 9.445 GHz and assembled. Their polarization and azimuthal response patterns were measured and the results were compared to theoretical predictions of the contribution of triple-bounce reflections to their response based on the analysis presented in the previous section. Details of the design and construction of the prototype reflectors are presented in section 4.4.1. The polarization and azimuthal response patterns of the prototype reflectors are presented in sections 4.4.2 and 4.4.3, respectively.

The response patterns of the prototype reflectors were measured using the microwave antenna range located on the roof of the Electrical Engineering building at the University of British Columbia. A side view of the outdoor portion of the range is shown in Figure 4.18. The model tower supports the target at a height of 2.2 metres and travels on a carriage along 15 metres of track down the center of the roof of the east wing of the Electrical Engineering building. The response pattern of the target will be distorted by near field effects if the range to the target is too short or by multipath propagation effects if the range is too long. Tests were conducted and it was found that the optimum range at which to measure the response of a prototype reflector is 11 metres. The model tower can be configured to either rotate the target about a vertical axis for conventional azimuthal pattern measurements or roll the target about a horizontal axis for polarization response measurements as shown in Figure 4.19. The CW radar apparatus and the digital pattern recorder which were used to measure and record the co-polar and cross-polar response of the target under test were developed specifically for use in this project. A description of the design and implementation of the instrumentation, the results of tests performed to verify the suitability of the range for use in the measurement program, and recommendations for future modifications and improvements are presented in Appendix D.
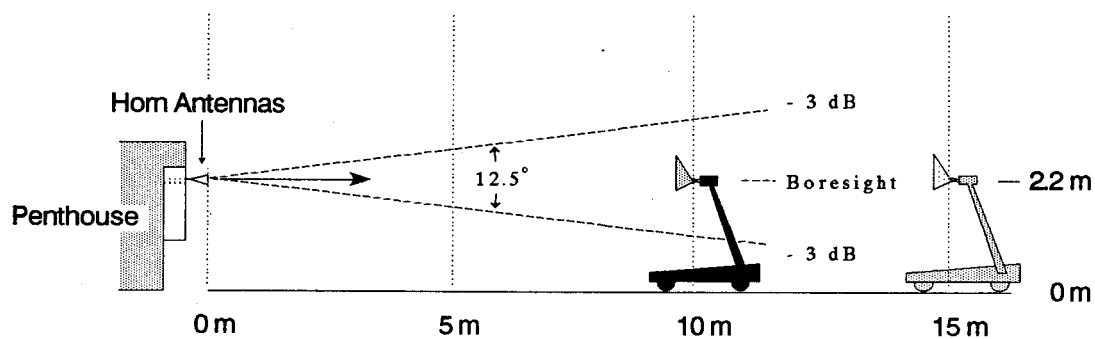
Figure 4.18: Profile view of the RCS measurement range.

(a)

(b)
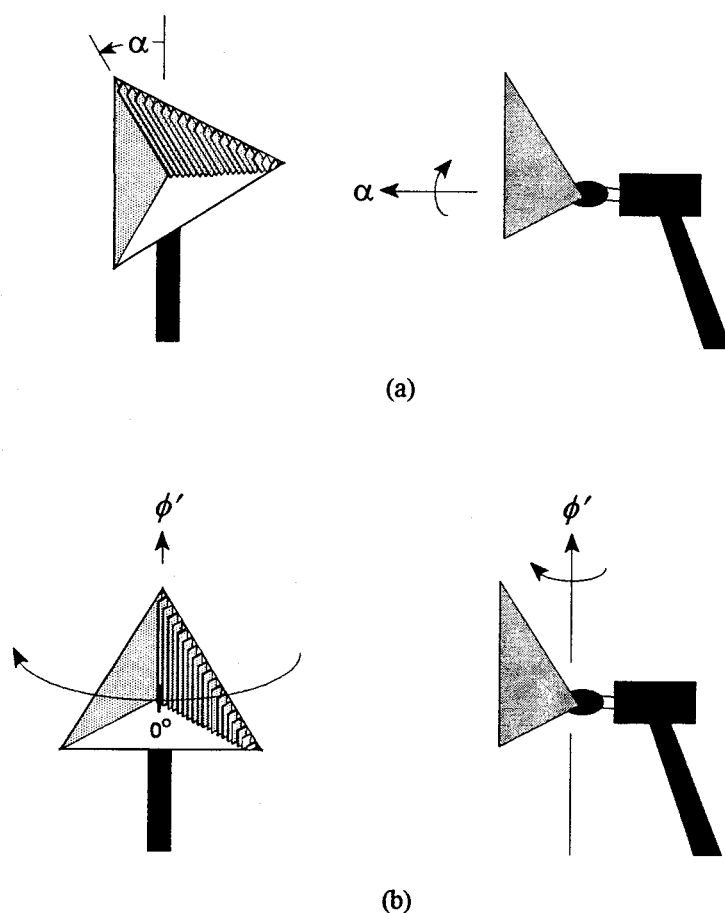
Figure 4.19: Measurement of the response of a prototype trihedral corner reflector. (a) Polarization response. (b) Azimuthal response.

4.4.1 Design and Construction of the Prototype Trihedral Corner Reflectors

A prototype trihedral corner reflector with a regular polarization response was assembled from triangular panels with equal corner lengths of 60 cm. At the design frequency of 9.445 GHz, the prototype reflector presents a maximum scattering cross section of approximately 540 square metres (27 dBsm) with a half-power beamwidth of approximately 38 degrees in both azimuth and elevation. The reflecting panels were cut from 12 gauge (approximately 2 mm in thickness) utility grade (3003) sheet aluminum and secured to 50 cm lengths of 90° angle aluminum of approximate dimensions 1 in × 1 in × $\frac{1}{8}$ in with rivets spaced approximately 5 cm apart. The right hand panel of the reflector (as viewed from the front) was secured to the angle aluminum with #6 flathead machine screws so that it could be removed easily. A mounting flange which matches the corresponding adapter on the antenna range model tower was secured to the rear of the reflector in line with the axis of symmetry. Prototype reflectors with twist-polarizing and circularly polarizing responses were realized by removing the right hand panel and replacing it with a suitable reflection polarizer. Details of the design and construction of the prototype depolarizing reflectors are shown in Figure 4.20. A photograph of a prototype reflector with a twist polarizer installed in place of the right hand panel is shown in Figure 4.21.

The extent to which the response of a trihedral corner reflector degrades as the reflecting panels deviate from perfect flatness and mutual orthogonality has been discussed by Trebits [29] and others. The tolerances on the corner angles of a trihedral corner reflector with triangular panels are presented as a function of the corner length of the reflector in Table 4.1. Each time the right hand panel of the prototype reflector was replaced, a set square with a corner length of 30 cm was used to verify that all three panels were mutually orthogonal and, if required, suitable adjustments were performed. Although commercially designed and fabricated trihedral corner reflectors intended for use under field conditions are typically manufactured from cast alumimum tooling plate between 10 and 15 mm thick in order to realize a structure which will meet the required tolerances [11], [30], [31], the simpler construction technique employed here was far easier to implement and was deemed adequate for use in the test program.
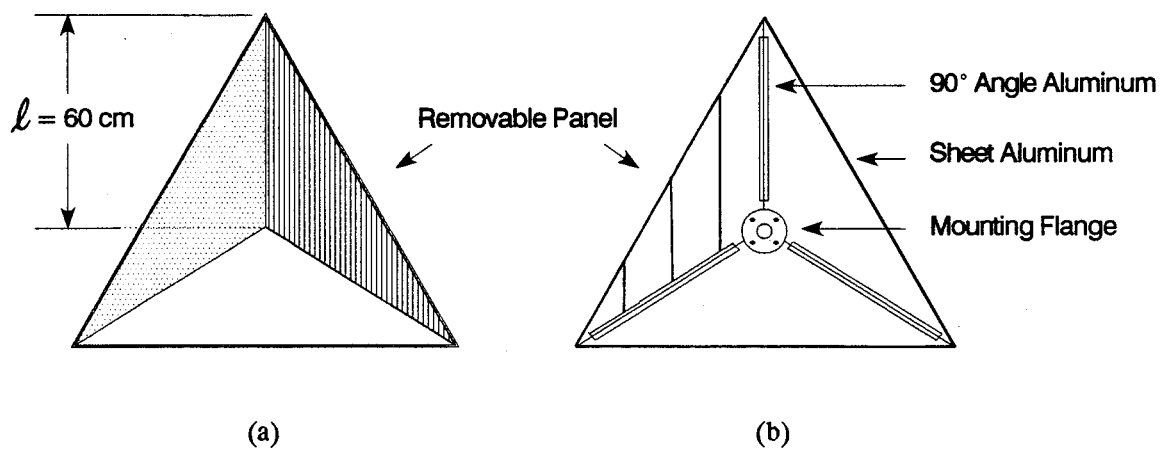
Figure 4.20: Construction details of the prototype depolarizing trihedral corner reflector. (a) Front view. (b) Rear View.
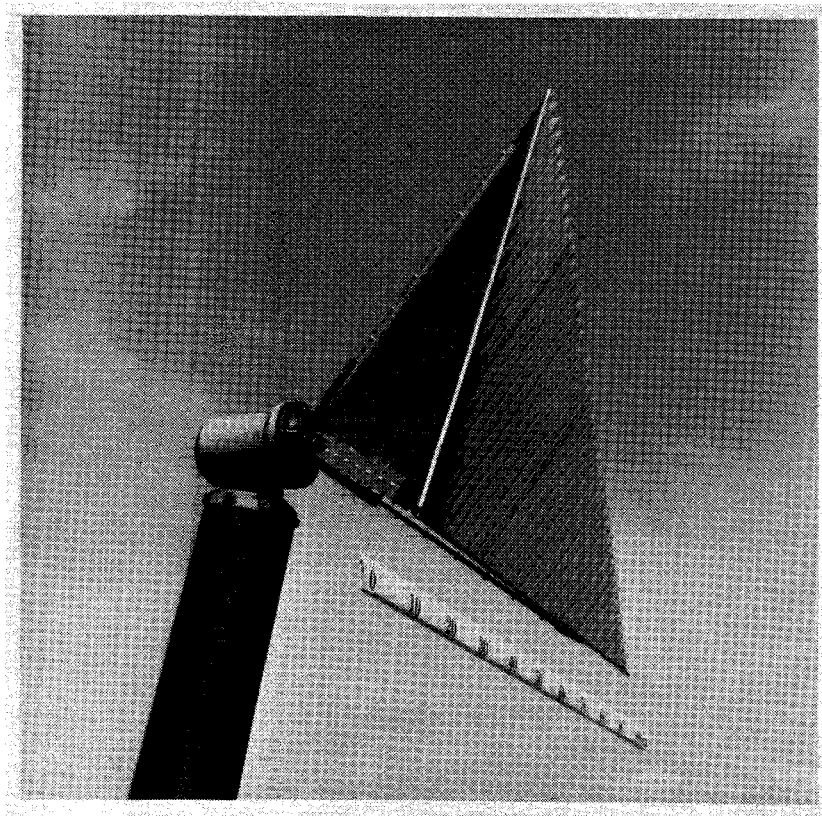
Figure 4.21: Photograph of the prototype twist-polarizing trihedral corner reflector mounted on the antenna range model tower.

Table 4.1:

Tolerances on the Corner Angles of a Trihedral Corner Reflector with Triangular Panels.

Corner Length[1]	Error in a Single Corner Angle[2]			Error in Three Corner Angles[2]		
	(-1 dB)	(-3 dB)	(-10 dB)	(-1 dB)	(-3 dB)	(-10 dB)
0.15 m (4.7λ)	±5.1°	±8.4°	±14.4°	±2.4°	±4.2°	±7.5°
0.30 m (9.4λ)	±2.5°	±4.2°	±7.3°	±1.2°	±2.1°	±3.8°
0.45 m (14.2λ)	±1.7°	±2.8°	±4.9°	±0.8°	±1.4°	±2.5°
0.60 m (18.9λ)	±1.3°	±2.1°	±3.7°	±0.6°	±1.1°	±1.9°
1.00 m (31.4λ)	±0.8°	±1.3°	±2.2°	±0.4°	±0.6°	±1.1°
3.00 m (94.3λ)	±0.3°	±0.4°	±0.7°	±0.1°	±0.2°	±0.4°

Notes: 1. $\lambda = 3.18$ cm.

2. which leads to the indicated reduction in the maximum response of the reflector.
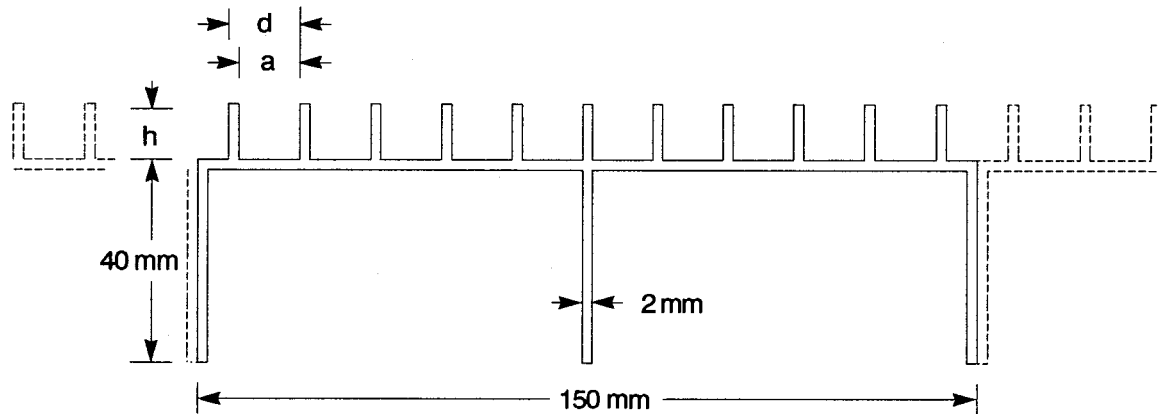
Figure 4.22: A single segment of a prototype reflection polarizer.

Table 4.2: Dimensions of the Prototype Reflection Polarizers

Type of Polarizer	Period d	Groove Width a	Groove Depth h	Aspect Ratio a/d
Twist	13.5 mm (0.426λ)	12.0 mm (0.379λ)	11.5 mm (0.355λ)	0.89
Circular	13.5 mm (0.426λ)	12.0 mm (0.379λ)	6.0 mm (0.186λ)	0.89

Note: $\lambda = 3.18$ cm

Reflecting panels which present twist-polarizing and circularly polarizing responses were designed using the methods described in section 4.3 and were assembled from extrusions that were custom manufactured for the purpose by Alcan Extrusions (Richmond, B.C.) from marine grade (6061) aluminum. A view of a single segment in cross section is depicted in Figure 4.22. The closely spaced row of fins along the top of the structure form the reflection polarizer while the three longer fins which form the base of the structure merely provide mechanical support during manufacture and points of attachment during assembly. The extrusion was designed to present a twist-polarizing response. In order to realize a circularly polarizing response, it was necessary to mill the upper row of fins down to the height specified in Table 4.2. During the milling procedure, the machinist found it difficult to secure the extrusion to the platform of the milling machine and problems with vibration were encountered. As a result, the height of the fins varied slightly along the length of the circularly polarizing reflecting panel. This may have contributed to the discrepancies that were observed between the measured response of the circularly polarizing trihedral corner reflector and theoretical predictions.

4.4.2 Polarization Response

The polarization response of each of the prototype reflectors was verified by rotating the target about its boresight and measuring the co-polar and cross-polar response of the target to a vertically polarized incident wave as a function of the angle of rotation α, as suggested by Figure 4.19(a). The result corresponds to taking a cross section through the normalized co-polar and cross-polar response patterns which are presented in Figures 4.4, 4.5, and 4.6 for ellipticity angle $\epsilon = 0°$. as suggested by Figure 4.23. The tilt angle τ of the incident wave in the reflector frame is related to the rotation angle α by

$$\tau = \alpha - 90° ,$$

where $\alpha = 0°$ corresponds to vertically polarized incidence. The response patterns of prototype reflectors designed to present regular, twist-polarizing, and circularly polarizing responses are presented in Figures 4.24, 4.25, and 4.26, respectively. In the case of the regular and twist-
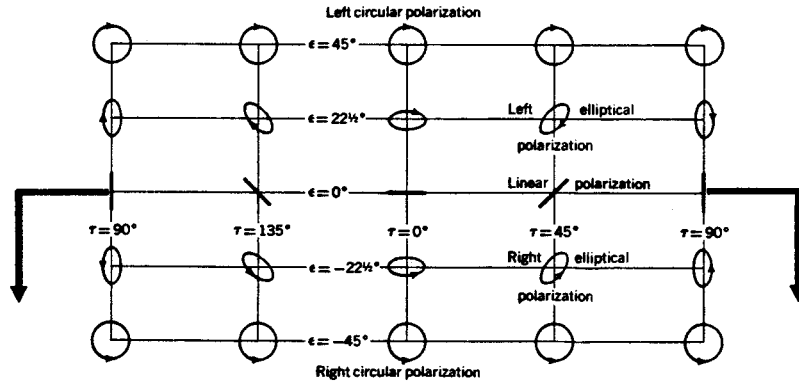
Figure 4.23: Evaluation of the polarization response of a radar target. Measuring the co-polar and cross-polar response of the target to a vertically polarized incident wave as a function of the angle of rotation α, as suggested by Figure 4.19(a), corresponds to taking a cross section through the normalized co-polar and cross-polar response patterns which are presented in Figures 4.4, 4.5, and 4.6 for ellipticity angle $\epsilon = 0°$.
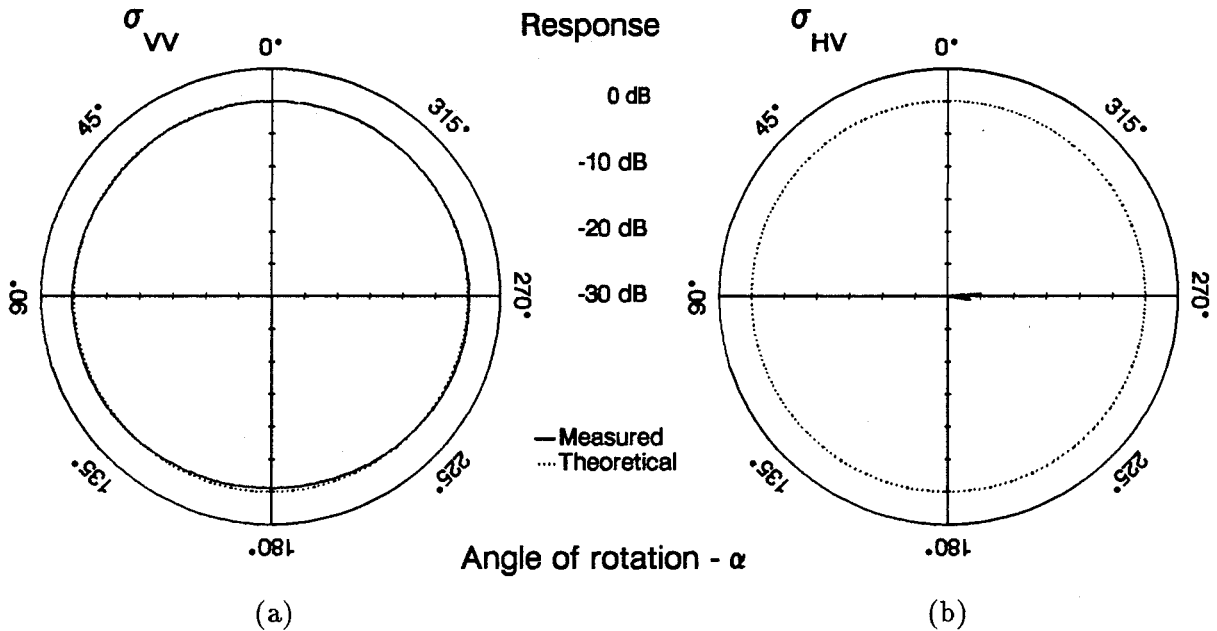
Figure 4.24: Polarization response of a prototype regular trihedral corner reflector as a function of rotation about the boresight. (a) Co-polar response - σ_{VV}. (b) Cross-polar response - σ_{HV}.
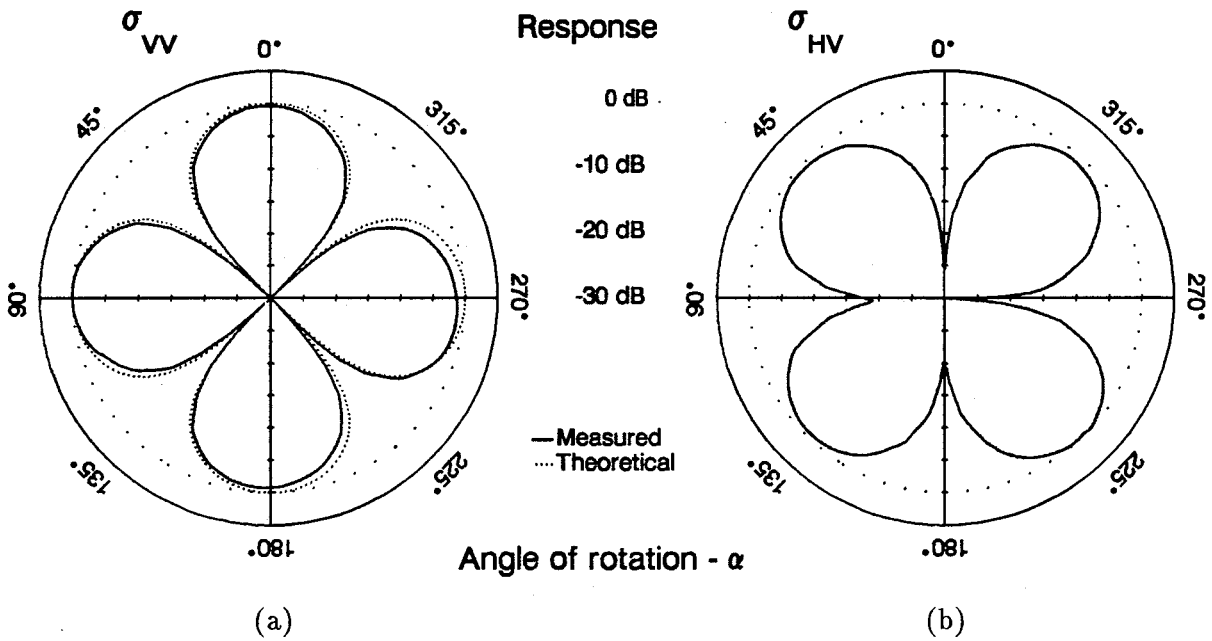
Figure 4.25: Polarization response of a prototype twist-polarizing trihedral corner reflector as a function of rotation about the boresight. (a) Co-polar response - σ_{VV}. (b) Cross-polar response - σ_{HV}.
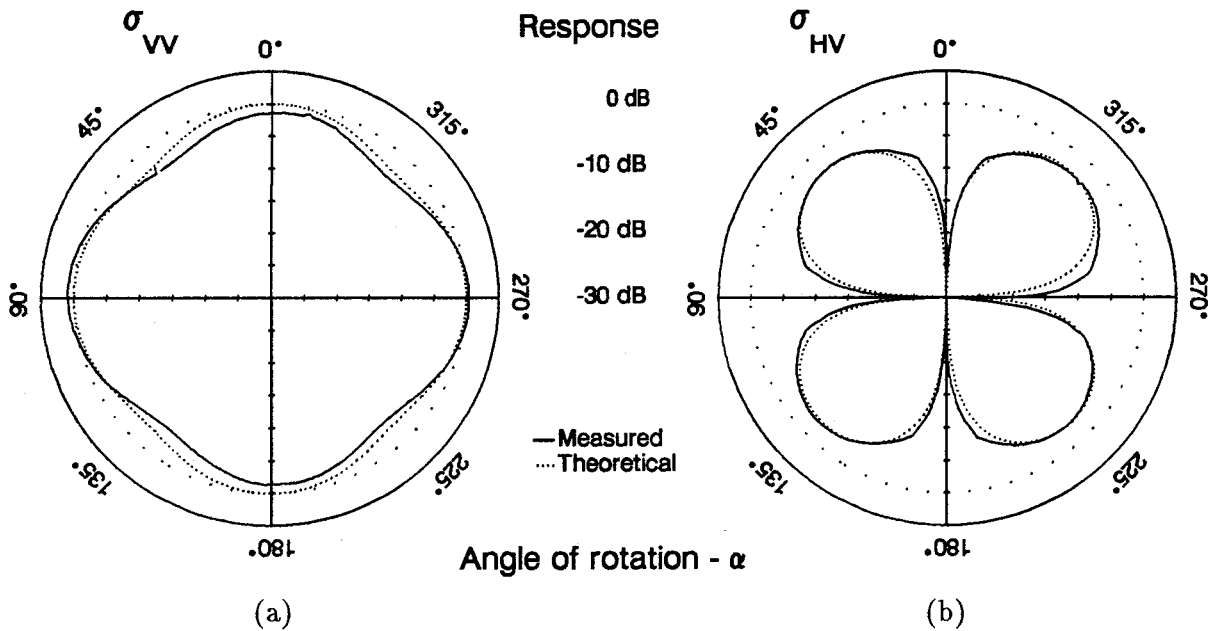
Figure 4.26: Polarization response of a prototype circularly-polarizing trihedral corner reflector as a function of rotation about the boresight. (a) Co-polar response - σ_{VV}. (b) Cross-polar response - σ_{HV}.

polarizing reflectors, the measured responses and the theoretical predictions agree reasonably well. In the case of the circularly polarizing reflector, the general form of the measured responses is correct but the discrepancy between measurement and theory is relatively large. As noted above, this may have been due to the problems encountered in milling the fins of the circular polarizer to the correct height.

4.4.3 Azimuthal Response

The co-polar and cross-polar azimuthal response σ_{VV} and σ_{HV} of each of the prototype trihedral corner reflectors were measured as a function of the azimuthal angle ϕ' for selected angles of rotation α with respect to the local vertical axis as suggested by Figure 4.19. The results are compared to theoretical predictions of the contribution of triple-bounce reflections to their response based on the analysis presented in section 4.3. The co-polar and cross-polar azimuthal response patterns of the prototype regular reflector for a rotation angle of 0 degrees are presented in Figures 4.27 and 4.28. The measured responses and the theoretical predictions generally agree. The co-polar and cross-polar azimuthal response patterns of the prototype twist-polarizing reflector after it has been rotated to 0 degrees for maximum co-polar response are presented in Figures 4.29 and 4.30 while the corresponding response patterns after the reflector has been rotated to 45 degrees for maximum cross-polar response are presented in Figures 4.31 and 4.32. Once again, the measured responses and the theoretical predictions generally agree. The rapid degradation in the polarization response for incidence off the boresight is apparent in both cases. The co-polar and cross-polar azimuthal response patterns of a prototype circularly polarizing reflector for rotation angles of 0 degrees and 45 degrees are presented in Figures 4.33 through 4.36. Although the general form of the measured response is correct, the measured co-polar azimuthal beamwidth of the prototype reflector is slightly wider than predicted in both cases. Also, the measured cross-polar azimuthal response pattern for a rotation angle of 0 degrees is substantially higher than predicted. However, the measured cross-polar azimuthal response pattern for a rotation angle of 45 degrees agrees very well with the predicted values.
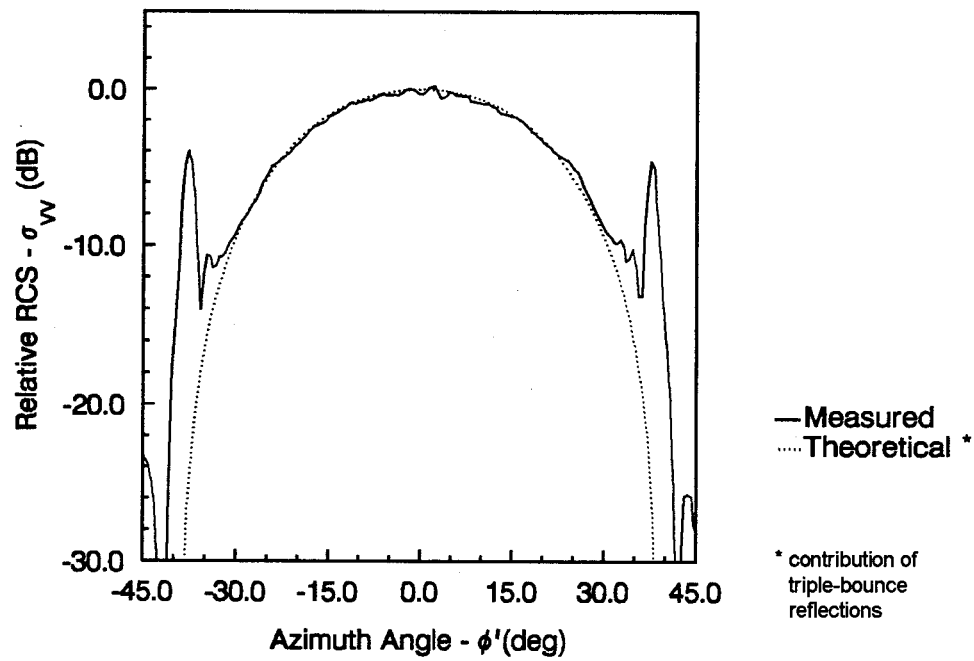
Figure 4.27: Co-polar azimuthal response pattern of a prototype regular trihedral corner reflector for rotation angle $\alpha = 0°$ and vertically polarized transmission.
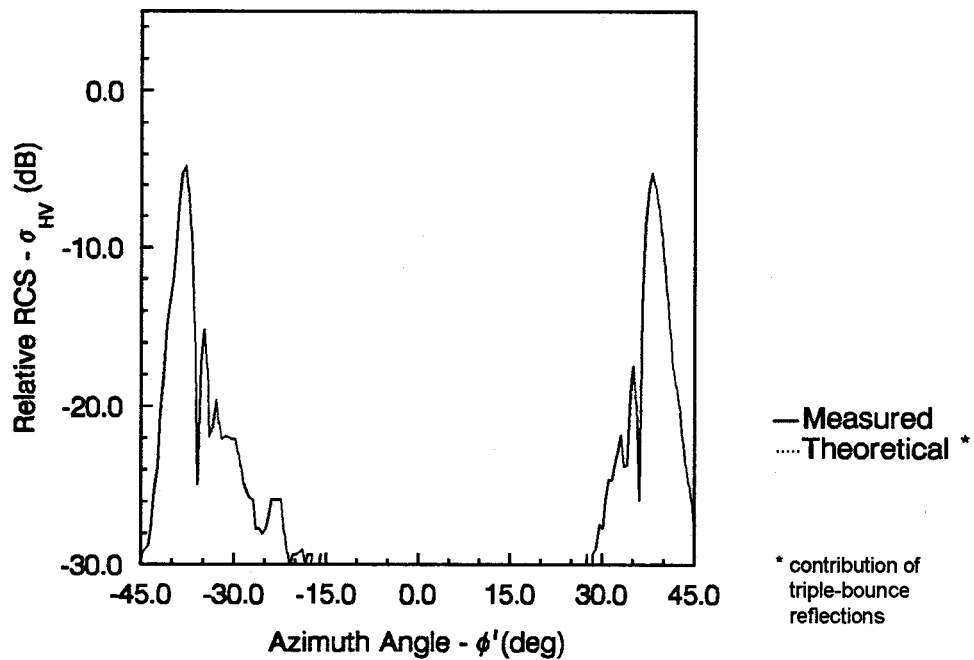
Figure 4.28: Cross-polar azimuthal response patterns of a prototype regular trihedral corner reflector for rotation angle $\alpha = 0°$ and vertically polarized transmission.
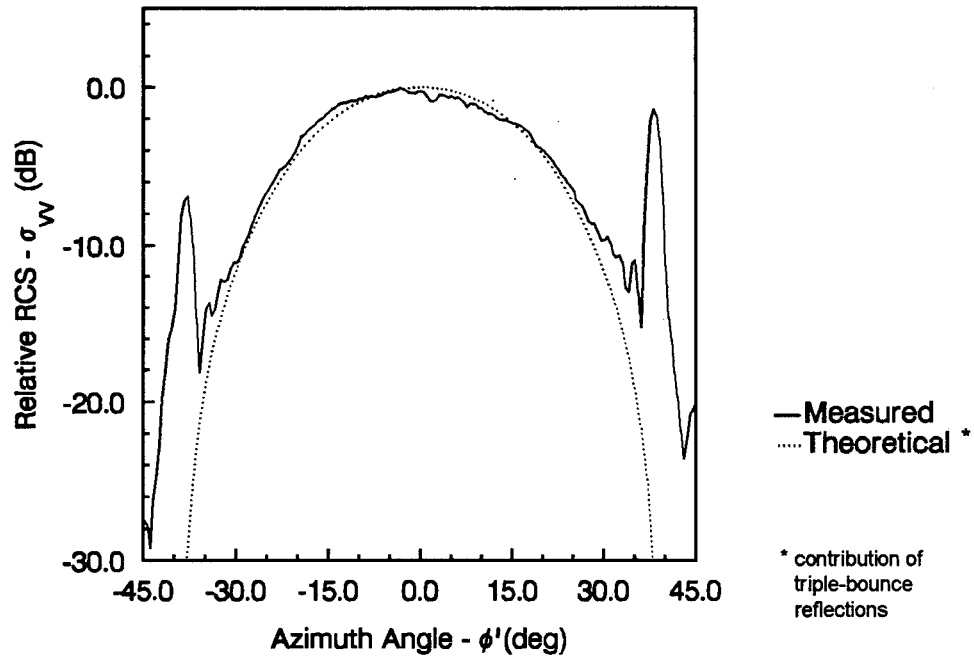
Figure 4.29: Co-polar azimuthal response pattern of a prototype twist-polarizing trihedral corner reflector for rotation angle $\alpha = 0°$ and vertically polarized transmission.
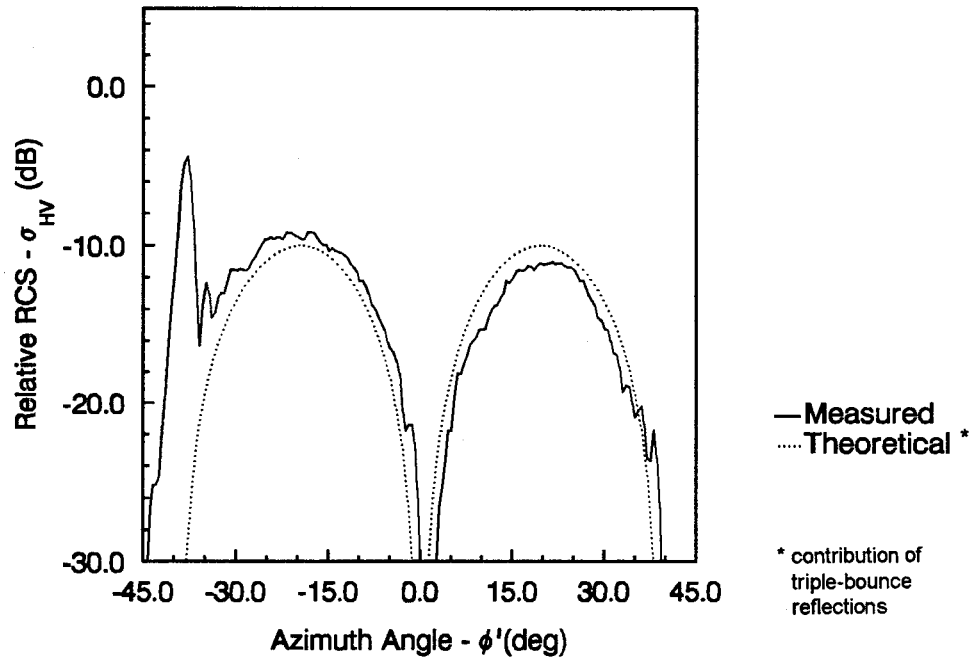
Figure 4.30: Cross-polar azimuthal response patterns of a prototype twist-polarizing trihedral corner reflector for rotation angle $\alpha = 0°$ and vertically polarized transmission.
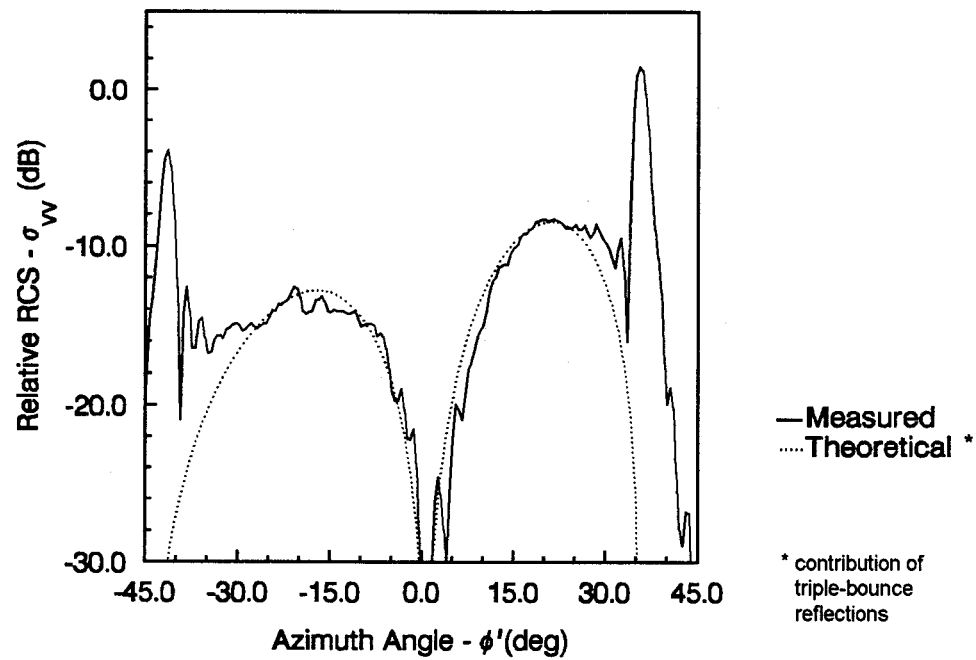
Figure 4.31: Co-polar azimuthal response pattern of a prototype twist-polarizing trihedral corner reflector for rotation angle $\alpha = 45°$ and vertically polarized transmission.
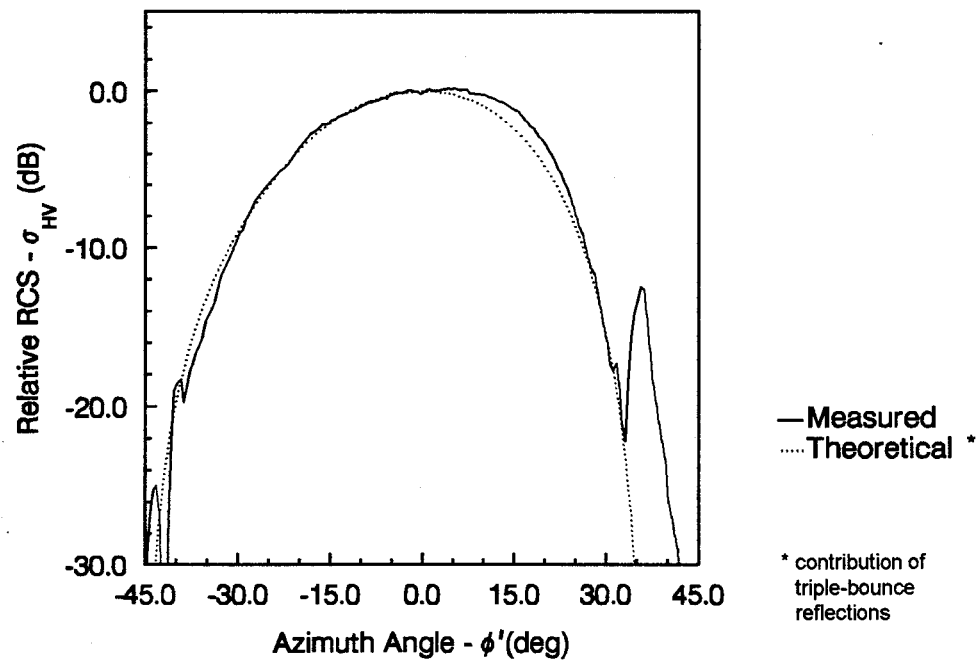
Figure 4.32: Cross-polar azimuthal response patterns of a prototype twist-polarizing trihedral corner reflector for rotation angle $\alpha = 45°$ and vertically polarized transmission.
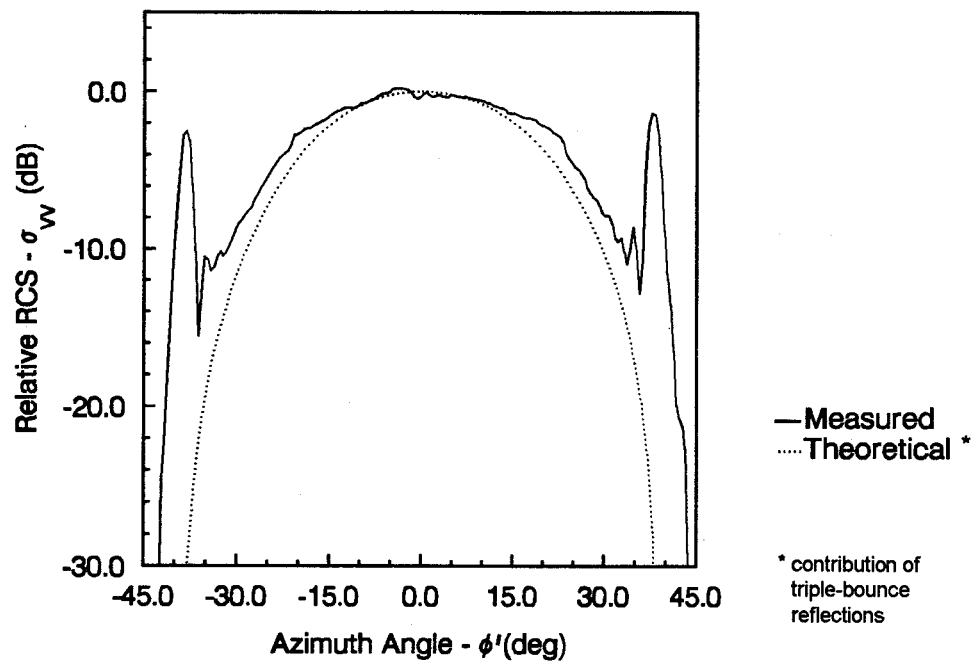
Figure 4.33: Co-polar azimuthal response pattern of a prototype circularly-polarizing trihedral corner reflector for rotation angle $\alpha = 0°$ and vertically polarized transmission.
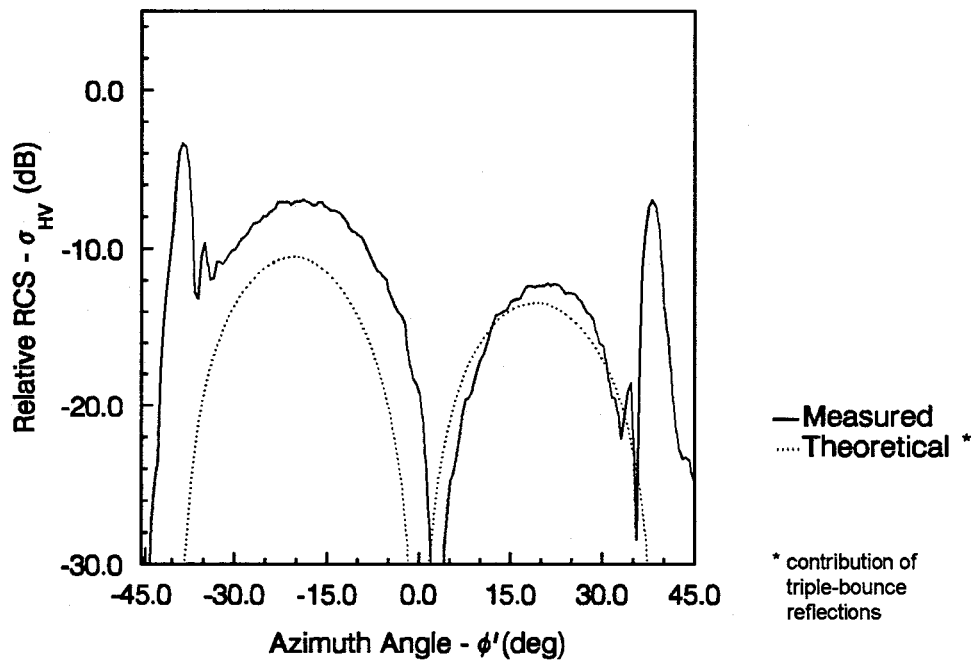
Figure 4.34: Cross-polar azimuthal response patterns of a prototype circularly-polarizing trihedral corner reflector for rotation angle $\alpha = 0°$ and vertically polarized transmission.
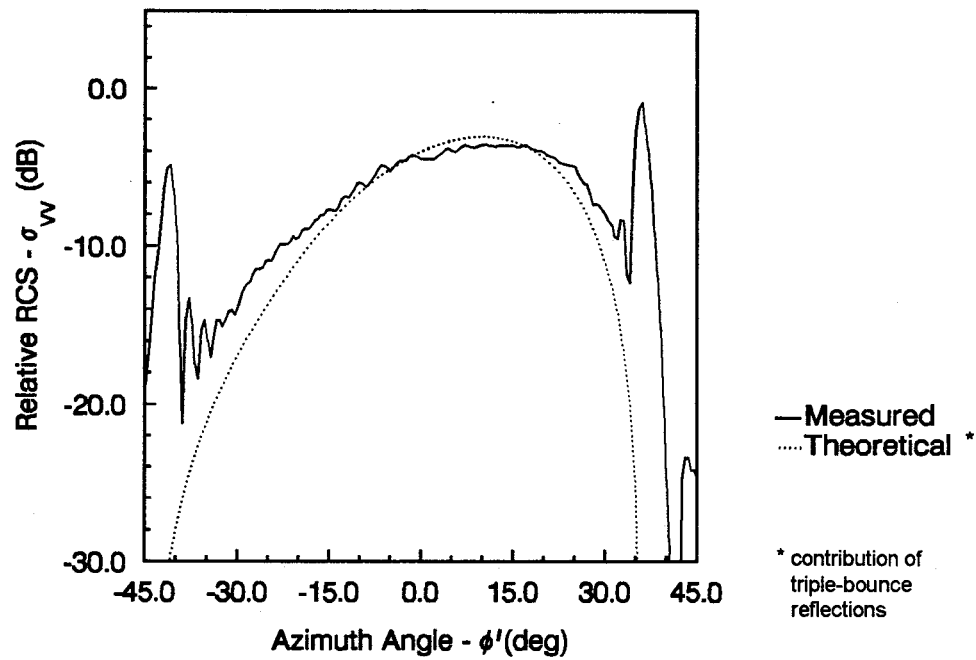
Figure 4.35: Co-polar azimuthal response pattern of a prototype circularly-polarizing trihedral corner reflector for rotation angle $\alpha = 45°$ and vertically polarized transmission.
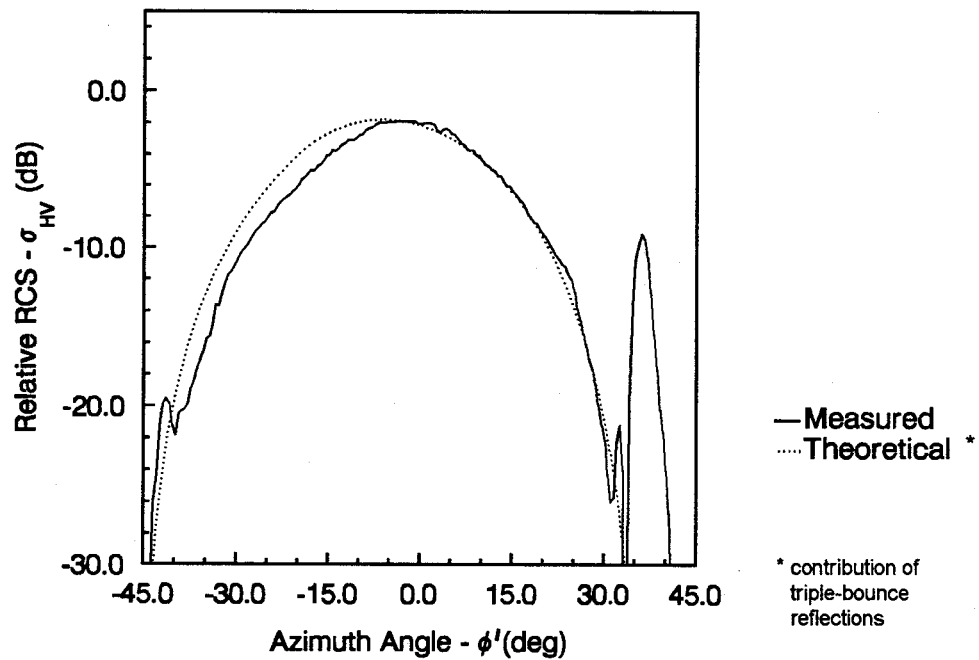
Figure 4.36: Cross-polar azimuthal response patterns of a prototype circularly-polarizing trihedral corner reflector for rotation angle $\alpha = 45°$ and vertically polarized transmission.

4.5 Conclusions

A method for altering the polarization response of a conventional trihedral corner reflector by replacing one of its reflecting panels by a reflection polarizer derived from a conducting grating with rectangular grooves of appropriate dimensions and orientation has been proposed. Since a depolarizing reflector of this type does not make use of wire grids or dielectric materials in its construction, it is less vulnerable to mechanical or environmental damage than other schemes which have been proposed in recent years. The scattering properties of conducting gratings with rectangular grooves have been reviewed and analytical solutions to the problem of scattering by a conducting grating with rectangular grooves have been derived for the cases of TM- and TE-polarized incident waves by mode-matching between the free space and groove regions. The results, including an implementation of the solution as a pair of subroutines coded in Fortran 77, are presented in Appendix B.

If the axis of the fins or corrugations are aligned with one of the axes of the trihedral then all rays incident from a given direction will experience the same polarization transformation upon reflection from the grating regardless of the sequence in which each ray is reflected from each of the three interior surfaces of the reflector. If the period of the grating is less than one-half wavelength and the reflector is oriented so that the projection of the grating axis into the aperture plane is oriented vertically, the phase difference δ between the TM and TE reflection coefficients of the specular reflected order can be exploited to yield a depolarizing response along the reflector boresight of the form,

$$[S] = \begin{bmatrix} S_{HH} & S_{HV} \\ S_{VH} & S_{VV} \end{bmatrix} = \begin{bmatrix} 1 & 0 \\ 0 & e^{j\delta} \end{bmatrix} ,$$

where S_{ij} is the ratio of the electric field components of the specular reflected order and the incident field. A phase difference of 0 yields a regular polarization response while phase differences of 180 and 90 degrees yield twist polarizing and circularly polarizing responses, respectively. Since the grating is uniform in one dimension, the TM- and TE-polarized fields are decoupled

and $S_{HV} = S_{VH} = 0$. Design curves for trihedral corner reflectors which present circularly polarizing and twist polarizing responses along their boresight have been given. The polarization response of the reflector can be modified by rotating the reflector about its boresight by an angle α, yielding a response of the form,

$$[S'] = \begin{bmatrix} \cos\alpha & \sin\alpha \\ -\sin\alpha & \cos\alpha \end{bmatrix} \begin{bmatrix} 1 & 0 \\ 0 & e^{j\delta} \end{bmatrix} \begin{bmatrix} \cos\alpha & -\sin\alpha \\ \sin\alpha & \cos\alpha \end{bmatrix}.$$

Methods for realizing trihedral corner reflectors which present a linear polarization selective response of the form,

$$[S] = \begin{bmatrix} S_{HH} & S_{HV} \\ S_{VH} & S_{VV} \end{bmatrix} = \begin{bmatrix} 1 & 0 \\ 0 & 0 \end{bmatrix},$$

have been proposed. The problem of realizing trihedral corner reflectors which present a circular polarization selective response is considered in Appendix C.

An algorithm for predicting the contribution of triple-bounce reflections to the polarization scattering matrix of a modified trihedral corner reflector as a function of the direction of incidence and the orientation of the reflector has been described. Although several factors cause the polarization response to degrade as the direction of incidence shifts away from the reflector boresight, rotation of the projection of the grating axis in the aperture plane with respect to the local vertical is the most important since it results in an effective rotation of the corresponding polarization scattering matrix. The polarization and azimuthal response patterns of prototype reflectors with regular, twist polarizing, and circularly polarizing responses were measured using the experimental facility which is described in Appendix D. The results show that the reflectors respond essentially as predicted.

References

[1] J. Croney, "Civil Marine Radar," in *Radar Handbook,* M.I. Skolnik, Ed., New York: McGraw-Hill, 1970, chap. 31.

[2] S. H. Yueh, J. A. Kong, R. M. Barnes, and R. T. Shin, "Calibration of polarimetric radars using in-scene reflectors," *J. Electromagn. Waves Appl.,* vol. 4, pp. 27–48, Jan. 1990.

[3] E.M. Kennaugh, *Dielectric Reflector.* U.S. Patent No. 2,872,675, dated Feb. 3, 1959.

[4] F.M. Weil, M.L. Ingalsbe, R.E. Stein, and J.G. McCann, *Radar Reflector for Circularly Polarized Radiation.* U. S. Patent No. 2,786,198, dated Mar. 19, 1957.

[5] S.J. Blank and L.H. Sacks, *Radar Target for Circularly Polarized Radiation.* U.S. Patent No. 3,309,705, dated Mar. 14, 1967.

[6] J.A. Scheer, "Radar Reflectivity Calibration Procedures," in *Radar Reflectivity Measurement: Techniques and Applications,* N.C. Currie, Ed. Norwood, MA: Artech House, 1989, p. 109.

[7] E.M. Kennaugh, *A Corner Reflector for Use with Circularly Polarized Radars.* Columbus, OH: Ohio State Univ., Rep. 601-8, 30 Jan. 1956. (cited in C.G. Bachman, *Radar Targets.* Lexington, MA: Heath, 1982, pp. 71–82.)

[8] P.Münzer, *Radar-Reflektor für zirkular, elliptisch oder in beliebiger Ebene linear polarisierte elektromagnetische Wellen.* (Radar reflector for circularly, elliptically, and most linearly polarized electromagtnetic waves.) Federal German Patent No. 1,196,255, dated Jul. 8, 1965.

[9] A. Macikunas, S. Haykin, and T. Greenlay, *Trihedral Radar Reflector.* U.S. Patent No. 4,843,396, dated Jun. 27, 1989.

[10] A. Macikunas and S. Haykin, "Trihedral twist-grid polarimetric reflector," *IEE Proc. F*, vol. 140, pp. 216–222, Aug. 1993.

[11] E. Johansen and A. Fromm. *Depolarizing Radar Corner Reflector*. U.S. Patent No. 4,724,436, dated Feb. 9, 1988.

[12] D.R. Sheen, E.L. Johansen, L.P. Elenbogen, and E.S. Kasischke, "The gridded trihedral: a new polarimetric SAR calibration reflector," *IEEE Trans. Geosci. Remote Sensing*, vol. GE-30, pp. 1149–1153, Mar. 1990.

[13] P.W. Hannan, *Twistreflector*. U.S. Patent No. 3,161,879, dated Dec. 15, 1964.

[14] L.G. Josefsson, "A broad-band twist reflector," *IEEE Trans. Antennas Propagat.*, vol. AP-19, pp. 552–554, July 1971.

[15] D.G. Michelson and E.V. Jull, "A Depolarizing Calibration Target for Radar Polarimetry," *Proc. IGARSS'90* (College Park, MD), May 20–24, 1990, p. 799.

[16] D.G. Michelson and E.V. Jull, "Depolarizing Trihedral Corner Reflectors," *IEEE/AP-S Symp. Dig.* (Ann Arbor, MI), June 28–July 2, 1993, pp. 238–241.

[17] J.D. Hanfling, G. Jerenic, and L.R. Lewis, "Twist reflector design using E-type and H-type modes," *IEEE Trans. Antennas Propagat.*, vol. AP-29, pp. 622–629, July 1981.

[18] W.B. Offut and L.K. DeSize, "Methods of Polarization Synthesis," in *Antenna Engineering Handbook*, 2nd ed., R. C. Johnson and H. Jasik, Eds. New York: McGraw-Hill, 1984, chap. 23.

[19] E.V. Jull, "Reflection circular polarisers," *Electron. Lett.*, vol. 15, pp. 423–424, July 5, 1979.

[20] R. Kastner and R. Mittra, "A spectral-iteration technique for analyzing a corrugated-surface twist polarizer for scanning reflector antennas," *IEEE Trans. Antennas Propagat.*, vol. AP-30, pp. 673–676, July 1982.

[21] D.G. Michelson, P. Phu, and E.V. Jull, "Millimetre-wave grating polarizers," *22nd URSI General Assembly*, Tel Aviv, Israel, Aug. 1987.

[22] A. Hessel, J. Shmoys, and D.Y. Tseng, "Bragg-angle blazing of diffraction gratings," *J. Opt. Soc. Am.*, vol. 65, pp. 380–384, Apr. 1975.

[23] E.F. Knott, J.F. Shaeffer, M.T. Tuley, *Radar Cross Section: Its Prediction, Measurement, and Reduction.* Norwood, MA: Artech House, 1985, pp. 244–247.

[24] A.K. Bhattacharyya and D.L. Sengupta, *Radar Cross Section Analysis and Control.* Norwood, MA: Artech House, 1991, pp. 208–212.

[25] E.V. Jull and J.W. Heath, "Reflection grating polarizers," *IEEE Trans. Antennas Propagat.*, vol. AP-28, pp. 586–588, July 1980.

[26] E.V. Jull and J.W. Heath, "Radio applications of rectangular groove corrugations," in *IEEE/AP-S Symp. Dig.* (Seattle, WA), June 1979, pp. 515-518.

[27] E.V. Jull, *Aperture Antennas and Diffraction Theory.* Stevenage, UK: Peregrinus, 1981, pp. 80–81.

[28] S.H. Bickel, "Some invariant properties of the polarization scattering matrix," *Proc. IEEE*, vol. 53, pp. 1070–1072, 1965.

[29] R.N. Trebits, "Radar Cross Section," in *Radar Reflectivity Measurement: Techniques and Applications*, N.C. Currie, Ed. Norwood, MA: Artech House, 1989, pp. 46–49.

[30] A. Freeman, Y. Shen, and C. L. Werner, "Polarimetric SAR calibration experiment using active radar reflectors," *IEEE Trans. Geosci. Remote Sensing*, vol. GE-28, pp. 224–240, Mar. 1990.

[31] *Precision Radar Corner Reflectors,* Product Brochure No. 9187F. Norcross, GA: Spectrum Technologies International, 1991.

Chapter 5

SUMMARY, CONCLUSIONS, AND RECOMMENDATIONS

5.1 Summary and Conclusions

It is often necessary to enhance the radar cross section of a cooperative target either to increase the maximum range at which the target can be reliably detected or to provide a target with a known response which may be used to assist in radar calibration and performance verification. In recent years, a requirement has arisen for rugged yet inexpensive radar reflectors which present both a very large scattering cross section and a specified polarization response over a wide angular range for use as calibration targets in airborne and spaceborne imaging radar systems for geophysical remote sensing and location markers in radar-assisted positioning systems for marine navigation. Passive targets, such as trihedral corner reflectors, are often better suited for use in such applications than active targets since they do not require an external source of power and are inherently more reliable. This study considers several problems related to the analysis, design, and implementation of passive targets including transformation of the polarization response of a target or the polarization state of an antenna between coordinate frames, modification of the angular coverage of a conventional trihedral corner reflector by appropriate shaping of its reflecting panels, modification of the polarization response of a conventional trihedral corner reflector by the addition of conducting fins or corrugations of appropriate dimensions and orientation to one of its interior surfaces, design of top hat reflectors with specified response characteristics, and design of reflection polarizers derived from conducting gratings with rectangular grooves.

In Chapter 2, it is shown that transformation of a polarization descriptor between coordinate frames corresponds to rotation of its basis by a prescribed angle which is a function of both the transformation matrix that relates the two coordinate frames and the direction of propagation. Two methods for determining the angle of rotation for the case in which the local vertical is defined by the $\hat{z}$ direction in each frame are derived using spherical trigonometry and vector algebra, respectively. Both methods are robust and will yield the correct result but the method based on vector algebra is more compact and would be easier to implement in software. Although the elements of the coordinate transformation matrix can be determined from either the relative directions of the three principal axes in each coordinate frame or the Euler angles which define a series of rotations which will transform one coordinate frame into the other, it may be difficult to obtain these parameters in practice. A third method is derived which overcomes this limitation by allowing the elements of the coordinate transformation matrix to be determined from any pair of directions which have been expressed in terms of both coordinate frames. Algorithms for rotating the basis of several polarization coordinates in common use, including the complex polarization ratio, the complex polarization vector, the Stokes vector and several of its variants, the coherency matrix, the polarization scattering matrix, and the Mueller matrix and several of its variants, are presented.

In Chapter 3, the problem of predicting the scattering cross section and angular coverage of a conventional trihedral corner reflector with panels of completely arbitrary shape is considered. Although general purpose numerical techniques such as the finite-difference time-domain (FD-TD) and the shooting and bouncing ray (SBR) methods can predict both the contributions of single, double, and triple-bounce reflections from the interior and the effect of deviations of the panels from perfect flatness and mutual orthogonality, they are extremely demanding computationally. For most purposes, it is sufficient to account for the contribution of triple-bounce reflections from the interior since they completely dominate the response for most directions of incidence. The empirical model originally proposed by Spencer for predicting the equivalent flat plate area of ideal trihedral corner reflectors with either triangular or square

panels (and the numerical implementation of the model that was devised by Keen) may fail without indication when applied to reflectors with complex panel shapes. A simple yet robust numerical prediction algorithm which overcomes this limitation is formulated by applying the approach used by Keen and a polygon-clipping algorithm formulated by Weiler and Atherton to an alternative model originally proposed by Robertson. The response patterns of ideal trihedral corner reflectors which present three-fold symmetry about the boresight are plotted on equal area projection grids and compared. If the corner length of the reflector is fixed, it is generally found that attempts to increase the beamwidth of the response by modifying the shape of the panels are accompanied by a reduction in the maximum response and vice versa. A set of design curves for bilaterally symmetric reflectors which are composed solely of triangular, elliptical, or rectangular reflecting panels are derived and the response patterns of selected bilaterally symmetric reflectors which are composed of combinations of panels with various shapes including triangular, circular, and square are presented and compared. It is found that if three-fold symmetry is broken so that the reflector simply presents bilateral symmetry about a mirror plane containing the boresight then the beamwidth of the response in one principal plane can be increased relative to the beamwidth in the orthogonal plane by modifying the shape of the reflector panels. The additional degree of freedom is shown to be useful when a reflector must be designed subject to a constraint such as a requirement that it present a planar aperture in order to facilitate the attachment of either a transmission polarizer or a protective cover.

In Chapter 4, a method for altering the polarization response of a conventional trihedral corner reflector by adding conducting fins or corrugations of appropriate dimensions and orientation to one of its interior surfaces is proposed. Since depolarizing reflectors of this type do not make use of wire grids and dielectric materials in their construction, they are less vulnerable to mechanical or environmental damage than other schemes which have been proposed in recent years. They also avoid many of the mechanical problems associated with the attachment of a transmission polarizer across the reflector aperture. If the axis of the fins or corrugations are

aligned with one of the axes of the trihedral then all rays incident from a given direction will experience the same polarization transformation upon reflection from the polarizer regardless of the sequence in which each ray is reflected from each of the three interior surfaces. If period of the grating is less than one-half wavelength and the reflector is oriented so that the projection of the grating axis into the aperture plane is oriented vertically, the phase difference δ between the TM and TE reflection coefficients of the specular reflected order can be exploited to yield a depolarizing response along the boresight of the reflector of the form,

$$[S] = \begin{bmatrix} S_{HH} & S_{HV} \\ S_{VH} & S_{VV} \end{bmatrix} = \begin{bmatrix} 1 & 0 \\ 0 & e^{j\delta} \end{bmatrix}, \tag{5.1}$$

where S_{ij} is the ratio of the electric field components of the specular reflected order and the incident field. A phase difference of 180 degrees yields a twist-polarizing response while a phase difference of 90 degrees yields a circularly polarizing response. Since the grating is uniform in one dimension, the TM and TE polarizations are decoupled and $S_{HV} = S_{VH} = 0$. Design curves for trihedral corner reflectors which present twist-polarizing and circularly polarizing responses along their boresight are given. The polarization response of the reflector can be modified by rotating the target about its boresight by an angle α, yielding a response of the form,

$$[S'] = \begin{bmatrix} \cos\alpha & \sin\alpha \\ -\sin\alpha & \cos\alpha \end{bmatrix} \begin{bmatrix} 1 & 0 \\ 0 & e^{j\delta} \end{bmatrix} \begin{bmatrix} \cos\alpha & -\sin\alpha \\ \sin\alpha & \cos\alpha \end{bmatrix}. \tag{5.2}$$

Methods for realizing linear polarization selective trihedral corner reflectors using similar techniques are proposed. An algorithm for predicting the contribution of triple-bounce reflections to the polarization scattering matrix of a modified trihedral corner reflector as a function of the direction of incidence and the orientation of the reflector is derived. Although several factors cause the polarization response to degrade as the direction of incidence shifts away from the boresight, rotation of the projection of the grating axis in the aperture plane with respect to the local vertical is the most important since it results in an effective rotation of the corresponding polarization scattering matrix. Prototype trihedral corner reflectors with

regular, twist-polarizing, and circularly polarizing responses were designed and assembled. Experimental results are presented which show that the prototype reflectors respond essentially as predicted.

In Appendix A, the problem of designing a top hat reflector with specified response characteristics is considered. Since the top hat reflector is a body of revolution, its response pattern is uniform in azimuth. Expressions for the elevation response pattern, maximum scattering cross section, angle of maximum response, and 1 and 3 dB elevation beamwidths of a top hat reflector are derived and design curves are presented. As the angle of maximum response becomes appreciably greater or less than 45 degrees, the elevation response pattern will become increasingly asymmetrical. In such cases, it may be preferable to consider the angle of median response for a given elevation beamwidth rather than the angle of maximum response. Expressions for the angle of median response are derived and design curves are presented. The results are used to solve a sample design problem.

In Appendix B, the problem of scattering by a conducting grating with rectangular grooves is considered. Analytical solutions are derived for the cases of TM- and TE-polarized incident waves by mode-matching between the free space and groove regions. Procedures for determining the validity of numerical results which are obtained using this formulation are discussed. Although the solution will invariably converge to an essentially constant result as the number of modes used in the field expansion are systematically and gradually increased, it is shown that the manner in which the solution converges and the value of the final result will depend on both the number of modes used to represent the fields in each region and their ratio. The phenomenon is commonly referred to as relative convergence. Numerical results are presented which suggest that the optimum ratio of groove modes to free space modes is similar in value to the ratio of the groove width to the grating period. An implementation of the analytical solutions as a pair of subroutines coded in Fortran 77 is presented.

In Appendix C, the problem of modifying a conventional trihedral corner reflector to present a circular polarization selective response is considered. It is shown that such a response cannot

be realized using the techniques described in Chapter 4 because the corresponding polarization scattering matrix cannot be diagonalized when expressed with respect to a linearly polarized basis. Alternative methods for obtaining such a response based on the addition of a transmission circular polarizer to a linear polarization selective reflector or a circular polarization selective surface to a twist-polarizing reflector are proposed. The performance of such reflectors and their usefulness in practice will depend on a number of factors that are not considered here including (1) degradation of the polarization response of either of the polarizers for incidence off the reflector boresight, (2) possible degradation of the polarization response due to multiple reflections between the transmission and reflection polarizers, and (3) the mechanical ruggedness of the modified reflector and the ease with which it can be fabricated.

In Appendix D, the experimental facility which was set up to measure the response of prototype trihedral corner reflectors is briefly described. Details of the physical layout and the design and implementation of the CW radar apparatus and digital pattern recorder are given. Test results show that the facility is suitable for use in the prototype reflector measurement program. Before the facility is used in future measurement programs, however, consideration should be given to replacing the existing microwave receiver with a newer model which is less prone to drift, correcting the backlash in the model tower positioner head, and evaluating the use of either a berm or a clutter fence to reduce multipath effects.

5.2 Recommendations for Further Work

Although depolarizing trihedral corner reflectors which incorporate conducting fins or corrugations along one of their interior surfaces will find immediate use as location markers and calibration targets in polarimetric radar systems used for radar-assisted positioning and geophysical remote sensing, consideration should also be given to using reflectors of this type as radar cross section enhancement devices in conventional marine radar navigation. An increasing number of civil marine radars are equipped with provision for transmitting and receiving circularly polarized waves in order to suppress rain clutter. However, mariners must exercise

caution when using them in this mode because the conventional trihedral corner reflectors which are used to augment the response of most buoys, channel markers, and navigations hazards are essentially invisible to a circularly polarized radar. Replacement of conventional reflectors by depolarizing reflectors which respond equally well to horizontally, vertically, and circularly polarized incident waves would significantly enhance the safety of marine navigation. Further engineering studies and field trials should be conducted in order to verify the suitability of depolarizing reflectors of the type proposed in Chapter 4 for use in such applications. Since such reflectors would be required in large numbers, it would also be desirable to study alternative methods of manufacture with the aim of minimizing their unit cost.

Detailed analysis of modified trihedral corner reflectors for engineering purposes would be simplified if the radar cross section prediction algorithms and software tools described in Chapters 3 and 4 were combined into a single integrated software package designed to run on a high performance UNIX workstation or other platform suitable for numerically intensive computing. A package designed to assist in the evaluation of alternative schemes for truncating and compensating trihedral corner reflectors should include implementations of the prediction algorithm for ideal trihedral corner reflectors based on Robertson's model (as described in Chapter 3), either the finite-difference time-domain (FD-TD) or the shooting and bouncing ray (SBR) methods for predicting the response of non-ideal trihedral corner reflectors, and suitable tools for entering the reflector geometry and displaying the results of the calculations. The FD-TD and SBR methods are sufficiently demanding of computing resources that it will probably be necessary to include provision for running them either as background tasks for extended periods or remotely on a sufficiently powerful host. A package designed to assist in the design of depolarizing trihedral corner reflectors which incorporate conducting fins or corrugations would also require code for predicting the response of a conducting grating with rectangular grooves. The packages should also include a facility for comparing numerical predictions with experimental results obtained by the user.

Although recent trials conducted by Transport Canada (Transportation Development Centre, Montreal, P.Q.) have shown that radar-assisted positioning systems based on measurement of the range and bearing to shore-based cooperative targets can provide vessels navigating in inland waterways, harbours, and harbour approaches with very accurate position data under optimum conditions, the lack of data concerning the scattering statistics of terrain at grazing incidence makes it difficult to give reliable estimates of the size of targets required to achieve specified probabilities of detection and false alarm. Future development of radar-assisted positioning systems for marine navigation should assign a high priority to the collection of such data in a variety of representative clutter environments in order to assist in system planning and evaluation. Future trials should include provision for determining the confidence with which the cooperative targets are detected against the clutter background in order to provide some measure of the reliability of such systems.

Three methods for realizing linear polarization selective reflective surfaces derived from conducting gratings with rectangular grooves are suggested in Chapter 4 including (1) gratings designed to reflect TE-polarized incident waves while diffracting TM-polarized incident waves into the $m = -1$ diffracted order, (2) gratings designed to reflect TE-polarized waves while dissipating TM-polarized incident waves in lossy groove media, and (3) gratings designed to reflect TE- and TM-polarized waves in different directions by utilizing a sloped grating profile. Each type of grating suffers from various limitations. The scattering characteristics of each scheme should be examined in further detail so that their relative performance and merits can be assessed in the context of both realizing linear and circular polarization selective trihedral corner reflectors and their possible use in other quasi-optical systems. The first scheme can be analyzed simply using the mode-matching formulation presented in Appendix B and some results have been presented in the literature. Analysis of the second scheme would require that the representation for the fields in the groove region be modified in order to account for the effects of the lossy groove media. In both cases, the impact of relative convergence on calculation of the amplitude of the diffracted orders should be assessed. Since the problem

geometry of the third scheme is not periodic and the free space and groove regions do not belong to separable coordinate systems, it will necessary to employ a different approach. Although a purely numerical technique could be used in such an investigation, it may be simpler to begin simply by setting up a design parameter matrix, constructing a set of prototype reflection polarizers, then measuring and comparing the response characteristics of the prototypes.

The task of coding solutions to antenna or scattering problems which involve the prediction of polarization dependent effects would be simplified if a standard library of functions and subroutines was available for performing polarization calculations. Such a library would include routines for transforming polarization descriptors between coordinate frames based on the results presented in this study and routines for converting polarization descriptors from one type to another (e.g., polarization scattering matrix to Mueller matrix), converting polarization descriptors between the backscatter and forward scatter alignment conventions, verifying the validity of polarization descriptor data, calculating polarization efficiency, and extracting co-polar and cross-polar nulls and related parameters from polarization response descriptors based on results generally available in the literature. Since these routines will make extensive use of matrices and complex variables, the library should initially be coded in Fortran 77. Consideration should also be given to producing libraries for use with more specialized numerical analysis and symbolic algebra packages such as *Matlab* (The Mathworks, Inc., Natick, MA), *Maple* (Waterloo Maple Software, Inc., Waterloo, Ont.), *Macsyma* (Macsyma, Inc., Arlington, MA), and *Mathematica* (Wolfram Research, Inc., Champaign, IL).

Appendix A

DESIGN CURVES FOR TOP HAT REFLECTORS

A.1 Introduction

The top hat reflector is a variant of the conventional dihedral corner reflector which has recently found use as a calibration target for airborne imaging radars. It may be regarded as a body of revolution formed by rotating a dihedral corner about an axis of symmetry which is perpendicular to both the seam of the dihedral and one of its two reflector panels. As such, its response is independent of azimuth angle. In practice, a top hat reflector is usually realized by attaching a right circular cylinder to a flat circular plate such that the cylinder axis is perpendicular to and passes through the center of the plate although other ground plane configurations have been considered. The requirements for the cylinder and base to be flat and mutually orthogonal are similar to those for the panels of a conventional dihedral corner reflector.

Although the top hat reflector was apparently introduced over twenty-five years ago, it was not discussed in the literature until the early 1980's [1]. It was not treated in standard references until much later still and, even so, the discussion is brief and contains obvious errors [2], [3]. Blejer [4] recently extended the simplified model introduced by Johansen [1] to account for the contribution of single bounce reflections from the cylinder, the cylinder cap, and the annular base. The design of top hat reflectors is complicated by the dependence of the scattering cross section and the angle of maximum response on three parameters: the radius and height of the cylinder and the width of the annular base. In addition, the main response lobe becomes increasingly asymmetrical as the angle of maximum response becomes either much greater or much less than 45 degrees to the vertical. Design curves and related material are not generally available.

In this appendix, the problem of designing top hat reflectors with specified response characteristics is considered. In section A.2, an approximate expression for the scattering cross section of a top hat reflector is derived as a function of the elevation angle of the incident ray using a simplified physical optics model which accounts only for the contribution of double-bounce reflections from the cylinder and the ground plane. In section A.3, design curves which relate the physical dimensions of a top hat reflector to the direction of its maximum response, its maximum scattering cross section, and its elevation beamwidth are presented. In section A.4, the results are used to solve a sample design problem.

A.2 Analysis

Consider a top hat reflector which consists of a right circular cylinder of radius a and height c attached to a circular ground plane of radius b as shown in Figure A.1. The cylinder axis coincides with the z-axis and the ground plane lies in the x-y plane. The angle of elevation θ is measured from the positive z-axis. If the plane of incidence contains the cylinder axis and the opposite panel is of sufficient extent, a top hat reflector will return an incident ray to the source in the same manner as would a dihedral corner. Since a top hat reflector is a body of revolution, its response pattern is uniform in azimuth. The locus of maximum response for double-bounce reflections is an inverted circular cone which intersects the cylinder in the x-y plane.
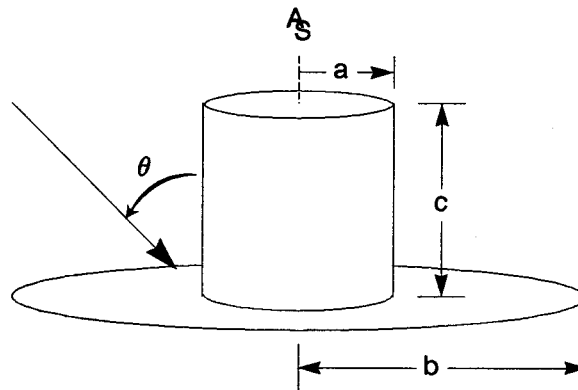
Figure A.1: Problem geometry for scattering by a top hat reflector.

The contribution of double-bounce reflections to the scattering cross section of a top hat reflector can be determined using a ray-optical model in which the ground plane is treated as an image plane of finite extent as shown in Figure A.2. If an incident ray intercepts the cylinder at height h, radius a, and angle θ, the reflected ray will intercept the x-y plane at a radius $h \tan \theta + a$. If $h > (b - a) \cot \theta$, the point of interception will occur beyond the ground plane radius b and the reflected ray will not be returned to the source. The effective height c' of the portion of the cylinder which contributes to the response is therefore a function of the angle of incidence and is given by

$$c' = \begin{cases} (b - a) \cot \theta \,, & 0 < \theta \leq \gamma \,, \\ c \,, & \gamma \leq \theta < \pi/2 \,, \end{cases} \tag{A.1}$$

where

$$\gamma = \tan^{-1} \left(\frac{b - a}{c} \right) \,. \tag{A.2}$$
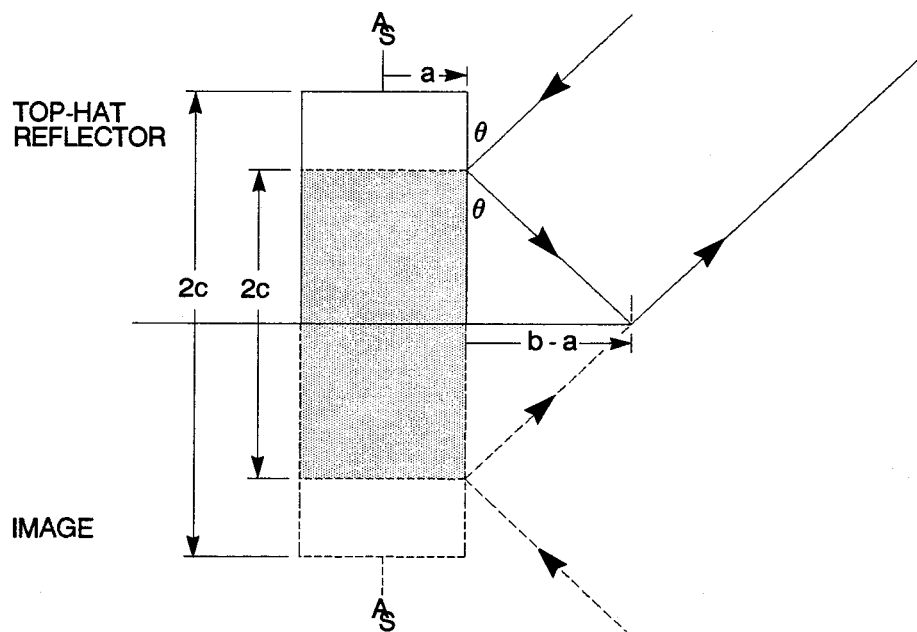
Figure A.2: A simplified ray-optical model for scattering by a top hat reflector.

If a top hat reflector is sufficiently large in terms of wavelength, the contribution of single bounce reflections from the cylinder, the cylinder cap, and the ground plane of the reflector to the backscatter response will be extremely small for other than vertical or horizontal incidence and can be neglected for the purposes of design. This reduces the problem to one of simply predicting the forward scattering cross section of a cylinder of radius a and height $2c'$ where the plane of incidence contains the cylinder axis. The corresponding problem geometry is shown in Figure A.3. The intersection of the plane of incidence with the surface of the cylinder is referred to as the *specular line*. The unit vectors $\hat{\imath}$ and $\hat{s}$ give the directions of the incident and scattered rays. The unit vectors $\hat{n}$ and $\hat{n}_o$ denote the outward normal to the cylinder at any point on its surface and along the specular line, respectively, and are given by

$$\hat{n} = \cos\phi\,\hat{x} + \sin\phi\,\hat{y}\,, \qquad (A.3)$$

and

$$\hat{n}_o = \cos\phi_o\,\hat{x} + \sin\phi_o\,\hat{y}\,. \qquad (A.4)$$
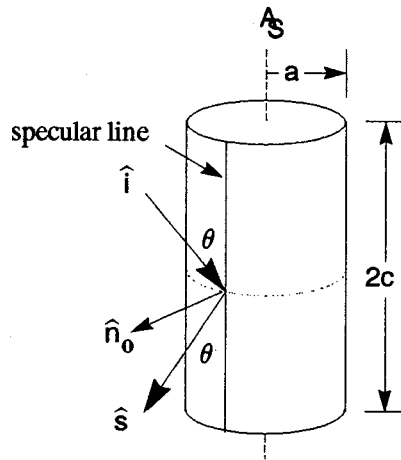
Figure A.3: Problem geometry for forward scattering by a cylinder.

Following Knott [5], an approximate expression for the bistatic scattering cross section of a target can be obtained by evaluating a physical optics integral over the illuminated portion

of its surface. In the case of scattering by a cylinder with radius a and height $2c'$, the physical optics integral can be expressed as the product of axial and circumferential components

$$\sqrt{\sigma} = -j\frac{ka}{\sqrt{\pi}}\, I_z\, I_\phi \,, \tag{A.5}$$

where the axial component I_z is given by

$$I_z = \int_{-c'}^{c'} e^{jkz(\hat{z}\cdot(\hat{\imath}-\hat{s}))}\, dz \,, \tag{A.6}$$

$$= 2c'\, \frac{\sin[kc'(\hat{z}\cdot(\hat{\imath}-\hat{s}))]}{kc'(\hat{z}\cdot(\hat{\imath}-\hat{s}))} \,, \tag{A.7}$$

and the circumferential component I_ϕ is given by

$$I_\phi = \int_{-\pi/2}^{\pi/2} (\hat{n}\cdot\hat{\imath})\, e^{jka(\hat{n}\cdot(\hat{\imath}-\hat{s}))}\, d\phi \,, \tag{A.8}$$

Although (A.8) will yield an exact solution, the resulting expression contains special functions and is difficult to handle. It is generally more convenient to approximate I_ϕ by the method of stationary phase where the stationary phase point is the specular line shown in Figure A.4 and the stationary phase approximation is of the form [6]

$$I_\phi = \int g(\phi)\, e^{jf(\phi)} d\phi \simeq \left[\frac{2\pi}{f''(\phi_o)}\right]^{1/2} g(\phi_o)\, e^{jf(\phi_o)}\, e^{j\pi/4} \,, \tag{A.9}$$

where

$$g(\phi) = (\hat{n}\cdot\hat{\imath}) \,, \tag{A.10}$$

$$f(\phi) = ka\,(\hat{n}\cdot(\hat{\imath}-\hat{s})) \,, \tag{A.11}$$

and

$$g(\phi_o) = (\hat{n}_o\cdot\hat{\imath}) \,, \tag{A.12}$$

$$f(\phi_o) = ka\,(\hat{n}_o\cdot(\hat{\imath}-\hat{s})) \,, \tag{A.13}$$

$$f''(\phi_o) = ka\,(\hat{n}_o\cdot(\hat{\imath}-\hat{s})) \,. \tag{A.14}$$

Substituting (A.12) – (A.14) into (A.9) gives

$$I_\phi \simeq (\hat{n}_o\cdot\hat{\imath})\, e^{jka(\hat{n}_o\cdot(\hat{\imath}-\hat{s}))}\, e^{j\pi/4} \left[\frac{\lambda}{a\,(\hat{n}_o\cdot(\hat{\imath}-\hat{s}))}\right]^{1/2} \,. \tag{A.15}$$

An expression for the bistatic scattering cross section of the cylinder is obtained by substituting (A.15) and (A.7) into (A.5) which gives

$$\sqrt{\sigma} = -j2c' \left[\frac{2ka}{\hat{n}_o \cdot (\hat{i} - \hat{s})} \right]^{1/2} \frac{\sin kc' \left(\hat{z} \cdot (\hat{i} - \hat{s}) \right)}{kc' \left(\hat{z} \cdot (\hat{i} - \hat{s}) \right)} (\hat{n}_o \cdot \hat{i}) \, e^{jka(\hat{n}_o \cdot (\hat{i} - \hat{s}))} \, e^{j\pi/4} \ . \tag{A.16}$$

In the case of forward scattering, the vectors $\hat{i}$, $\hat{s}$, $\hat{n}_o$, and $\hat{z}$ are related as follows:

$$(\hat{i} - \hat{s}) \quad = \quad -2\sin\theta \, \hat{n}_o \ , \tag{A.17}$$

$$\hat{n}_o \cdot (\hat{i} - \hat{s}) \quad = \quad -2\sin\theta \ , \tag{A.18}$$

$$\hat{z} \cdot (\hat{i} - \hat{s}) \quad = \quad 0 \ , \tag{A.19}$$

$$\hat{n}_o \cdot \hat{i} \quad = \quad -\sin\theta \ . \tag{A.20}$$

An expression for the forward scattering cross section of the cylinder is obtained by substituting (A.17) – (A.20) into (A.16) which gives

$$\sqrt{\sigma} = -j2c' \sqrt{ka\sin\theta} \, e^{-j2ka\sin\theta} \, e^{-j\pi/4} \ . \tag{A.21}$$

Since (A.18) is negative, a phase factor $e^{j\pi/2}$ is introduced when its square root is extracted. Taking the amplitude of (A.21) and squaring the result gives

$$\sigma = \frac{8\pi}{\lambda} ac'^2 \sin\theta \ . \tag{A.22}$$

Finally, an approximate expression for the scattering cross section of a top-hat reflector is obtained by substituting (A.1) into (A.22) to give

$$\sigma(\theta) = \begin{cases} \dfrac{8\pi}{\lambda} ac^2 \sin\theta \ , & 0 < \theta \le \gamma \ , \\[3mm] \dfrac{8\pi}{\lambda} a(b-a)^2 \dfrac{\cos^2\theta}{\sin\theta} \ , & \gamma \le \theta < \pi/2 \ , \end{cases} \tag{A.23}$$

where a, b, c, and θ are defined in Figure A.1 and the parameter γ is given by (A.2). If the ground plane of the reflector is of very large extent, i.e., $b \gg c$, the angle $\gamma \to \pi/2$ and (A.23) reduces to

$$\sigma(\theta) = \frac{8\pi}{\lambda} ac^2 \sin\theta \ , \qquad 0 < \theta < \pi/2 \ . \tag{A.24}$$

A.3 Design Curves

Angle of Maximum Response

The contribution of double-bounce reflections to the response of a top hat reflector will reach its maximum value when the angle of incidence is such that any ray incident on the cylinder will intercept the annulus and vice versa. From Figure A.2, this will occur when $c = (b - a)\cot\theta$ so the angle of maximum response θ_{max} is given by

$$\theta_{max} = \tan^{-1}\left(\frac{b-a}{c}\right) = \tan^{-1}\xi , \qquad (A.25)$$

where ξ is defined as the ratio of the width of the annulus to the height of the cylinder. A graph depicting θ_{max} as a function of ξ is presented in Figure A.4. If the height of the cylinder and the width of the base are equal, the angle of maximum response is 45 degrees. Doubling the ratio ξ will lower the angle of maximum response to approximately 65 degrees while halving it will raise the angle to approximately 25 degrees.
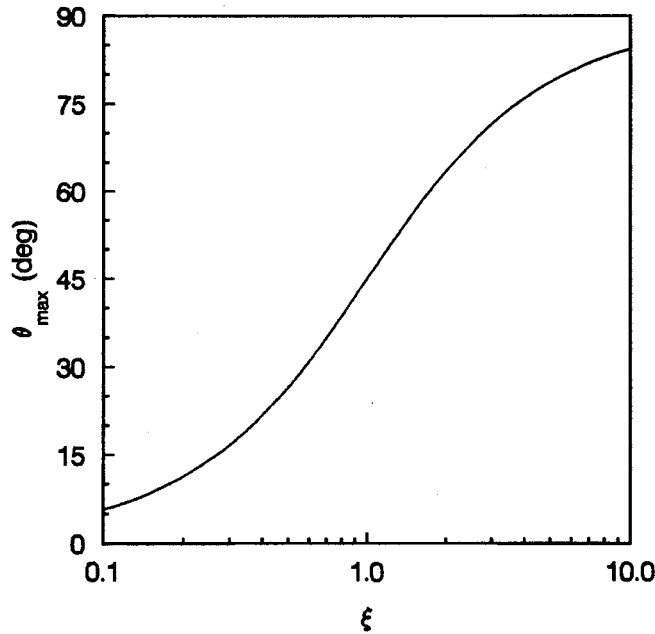
Figure A.4: Angle of maximum response of a top hat reflector vs. ξ, the ratio of the annulus width to the cylinder height.

Maximum Scattering Cross Section

Substitution of (A.25) into (A.23) gives an expression for the maximum scattering cross section of a top hat reflector

$$\sigma_{max} = \frac{8\pi}{\lambda} \frac{a(b-a)c^2}{\sqrt{c^2 + (b-a)^2}} , \tag{A.26}$$

$$= \frac{8\pi}{\lambda} ac^2 \frac{\xi}{\sqrt{1+\xi^2}} ,$$

where $(\sin \theta_{max})$ is given by

$$\sin \theta_{max} = \frac{\xi}{\sqrt{1+\xi^2}} . \tag{A.27}$$

Consider a top hat reflector with a cylindrical component of fixed radius a_o and height c_o which presents a maximum scattering cross section of σ_o for $\xi = 1$. As the ratio ξ is altered to obtain the desired angle of maximum response, the maximum scattering cross section of the reflector will vary as shown in Figure A.5. The response will drop off rapidly for $\xi < 1$ and will asymptotically approach a value of $\sqrt{2}\,\sigma_o$ for $\xi > 1$.

The radius and height of the cylinder can be scaled to compensate for this variation and so yield a family of top hat reflectors with different angles of maximum response but the same maximum scattering cross section. With the cylinder height c fixed, the scale factor for the cylinder radius a is given by

$$\frac{a}{a_o} = \sqrt{\frac{1+\xi^2}{2\xi}} . \tag{A.28}$$

With the cylinder radius a fixed, the scale factor for the cylinder height c (and the corresponding annulus width $b - a$) is given by

$$\frac{c}{c_o} = \sqrt[4]{\frac{1+\xi^2}{2\xi}} . \tag{A.29}$$

In either case, the corresponding value of b is simply given by

$$b = a + \xi c . \tag{A.30}$$

A graph depicting the scale factors (A.28) and (A.29) as functions of the ratio ξ is presented in Figure A.6.
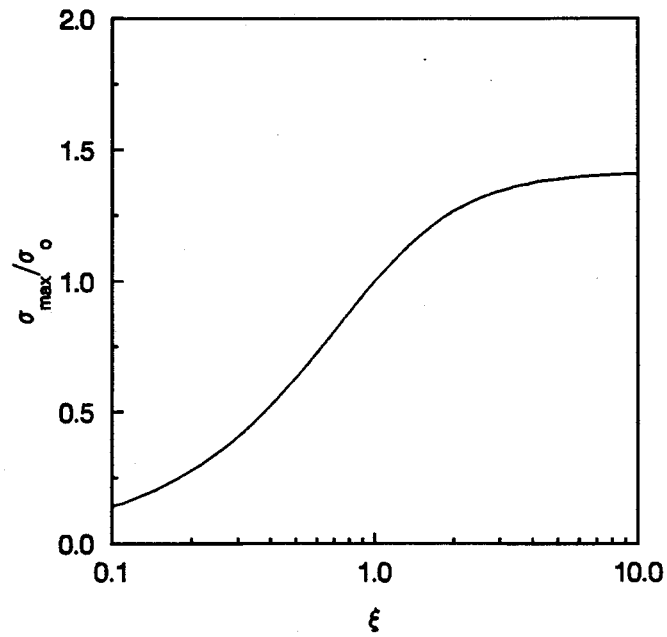
Figure A.5: Maximum scattering cross section of a top hat reflector vs. ξ, the ratio of the annulus width to the cylinder height for fixed values of a and c.
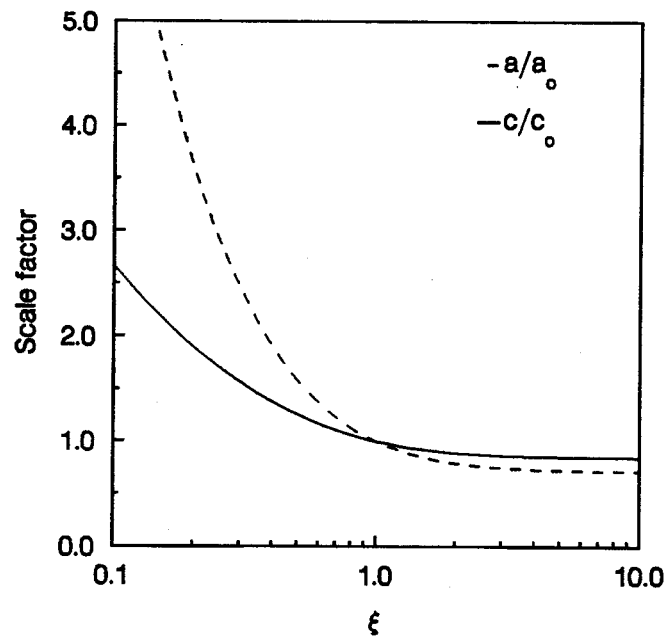
Figure A.6: Scale factors for the cylinder radius a and height c of a top hat reflector vs. ξ, the ratio of the annulus width to the cylinder height.

Half Power Beamwidth

The half-power elevation beamwidth of a top hat reflector is determined by finding the angles of incidence above and below the angle of maximum response, $\theta_{\max}$, for which the scattering cross section falls to half its maximum value and taking their difference. From (A.26),

$$\frac{\sigma_{\max}}{2} = \frac{4\pi}{\lambda} \frac{a(b-a)c^2}{\sqrt{c^2 + (b-a)^2}} \, . \tag{A.31}$$

Equating (A.23a) and (A.31) then solving for θ gives the upper half-power angle,

$$\theta_{u_{3\mathrm{dB}}} = \sin^{-1}\left(\frac{\xi}{2\sqrt{1+\xi^2}}\right) \, . \tag{A.32}$$

The lower half-power angle $\theta_{\ell_{3\mathrm{dB}}}$ is determined in a similar fashion. Equating (A.23b) and (A.28) then cancelling common factors gives a quadratic equation in $\sin\theta$,

$$\frac{1}{2\xi\sqrt{1+\xi^2}} = \frac{1 - \sin^2\theta}{\sin\theta} \, . \tag{A.33}$$

Rearranging terms gives an expression in standard form,

$$\sin^2\theta + \left(\frac{1}{2\xi\sqrt{1+\xi^2}}\right)\sin\theta - 1 = 0 \, , \tag{A.34}$$

with roots given by

$$\sin\theta = \frac{-B \pm \sqrt{B^2 + 4}}{2} \, , \tag{A.35}$$

where

$$B = \frac{1}{2\xi\sqrt{1+\xi^2}} \, . \tag{A.36}$$

Since ξ is always positive, so too are B and the solution to (A.34) given by

$$\sin\theta = \frac{-B + \sqrt{B^2 + 4}}{2} \, . \tag{A.37}$$

Solving for θ gives the lower half-power angle,

$$\theta_{\ell_{3\mathrm{dB}}} = \sin^{-1}\left(\frac{-B + \sqrt{B^2 + 4}}{2}\right) \, . \tag{A.38}$$

Finally, taking the difference between (A.38) and (A.32) gives the total half-power elevation beamwidth of the reflector

$$\Theta_{3dB} = \sin^{-1}\left(\frac{-B + \sqrt{B^2 + 4}}{2}\right) - \sin^{-1}\left(\frac{\xi}{2\sqrt{1 + \xi^2}}\right). \qquad (A.39)$$

Care must be taken in applying (A.39) since the main response lobe of a top hat reflector is not symmetric about the angle of maximum response, particularly if $\xi > 1$. In addition to Θ_{3dB}, the total half-power beamwidth, it is convenient to define the quantities $\Theta_{u_{3dB}} = \theta_{u_{3dB}} - \theta_{max}$ and $\Theta_{\ell_{3dB}} = \theta_{max} - \theta_{\ell_{3dB}}$ as the half-power beamwidths above and below the angle of maximum response, respectively. All three quantities are graphed in Figure A.7 as a function of the ratio ξ. Although both the total and upper half-power beamwidths increase with ξ, the lower half-power beamwidth reaches its maximum value when $\xi \simeq 0.55$. The upper and lower half-power beamwidths are equal and the top hat presents a symmetrical elevation response pattern when $\xi \simeq 0.51$.
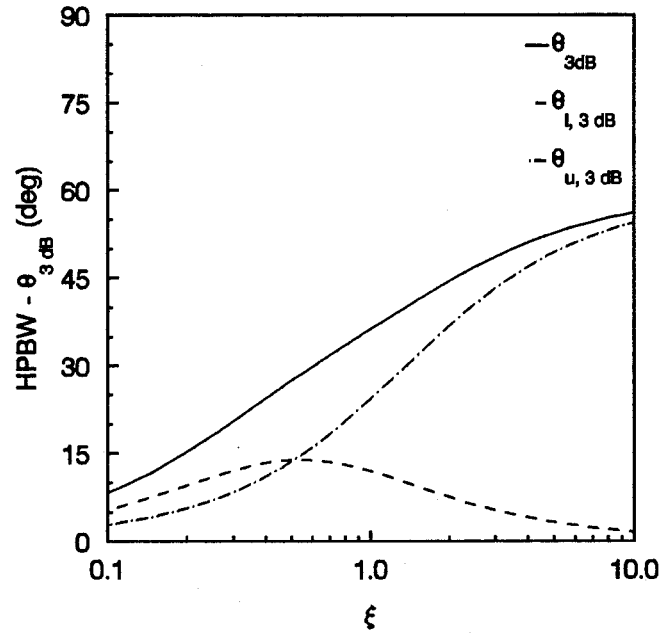
Figure A.7: Half-power elevation beamwidth of a top hat reflector vs. ξ, the ratio of the annulus width to the cylinder height.

Similar relations may be derived for the 1 dB beamwidth of the elevation response. The upper and lower 1 dB angles are given by

$$\theta_{u_{1dB}} = \sin^{-1}\left(\frac{10^{-0.1}\,\xi}{\sqrt{1+\xi^2}}\right),$$ (A.40)

$$\theta_{\ell_{1dB}} = \sin^{-1}\left(\frac{-B' + \sqrt{B'^2 + 4}}{2}\right),$$ (A.41)

where B' is given by

$$B' = \frac{10^{-0.1}}{\xi\sqrt{1+\xi^2}},$$ (A.42)

and the total 1 dB elevation beamwidth is given by $\theta_{u_{1dB}} - \theta_{\ell_{1dB}}$ or

$$\Theta_{1dB} = \sin^{-1}\left(\frac{-B' + \sqrt{B'^2 + 4}}{2}\right) - \sin^{-1}\left(\frac{10^{-0.1}\,\xi}{\sqrt{1+\xi^2}}\right).$$ (A.43)

As in the previous case, it is convenient to define the quantities $\Theta_{u_{1dB}} = \theta_{u_{1dB}} - \theta_{max}$ and $\Theta_{\ell_{1dB}} = \theta_{max} - \theta_{\ell_{1dB}}$ as the 1 dB beamwidths above and below the angle of maximum response, respectively. All three quantities are graphed in Figure A.8 as a function of the ratio ξ.
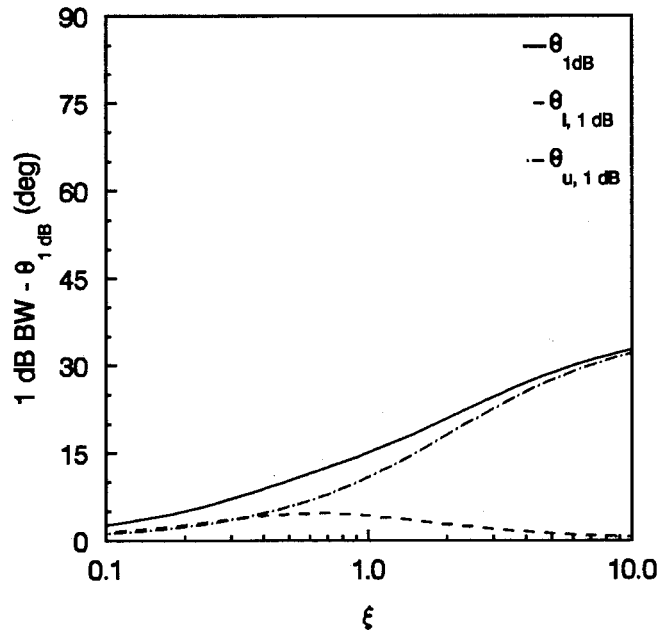
Figure A.8: 1 dB elevation beamwidth of a top hat reflector vs. ξ, the ratio of the annulus width to the cylinder height.

Since the elevation response pattern of a top hat reflector is generally asymmetric about the direction of maximum response, it may be useful to instead specify the median angle of response given by $\theta_m = (\theta_u + \theta_\ell)/2$. The angle of maximum response and angles of median response for 1 and 3 dB elevation beamwidths are graphed as a function of the ratio ξ in Figure A.9.
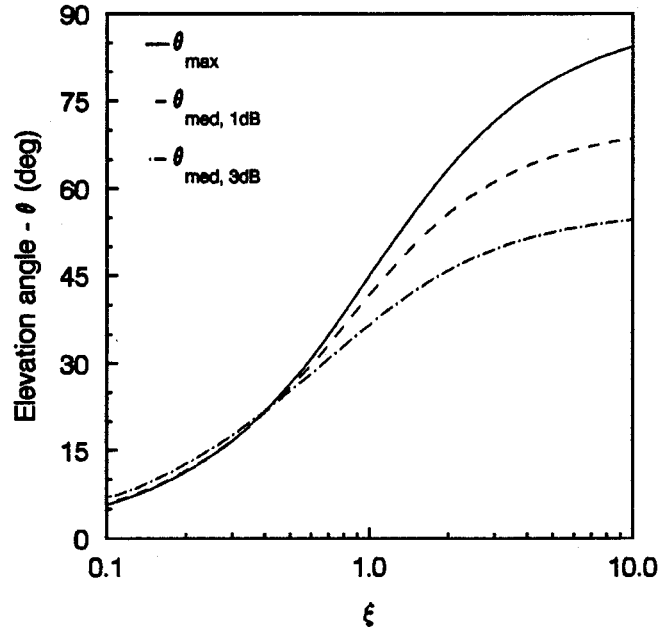
Figure A.9: Angle of maximum response and angles of median response for 1 and 3 dB elevation beamwidths vs. ξ, the ratio of the annulus width to the cylinder height.

A.4   Design Example

Consider a requirement for three even-bounce targets to be used in the calibration of an airborne radar system which operates at a frequency of 10 GHz. The three targets must each present a maximum scattering cross section of 30 dBsm at elevation angles of 25, 45, and 65 degrees, respectively, over a wide range in azimuth. Top hat reflectors which meet these requirements can be designed using the results presented in the previous section.

The ratio ξ which gives the desired angle of maximum response can be determined using either (A.25) or the graph in Figure A.4. It is found that top hat reflectors which present a ratio of annulus width to cylinder height of 0.5, 1.0, and 2.0, respectively, will present their

maximum response at the specified angles. This information is sufficient to obtain the 1 and 3 dB beamwidths of the three reflectors using either (A.39) and (A.43) or the graphs in Figures A.7 and A.8.

The reflector dimensions required to realize a maximum scattering cross section of 30 dBsm at 10 GHz are determined using (A.26). Once the radar wavelength λ and the specified angle of maximum response have been specified, the maximum scattering cross section depends only on the product of the cylinder radius a and the square of the cylinder height c. The design of a top hat reflector which presents its maximum response at 45 degrees is considered first. It is convenient to choose the diameter and height of the cylinder to be approximately equal. From (A.26), this gives a cylinder radius a of 0.75 m and a height c of 1.5 m. Since the ratio ξ is 1, the annulus width $(b - a)$ is also 1.5 m which gives a total radius b of 2.25 m. The results are then scaled to obtain suitable dimensions for the other two reflectors. Assuming that the cylinder radius is fixed, the dimensions of the other two reflectors can be determined using the scale factors presented in (A.28) and (A.29) and graphed in Figure A.6.

The results are summarized in Table A.1. In Figure A.10, the three reflectors are drawn to scale for comparison. In each case, the direction of the maximum response is indicated by a vector. In Figure A.11, the elevation response patterns of the three reflectors are predicted using Blejer's [4] formulation which accounts for double-bounce reflections from the interior of the reflector and single bounce reflections from cylinder, cylinder cap, and annular base.

Table A.1: Response Characteristics of Selected Top Hat Reflectors at $f = 10$ GHz

Figure	Dimensions				Response Characteristics			
	a	b	c	ξ	σ_{max}	θ_{max}	Θ_{3dB}	Θ_{1dB}
A.10(a)	0.75 m	1.69 m	1.89 m	0.5	30 dBsm	25°	27°	10°
A.10(b)	0.75 m	2.25 m	1.50 m	1.0	30 dBsm	45°	36°	15°
A.10(c)	0.75 m	3.75 m	1.33 m	2.0	30 dBsm	65°	45°	21°

(a)

(b)

(c)
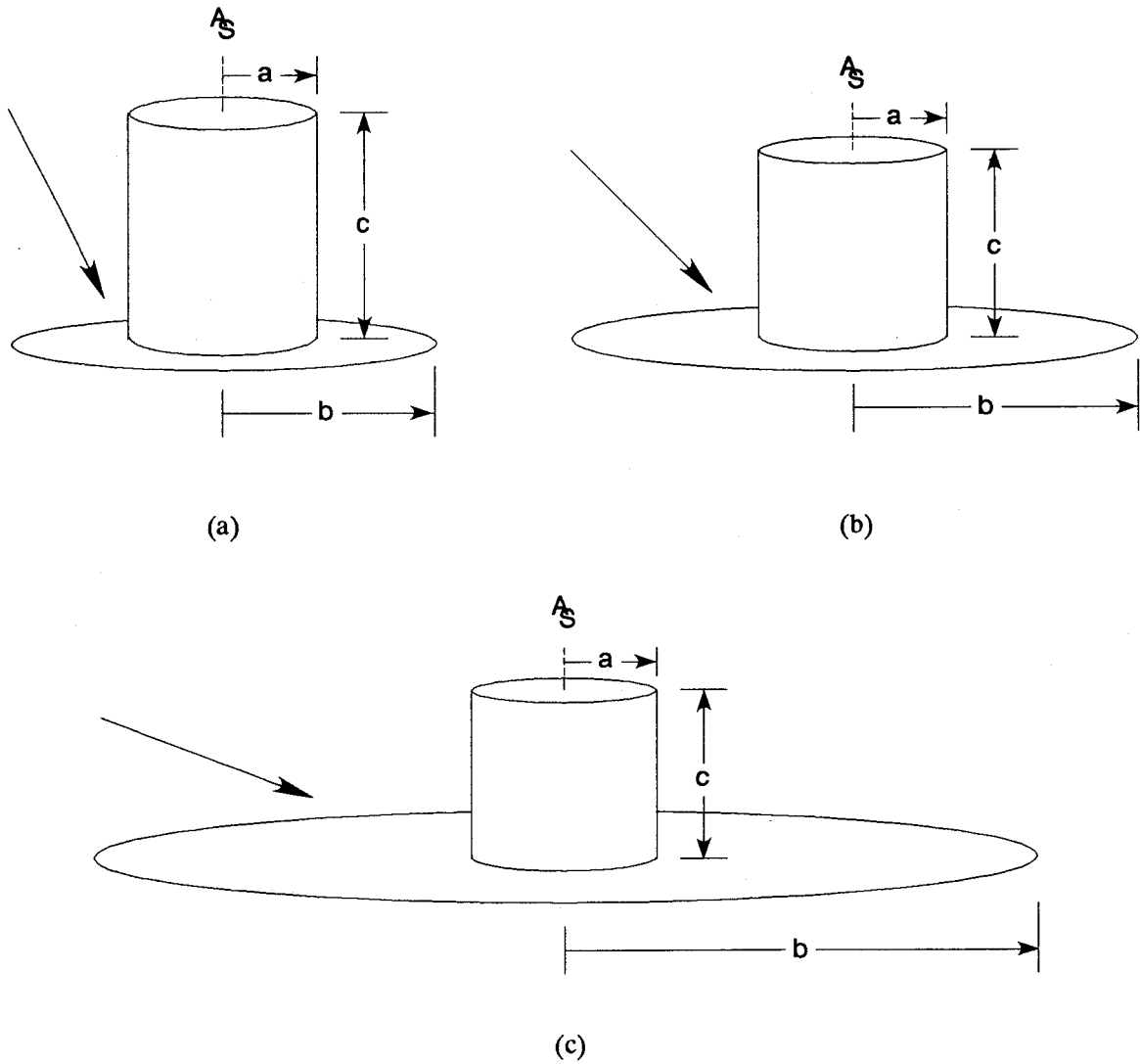
Figure A.10: Relative size of selected top hat reflectors which present the same maximum scattering cross section. The direction of maximum response is indicated by a vector. (a) $\xi = 0.5$. (b) $\xi = 1.0$. (c) $\xi = 2.0$.

(a)

(b)
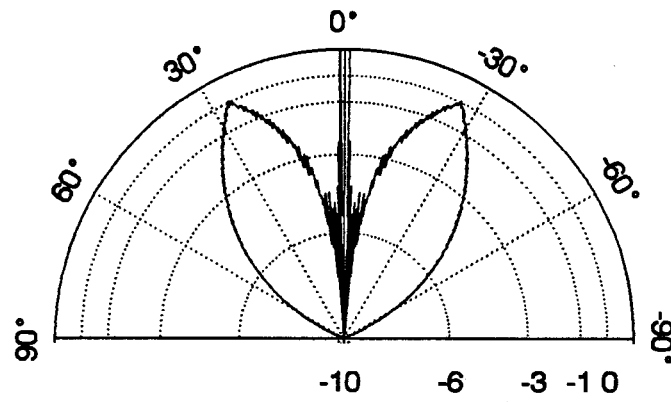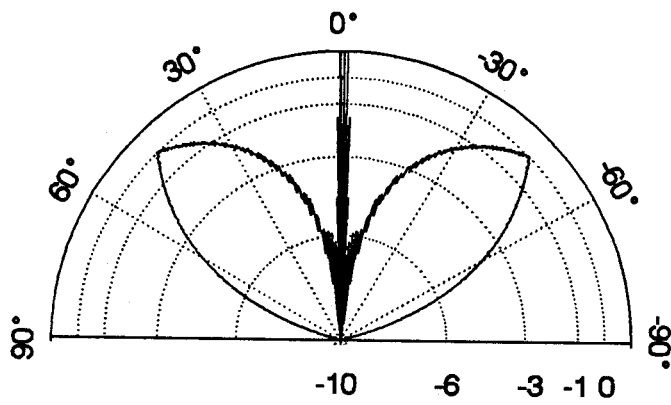
σ (dB)
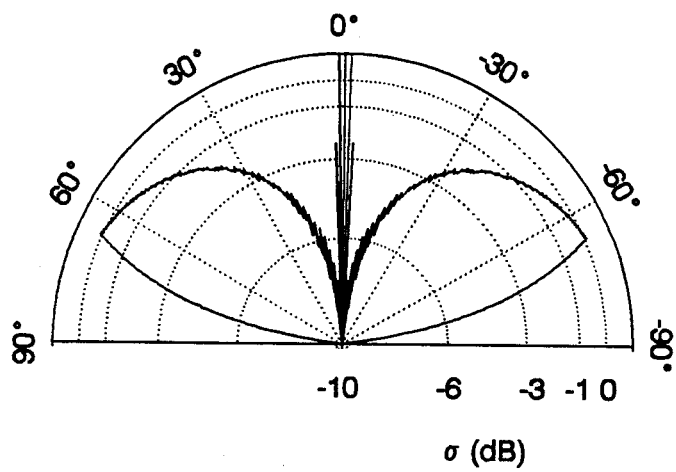
(c)

Figure A.11: Elevation response patterns of selected top hat reflectors which present the same maximum scattering cross section. (a) $\xi = 0.5$. (b) $\xi = 1.0$. (c) $\xi = 2.0$.

References

[1] E.L. Johansen, "Top hat reflectors cap radar calibration," *Microwaves,* vol. 20, no. 12, pp. 65–66, Dec. 1981.

[2] C.H. Currie and N.C. Currie, "MMW Reflectivity Measurement Techniques," in *Principles and Applications of Millimetre-Wave Radar,* N. C. Currie and C.E. Brown, Eds. Norwood, MA: Artech House, 1987, pp. 767–774.

[3] R. N. Trebits "Radar Cross Section," in *Radar Reflectivity Measurement: Techniques and Applications,* N. C. Currie, Ed. Norwood, MA: Artech House, 1989, pp. 44–48.

[4] D. Blejer, "Physical optics polarization scattering matrix for a top hat reflector," *IEEE Trans. Antennas Propagat.,* vol. AP-39, pp. 857–859, June 1991.

[5] E.F. Knott, J.F. Shaeffer, and M.T. Tuley, *Radar Cross Section: Its Prediction, Measurement, and Reduction.* Norwood, MA: Artech House, 1985, pp. 119–130.

[6] N. Bleistein and R.A. Handelsman, *Asymptotic Expansions of Integrals.* New York: Holt, Rinehart, and Winston, 1975, pp. 219–220.

Appendix B

SCATTERING BY A CONDUCTING GRATING
WITH RECTANGULAR GROOVES

B.1 Introduction

In this appendix, the problem of scattering by a conducting grating with rectangular grooves is solved for the case in which the plane of incidence is perpendicular to the direction of the grooves [1], [2]. In section B.2, analytical solutions to the scattering problem are derived for the cases of TM- and TE-polarized incidence by mode-matching across the boundary between the free space and groove regions. Since the grating is periodic in y, the fields in adjacent unit cells differ only by the phase factor $\exp(jkd\sin\phi_i)$ and it is sufficient to consider the fields in a single unit cell such as the one shown in Figure B.1. Symbols are defined in Table B.1. The fields in the free space region ($x > 0$) are represented by an infinite sum of propagating plane waves and evansecent waves while the fields in the groove region ($x < 0$) are represented by an infinite sum of propagating and evanescent parallel-plate waveguide modes. A doubly infinite set of linear equations in the complex coefficients of either the free space or groove modes is obtained by applying the condition of continuity of the tangential electric and magnetic fields over the planar junction between the free space and groove regions and the property of orthogonality between the normal modes in each set. The set must be truncated or partitioned before it can be solved numerically. In section B.3, procedures for verifying the correctness and accuracy of numerical results obtained by mode-matching are described and the problem of determining the minimum number of modes required to accurately represent the fields in the free space and groove regions and their optimum ratio is considered. In section B.4, an implementation of the analytical solutions as a pair of subroutines coded in Fortran 77 is presented.
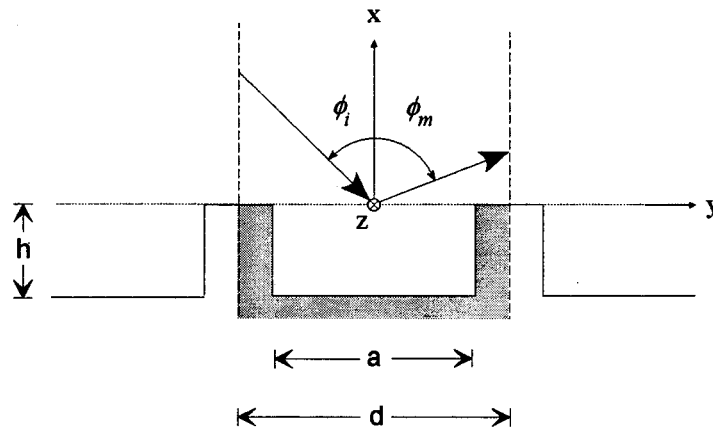
Figure B.1: A unit cell of a conducting grating with rectangular grooves.

Table B.1: Definition of Symbols

Symbol	Definition
d	period of the grating
a	width of the groove
h	height of the groove
a/d	aspect ratio of the grating
λ	wavelength
ϕ_i	angle of incidence
ϕ_m	angle of reflection for the mth free space mode or diffracted order
m	index for free space modes
n	index for groove modes
M	number of free space modes in the truncated set of equations
N	number of groove modes in the truncated set of equations
k	propagation constant in free space ($= 2\pi/\lambda$)
k_n	propagation constant of the nth groove mode
f_m	orthonormal basis function for TM and TE free space modes
g_n	orthonormal basis function for TM groove modes
g'_n	orthonormal basis function for TE groove modes
$\mathcal{A}_i$	complex amplitude of the incident TM free space mode
$\mathcal{B}_i$	complex amplitude of the incident TE free space mode
$\mathcal{A}_m$	complex amplitude of the mth scattered TM free space mode
$\mathcal{C}_n$	complex amplitude of the nth TM groove mode
$\mathcal{B}_m$	complex amplitude of the mth scattered TE free space mode
$\mathcal{D}_n$	complex amplitude of the nth TE groove mode
η_o	characteristic impedance of free space ($= \sqrt{\frac{\mu_o}{\epsilon_o}}$)
Γ_m	complex reflection coefficient of the mth free space mode

B.2 Analysis

B.2.1 TM Polarization

Free Space Region

If a TM-polarized plane wave is incident on a grating of infinite extent such that the plane of incidence is perpendicular to the direction of the grooves, the tangential components of the electric and magnetic fields in the free space region are given by

$$H_z(x,y) \;=\; \mathcal{A}_i\, e^{jk\cos\phi_i x} f_0 + \sum_{m=-\infty}^{\infty} \mathcal{A}_m\, e^{-jk\cos\phi_m x} f_m \;, \tag{B.1}$$

$$E_y(x,y) \;=\; -\mathcal{A}_i\, \eta_o \cos\phi_i\, e^{jk\cos\phi_i x} f_o + \sum_{m=-\infty}^{\infty} \mathcal{A}_m\, \eta_o \cos\phi_m\, e^{-jk\cos\phi_m x} f_m \;, \tag{B.2}$$

where

$$E_y(x,y) \;=\; \frac{j\eta_o}{k}\frac{\partial H_z(x,y)}{\partial y} \;, \tag{B.3}$$

$$f_m \;=\; \frac{1}{\sqrt{d}}\, e^{-jk\sin\phi_m y} \;, \tag{B.4}$$

$$k \;=\; \frac{2\pi}{\lambda} \;, \tag{B.5}$$

$$\sin\phi_m \;=\; \sin\phi_i + m\,\frac{\lambda}{d} \;, \tag{B.6}$$

$$\cos\phi_m \;=\; \sqrt{1 - \sin^2\phi_m} \;, \qquad |\sin\phi_m| < 1 \;, \tag{B.7}$$

$$\;=\; -j\sqrt{\sin^2\phi_m - 1} \;, \qquad |\sin\phi_m| > 1 \;.$$

The first term in each of (B.1) and (B.2) represents the incident field while the second term represents the infinite sum of propagating and non-propagating waves which comprise the scattered field. The function f_m is an orthonormal basis function for both TM- and TE-polarized modes in the free space region. Equation (B.6) is usually referred to as the *grating equation*. The remaining quantities and symbols are defined in Table B.1 and Figure B.1.

Groove Region

The tangential components of the TM-polarized fields in the groove region are given by

$$H_z(x, y) = \sum_{n=0}^{\infty} C_n \frac{\cos(k_n(x + h))}{\cos k_n h} g_n , \qquad (B.8)$$

$$E_y(x, y) = \sum_{n=0}^{\infty} -jC_n \frac{\eta_o}{k} k_n \frac{\sin(k_n(x + h))}{\cos k_n h} g_n , \qquad (B.9)$$

where the function g_n is an orthonormal basis function for TM-polarized modes in the groove region given by

$$g_n = \sqrt{\frac{\varepsilon}{a}} \cos\left(\frac{n\pi(x + a/2)}{a}\right) , \qquad (B.10)$$

and,

$$k_n = \sqrt{k^2 - (\frac{n\pi}{a})^2} , \qquad |\frac{n\pi}{a}| < k , \qquad (B.11)$$

$$= -j\sqrt{(\frac{n\pi}{a})^2 - k^2} , \qquad |\frac{n\pi}{a}| > k ,$$

$$\varepsilon = 1 , \qquad n = 0 , \qquad (B.12)$$

$$= 2 , \qquad n = 1, 2, 3, \ldots .$$

Boundary Conditions

The y-z plane is the interface between the free space and groove regions. The boundary conditions for the tangential components of the TM-polarized field are given by

$$
\begin{aligned}
H_z(0^+, y) &= H_z(0^-, y) , & |y| &\leq a/2 , \\
H_z(0^+, y) &= -K_y(0, y) , & a/2 &\leq |y| \leq d/2 ,
\end{aligned}
\qquad (B.13)
$$

and

$$
\begin{aligned}
E_y(0^+, y) &= E_y(0^-, y) , & |y| &\leq a/2 , \\
E_y(0^+, y) &= 0 , & a/2 &\leq |y| \leq d/2 ,
\end{aligned}
\qquad (B.14)
$$

where K represents the surface current density along the top surface of the corrugation.

Mode Matching

The modal expansions of the tangential magnetic field, (B.1) and (B.8), and the tangential electric field, (B.2) and (B.9), are evaluated at $x = 0$ then substituted into the boundary conditions (B.13) and (B.14), respectively. Continuity of the tangential magnetic field across the boundary gives

$$\sum_{m=-\infty}^{\infty} \mathcal{A}_m f_m = \sum_{n=0}^{\infty} C_n g_n , \qquad |y| < a/2 , \qquad \text{(B.15)}$$

while continuity of the tangential electric field across the boundary gives

$$-2\mathcal{A}_i \cos\phi_i f_0 + \sum_{m=-\infty}^{\infty} \mathcal{A}_m \cos\phi_m f_m = \sum_{n=0}^{\infty} C_n \frac{k_n}{jk} \tan(k_n h) g_n , \qquad |y| < a/2 , \qquad \text{(B.16)}$$

$$= 0 , \qquad a/2 < |y| < d/2 .$$

These expressions have been simplified by combining the contribution of the incident and specularly reflected components of the fields in the free space region at $x = 0$ into a single term and redefining $\mathcal{A}_0$ as

$$\mathcal{A}_0 = \mathcal{A}_i + \mathcal{A}_{Ref} , \qquad \text{(B.17)}$$

where $\mathcal{A}_i$ is the complex amplitude of the incident field and $\mathcal{A}_{Ref}$ is the complex amplitude of the specularly reflected component of the scattered field.

Inner Products

The inner products of the free space and groove mode basis functions are defined as

$$\langle f_m, f_{m'} \rangle = \int_{-d/2}^{d/2} f_m \cdot f_{m'}^* \, dx , \qquad \text{(B.18)}$$

$$\langle g_n, g_{n'} \rangle = \int_{-a/2}^{a/2} g_n \cdot g_{n'}^* \, dx , \qquad \text{(B.19)}$$

$$\langle f_m, g_n \rangle = \int_{-a/2}^{a/2} f_m \cdot g_n^* \, dx , \qquad \text{(B.20)}$$

$$\langle g_n, f_m \rangle = \int_{-a/2}^{a/2} g_n \cdot f_m^* \, dx . \qquad \text{(B.21)}$$

Since the basis functions are orthonormal,

$$\langle f_m, f_{m'} \rangle = 0 \,, \qquad\qquad m \neq m' \,, \qquad\qquad\qquad \text{(B.22)}$$

$$= 1 \,, \qquad\qquad m = m' \,, \qquad\qquad\qquad \text{(B.23)}$$

$$\langle g_n, g_{n'} \rangle = 0 \,, \qquad\qquad n \neq n' \,, \qquad\qquad\qquad \text{(B.24)}$$

$$= 1 \,, \qquad\qquad n = n' \,. \qquad\qquad\qquad \text{(B.25)}$$

The inner products $\langle f_m, g_n \rangle$ and $\langle g_n, f_m \rangle$ are given by

$$\langle f_m, g_n \rangle = \begin{cases} j\sqrt{\dfrac{1}{ad}} \dfrac{2k \sin \phi_m}{(k \sin \phi_m)^2 - (n\pi/a)^2} \cos\left(\dfrac{ka \sin \phi_m}{2}\right) \,, & n = 1, 3, 5, \ldots \\[4mm] \sqrt{\dfrac{\varepsilon}{ad}} \dfrac{2k \sin \phi_m}{(k \sin \phi_m)^2 - (n\pi/a)^2} \sin\left(\dfrac{ka \sin \phi_m}{2}\right) \,, & n = 0, 2, 4, \ldots \end{cases} \qquad \text{(B.26)}$$

and

$$\langle g_n, f_m \rangle = \begin{cases} -\langle f_m, g_n \rangle \,, & n = 1, 3, 5, \ldots \\[2mm] \langle f_m, g_n \rangle \,, & n = 0, 2, 4, \ldots \end{cases} \qquad\qquad \text{(B.27)}$$

since $\langle f, g \rangle = \langle g, f \rangle^*$, by definition [4, p. 26].

Substitution and Solution

The inner product of (B.15) with g_n yields an expression for the groove mode coefficients C_n in terms of the free space mode coefficients $\mathcal{A}_m$,

$$\sum_{m=-\infty}^{\infty} \mathcal{A}_m \langle f_m, g_n \rangle = C_n \,, \qquad\qquad\qquad \text{(B.28)}$$

while the inner product of (B.16) with f_m yields

$$-2\mathcal{A}_i \cos \phi_i\, \delta_m^o + \mathcal{A}_m \cos \phi_m = \sum_{n=0}^{\infty} C_n \frac{k_n}{jk} \tan(k_n h) \langle g_n, f_m \rangle \,. \qquad \text{(B.29)}$$

The result is then rearranged to give an expression for the free space mode coefficient $\mathcal{A}_m$ in terms of the groove mode coefficients C_n,

$$\mathcal{A}_m = \sum_{n=0}^{\infty} C_n \frac{k_n}{jk} \frac{\tan(k_n h)}{\cos \phi_m} \langle g_n, f_m \rangle + 2\mathcal{A}_i \delta_m^o \,. \qquad\qquad \text{(B.30)}$$

A direct solution for the coefficients of the free space modes can be obtained by substituting (B.28) into (B.30) to give

$$\sum_{m'=-\infty}^{\infty} A_{m'}\, \delta_m^{m'} = \sum_{n=0}^{\infty} \sum_{m'=-\infty}^{\infty} \mathcal{A}_{m'} \langle f_{m'}, g_n \rangle \frac{k_n}{jk} \frac{\tan(k_n h)}{\cos \phi_m} \langle g_n, f_m \rangle + 2\mathcal{A}_i \delta_m^o \,, \qquad \text{(B.31)}$$

then rearranging the result to yield an infinite set of linear simultaneous equations in the coefficients of the free space modes $\mathcal{A}_{m'}$:

$$\sum_{m'=-\infty}^{\infty} \mathcal{A}_{m'} \sum_{n=0}^{\infty} \langle f_{m'}, g_n \rangle \langle g_n, f_m \rangle \frac{k_n}{jk} \frac{\tan(k_n h)}{\cos \phi_m} - \delta_{m'}^m = -2\mathcal{A}_i \delta_m^o \,. \qquad \text{(B.32)}$$

It is convenient to express (B.32) as a matrix equation in the form

$$([B][C] + [G])\mathbf{A} = \mathbf{F} \,, \qquad \text{(B.33)}$$

where the elements of $[B]$, $[C]$, $[G]$, $\mathbf{A}$, and $\mathbf{F}$ are given by

$$B_{mn} = \langle g_n, f_m \rangle \frac{k_n}{jk} \frac{\tan(k_n h)}{\cos \phi_m} \,, \qquad \text{(B.34)}$$

$$C_{nm'} = \langle f_{m'}, g_n \rangle \,, \qquad \text{(B.35)}$$

$$G_{mm'} = -\delta_{m'}^m \,, \qquad \text{(B.36)}$$

$$A_{m'} = \mathcal{A}_{m'} \,, \qquad \text{(B.37)}$$

$$F_m = -2\mathcal{A}_i \delta_m^o \,. \qquad \text{(B.38)}$$

The number of free space and groove modes included in the solution must be reduced from an infinite number to M and N, respectively, before a numerical solution to (B.33) can be obtained. The resulting truncated set of equations is of order M.

Alternatively, the coefficients of the free space modes can be determined in an indirect way by first solving for the coefficients of the groove modes then multiplying the result by the matrix which relates the two. Since this truncated set of equations is the order N, the time required to compute a solution can be considerably reduced compared to the direct approach if the ratio of groove modes to free space modes N/M in the truncated set is much less than unity. First,

(B.30) is substituted into (B.28) to yield

$$\sum_{m=-\infty}^{\infty} \left(\sum_{n'=0}^{\infty} C_{n'} \frac{k_{n'}}{jk} \frac{\tan(k_n h)}{\cos \phi_m} \langle g_{n'}, f_m \rangle + 2A_i \delta_m^o \right) \langle f_m, g_n \rangle = \sum_{n'=0}^{\infty} C_{n'} \delta_n^{n'} , \qquad (B.39)$$

then the result is rearranged to yield an infinite set of linear simultaneous equations for the coefficients of the groove modes $C_{n'}$:

$$\sum_{n=0}^{\infty} C_{n'} \tan(k_n h) \left(\frac{k_{n'}}{jk} \sum_{m=-\infty}^{\infty} \frac{\langle g_{n'}, f_m \rangle \langle f_m, g_n \rangle}{\cos \phi_m} - \delta_{n'}^n \cot(k_{n'} h) \right) = -2A_i \langle f_o, g_n \rangle . \qquad (B.40)$$

It is convenient to express (B.40) as a matrix equation in the form

$$([C'][B'] + [G'])\mathbf{X} = \mathbf{F}' , \qquad (B.41)$$

where the elements of $[C']$, $[B']$, $[G']$, $\mathbf{X}$, and $\mathbf{F}'$ are given by

$$C'_{nm} = \langle f_m, g_n \rangle , \qquad (B.42)$$

$$B'_{mn'} = \frac{k_{n'}}{jk \cos \phi_m} \langle g_{n'}, f_m \rangle , \qquad (B.43)$$

$$G'_{nn'} = -\delta_{n'}^n k_{n'} \cot k_{n'} h , \qquad (B.44)$$

$$X_{n'} = C_{n'} \tan k_{n'} h , \qquad (B.45)$$

$$F'_n = -2A_i \langle f_o, g_n \rangle . \qquad (B.46)$$

On solution, the vector $\mathbf{X}$ contains the groove mode coefficients C_n multiplied by the factor $\tan(k_n h)$. From (B.30), the free space mode coefficients A_m are determined by applying the relation

$$\mathbf{A} = [C'] \mathbf{X} + 2A_i \delta_m^o . \qquad (B.47)$$

From (B.17), the specularly reflected component of the scattered field is given by

$$A_{Ref} = A_o - A_i , \qquad (B.48)$$

so the specular reflection coefficient for a TM-polarized incident wave is given by

$$\Gamma_o^{EE} = -\frac{A_{Ref}}{A_i} , \qquad (B.49)$$

$$= -\frac{A_0}{A_i} + 1 .$$

B.2.2   TE Polarization

Free Space Region

If a TE-polarized plane wave is incident on a grating of infinite extent such that the plane of incidence perpendicular to the direction of the grooves, the tangential components of the electric and magnetic fields in the free space region are given by

$$E_z(x,y) = \mathcal{B}_i e^{jk\cos\phi_i x} f_o + \sum_{m=-\infty}^{\infty} \mathcal{B}_m e^{-jk\cos\phi_m x} f_m \, , \tag{B.50}$$

$$H_y(x,y) = \frac{\mathcal{B}_i \cos\phi_i}{\eta_o} e^{jk\cos\phi_i x} f_o - \sum_{m=-\infty}^{\infty} \frac{\mathcal{B}_m \cos\phi_m}{\eta_o} e^{-jk\cos\phi_m x} f_m \, , \tag{B.51}$$

where f_m, k, η_o, $\sin\phi_m$, and $\cos\phi_m$ are defined in (B.3) through (B.7) and

$$H_y(x,y) = -\frac{j}{k\eta_o} \frac{\partial E_z(x,y)}{\partial y} \, . \tag{B.52}$$

Groove Region

The tangential components of the TE-polarized fields in the groove region are given by

$$E_z(x,y) = \sum_{n=1}^{\infty} \mathcal{D}_n \frac{\sin(k_n(x+h))}{\sin k_n h} g_n' \, , \tag{B.53}$$

$$H_y(x,y) = \sum_{n=1}^{\infty} -j\mathcal{D}_n \frac{k_n}{k\eta_o} \frac{\cos(k_n(x+h))}{\sin k_n h} g_n' \, , \tag{B.54}$$

where k_n is given by (B.11) and g_n' is the orthonormal basis function for TE-polarized modes in the groove region and is given by

$$g_n' = \sqrt{\frac{2}{a}} \sin\left(\frac{n\pi(y+a/2)}{a}\right) \, . \tag{B.55}$$

Boundary Conditions

The y-z plane is the interface between the free space and groove regions. The boundary conditions for the tangential components of the TE-polarized field are given by

$$\begin{aligned} H_y(0^+,y) &= H_y(0^-,y) \, , & |y| &\leq a/2 \, , \\ H_y(0^+,y) &= K_z(0,y) \, , & a/2 &\leq |y| \leq d/2 \, , \end{aligned} \tag{B.56}$$

where K represents the surface current density along the top surface of the corrugation and

$$
\begin{aligned}
E_z(0^+, y) &= E_z(0^-, y), & |y| \leq a/2, \\
E_z(0^+, y) &= 0, & a/2 \leq |y| \leq d/2.
\end{aligned}
\tag{B.57}
$$

Mode Matching

The modal expansions of the tangential electric field, (B.50) and (B.53), and the tangential electric field, (B.51) and (B.54), are evaluated at $x = 0$ then substituted into the boundary conditions (B.56) and (B.57). Continuity of the magnetic field across the boundary gives

$$
2\mathcal{B}_i \cos\phi_i \, f_o - \sum_{m=-\infty}^{\infty} \mathcal{B}_m \cos\phi_m \, f_m = \sum_{n=1}^{\infty} D_n \frac{k_n}{jk} \cot(k_n h) \, g_n, \qquad |x| < a/2, \tag{B.58}
$$

while continuity of the electric field gives

$$
\sum_{m=-\infty}^{\infty} \mathcal{B}_m f_m = \sum_{n=1}^{\infty} D_n g_n, \qquad\qquad |x| < a/2, \tag{B.59}
$$

$$
= 0, \qquad\qquad a/d < |x| < d/2.
$$

These expressions have been simplified by combining the contribution of the incident and specularly reflected components of the fields in the free space region into a single term and redefining $\mathcal{B}_o$ as

$$
\mathcal{B}_o = \mathcal{B}_i + \mathcal{B}_{Ref}, \tag{B.60}
$$

where $\mathcal{B}_i$ is the complex amplitude of the incident field and $\mathcal{B}_{Ref}$ is the complex amplitude of the specularly reflected component of the scattered field.

Inner Products

The inner products of the TE mode basis functions are defined in a similar way to those for the TM modes with $\langle f_m, g_n' \rangle$ and $\langle g_n', f_m \rangle$ given by

$$
\langle f_m, g_n' \rangle = \begin{cases}
-\sqrt{\dfrac{2}{ad}} \dfrac{2n\pi/a}{(k\sin\phi_m)^2 - (n\pi/a)^2} \cos\left(\dfrac{ka\sin\phi_m}{2}\right), & n = 1, 3, 5, \ldots \\[4mm]
-j\sqrt{\dfrac{2}{ad}} \dfrac{2n\pi/a}{(k\sin\phi_m)^2 - (n\pi/a)^2} \sin\left(\dfrac{ka\sin\phi_m}{2}\right), & n = 2, 4, 6, \ldots
\end{cases}
\tag{B.61}
$$

and

$$
\langle g'_n, f_m \rangle = \begin{cases} \langle f_m, g'_n \rangle \ , & n = 1, 3, 5, \ldots \\ \\ -\langle f_m, g'_n \rangle \ , & n = 2, 4, 6, \ldots \end{cases} \qquad (B.62)
$$

Substitution and Solution

The inner product of (B.59) with g_n yields an expression for the free space mode coefficients $\mathcal{B}_m$,

$$
\sum_{n=1}^{\infty} \mathcal{D}_n \langle g'_n, f_m \rangle = \mathcal{B}_m \ , \qquad (B.63)
$$

while the inner product of (B.58) with f_m yields

$$
\mathcal{D}_n k_n \cot(k_n h) = 2\mathcal{B}_i \, jk \cos \phi_i \, \langle f_o, g'_n \rangle - \sum_{m=-\infty}^{\infty} \mathcal{B}_m jk \cos \phi_m \, \langle f_m, g'_n \rangle \ . \qquad (B.64)
$$

The result can be rearranged to yield an expression for the groove mode coefficients $\mathcal{D}_n$,

$$
\mathcal{D}_n = 2\mathcal{B}_i \frac{jk}{k_n} \frac{\cos \phi_i}{\cot(k_n h)} \langle f_o, g'_n \rangle - \sum_{m=-\infty}^{\infty} \mathcal{B}_m \frac{jk}{k_n} \frac{\cos \phi_m}{\cot(k_n h)} \langle f_m, g'_n \rangle \ . \qquad (B.65)
$$

A direct solution for the coefficients of the free space modes can be obtained by substituting (B.65) into (B.63) to yield

$$
-\mathcal{B}_m = \sum_{n=1}^{\infty} \left(\sum_{m'=-\infty}^{\infty} \mathcal{B}_{m'} \frac{jk}{k_n} \frac{\cos \phi_{m'}}{\cot(k_n h)} \langle f_{m'}, g'_n \rangle - 2\mathcal{B}_i \frac{jk}{k_n} \frac{\cos \phi_i}{\cot(k_n h)} \langle f_o, g'_n \rangle \right) \langle g'_n, f_m \rangle \ , \quad (B.66)
$$

then rearranged to give

$$
-\sum_{m'=-\infty}^{\infty} \mathcal{B}_m \delta_{m'}^m = \sum_{m'=-\infty}^{\infty} \sum_{n=1}^{\infty} \mathcal{B}_{m'} \frac{jk}{k_n} \frac{\cos \phi_{m'}}{\cot(k_n h)} \langle f_{m'}, g'_n \rangle \langle g'_n, f_m \rangle - 2\mathcal{B}_i \frac{jk}{k_n} \frac{\cos \phi_i}{\cot(k_n h)} \langle f_o, g'_n \rangle \langle g'_n, f_m \rangle \ .
$$
$$ (B.67) $$

The final result is an infinite set of linear simultaneous equations for the coefficients of the free space modes $\mathcal{B}_{m'}$:

$$
\sum_{m'=-\infty}^{\infty} \mathcal{B}_{m'} \sum_{n=1}^{\infty} \frac{jk}{k_n} \frac{\cos \phi_{m'}}{\cot(k_n h)} \langle f_{m'}, g'_n \rangle \langle g'_n, f_m \rangle + \delta_{m'}^m = \sum_{n=1}^{\infty} 2\mathcal{B}_i \frac{jk}{k_n} \frac{\cos \phi_i}{\cot(k_n h)} \langle f_o, g'_n \rangle \langle g'_n, f_m \rangle
$$
$$ (B.68) $$

It is convenient to express (B.68) in the form

$$([B][C] + [G]) \mathbf{X} = [B] \mathbf{F} \,, \tag{B.69}$$

where the elements of $[B]$, $[C]$, $[G]$, $\mathbf{X}$, and $\mathbf{F}$ are given by:

$$B_{mn} = \langle g'_n, f_m \rangle \,, \tag{B.70}$$

$$C_{nm'} = \frac{jk}{k_n} \frac{\cos \phi_{m'}}{\cot(k_n h)} \langle f_{m'}, g'_n \rangle \,, \tag{B.71}$$

$$G_{mm'} = \delta^m_{m'} \,, \tag{B.72}$$

$$X_{m'} = \mathcal{B}_{m'} \,, \tag{B.73}$$

$$F_n = 2B_i \frac{jk}{k_n} \frac{\cos \phi_i}{\cot(k_n h)} \langle f_o, g'_n \rangle \,. \tag{B.74}$$

On solution, the vector $\mathbf{X}$ contains the free space mode coefficients $\mathcal{B}_m$.

As in the case of a TM-polarized incident wave, it may be advantageous to solve for the coefficients of the groove modes then multiply the result by a matrix which relates the coefficients of the groove modes to those of the free space modes if $N \ll M$. First, (B.63) is substituted into (B.64) to yield

$$\mathcal{D}_n k_n \cot(k_n h) = 2\mathcal{B}_i \, jk \cos \phi_i \, \langle f_o, g'_n \rangle - \sum_{m=-\infty}^{\infty} \left(\sum_{n=1}^{\infty} \mathcal{D}_{n'} \langle g'_{n'}, f_m \rangle \right) jk \cos \phi_m \, \langle f_m, g'_n \rangle \tag{B.75}$$

which is rearranged to give

$$\sum_{m=-\infty}^{\infty} \left(\sum_{n'=1}^{\infty} \mathcal{D}_{n'} \langle g_{n'} f_m \rangle \right) jk \cos \phi_m \, \langle f_m, g'_n \rangle + \sum_{n'=1}^{\infty} \delta^{n'}_n \mathcal{D}_{n'} k_{n'} \cot(k'_n h) = 2\mathcal{B}_i \, jk \cos \phi_i \, \langle f_o, g'_n \rangle \,. \tag{B.76}$$

The final result is an infinite set of linear simultaneous equations for the coefficients of the groove modes $\mathcal{D}_{n'}$:

$$\sum_{n'=1}^{\infty} \mathcal{D}_{n'} \sum_{m=-\infty}^{\infty} jk \cos \phi_m \, \langle g_{n'}, f_m \rangle \, \langle f_m, g'_n \rangle + \delta^n_{n'} k_{n'} \cot(k_{n'} h) = 2\mathcal{B}_i \, jk \cos \phi_i \, \langle f_o, g'_n \rangle \,. \tag{B.77}$$

It is convenient to express (B.77) in the form

$$([B'][C'] + [G']) \mathbf{X}' = \mathbf{F}' \,, \tag{B.78}$$

where the elements of $[B']$, $[C']$, $[G']$, $\mathbf{X}'$, and $\mathbf{F}'$ are given by:

$$B'_{nm} = \langle f_m, g'_n \rangle , \tag{B.79}$$

$$C'_{mn} = jk \cos \phi_m \langle g'_n, f_m \rangle , \tag{B.80}$$

$$G'_{nn'} = \delta^n_{n'} k_n \cot(k_n h) , \tag{B.81}$$

$$X'_n = \mathcal{D}_n , \tag{B.82}$$

$$F'_n = 2B_i \, jk \cos \phi_i \langle f_o, g'_n \rangle . \tag{B.83}$$

On solution, the vector $\mathbf{X}$ contains the groove mode coefficients $\mathcal{D}_n$. From (B.63), the free space mode coefficients $\mathcal{B}_m$ are given by

$$\mathcal{B}_m = \frac{1}{jk \cos \phi_m} \cdot [B'] \, \mathbf{X} , \tag{B.84}$$

From (B.60), the complex amplitude of the specularly reflected component of the scattered field is given by

$$\mathcal{B}_{Ref} = \mathcal{B}_o - \mathcal{B}_i , \tag{B.85}$$

so the specular reflection coefficient for a TE-polarized incident wave is given by:

$$\Gamma_o^{HH} = \frac{\mathcal{B}_{Ref}}{\mathcal{B}_i} , \tag{B.86}$$

$$= \frac{\mathcal{B}_o}{\mathcal{B}_i} - 1 .$$

B.3   Verification of Numerical Results

The analysis presented in section B.2 is exact but truncation of the mode-matching matrix and use of a finite word length during computation introduce unavoidable approximations. Furthermore, errors in analysis and coding sometimes occur. It is therefore desirable to implement procedures to assess the correctness and accuracy of the numerical solutions which are obtained. Three numerical checks which are applicable to this problem include conservation of energy, reciprocity, and convergence [5].

Conservation of Energy and Reciprocity

The physical plausibility of numerical results obtained by mode-matching may be verified by testing for conservation of energy and/or reciprocity among the propagating modes but neither is a sufficient condition for a valid solution. Such tests serve mainly to indicate problems introduced by errors in coding or excessive round-off during computation [5], [6]. In the context of scattering by a reflection grating, conservation of energy among the free space modes may be expressed as

$$|A_i|^2 \cos \phi_i = \sum_m |A_m|^2 \cos \phi_m \ , \tag{B.87}$$

where A_i and ϕ_i are the complex amplitude and the direction of the incident wave, A_m and ϕ_m are the complex amplitude and the direction of the mth free space mode, and the summation includes only those free space modes which are propagating. Reciprocity is a statement that the response of a system will be unchanged when the source and the observer are interchanged and can be expressed as

$$\Gamma_m(\phi_i) = \Gamma_m(-\phi_m) \ , \tag{B.88}$$

where $\Gamma_m(\phi)$ is the complex reflection coefficient of the mth diffracted order in response to a wave incident at angle ϕ. In the case of the specularly reflected free space mode, $\phi_m = \phi_i$ and (B.88) reduces to

$$\Gamma_o(\phi_i) = \Gamma_o(-\phi_i) \ . \tag{B.89}$$

Testing for conservation of energy incurs little computational overhead but testing for reciprocity effectively doubles the length of time required to compute a solution and is rarely done so routinely.

Convergence

It is necessary to determine whether a sufficient number of modes have been used to approximate the fields in the free space and groove regions. Although the solution will invariably converge to an essentially constant result as the number of modes used in the field expansion

are systematically and gradually increased, the manner in which the solution converges and the value of the final result will depend on both the number of modes used in each region and their ratio, N/M. The phenomenon, which has been dubbed *relative convergence*, was originally identified in connection with the formulation of the boundary value problem associated with a bifurcated waveguide [7]. It has since been shown to occur in a variety of other problems including diffraction by a strip grating on a dielectric slab [8], [9]. In these cases, Mittra and others have shown that there usually exists a unique choice for the so-called partitioning ratio which will yield the correct solution. Although results obtained using an arbitrary partioning ratio and a large number of modes are usually accurate to within engineering tolerances, use of the optimum ratio provides both greater accuracy and greater computational efficiency [10].

In Figures B.3 through B.6, the phase difference between the TE and TM specular reflection coefficients of selected gratings are plotted as a function of the number of groove modes N used in the solution for fixed values of the corresponding number of free space modes M. In all cases, the gratings have a period of 0.3333λ and are illuminated perpendicular to the direction of the grooves at an angle of 45 degrees to the normal. Figures B.3 and B.4 present the results for a pair of twist polarizers with aspect ratios a/d of 0.5000 and 0.9999, respectively, while Figures B.5 and B.6 present the results for a corresponding pair of circular polarizers. The phase difference converges monotonically until the ratio of groove modes to free space modes reaches a value equal to the aspect ratio of the grating. At that point, the slope of the curve increases abruptly and the phase difference begins to converge to a new value which depends on the number of free space modes. In the limit as the number of free space modes becomes very large, the difference between the final result and the result obtained at the point of inflection vanishes which suggests that the result obtained at the point of inflection corresponds to the correct solution. This is similar to behaviour reported in connection with other formulations in which relative convergence has been observed and implies that the optimum number of groove modes is given by truncating the product of the aspect ratio of the grating and the number of free space modes to be used in the solution, i.e., $N_{\text{opt}} = \text{Trunc}(a/d \cdot M)$.
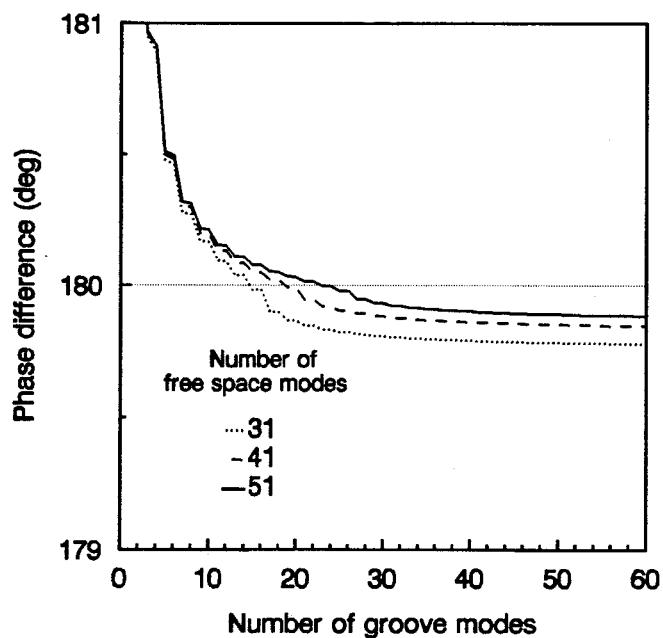
Figure B.2: Convergence of the phase difference between the TE and TM specular reflection coefficients with the number of groove modes for a reflection twist polarizer with $d = 0.3333\lambda$, $a/d = 0.5000$, and $h = 0.2302\lambda$ illuminated by a plane wave incident at $\phi = 45$ degrees.
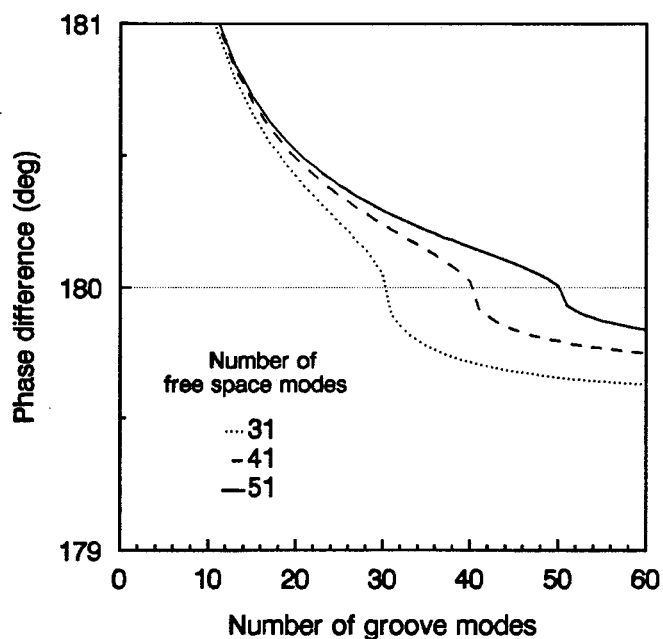
Figure B.3: Convergence of the phase difference between the TE and TM specular reflection coefficients with the number of groove modes for a reflection twist polarizer with $d = 0.3333\lambda$, $a/d = 0.9999$, and $h = 0.3172\lambda$ illuminated by a plane wave incident at $\phi = 45$ degrees.
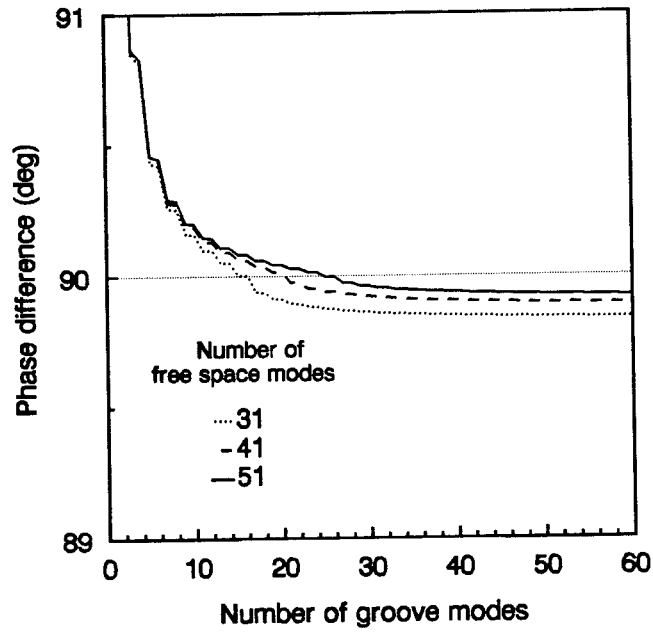
Figure B.4: Convergence of the phase difference between the TE and TM specular reflection coefficients with the number of groove modes for a reflection circular polarizer with $d = 0.3333\lambda$, $a/d = 0.5000$, and $h = 0.1466\lambda$ illuminated by a plane wave incident at $\phi = 45$ degrees.
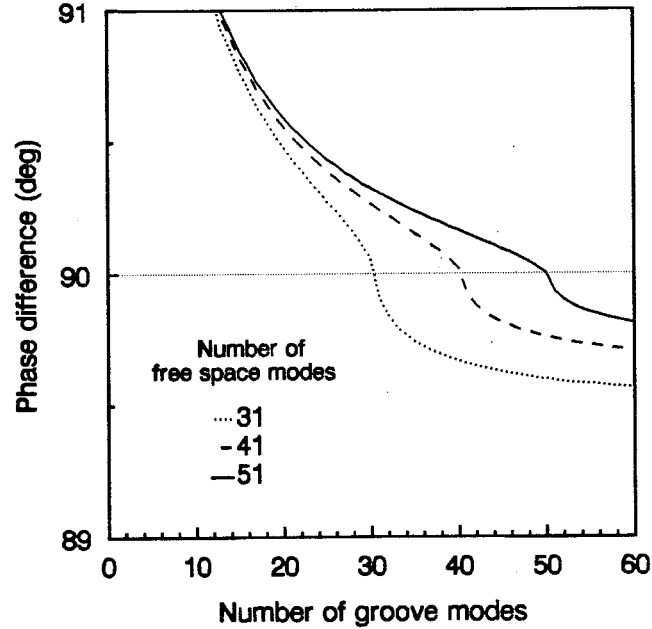
Figure B.5: Convergence of the phase difference between the TE and TM specular reflection coefficients with the number of groove modes for a reflection circular polarizer with $d = 0.3333\lambda$, $a/d = 0.9999$, and $h = 0.1641\lambda$ illuminated by plane wave incident at $\phi = 45$ degrees.

B.4 Implementation

Subroutines TMREFL and TEREFL implement the analytical solutions given by (B.41) and (B.78) and are presented in Listings B.1 and B.2. Given the period d, groove width a, and groove depth h of the grating (in metres), the angle of incidence ϕ (in degrees) and wavelength λ (in metres) of the incident wave, and the number of free space and groove modes M and N to be used in the solution, they return the complex specular reflection coefficient Γ_o for TM- and TE-polarized incident waves, respectively, and an error code to the calling program. Error code 1 indicates that the solution violates conservation of energy among the free space modes while error code 2 indicates that the mode-matching matrix passed to subroutine CDSOLN is singular. Error code 0 indicates that the solution has passed both these tests. If tests for either reciprocity or convergence are required, they must be performed by the calling program.

Because the solution makes extensive use of complex variables, the subroutines were coded in Fortran 77. Although the use of language extensions was generally avoided in order to keep the source code portable between different compilers and platforms, two extensions which are supported by virtually all modern Fortran 77 compilers were allowed. First, double precision complex variables (type COMPLEX*16) and the corresponding intrinsic functions were used so that all floating point calculations could be performed using double precision. Second, variables of type DOUBLE PRECISION were identified as REAL*8 in type declaration statements for clarity. Otherwise, the code is fully compliant with the ANSI standard and adheres to the generally accepted principles of programming style [11]–[13].

A chart depicting the hierarchy of subprograms which are called by subroutines TMREFL and TEREFL is presented in Figure B.6. Functions TMINNR and TEINNR are presented in Listings B.3 and B.4. Given the indices of the free space and groove modes m and n, the propagation constant k, the grating period d, the groove width a, and a character variable O which specifies the desired sequence of factors, they return the value of the inner products $\langle f, g \rangle$ and $\langle g, f \rangle$ as given by (B.26/27) and (B.61/62), respectively. Functions KN, ODD, SEQ, E, and CDCOT are presented in Listings B.5 through B.9. Complex function KN returns the propagation constant

of the *n*th groove mode as given by (B.11). Logical function ODD returns true if its argument is an odd integer. In conjunction with ODD and IF... THEN constructs in functions TMINNR and TEINNR, real function SEQ is used to select the appropriate sign for the inner products as specified by (B.27) and (B.55). Complex function CDCOT implements the complex cotangent function. The remaining subprograms called by subroutines TMREFL and TEREFL were supplied by University Computing Services and perform operations not directly supported by Fortran 77 such as addition and subtraction of matrices, multiplication of matrices with vectors, and solution of systems of linear equations. They are presented in Listing B.10 and are documented in the publication *UBC Matrix* [14].

```
              TMREFL                              TEREFL
      ┌─────────┴─────────┐            ┌─────────┴─────────┐
   TMINNR               KN          TEINNR                KN
      │                CDCOT           │                 CDCOT
    ODD               CDADD          ODD                 CDADD
    SEQ               CDMATV         SEQ                 CDMATV
     E                CDMULT                             CDMULT
                      CDSET                              CDSET
                      CDSOLN                             CDSOLN
```
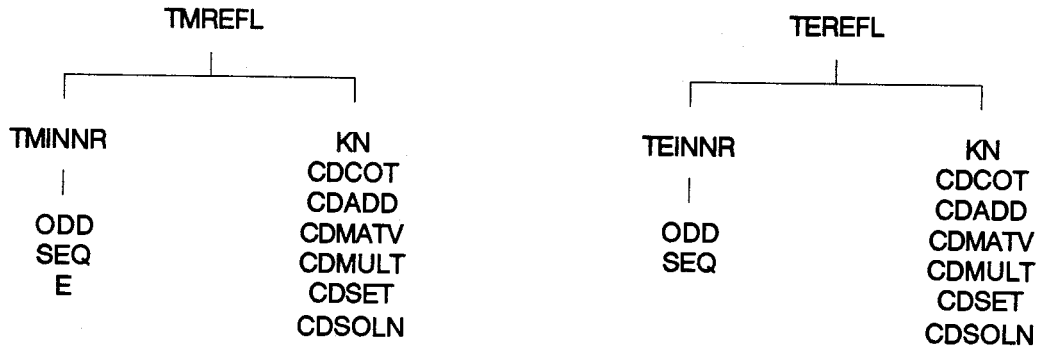
Figure B.6: Hierarchy of subprograms called by subroutines TMREFL and TEREFL.

The subroutines were compiled on a Sun 4/380 workstation (equipped with 32 Megabytes of RAM) under SunOS 4.1.1 (a variant of 4.2 BSD UNIX) using the standard Sun Fortran compiler, f77, with all options set to their default values. The UNIX operating system provides a variety of timing and profiling tools which can be used to assist in the evaluation and optimization of Fortran programs [15]. The total length of time required to execute the two subroutines, including both system and user time, was determined by running the shell utility time in conjunction with a test program which simply set the parameters to be passed, called subroutines TMREFL and TEREFL in succession, then terminated. The results are presented in Figures B.7 and B.8 as a function of the number of free space and groove modes used in the solution.
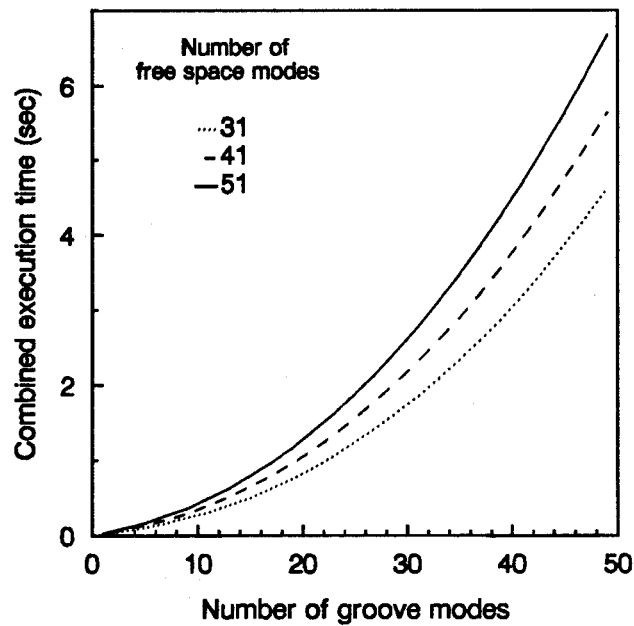
Figure B.7: Combined execution time of subroutines TMREFL and TEREFL on a Sun 4/380 workstation vs. the number of groove modes used in the solution.
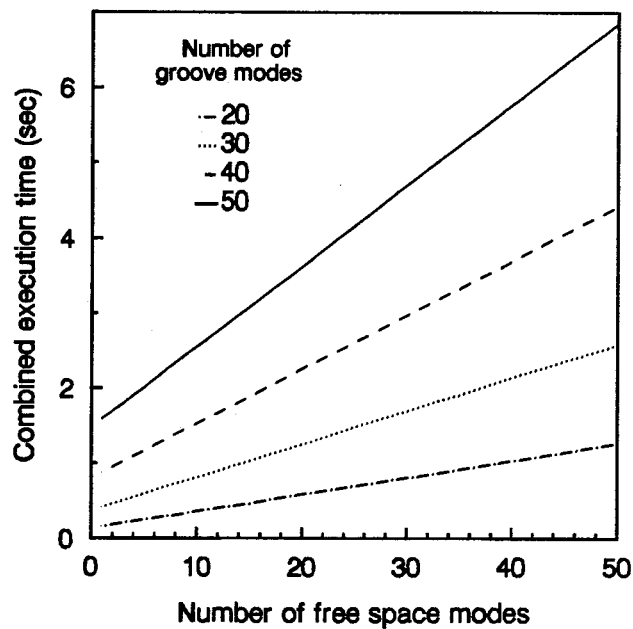
Figure B.8: Combined execution time of subroutines TMREFL and TEREFL on a Sun 4/380 workstation vs. the number of free space modes used in the solution.

A call graph analysis of the code was conducted using the profiling utility **gprof**. The results are presented in Figure B.9 for numerical solutions using (a) 25 groove modes and 51 free space modes and (b) 50 groove modes and 51 free space modes. In each case, calls to subroutine **CDMULT** (which calculates the product of matrices $[B]$ and $[C]$ from (B.41) and $[B']$ and $[C']$ from (B.78)) account for approximately two-thirds of the total execution time. The loading increases quadratically with the number of groove modes and linearly with the number of free space modes. In contrast, calls to subroutine **CDSOLN** (which solves for the amplitude of the groove modes) account for only one-fifth of the total execution time where the loading also increases quadratically with the number of groove modes but is independent of the number of free space modes. The remainder of the execution time is spent calculating the elements of the various vectors and matrices in (B.41) and (B.78). Since the elements of matrices $[B]$ and $[C]$ (and $[B']$ and $[C']$) are independent on the groove depth h, these results suggest that execution time could be reduced considerably by not recalculating their product if h is the only parameter which has changed since the previous call. Such a modification could be implemented by inserting a **SAVE** statement into each subroutine in order to preserve the values of the local variables between calls and applying an appropriate branch on entry.

(a)   (b)
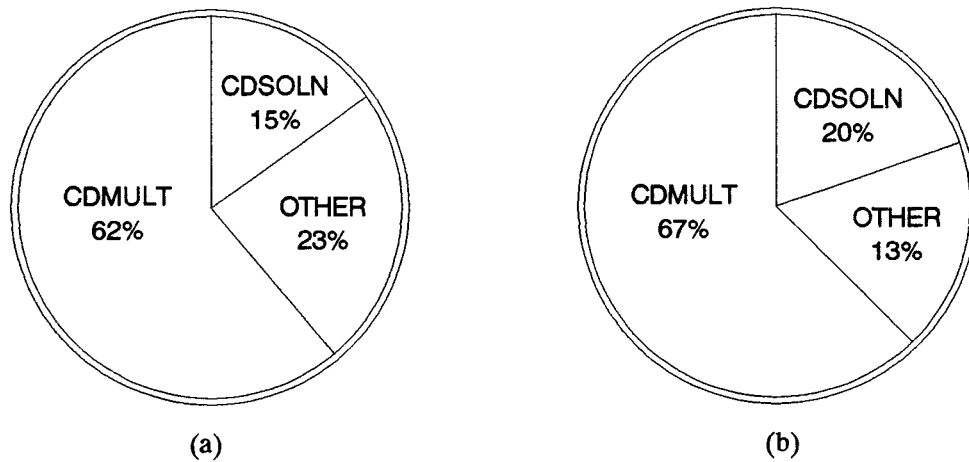
Figure B.9: Execution profile of subroutines **TMREFL** and **TEREFL** for numerical solutions using (a) 25 groove modes and 51 free space modes and (b) 50 groove modes and 51 free space modes.

Listing B.1: SUBROUTINE TMREFL(D, A, H, PHI, L, MFS, NWG, REFL, ERR)

```
       SUBROUTINE TMREFL( D, A, H, PHI, L, MFS, NWG, REFL, ERR)

*------ Given:
*    D    - grating period     (metres)
*    A    - groove width        (metres)
*    H    - grating depth        (metres)
*    PHI  - angle of incidence  (degrees)
*    L    - wavelength           (metres)
*    MFS  - number of free space modes
*    NWG  - number of groove modes

*------ Result:
*    REFL - complex reflection coefficient of zeroth free space mode
*    ERR  - error return 0 = no errors,
*                        1 = energy in free space modes not conserved,
*                        2 = matrix to be inverted is singular.
*---------------------------------------------------------------------
*    All floating point calculations are done in double precision

       PARAMETER (MAXFS=51, MAXWG=51)

*    MAXFS, MAXWG - maximum array dimensions
*                   (see also SUBROUTINE TMINNR)


       EXTERNAL CDCOT

       INTEGER MFS, NWG, ERR, I, J, M, N, ZERO
       REAL*8  D, A, H, PHI, L, K, PHRAD, PI, S, SINPH, SUM
       COMPLEX*16 REFL, B, C, E, F, G, R
       COMPLEX*16 CDCOT, CDET, COSPH, KN, TMINNR
       DIMENSION R(MAXFS)
       DIMENSION COSPH(-MAXFS/2:MAXFS/2), SINPH(-MAXFS/2:MAXFS/2)
       DIMENSION B(MAXFS,MAXWG), C(MAXWG,MAXFS)
       DIMENSION G(MAXWG,MAXWG), E(MAXWG,MAXWG)
       DIMENSION F(MAXWG)

       COMMON PI, SINPH

       ZERO = (MFS+1)/2

       PI = 4D0*DATAN(1D0)

*---------------------------------------------------------------------
* convert angle to radians
       PHRAD = PHI * PI/180D0

* calculate free space propagation constant
       K = 2D0*PI/L

* tabulate values of sin[phi(m)] and cos[phi(m)] for later use

       DO 50, M = -MFS/2, MFS/2
                    S = DSIN(PHRAD) + DBLE(M)*L/D
              SINPH(M) = S
          IF ((S*S).LE.1D0) THEN
              COSPH(M) = DCMPLX(DSQRT(1D0-S*S), 0D0)
          ELSE
              COSPH(M) = DCMPLX(0D0, -DSQRT(S*S-1D0))
          ENDIF
50     CONTINUE
```

Listing B.1: (continued)

```
* set up the matrices
* ------------------------------- matrix B -----
      DO 100, I = 1, MFS
        DO 100, J = 1, NWG
          M = I - ZERO
          N = J - 1
          B(I,J) = TMINNR(M, N, K, D, A, 'gf') *
     $             KN(K,N,A)/(DCMPLX(ODO,K)*COSPH(M))
100   CONTINUE
* ------------------------------- matrix C -----
      DO 200, J = 1, NWG
        DO 200, I = 1, MFS
          N = J - 1
          M = I - ZERO
          C(J,I) = TMINNR(M, N, K, D, A, 'fg')
200   CONTINUE
* -------------------------------------------------
* [C]*[B] -> [E]
      CALL CDMULT(C,B,E,NWG,MFS,NWG,MAXWG,MAXFS,MAXWG)
* ------------------------------- vector F -----
      DO 300, J = 1, NWG
        N = J - 1
        M = 0
        F(J) = -2.0*TMINNR(M, N, K, D, A, 'fg')
300   CONTINUE
* ------------------------------- matrix G -----
400   CALL CDSET(G, NWG, NWG, MAXWG, (ODO,ODO))
      DO 500, J = 1, NWG
        N = J - 1
        G(J,J) = -CDCOT(KN(K,N,A)*H)
500   CONTINUE
*------------------------------------------------------------------
* [E]+[G] -> [E]
      CALL CDADD(E,G,E,NWG,NWG,MAXWG,MAXWG,MAXWG)

* [E]*[X] = [F]; solve for [X]; [X]->[F]
      CALL CDSOLN(E,F,NWG,MAXWG,CDET)

      IF (ABS(CDET).LT.1E-20) THEN
        REFL = (ODO,ODO)
        ERR=2
        RETURN
      ENDIF

* [B]*[F] -> [R]
      CALL CDMATV(B,F,R,MFS,NWG,MAXFS)

      R(ZERO) = R(ZERO) + (1DO,ODO)

* check for conservation of energy in propagating free space modes
* (a necessary but not a sufficient condition for a valid solution)

      SUM = ODO
      ERR = 0

      DO 1000, I = 1, MFS
        M = I - ZERO
        IF (ABS(SINPH(M)).LE.1DO)
     $    SUM = SUM + (CDABS(R(I))**2) * COSPH(M)
1000  CONTINUE

      IF ( ABS(SUM-DCOS(PHRAD)).GT.0.0001DO ) ERR = 1

* calculation complete!

      REFL = R(ZERO)*(-1DO,ODO)

      RETURN
      END
```

Listing B.2: SUBROUTINE TEREFL(D, A, H, PHI, L, MFS, NWG, REFL, ERR)

```
      SUBROUTINE TEREFL( D, A, H, PHI, L, MFS, NWG, REFL, ERR)
*------ Given:
*     D    - grating period     (metres)
*     A    - groove width       (metres)
*     H    - grating depth       (metres)
*     PHI  - angle of incidence (degrees)
*     L    - wavelength          (metres)
*     MFS  - number of free space modes
*     NWG  - number of groove modes
*
*------ Result:
*     REFL - complex reflection coefficient of zeroth free space mode
*     ERR  - error return 0 = no errors,
*                         1 = energy in free space modes not conserved,
*                         2 = matrix to be inverted is singular.
*----------------------------------------------------------------
*     All floating point calculations are done in double precision

      PARAMETER (MAXFS=51, MAXWG=51)

*     MAXFS, MAXWG - maximum array dimensions
*                   (see also SUBROUTINE TEINNR)

      EXTERNAL CDCOT

      INTEGER MFS, NWG, ERR, I, J, M, N, ZERO
      REAL*8 D, A, H, PHI, L, K, PHRAD, PI, S, SINPH, SUM
      COMPLEX*16 REFL, B, C, E, F, G, R
      COMPLEX*16 CDCOT, CDET, COSPH, KN, TEINNR
      DIMENSION R(MAXFS)
      DIMENSION COSPH(-MAXFS/2:MAXFS/2), SINPH(-MAXFS/2:MAXFS/2)
      DIMENSION B(MAXFS,MAXWG), C(MAXWG,MAXFS)
      DIMENSION G(MAXWG,MAXWG), E(MAXWG,MAXWG)
      DIMENSION F(MAXWG)

      COMMON PI, SINPH

      ZERO = (MFS+1)/2

      PI = 4D0*DATAN(1D0)
*----------------------------------------------------------------
* convert angle to radians
      PHRAD = PHI * PI/180D0

* calculate free space propagation constant
      K = 2D0*PI/L

* tabulate values of sin[phi(m)] and cos[phi(m)] for later use

      DO 50, M = -MFS/2, MFS/2
               S = DSIN(PHRAD) + DBLE(M)*L/D
            SINPH(M) = S
         IF ((S*S).LE.1D0) THEN
            COSPH(M) = DCMPLX(DSQRT(1D0-S*S), 0D0)
         ELSE
            COSPH(M) = DCMPLX(0D0, -DSQRT(S*S-1D0))
         ENDIF
50    CONTINUE
*----------------------------------------------------------------
```

Listing B.2: (Continued)

```
* set up the matrices
* ---------------------------- matrix B -----
      DO 100, I = 1, MFS
        DO 100, J = 1, NWG
          M = I - ZERO
          N = J
          B(I,J) = TEINNR(M, N, K, D, A, 'gf') *
     $              DCMPLX(ODO,K)*COSPH(M)
100   CONTINUE
* ---------------------------- matrix C -----
      DO 200, J = 1, NWG
        DO 200, I = 1, MFS
          N = J
          M = I - ZERO
          C(J,I) = TEINNR(M, N, K, D, A, 'fg')
200   CONTINUE
* ------------------------------------------------
* [C]*[B] -> [E]
      CALL CDMULT(C,B,E,NWG,MFS,NWG,MAXWG,MAXFS,MAXWG)
* ---------------------------- vector F -----
      DO 300, J = 1, NWG
        N = J
        M = 0
        F(J) =  2.0*TEINNR(M, N, K, D, A, 'fg') *
     $            DCMPLX(ODO,K)* DCMPLX(DCOS(PHRAD))
300   CONTINUE
* ---------------------------- matrix G -----
400   CALL CDSET(G, NWG, NWG, MAXWG, (ODO,ODO))
      DO 500, J = 1, NWG
        N = J
        G(J,J) =  KN(K,N,A)*CDCOT(KN(K,N,A)*H)
500   CONTINUE

* [E]+[G] -> [E]
      CALL CDADD(E,G,E,NWG,NWG,MAXWG,MAXWG,MAXWG)

* [E]*[X] = [F]; solve for [X]; [X]->[F]
      CALL CDSOLN(E,F,NWG,MAXWG,CDET)

      IF (ABS(CDET).LT.1E-20) THEN
        REFL = (ODO,ODO)
        ERR=2
        RETURN
      ENDIF

* [B]*[F] -> [R]
      CALL CDMATV(B,F,R,MFS,NWG,MAXFS)

      R(ZERO) = R(ZERO)-DCMPLX(ODO,K) * DCMPLX(DCOS(PHRAD))

* check for conservation of energy in propagating free space modes

      SUM = ODO
      ERR = 0

      DO 1000, I = 1, MFS
        M = I - ZERO
        IF (ABS(SINPH(M)).LE.1DO)
     $     SUM = SUM + ( CDABS( R(I)/( DCMPLX(ODO,K) *
     $            COSPH(M) ) ) )**2 * COSPH(M)
1000  CONTINUE

      IF ( ABS(SUM-DCOS(PHRAD)).GT.0.0001DO ) ERR = 1

* calculation complete!

      REFL = R(ZERO)/(DCMPLX(ODO,K)*DCMPLX(DCOS(PHRAD)))

      RETURN
      END
```

Listing B.3: COMPLEX*16 FUNCTION TMINNR(M, N, K, D, A, O)

```
COMPLEX*16 FUNCTION TMINNR(M, N, K, D, A, O)

PARAMETER (MAXFS=51)

LOGICAL ODD
INTEGER M, N
REAL*8 K, D, A, DEN, E, NUM, PI, SEQ, SINPH
CHARACTER*2 O

DIMENSION SINPH(-MAXFS/2:MAXFS/2)

COMMON PI, SINPH

  DEN = K*SINPH(M)*K*SINPH(M) - (DBLE(N)*PI/A)*(DBLE(N)*PI/A)

IF (ODD(N)) THEN

  NUM = DCOS(A*K*SINPH(M)/2D0)*2D0*K*SINPH(M)
  TMINNR = DCMPLX(SEQ(O))*DCMPLX(0D0,-NUM/(DEN*DSQRT(A*D)))

ELSE

  NUM = SIN(A*K*SINPH(M)/2D0)*2D0*K*SINPH(M)
  TMINNR = DCMPLX(DSQRT(E(N)/(A*D)) * NUM/DEN,0D0)

ENDIF

RETURN
END
```

Listing B.4: COMPLEX*16 FUNCTION TEINNR(M, N, K, D, A, O)

```
COMPLEX*16 FUNCTION TEINNR(M, N, K, D, A, O)

PARAMETER (MAXFS=51)

LOGICAL ODD
INTEGER M, N
REAL*8 K, D, A, DEN, NUM, PI, SEQ, SINPH
CHARACTER*2 O

DIMENSION SINPH(-MAXFS/2:MAXFS/2)

COMMON PI, SINPH

  DEN = K*SINPH(M)*K*SINPH(M) - (DBLE(N)*PI/A)*(DBLE(N)*PI/A)

IF (ODD(N)) THEN

  NUM = DCOS(A*K*SINPH(M)/2D0)*2D0*DBLE(N)*PI/A
  TEINNR = DCMPLX(-(NUM/DEN)*DSQRT(2D0/(A*D)),0D0)

ELSE

  NUM = SIN(A*K*SINPH(M)/2D0)*2D0*DBLE(N)*PI/A
  TEINNR = DCMPLX(SEQ(O))*
$          DCMPLX(0D0,-(NUM/DEN)*DSQRT(2D0/(A*D)))

ENDIF

RETURN
END
```

Listing B.5: COMPLEX*16 FUNCTION KN(M, N, K, D, A, O)

```
COMPLEX*16 FUNCTION KN(K,N,A)

REAL*8 K, A, PI, Q
INTEGER N

PI = 4D0*DATAN(1D0)
Q = DBLE(N)*PI/A
IF (ABS(Q).LE.K) THEN
   KN = DCMPLX(DSQRT(K*K-Q*Q), 0D0)
ELSE
   KN = DCMPLX(0D0, -DSQRT(Q*Q-K*K))
ENDIF

RETURN
END
```

Listing B.6: LOGICAL FUNCTION ODD(N)

```
LOGICAL FUNCTION ODD(N)

* true if N is odd, false if N is even

   INTEGER N

   IF (MOD(N,2).EQ.0) THEN
      ODD = .FALSE.
   ELSE
      ODD = .TRUE.
   ENDIF

   RETURN
   END
```

Listing B.7: REAL*8 FUNCTION SEQ(O)

```
REAL*8 FUNCTION SEQ(O)

* if n is odd,  <fm,gn> =  <gn,fm> : the order is unimportant
* if n is even, <fm,gn> = -<gn,fm> : the order must be accounted for!

   CHARACTER*2 O

   IF (O.EQ.'fg') THEN
      SEQ =  1D0
   ELSE
      SEQ = -1D0
   ENDIF
   RETURN
   END
```

Listing B.8: REAL*8 FUNCTION E(N)

```
REAL*8 FUNCTION E(N)

* calculates the Neumann number

   INTEGER N
   IF (N.EQ.0) THEN
      E = 1D0
   ELSE
      E = 2D0
   ENDIF

   RETURN
   END
```

Listing B.9: COMPLEX*16 FUNCTION CDCOT(ARG)

```
COMPLEX*16 FUNCTION CDCOT(ARG)

* find the cotangent of a complex number

      COMPLEX*16 CDSIN, CDCOS, ARG
      REAL*8 DIMAG

          IF (DIMAG(ARG).GT.100D0) THEN
              CDCOT = (0D0,-1D0)
      ELSE IF (DIMAG(ARG).LT.-100D0) THEN
              CDCOT = (0D0,1D0)
      ELSE IF (ABS(CDSIN(ARG)).LT.1E-10) THEN
              CDCOT = (1E10,0.0)
      ELSE
              CDCOT = CDCOS(ARG)/CDSIN(ARG)
      ENDIF

      RETURN
      END
```

Listing B.10: UBC Complex Matrix Subroutines

```
      SUBROUTINE CDADD(A,B,C,M,N,NDIMA,NDIMB,NDIMC)

*     [C] <- [A]+[B]                    Ref: UBC Matrix, p. 15

      COMPLEX*16 A(NDIMA,*),B(NDIMB,*),C(NDIMC,*)
      DO 1 J=1,N
      DO 1 I=1,M
1     C(I,J) = A(I,J) + B(I,J)
      RETURN
      END



      SUBROUTINE CDMATV(A,V,W,M,N,NDIMA)
*
*     w <- [A].v                        Ref: UBC Matrix, p. 17

      COMPLEX*16  A(NDIMA,*),V(*),W(*)
      DO 1 I=1,M
      W(I) = (0.D0,0.D0)
      DO 1 J=1,N
1     W(I) = W(I) + A(I,J) * V(J)
      RETURN
      END



      SUBROUTINE CDMULT(A,B,C,M,N,L,NDIMA,NDIMB,NDIMC)

*     [C] <- [A].[B]                    Ref: UBC Matrix, p. 18

      COMPLEX*16 A(NDIMA,*),B(NDIMB,*),C(NDIMC,*)
      DO 1 J=1,L
      DO 1 I=1,M
      C(I,J) = (0.D0,0.D0)
      DO 1 K=1,N
1     C(I,J) = C(I,J) + A(I,K) * B(K,J)
      RETURN
      END



      SUBROUTINE CDSET(A,M,N,NDIMA,X)

*     [C] <- [A]+[B]                    Ref: UBC Matrix, p. 21

      COMPLEX*16 A(NDIMA,*),X
      DO 1 J=1,N
      DO 1 I=1,M
1     A(I,J) = X
      RETURN
      END



      SUBROUTINE CDSUB(A,B,C,M,N,NDIMA,NDIMB,NDIMC)

*     [C] <- [A]-[B]                    Ref: UBC Matrix, p. 22

      COMPLEX*16  A(NDIMA,*),B(NDIMB,*),C(NDIMC,*)
      DO 1 J=1,N
      DO 1 I=1,M
1     C(I,J) = A(I,J) - B(I,J)
      RETURN
      END



      SUBROUTINE CDVMAT(V,A,W,M,N,NDIMA)
*
*     w <- v.[A]                        Ref: UBC Matrix, p. 24

      COMPLEX*16  A(NDIMA,*),V(*),W(*)
      DO 1 J=1,N
      W(J) = (0.D0,0.D0)
      DO 2 I=1,M
2     W(J) = W(J) + V(I) * A(I,J)
1     CONTINUE
      RETURN
      END
```

Listing B.10: (continued)

```
      SUBROUTINE CDSOLN(A,B,N,MM,DET)
*
*     [A].x = b;  x->b                          Ref: UBC Matrix, p. 55

C This routine finds the solution of a system of equations AX=B, and takes
C paging into consideration; i.e., operations are done by columns.
C A- matrix of coefficints
C B- vector of right hand sides; on exit array B will contain the solution.
C N- order of matrix.
C MM- first dimension of a.
C DET- determinant of matrix is DET*10**JEX

      COMMON /MATEXP/ JEX
      DIMENSION A(MM,N),B(*)
      COMPLEX*16 A,B,DET,T,TB,DCMPLX
      REAL*8 RMAX,QDET,CDABS

      JEX=0
      DET=DCMPLX(1.D0,0.D0)
C decompose a into upper triangular matrix
      DO 6 K=1,N
      M=K
      RMAX=CDABS(A(K,K))
      IF(K.EQ.N) GO TO 14
      KP1=K+1
      DO 1 I=KP1,N
      IF(CDABS(A(I,K)).LE.RMAX) GO TO 1
      M=I
      RMAX=CDABS(A(I,K))
    1 CONTINUE
   14 T=A(M,K)
      IF(RMAX.LT.1.D-20) GO TO 20
      IF(K.EQ.N) GO TO 5
      A(M,K)=A(K,K)
      A(K,K)=T
      TB=B(M)
      B(M)=B(K)
      B(K)=TB
      DO 2 I=KP1,N
      A(I,K)=-A(I,K)/T
    2 B(I)=B(I)+A(I,K)*TB
      DO 4 J=KP1,N
      TB=A(M,J)
      A(M,J)=A(K,J)
      A(K,J)=TB
      IF(CDABS(TB).EQ.0.D0) GO TO 4
      DO 3 I=KP1,N
    3 A(I,J)=A(I,J)+A(I,K)*TB
    4 CONTINUE
C now get determinant
    5 DET=DET*T
      QDET=CDABS(DET)
      IF(QDET.LT.1.D15) GO TO 25
      DET=DET*1.D-15
      JEX=JEX+15
   25 IF(QDET.GT.1.D-15) GO TO 30
      DET=DET*1.D15
      JEX=JEX-15
   30 IF(M.NE.K) DET=-DET
    6 CONTINUE
C now do back substitution
      IF(N.EQ.1) GO TO 9
      NM1=N-1
      DO 8 KB=1,NM1
      KM1=N-KB
      K=KM1+1
      B(K)=B(K)/A(K,K)
      T=-B(K)
      DO 8 I=1,KM1
    8 B(I)=B(I)+A(I,K)*T
    9 B(1)=B(1)/A(1,1)
      RETURN
   20 DET=DCMPLX(0.D0,0.D0)
      JEX=0

      RETURN
      END
```

References

[1] A. Hessel, J. Shmoys, and D. Y. Tseng, "Bragg-angle blazing of diffraction gratings," *J. Opt. Soc. Am.*, vol. 65, pp. 380–384, Apr. 1975.

[2] J. W. Heath, *Scattering by a Conducting Periodic Surface with a Rectangular Groove Profile*, M.A.Sc. Thesis, Univ. of British Columbia, Vancouver, B.C., 1977.

[3] J.J. Van Zyl and F.T. Ulaby, "Scattering matrix representation for simple targets," in *Radar Polarimetry for Geoscience Applications*. F.T. Ulaby and C. Elachi, Eds. Norwood, MA: Artech House, 1990, pp. 17–19.

[4] J. W. Dettman, *Mathematical Methods in Physics and Engineering*. New York: McGraw-Hill, 1969, p. 26.

[5] C. P. Wu, "Methods of Solution," in *Theory and Analysis of Phased Array Antennas*, N. Amitay, V. Galindo, and C. P. Wu, Eds. New York: Wiley, 1972, pp. 75–119.

[6] N. Amitay and V. Galindo, "On energy conservation and the method of moments in scattering problems," *IEEE Trans. Antennas Propagat.*, vol. AP-17, pp. 747–751, Nov. 1969.

[7] R. Mittra, "Relative convergence of the solution of a doubly infinite set of equations," *J. Res. Nat. Bur. Stand.*, vol. 67D, Mar-Apr. 1963, pp. 245–254.

[8] T. Itoh and R. Mittra, "Relative convergence phenomenon arising in the solution of diffraction from strip grating on a dielectric slab," *Proc. IEEE*, vol. 59, pp. 1363–1365, Sept. 1971.

[9] R. Mittra, T. Itoh, and T-S Li, "Analytical and numerical studies of the relative convergence phenomenon arising in the solution of an integral equation," *IEEE Trans. Microwave Theory Tech.*, vol. MTT-20, pp. 96–104, Feb. 1972.

[10] C.P. Wu, "Convergence test and the relative convergence problem," in *Computer Techniques for Electromagnetics*. Oxford: Pergamon, 1973, pp. 300–304.

[11] B.W. Kernighan and P.J. Plauger, *The Elements of Programming Style*. New York: McGraw-Hill, 1974.

[12] M. Metcalf, *Effective Fortran 77*. Oxford: Clarendon Press, 1985.

[13] B. Kruger, *Efficient Fortran Programming*. New York: Wiley, 1990.

[14] T. Nicol, Ed. *UBC Matrix: A Guide to Solving Matrix Problems*. Vancouver, B.C.: Univ. of British Columbia Computing Centre, Mar. 1982.

[15] M. Loukides, *UNIX for Fortran Programmers*. Sebastopol, CA: O'Reilley & Associates, 1990.

Appendix C

CIRCULAR POLARIZATION SELECTIVE REFLECTORS

C.1 Introduction

Because the polarization scattering matrix which corresponds to a circular polarization selective response cannot be diagonalized when expressed with respect to a linearly polarized basis, a trihedral corner reflector cannot be modified to present such a response simply by placing fins or corrugations of appropriate dimensions and orientation along one of its interior surfaces or across its aperture. Alternative methods for obtaining such a response based on the addition of a suitable transmission polarizer to either a linear polarization selective or a twist polarizing trihedral corner reflector are proposed.

C.2 Concept

A circular polarization selective reflector will return an incident wave of the chosen sense back to the source but will either absorb an incident wave of the opposite sense or scatter it in a different direction. With respect to a circularly polarized basis, the normalized polarization scattering matrices of left and right circular polarization selective reflectors are given by

$$[\mathcal{S}_{\mathcal{L}}] = \left[\begin{array}{cc} S_{LL} & S_{LR} \\ S_{RL} & S_{RR} \end{array} \right] = \left[\begin{array}{cc} 1 & 0 \\ 0 & 0 \end{array} \right] \tag{C.1}$$

and

$$[\mathcal{S}_{\mathcal{R}}] = \left[\begin{array}{cc} S_{LL} & S_{LR} \\ S_{RL} & S_{RR} \end{array} \right] = \left[\begin{array}{cc} 0 & 0 \\ 0 & 1 \end{array} \right] . \tag{C.2}$$

The co-polar and cross-polar response of circular polarization selective reflectors are plotted as a function of the polarization state of the incident wave in Figures C.1 and C.2. The

189

parameters ϵ and τ refer to the ellipticity and tilt angles of the corresponding polarization ellipse. Although the amplitudes of the co-polar and cross-polar responses of a circular polarization reflector are invariant under rotation of the target about the line-of-sight, the relative phase of the response varies linearly with the angle of rotation.

In Chapter 4, it is shown that a conventional trihedral corner reflector can be modified to present a given polarization response along its boresight simply by placing conducting fins or corrugations of appropriate dimensions and orientation along one of its three interior surfaces or across its aperture if the corresponding polarization scattering matrix $[S]$ can be transformed through rotation about the line-of-sight into a diagonal matrix $[S']$ of the form

$$[S'] = \begin{bmatrix} S'_{HH} & 0 \\ 0 & S'_{VV} \end{bmatrix} , \tag{C.3}$$

A polarization scattering matrix expressed with respect to a circularly polarized basis $[\mathcal{S}]$ can be transformed to the equivalent polarization scattering matrix expressed with respect to a linearly polarized basis $[S]$ by applying the unitary change of basis transformation

$$[S] = [U^*][\mathcal{S}][U^*]^{-1} , \tag{C.4}$$

where $[U]$ is the transformation matrix for change of basis from linear to circular polarization given by

$$[U] = \frac{1}{\sqrt{2}} \begin{bmatrix} 1 & 1 \\ j & -j \end{bmatrix} . \tag{C.5}$$

Applying (C.4) to the matrices of (C.1) and (C.2) gives the normalized linear polarization scattering matrices of left and right circular polarization selective reflectors,
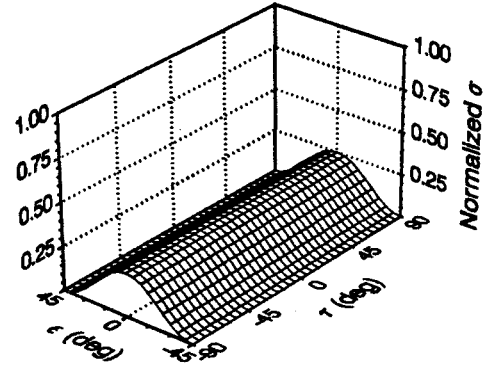
$$[S_{\mathcal{L}}] = \begin{bmatrix} S_{HH} & S_{HV} \\ S_{VH} & S_{VV} \end{bmatrix} = \frac{1}{2} \begin{bmatrix} -1 & j \\ j & 1 \end{bmatrix} \tag{C.6}$$

and

$$[S_{\mathcal{R}}] = \begin{bmatrix} S_{HH} & S_{HV} \\ S_{VH} & S_{VV} \end{bmatrix} = \frac{1}{2} \begin{bmatrix} -1 & -j \\ -j & 1 \end{bmatrix} . \tag{C.7}$$
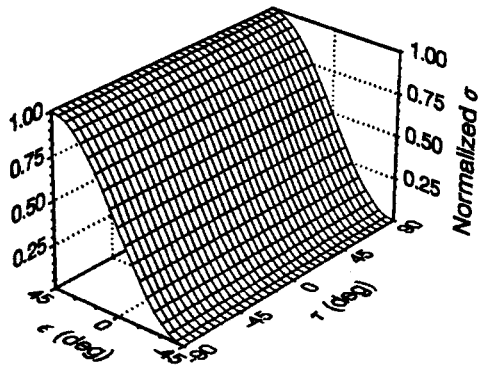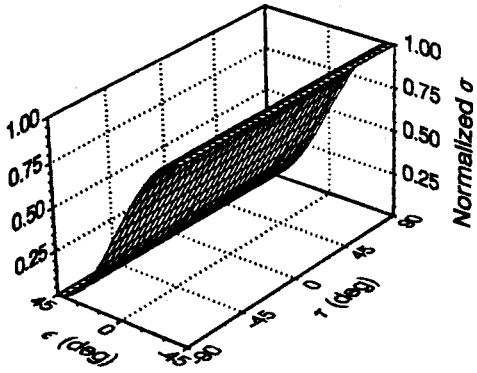
(a)   (b)

Figure C.1: Normalized response of a left circular polarization selective reflector as a function of the polarization state of the incident wave. (a) Co-polar response. (b) Cross-polar response.

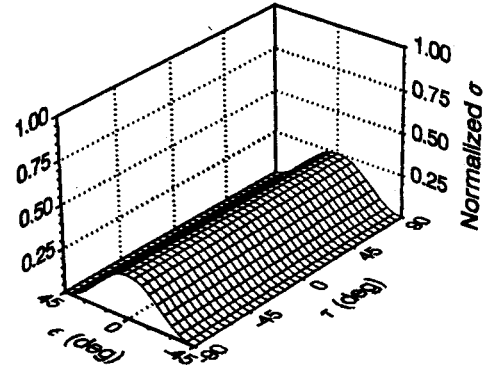(a)   (b)

Figure C.2: Normalized response of a right circular polarization selective reflector as a function of the polarization state of the incident wave. (a) Co-polar response. (b) Cross-polar response.

If a depolarizing reflector with the polarization scattering matrix of (C.6) or (C.7) is rotated about the line-of-sight through an angle α, the off diagonal elements of its new polarization scattering matrix $[S']$ are given by

$$S'_{HV} = 2S_{HV}\cos^2\alpha - S_{HV} + (S_{VV} - S_{HH})\sin\alpha\cos\alpha \,, \tag{C.8}$$

where the off diagonal elements S_{HV} and S_{VH} are identical in all coordinate frames for the monostatic case [1]. Since the diagonal elements of the original matrix are real and the off diagonal elements are imaginary, S'_{HV} is complex. In order to diagonalize $[S']$, the angle of rotation α must be chosen such that both the real and imaginary components of S'_{HV} are set to zero, i.e.,

$$\text{Re}(S'_{HV}) = (S_{VV} - S_{HH})\sin\alpha\cos\alpha = 0 \,, \tag{C.9}$$

$$\text{Im}(S'_{HV}) = 2S_{HV}\cos^2\alpha - S_{HV} = 0 \,. \tag{C.10}$$

Since $S_{HH} \neq S_{VV}$, (C.9) is satisfied only if $\alpha = n\,\pi/2$ where n is an integer. However, these values of α will not satisfy (C.10) unless $S_{HV} = 0$. Therefore, the polarization scattering matrices of (C.6) and (C.7) cannot be diagonalized and it is not possible to realize a trihedral corner reflector with a circular polarization selective response simply by placing conducting fins or corrugations of appropriate dimensions and orientation along one of its interior surfaces or across its aperture.

C.3 Proposed Implementations

Method I

It may be possible to realize a trihedral corner reflector with a circular polarization selective response by incorporating both transmission and reflection polarizers in the modified reflector. One such scheme is shown in Figure C.3. Here a transmission circular polarizer of the type shown in Figure C.4 is placed across the aperture of a linear polarization selective reflector which has been oriented to return horizontally polarized incident waves but reject vertically polarized incident waves. Subject to mechanical constraints, any of the several types of transmission circular polarizers that have been described in the literature (e.g., [2]) would be satisfactory.
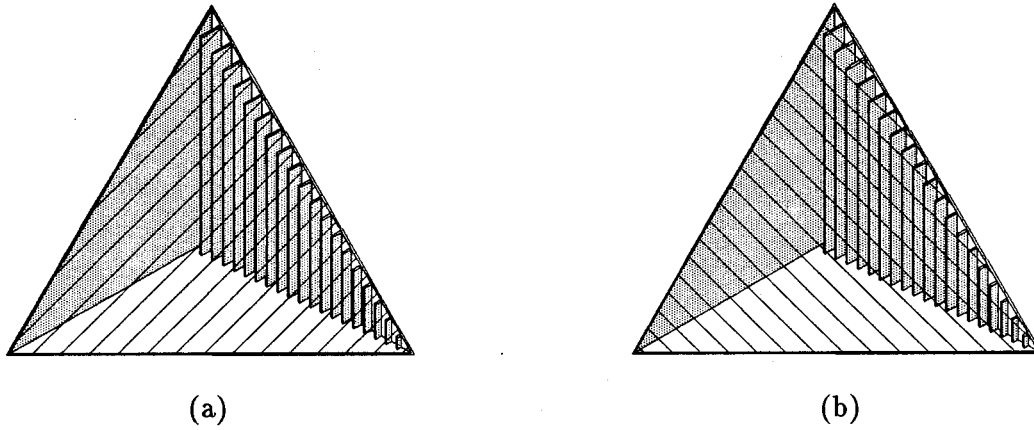
(a)   (b)

Figure C.3: A proposed implementation of a circular polarization selective reflector using a transmission circular polarizer and a linear polarization selective reflector. (a) Left circular polarization selective reflector. (b) Right circular polarization selective reflector.

In Figure C.3(a), the axis of the transmission circular polarizer is oriented at -45 degrees to the vertical. Since left circularly polarized incident waves are converted to horizontal polarization by the transmission polarizer, they are returned by the linear polarization selective reflector then converted back to left circular polarization as they pass through the transmission polarizer a second time. However, right circularly polarized incident waves are converted to vertical polarization by the transmission polarizer and are either scattered away from the source or absorbed by the linear polarization selective reflector. Thus, a left circular polarization selective reflector has been realized. The polarization scattering matrix of the reflector is given by

$$[S_{\mathcal{L}}] = [T][S][T],$$

$$= \frac{1}{2}\begin{bmatrix} 1+j & 1+j \\ 1-j & 1+j \end{bmatrix} \cdot \begin{bmatrix} -1 & 0 \\ 0 & 0 \end{bmatrix} \cdot \frac{1}{2}\begin{bmatrix} 1+j & 1-j \\ 1-j & 1+j \end{bmatrix}, \qquad \text{(C.11)}$$

$$= \frac{j}{2}\begin{bmatrix} -1 & j \\ j & 1 \end{bmatrix},$$

where $[T]$ and $[S]$ are the polarization matrices of the transmission circular polarizer oriented as shown and a vertical polarization selective reflector, respectively, according to the BSA
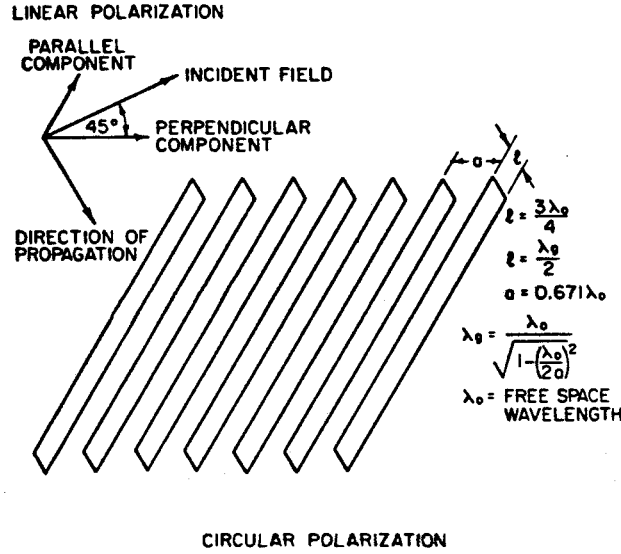
Figure C.4: A parallel plate transmission circular polarizer. (from [2, sec. 23-5])

convention. If the transmission circular polarizer is oriented with its axis at 45 degrees to the vertical instead, as shown in Figure C.4(b), a right circular polarization selective reflector is realized. If the response of the polarizer is now given by $[T']$, the polarization scattering matrix of the reflector will be given by

$$
\begin{aligned}
[S_{\mathcal{R}}] &= [T'][S][T'], \\
&= \frac{1}{2}\begin{bmatrix} 1+j & -1+j \\ -1+j & 1+j \end{bmatrix} \cdot \begin{bmatrix} -1 & 0 \\ 0 & 0 \end{bmatrix} \cdot \frac{1}{2}\begin{bmatrix} 1+j & -1+j \\ -1+j & 1+j \end{bmatrix}, \\
&= \frac{j}{2}\begin{bmatrix} -1 & -j \\ -j & 1 \end{bmatrix}.
\end{aligned}
\tag{C.12}
$$

Method II

A second scheme for implementing a circular polarization selective trihedral corner reflector is shown in Figure C.5. Here a *circular polarization selective surface* (CPSS) [4, 5] is placed across the aperture of a trihedral twist reflector. Over most aspects, incident waves of the chosen sense pass through the CPSS and are returned back to the source by the trihedral twist reflector while incident waves of the opposite sense are specularly reflected away from the source as suggested by Figure C.6(a).
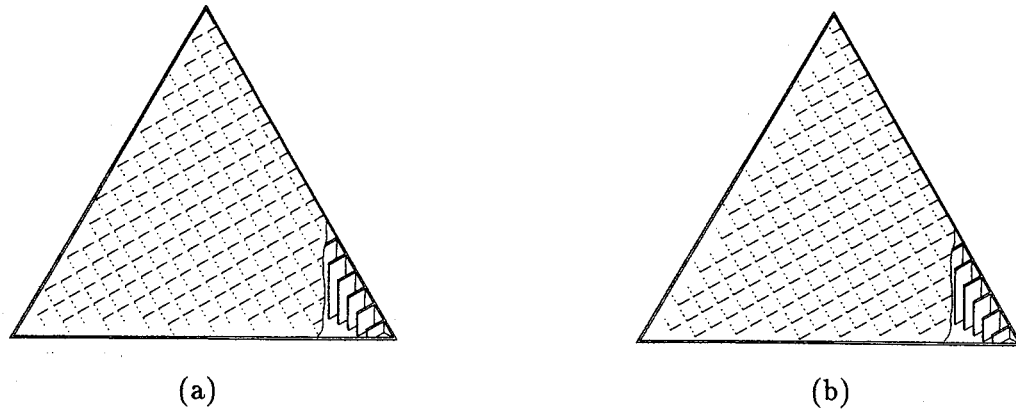
(a) (b)

Figure C.5: A proposed implementation of a circular polarization selective reflector using a circular polarization selective surface and a trihedral twist reflector. (a) Left circular polarization selective reflector. (b) Right circular polarization selective reflector.

If the angle of incidence is normal to the reflector aperture, however, both incident polarizations will be returned to the source and the response will no longer appear to be polarization selective, as shown in Figure C.6(b). For a reflector with corners of equal length, this condition occurs along the boresight or direction of maximum response which is clearly undesirable. This problem also limits the performance of the *gridded trihedral*, a linear polarization selective reflector which is realized by mounting a closely spaced parallel grid of thin wires across the reflector aperture as shown in Figure C.7.
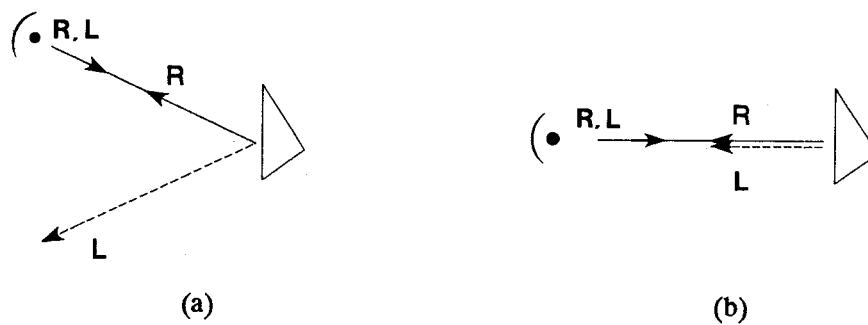

(a) (b)

Figure C.6: Scattering by a right circular polarization selective trihedral corner reflector. (a) Oblique incidence. (b) Normal incidence.
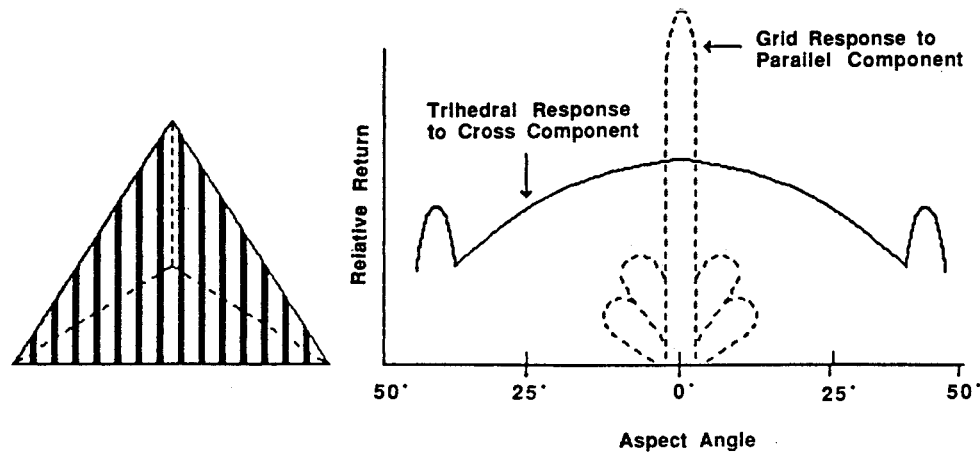
Figure C.7: A linear polarization selective gridded trihedral and its co-polar and cross-polar azimuthal response patterns. (from [3])

Backscatter returns from either the circular polarization selective surface or the closely spaced grid of parallel wires can be avoided by mounting the reflector in such a way that its boresight is pointed away from the radar over most aspects. However, this is undesirable if the corners of the reflector are of equal length because the scattering cross section of the reflector will be substantially reduced compared to its maximum value and will become much more sensitive to small changes in the orientation of the reflector. An alternative solution is to force the boresight and the normal to the aperture to point in different directions by incorporating bilateral symmetry into the reflector geometry. Consider a trihedral corner reflector with one corner of length c and two of length a as shown in Figure C.8. If the ratio of the center and side corner lengths of the reflector (c/a) is increased slightly from unity, the normal to the reflector aperture will rise in elevation relative to the the reflector boresight angle as described in Chapter 3. The elevation beamwidth of the reflector will also increase slightly at the expense of its azimuthal beamwidth. Decreasing the ratio (c/a) instead would have the opposite effect although the angle of separation will be less pronounced. In either case, the angle of separation β between the normal to the aperture and the reflector boresight will increase and the desired result will be achieved as suggested by Figure C.8(b).
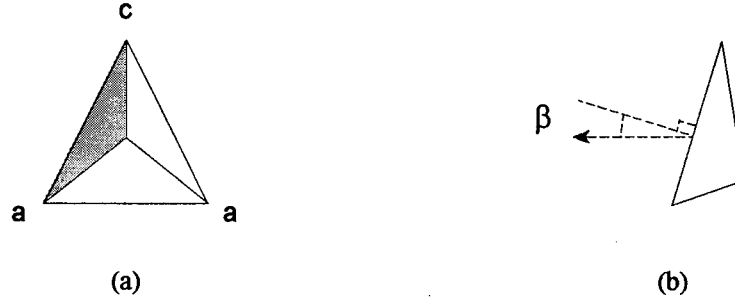
Figure C.8: A bilaterally symmetric trihedral corner reflector with triangular panels. β is the angle between the boresight and the normal to the aperture. (a) Front view. (b) Side view.

The polarization scattering matrix of a hybrid reflector which combines a left CPSS with polarization matrix $[T]$ and a trihedral twist reflector with polarization matrix $[S]$ is given by

$$
\begin{aligned}
[S_{\mathcal{L}}] &= [T][S][T], \\
&= \frac{1}{2}\begin{bmatrix} -1 & j \\ j & 1 \end{bmatrix} \cdot \begin{bmatrix} -1 & 0 \\ 0 & 1 \end{bmatrix} \cdot \frac{1}{2}\begin{bmatrix} -1 & j \\ j & 1 \end{bmatrix}, \\
&= \frac{1}{2}\begin{bmatrix} -1 & j \\ j & 1 \end{bmatrix}.
\end{aligned}
\tag{C.13}
$$

By substituting a right CPSS with polarization transmission matrix $[T']$ for the original, a right circular polarization selective reflector can be realized. Its polarization scattering matrix is given by

$$
\begin{aligned}
[S_{\mathcal{R}}] &= [T'][S][T'], \\
&= \frac{1}{2}\begin{bmatrix} -1 & -j \\ -j & 1 \end{bmatrix} \cdot \begin{bmatrix} -1 & 0 \\ 0 & 1 \end{bmatrix} \cdot \frac{1}{2}\begin{bmatrix} -1 & -j \\ -j & 1 \end{bmatrix}, \\
&= \frac{1}{2}\begin{bmatrix} -1 & -j \\ -j & 1 \end{bmatrix}.
\end{aligned}
\tag{C.14}
$$

A method for realizing a circular polarization selective surface was first described by Tilston *et al.* [4]. An alternative implementation which is easier and less expensive to fabricate than the original was subsequently devised by Morin [5]. The improved surface consists of a slab of low dielectric constant material of thickness $\lambda/4$ which has been divided into a square pattern of cells of dimension $\lambda/2$ by $\lambda/2$. A resonant element which consists of a single piece of wire which has been bent into three sections is inserted into each cell such that the two end sections are flush against the front and back faces of the dielectric slab. Left and right CPSS elements are shown in Figure C.9 where the x-y plane is the plane of the aperture.
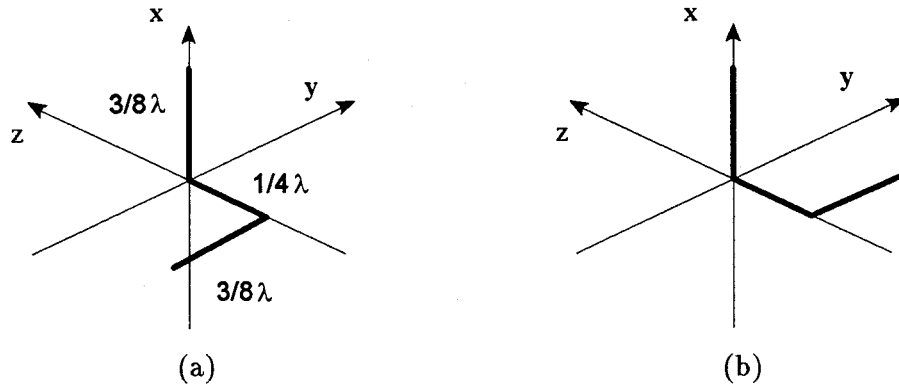
Figure C.9: Elements of a circular polarization selective surface (CPSS). (a) Left CPSS element. (b) Right CPSS element.

C.4 Discussion

Two methods for realizing circular polarization selective trihedral corner reflectors have been proposed in this appendix. The performance of such reflectors and their usefulness in practice will depend on a number of factors which have not been considered here including (1) degradation of the polarization response of either of the polarizers for incidence off the reflector boresight, (2) possible degradation of the polarization response due to multiple reflections between the transmission and reflection polarizers, and (3) the ease with which the modified reflector can be assembled and the mechanical ruggedness of the finished product.

References

[1] S.H. Bickel, "Some invariant properties of the polarization scattering matrix," *Proc. IEEE*, vol. 53, pp. 1070–1072, Aug. 1965.

[2] W.B. Offut and L.K. DeSize, "Methods of Polarization Synthesis," in *Antenna Engineering Handbook*, 2nd ed., R. C. Johnson and H. Jasik, Eds. New York: McGraw-Hill, 1984, chap. 23.

[3] J.A. Scheer, "Radar Reflectivity Calibration Procedures," in *Radar Reflectivity Measurement: Techniques and Applications*, N.C. Currie, Ed. Norwood, MA: Artech House, 1989, p. 109.

[4] W.V. Tilston, T. Tralman, and S.M. Khanna, "A polarization selective surface for circular polarization," in *IEEE/AP-S Symp. Dig.* (Syracuse, NY), June 1988, pp. 762–765.

[5] G.A. Morin, "A simple circular polarization selective surface (CPSS)," in *IEEE/AP-S Symp. Dig.* (Dallas, TX), May 1990, pp. 100–103.
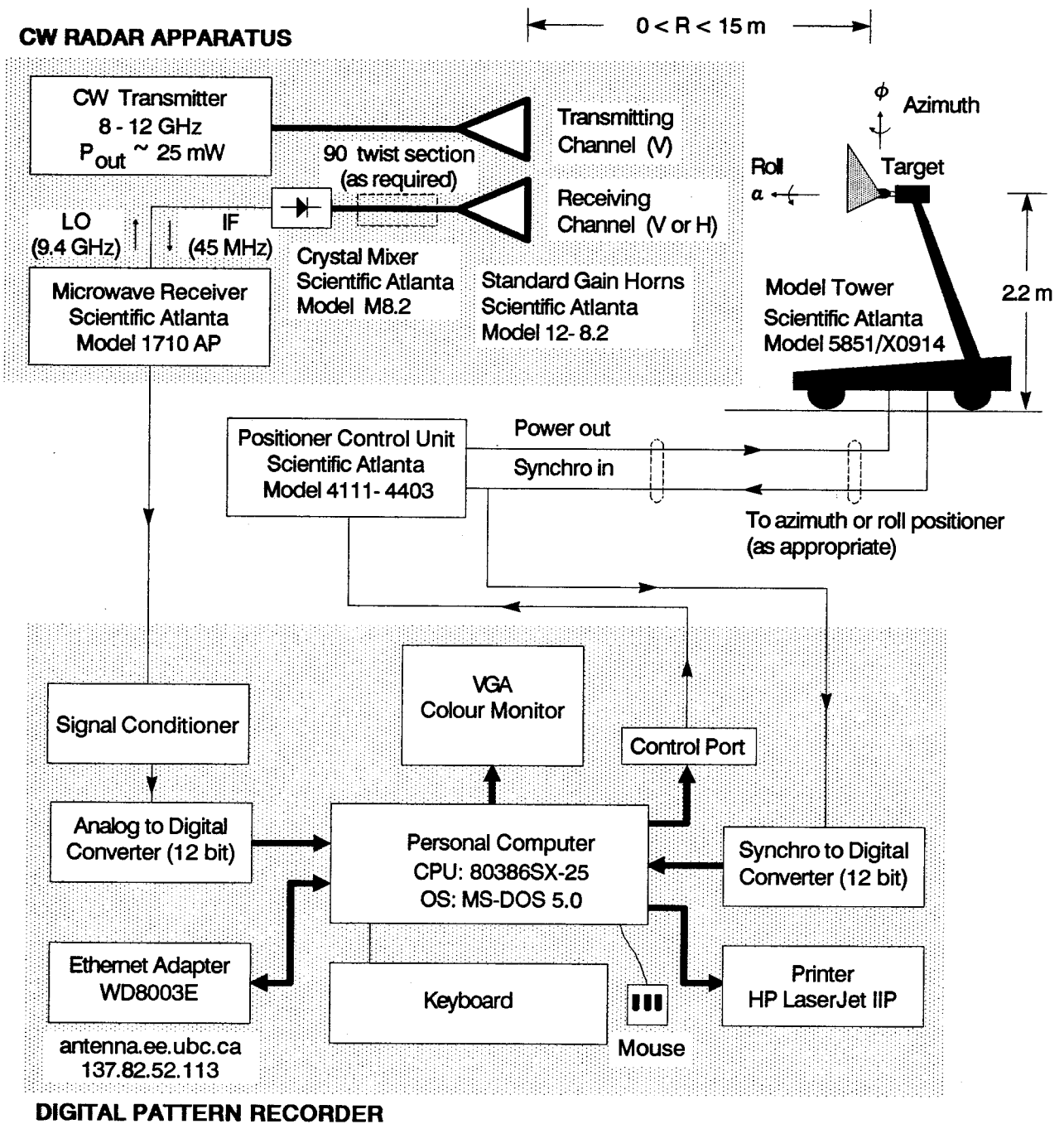
Appendix D

EXPERIMENTAL ARRANGEMENT

D.1 Introduction

During the course of this study, the microwave antenna range located on the roof of the Electrical Engineering building at the University of British Columbia was upgraded and used to measure the response patterns of prototype depolarizing trihedral corner reflectors as described in Chapter 4. The principles of radar cross section measurement have been widely discussed in the literature, e.g., [1]–[5]. In this appendix, the modifications and improvements that were made to the UBC antenna range in support of the prototype reflector measurement program are briefly described. In section D.2, the general layout of the antenna range is described. In sections D.3 and D.4, respectively, the design and implementation of the CW radar apparatus and digital pattern recorder that are discussed. In section D.5, the results of tests performed to verify the suitability of the antenna range for use in the measurement program are presented. Recommendations for future modifications and improvements are offered.

D.2 Overview

A block diagram of the UBC microwave antenna range as it was configured for the prototype reflector measurement program is shown in Figure D.1. The CW radar apparatus is designed to measure the co-polar and cross-polar response of targets in the range from 8–12 GHz. The digital pattern recorder is designed to calibrate the CW radar apparatus and record the response patterns of antennas or targets under test. It replaces the Scientific Atlanta series 1520 mechanical chart recorder used previously.

CW RADAR APPARATUS

|← ———— 0 < R < 15 m ————→|

CW Transmitter
8 - 12 GHz
P_{out} ~ 25 mW

90 twist section
(as required)

Transmitting
Channel (V)

Receiving
Channel (V or H)

LO
(9.4 GHz)

IF
(45 MHz)

Crystal Mixer
Scientific Atlanta
Model M8.2

Microwave Receiver
Scientific Atlanta
Model 1710 AP

Standard Gain Horns
Scientific Atlanta
Model 12- 8.2

ϕ Azimuth

Roll
a

Target

Model Tower
Scientific Atlanta
Model 5851/X0914

2.2 m

Positioner Control Unit
Scientific Atlanta
Model 4111- 4403

Power out

Synchro in

To azimuth or roll positioner
(as appropriate)

Signal Conditioner

VGA
Colour Monitor

Control Port

Analog to Digital
Converter (12 bit)

Personal Computer
CPU: 80386SX-25
OS: MS-DOS 5.0

Synchro to Digital
Converter (12 bit)

Ethernet Adapter
WD8003E

Keyboard

Mouse

Printer
HP LaserJet IIP

antenna.ee.ubc.ca
137.82.52.113

DIGITAL PATTERN RECORDER

Figure D.1: Block diagram of the radar cross section measurement range.

The outdoor portion of the antenna range is shown in Figure D.2. The Scientific Atlanta model 5851 model tower travels on a carriage along 15 metres of track down the center of the roof of the east wing of the Electrical Engineering building. The model tower supports the antenna or target under test at a height of 2.2 metres and can be configured either to rotate the device about a vertical axis for conventional azimuthal pattern measurements or to roll the device about a horizontal axis for polarization response measurements. Detailed mechanical specifications are presented in the model tower operating manual [6].
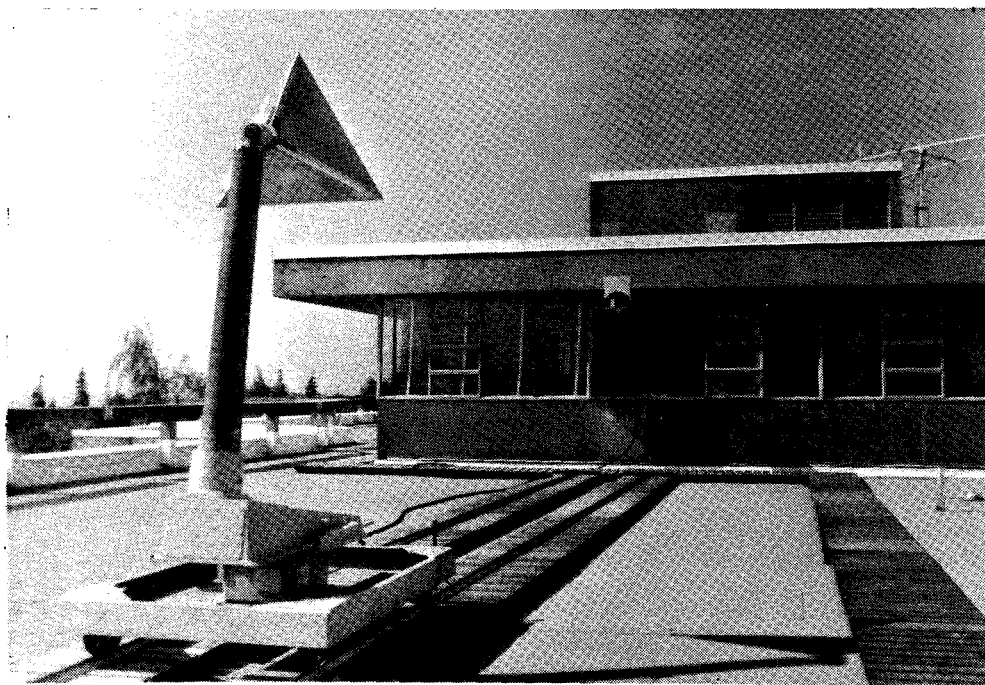
Figure D.2: Photograph of the radar cross section measurement range.

D.3 CW Radar Apparatus

The CW radar apparatus consists of a CW transmitter, a microwave receiver equipped with an external crystal mixer, and two standard gain horns mounted side by side on a custom-built feedthrough mounting adapter. A block diagram of the transmitter and a photograph of the transmitter shelf are shown in Figures D.3 and D.4, respectively. The signal source is a Marconi

6052B microwave signal generator which can provide at least 25 mW (14 dBm) of power to a matched load over the range from 8–12 GHz. The transmitted signal is sampled using an HP X752C 20 dB directional coupler and monitored using a Marconi 6593A VSWR meter equipped with a HP X485B detector mount. The exact frequency of the transmitted signal is determined by tuning the HP X532B frequency wavemeter until a dip is observed on the VSWR meter. The HP X382A precision attenuator is used to adjust the transmitter output power during calibration. Detailed specifications for each component are presented in references [7]–[9].

The receiver section of the radar apparatus consists of a Scientific Atlanta model 1710AP portable microwave receiver equipped with a model M8.2 external crystal mixer. Detailed specifications are given in the receiver operating manual [10]. The receiver local oscillator (LO) is tunable from 0.985–2.5 GHz. During operation, the LO output is fed through a RF pad to the LO arm of a frequency selective tee. This tee couples the LO signal through a coaxial cable to the external mixer where harmonic mixing takes place. The resulting 45 MHz IF signal is conducted back through the same coaxial cable and frequency selective tee to a 45 MHz IF preamplifier and subsequent stages. The receiver provides a signal to the monitor meter on its front panel which is proportional to the received signal strength. This signal was tapped and passed through a signal conditioning unit containing an op-amp based current-to-voltage converter, a low pass filter, and an adjustable gain block in order to provide the 0–10 VDC output signal required by the digital pattern recorder.

A pair of Scientific Atlanta model 12-8.2 standard gain horn antennas are used as the transmitting and receiving antennas. The antennas present a boresight gain of 22.10 ± 0.05 dB at a wavelength of 3.2 cm with E-plane and H-plane half-power beamwidths of 12.5 and 13.5 degrees, respectively [11]. They are mounted side by side on a custom-built feedthrough mounting adapter which is attached to the side of the building penthouse at a height of 2.2 metres as shown in Figures D.5 and D.6. The transmitting horn is mounted so that it is vertically polarized. The mounting adapter permits the receiving horn to be rotated by 90 degrees in order to permit either the co-polar (σ_{VV}) and cross-polar (σ_{HV}) response of the

target to be measured. Arrangements for aligning the horns are shown in Figure D.7. Coarse alignment is performed using bubble levels which are mounted on the horns and waveguide as shown. The alignment is completed by optical sighting an alignment target mounted on the model tower using cross hairs mounted on the front of the horns and the flanges of the waveguide.
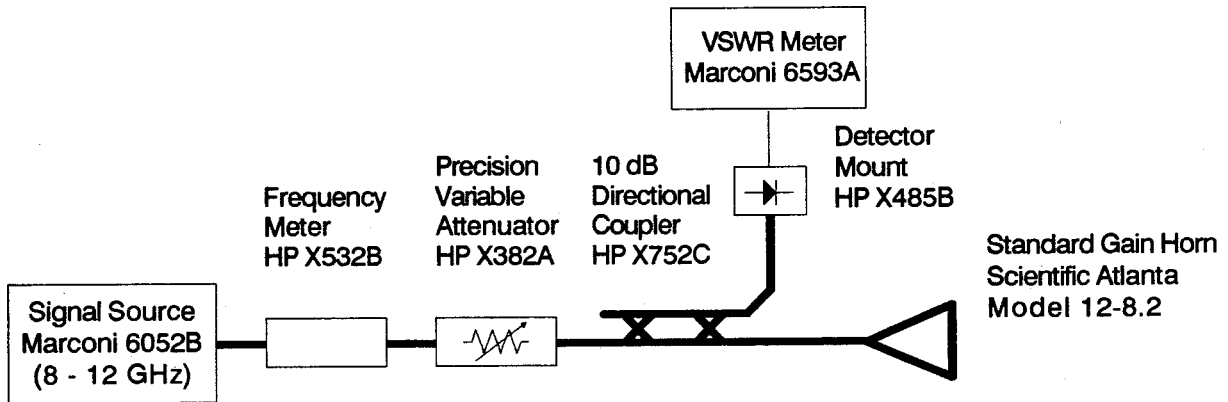

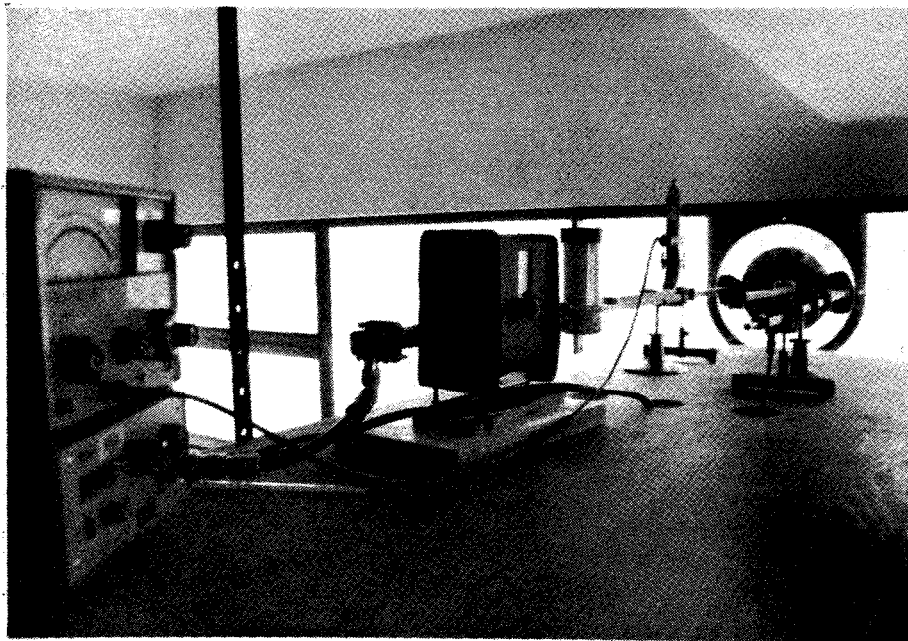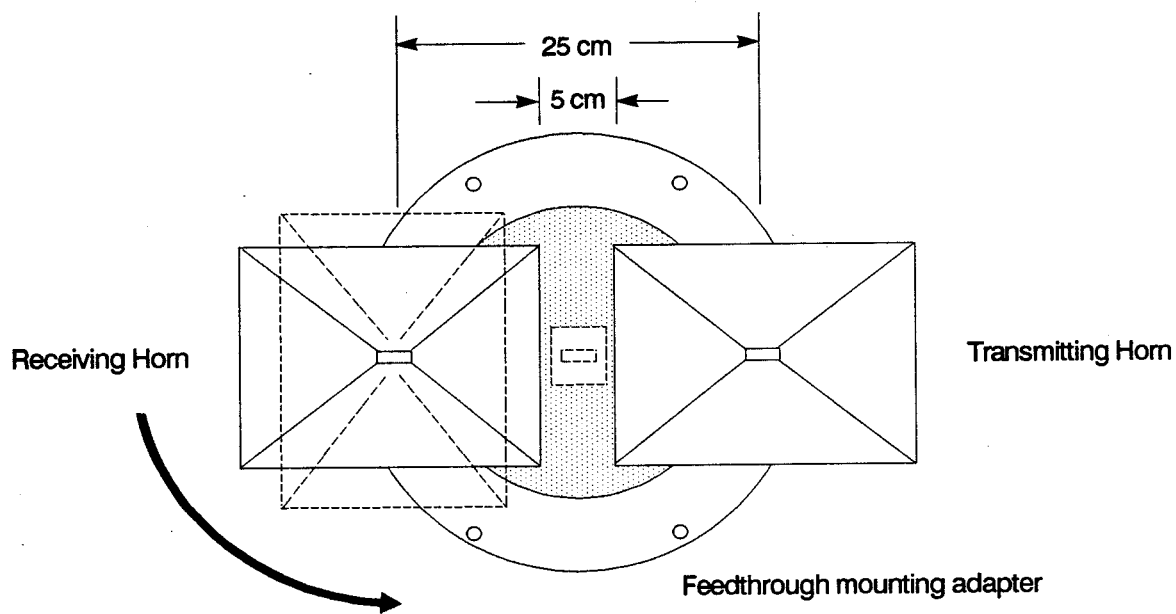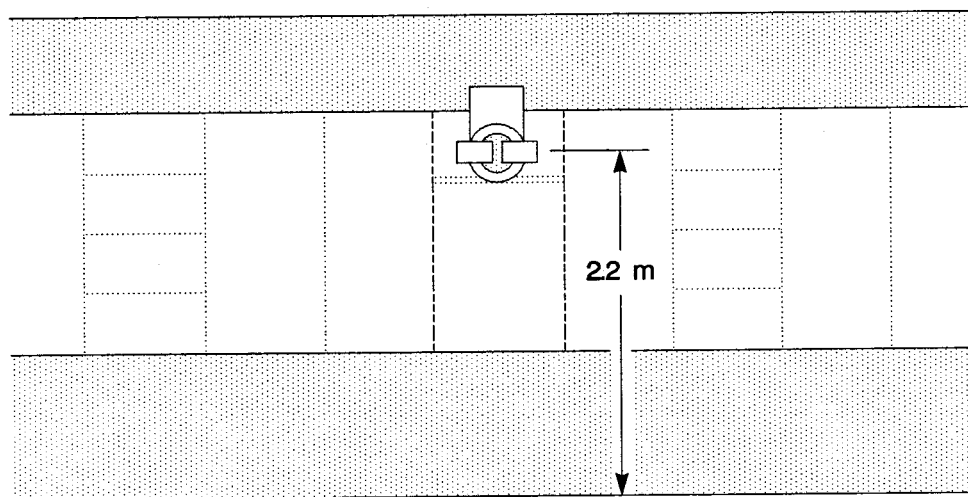Figure D.3: Block diagram of the CW radar transmitter.

Figure D.4: Photograph of the CW radar transmitter.

(a)

(b)

Figure D.5: Mounting arrangement for the transmitting and receiving antennas. (a) Details of the feedthrough mounting adapter. (b) Front view of the building penthouse.
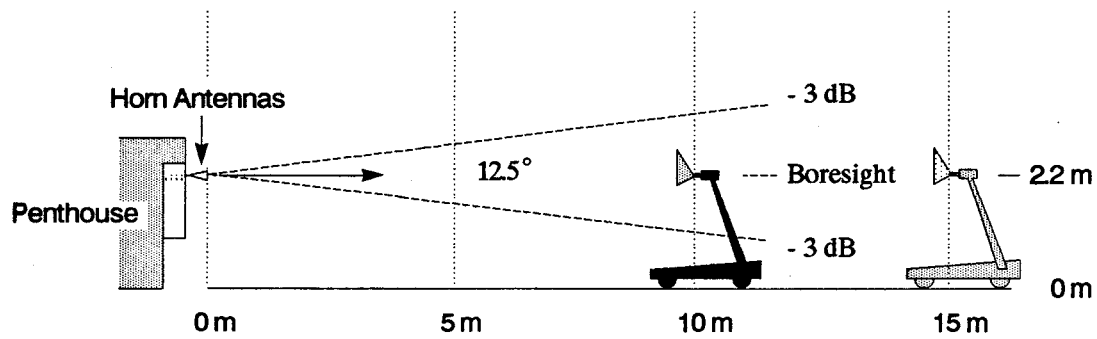
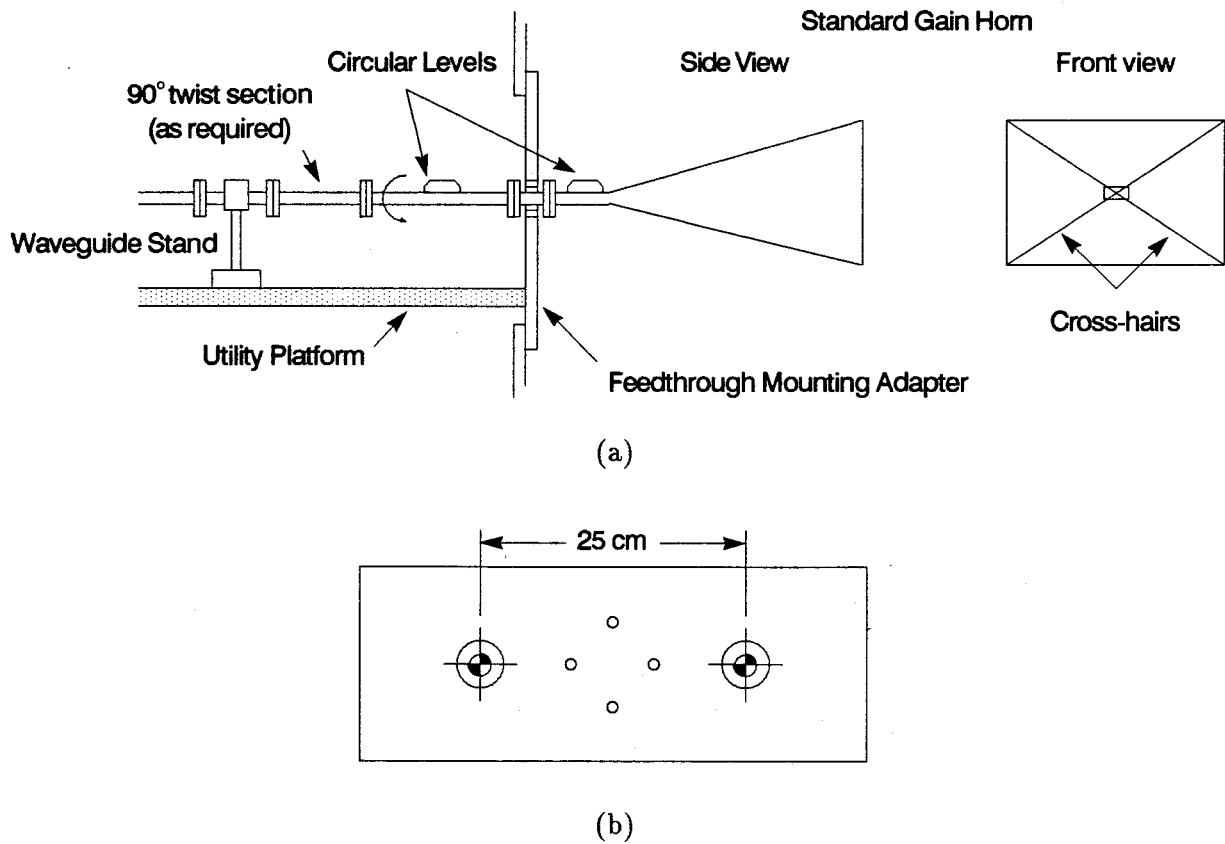Figure D.6: Profile view of the RCS measurement range.

(a)

(b)

Figure D.7: Arrangement for mechanically aligning the transmitting and receiving antennas. (a) Alignment aids mounted on the transmitter shelf. (b) Alignment target mounted on the model tower.

A graphical representation of the link budget for the radar cross section measurement range as configured for measurement of prototype trihedral corner reflectors with a corner length of 60 cm is presented in Figure D.8. The results correspond to the ideal case in which the power available to the radar receiver is given by the radar range equation,

$$P_r = \frac{P_t\,G_t\,G_r\,(\sigma/\lambda^2)}{(4\pi)^3\,(R/\lambda)^4} \; ,$$

where $G_t = G_r = 22.1$ dB are the gains of the transmitting and receiving antennas, respectively, $\sigma = 27.3$ dBsm is the radar cross section of the target, $\lambda = 3.18$ cm is the radar wavelength, and $R = 11$ m is the range to the target. In order to achieve the required dynamic range, the minimum return from the target must be greater than either the background reflectivity of the facility or the receiver thermal noise level.
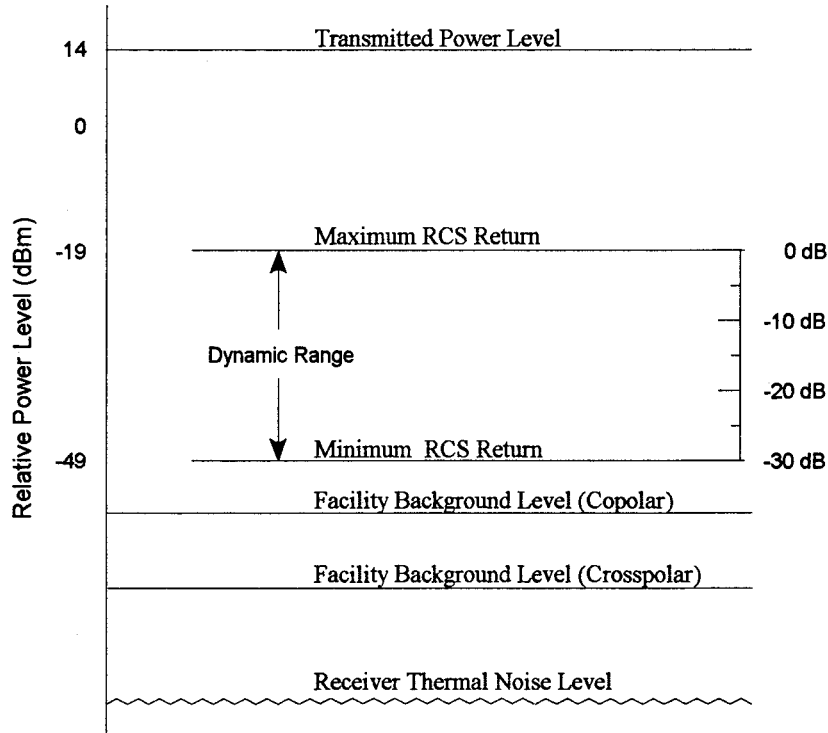

Figure D.8: Radar cross section measurement range link budget.

D.4 Digital Pattern Recorder

The digital pattern recorder consists of an industry standard personal computer equipped with a colour VGA display, an 80386SX-25 CPU with a numerical coprocessor, 2 MB RAM, an 80 MB hard disk drive, and custom-designed interface hardware and data acquisition software. A PC-26 analog-to-digital converter (ADC) expansion card (Boston Technologies, Boston, MA) equipped with the custom-designed signal conditioning unit described in the previous section is used to measure the output from the portable microwave receiver. A custom-built 12-bit synchro-to-digital converter (SDC) expansion card based on a Control Sciences Inc. (Chatsworth, CA) 168F309 integrated 12-bit SDC module is used to measure the angle of rotation of the antenna or target under test. Design considerations for PC-based laboratory instrumentation have been widely discussed in the literature, e.g., [12], [13]. A photograph of the digital pattern recorder, the positioner control unit, and the portable microwave receiver is shown in Figure D.9.
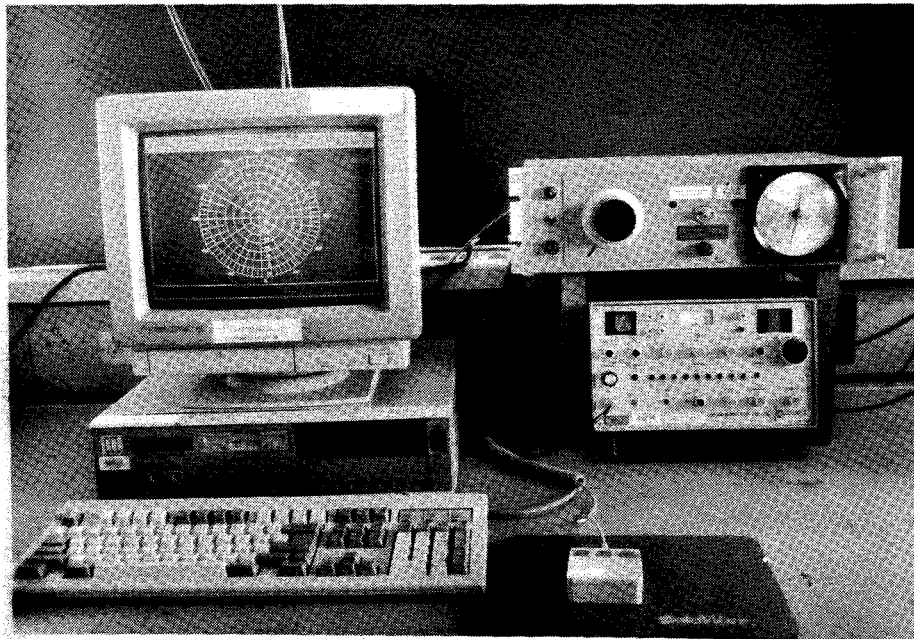

Figure D.9: Photograph of the digital pattern recorder, positioner control unit, and portable microwave receiver.

A set of five independent program modules perform calibration, data acquisition, and diagnostic functions. The program modules store calibration data, configuration notes, and response pattern data in ASCII format and employ a consistent user interface. They were coded using *Turbo Pascal,* version 5.5 (Borland International, Scotts Valley, CA) and make use of graphics routines from the *Science and Engineering Tools for Turbo Pascal* subroutine library, version 6.1 (Quinn-Curtis, Needham, MA). The function of each module is summarized in Table D.1.

Table D.1: Digital Pattern Recorder Program Modules

Module	Name	Function
Synchro Test	DPR_SYN	• display position of model tower in real time and verify correct operation of the synchro interface
Receiver Calibration	DPR_CAL	• generate relative calibration curve for receiver and verify correct operation of the receiver interface
Pattern Recorder	DPR_PAT	• record pattern data and configuration notes for analysis and presentation
Data View	DPR_VIEW	• view and compare previously recorded data
Receiver Stability	DPR_STAB	• sample receiver output signal and generate amplitude distributions and frequency spectra

The synchro test module, DPR_SYN, is used to verify that the model tower synchro, the positioner control unit synchro repeater, the synchro-to-digital converter and the interconnecting cables are functioning correctly. It can also be used to calibrate the speed control on the positioner control unit. The program displays the current angle of rotation and rate of rotation of the antenna or target under test while it generates a plot of the angle of rotation versus time. A sample screen display is presented in Figure D.10.

The receiver calibration module, DPR_CAL, is used to measure the transfer characteristic of the microwave receiver. During a measurement sequence, the pattern recorder module uses this data to translate the binary code read from the ADC into a relative measure of the received signal strength in decibels. Relative calibration of the CW radar apparatus is performed with the equipment configured as shown in Figure D.11(a). After the operator has set the receiver input signal to the highest level likely to be encountered during the measurement, the program

prompts the operator to decrement the received signal strength in 5 dB steps using either the precision microwave attenuator in the transmitter or the IF step attenuator in the receiver and sample the receiver output. A sample screen display is presented in Figure D.10. After the calibration sequence is complete, the operator is prompted to either save the relative calibration data to a file or begin the calibration sequence again. Absolute calibration of the CW radar apparatus can be performed either directly by measuring the response of a calibration target of similar size to the target under test or indirectly by measuring the effective path loss between the transmitter and receiver.

An arrangement for performing absolute calibration using an indirect method is shown in Figure D.12. First, the response of the target is measured using the configuration of Figure D.12(a). Next, the crystal mixer is removed from the receiving horn and mounted on the 10 dB directional coupler in the transmitter as shown in Figure D.12(b). Finally, the precision microwave attenuator is adjusted until an identical response is observed at the receiver output. The total insertion loss includes the contributions of both the attenuator and the directional coupler. Since the distance to the target, the radar wavelength, and the gain of transmitting and receiving antennas are known, the absolute radar cross section of the target can be determined simply by equating the geometric path loss predicted by the radar equation to the total insertion loss. Closure is obtained when the results of direct and indirect calibration agree to within a prescribed tolerance.

The pattern recorder module, DPR_PAT, is used to record both the parameters of the test configuration and the response pattern of the antenna or target under test. A sample parameter entry screen is shown in Figure D.13. When a new measurement sequence is begun, the parameter entry screen is replaced by a data acquisition screen which displays the response pattern as it is being measured. The data acquisition screen can be configured to present the results on either a rectangular or polar chart spanning either $\pm$ 90 or $\pm$180 degrees. A sample $\pm$ 180 degree polar display with a dynamic range of 30 dB is shown in Figure D.14. After data collection is complete, the operator is returned to the parameter entry screen and prompted to either save the response pattern data to a file or begin the measurement sequence again.
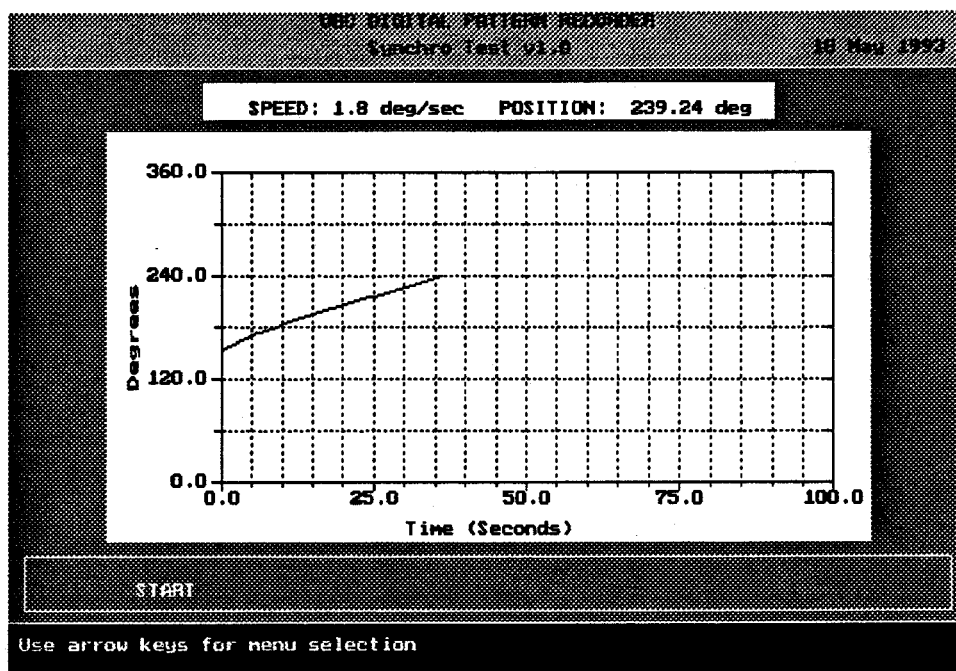
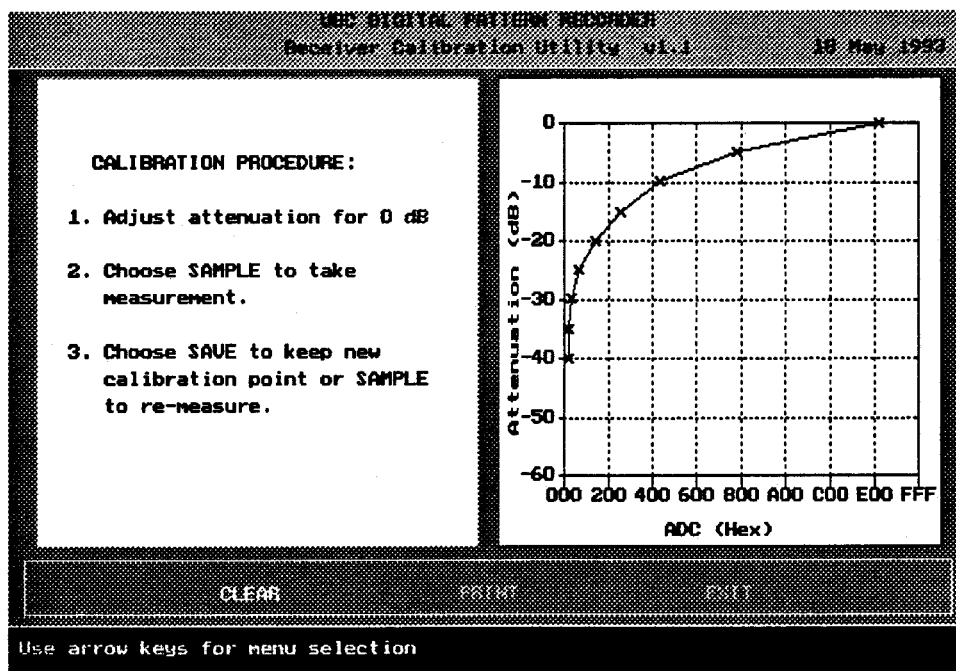Figure D.10: Digital pattern recorder: synchro test screen.

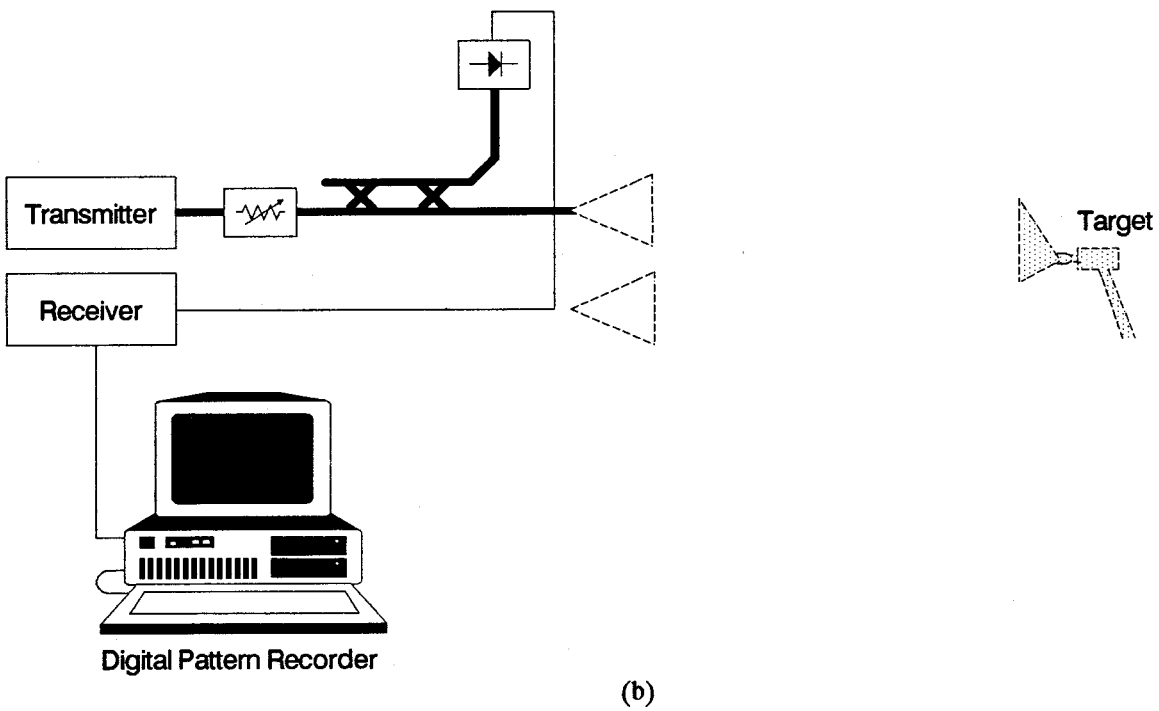Figure D.11: Digital pattern recorder: receiver calibration screen.
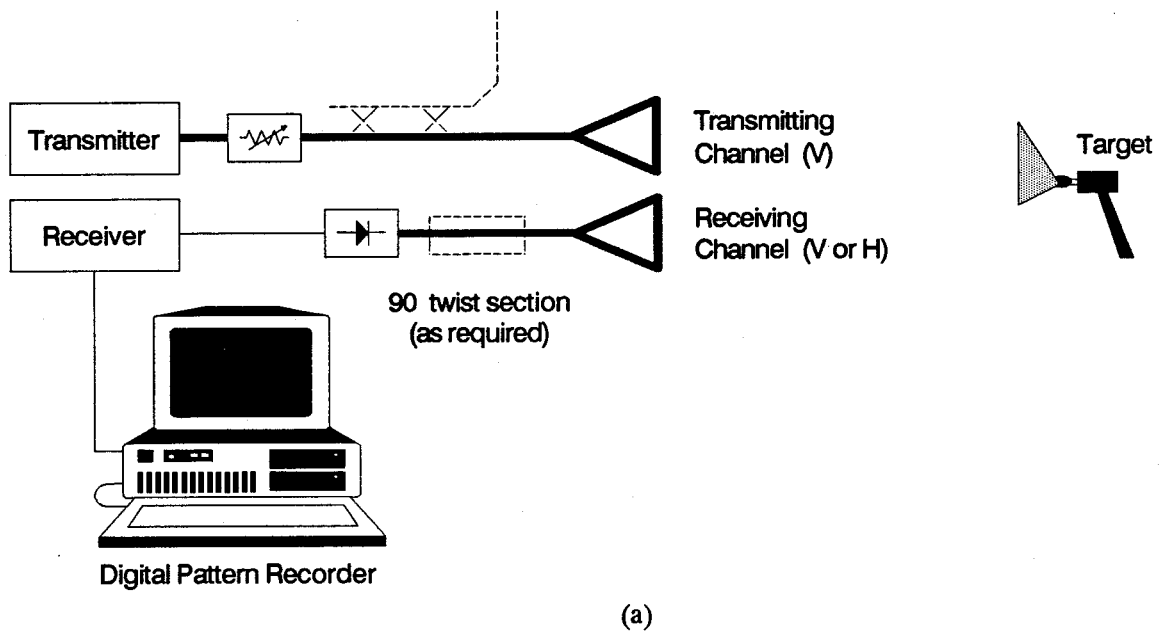
Figure D.12: Equipment configuration for performing relative and absolute calibration of the CW radar apparatus.

Figure D.13: Digital pattern recorder: parameter entry screen.
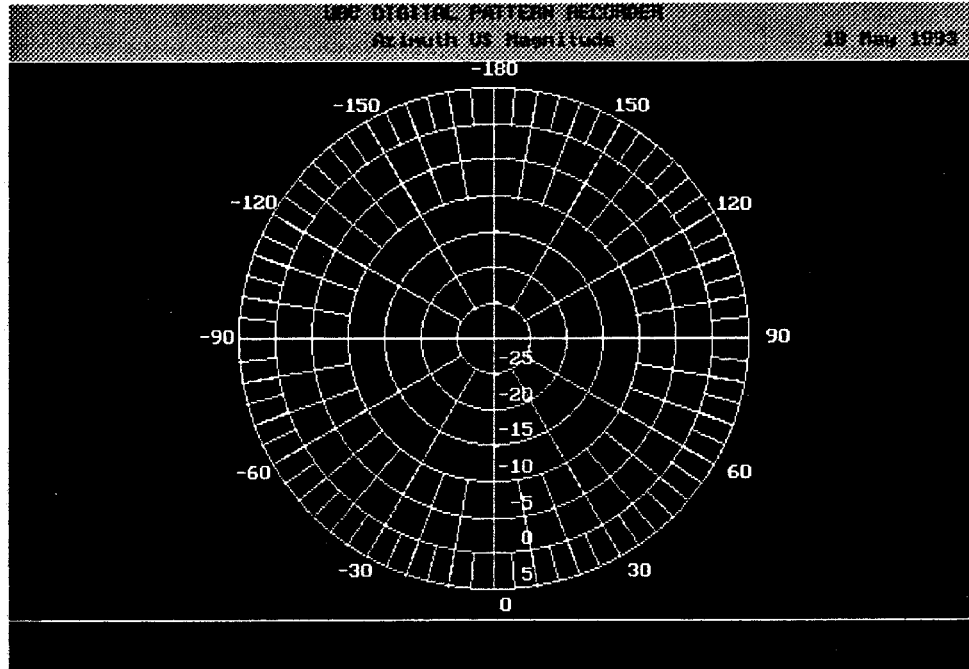

Figure D.14: Digital pattern recorder: data acquisition screen.

The last two program modules are test articles used to evaluate functions which will be incorporated into future versions of the receiver calibration and pattern recorder modules. The receiver stability module, DPR_STAB, is used to assess the short and long-term stability of the portable microwave receiver while a constant amplitude signal is applied to its input. After the output of the receiver has been sampled over a period of time ranging from several minutes to several hours, the results are either viewed directly as time series or processed to yield amplitude distribution functions and/or frequency spectra. The data viewing module, DPR_VIEW, is a modified version of the pattern recorder module which is used to view and compare previously recorded data.

D.5 Facility Evaluation

Radar cross section measurements are affected by a combination of random and systematic errors. It is convenient to depict these errors by the signal flow graph presented in Figure D.15 where S represents the actual response of the target, R and T represent errors due to (1) deviation of the incident field from a plane wave and (2) multipath reflections from the surrounding facility, and I represents the contribution of general background due to (3) returns from the target support structure and surroundings and (4) direct transmission between the transmitting and receiving antennas. In order to determine the suitability of a RCS facility for use in a measurement program, a series of tests must be performed to assess the magnitude of these errors and their potential impact on the accuracy of the results obtained.
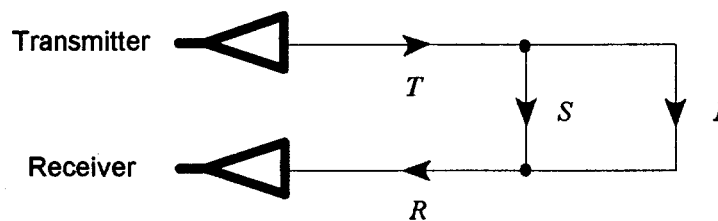

Figure D.15: Error model for radar cross section measurement.

Ideally, the target is located sufficiently far away from the transmitting antenna that the incident field presents a planar wavefront. For a small outdoor antenna range of the type considered here, such an arrangement is rarely practical since the contribution of the multipath ray to the response increases rapidly with range. It is often suggested that satisfactory results will be obtained if the phase deviation over the largest dimension of the target is less than $\pi/8$ radians. This leads to the so-called far-field criterion which requires that the range to the target be greater than

$$R = \frac{2\,d^2}{\lambda} \, ,$$

where d is the largest dimension of the target and λ is the radar wavelength. In practice, physical constraints often make it necessary to measure radar cross section of targets at ranges as low as one-quarter of the recommended value. The consequences are similar to those encountered when conducting antenna measurements under similar circumstances. In particular, the apparent value of the radar cross section obtained by direct solution of the radar range equation will be less than the actual value that would have been obtained had the incident field been a plane wave.

A trihedral corner reflector of the type used in the measurement program has triangular panels of equal length and presents a maximum radar cross section of

$$\sigma_{\max} = \frac{4\pi}{3}\,\frac{\ell^4}{\lambda^2} \, ,$$

where ℓ is the corner length of the reflector and λ is the radar wavelength. Although the largest physical dimension of a reflector of this type is the distance from the tip of one corner to the mid-point of the opposite panel, the maximum dimension of the effective aperture is much smaller and is given by

$$d = \frac{2\sqrt{2}}{3}\,\ell \, ,$$

as suggested by Figure D.16. The maximum aperture dimension, maximum radar cross section, and far-field range of trihedral corner reflectors with various corner lengths are summarized in Table D.2.
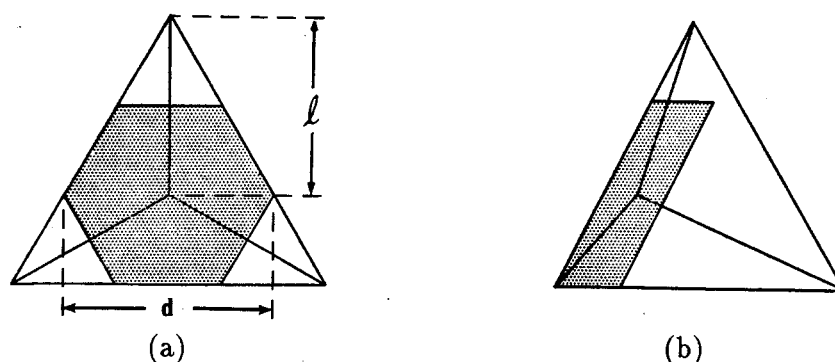
Figure D.16: The effective aperture of a trihedral corner reflector with triangular panels for incidence (a) along the boresight and (b) at an azimuth angle of 30 degrees.

Table D.2: Response of Trihedral Corner Reflectors with Triangular Panels at 9.445 GHz

Corner length (cm)	Max. aperture dimension (cm)	Maximum RCS		Far-field range (m)
		(m^2)	(dBsm)	
15	14	2	3.2	2
30	28	33	15.3	5
45	42	169	22.3	11
60	57	537	27.3	20
75	71	1310	31.2	31

Four tests were conducted in order to assess the suitability of the antenna range for use in the prototype reflector measurement program. All the tests were performed at the standard marine radar frequency of 9.445 GHz.

In the first test, the polarization response of the CW radar apparatus was evaluated. The receiving horn was removed from the feedthrough mounting adapter and attached to the model tower. The response of the receiving horn was measured at a range of 11 metres as the horn was rotated about its boresight. The results generally agree with the predicted values and are presented in Figure D.17. The isolation between the transmitting and receiving horns is considerably greater than 30 dB when the horns are orthogonally polarized.

In the next two tests, the contributions of near-field and multipath effects to the response of a target under test were evaluated. A conventional trihedral corner reflector with a corner

length of 60 cm was attached to the model tower. First, the response of the target was measured as its range was increased from 8 to 16 metres in 0.25 m increments. The results are presented in Figure D.18. At ranges greater than about 12 metres, rapid variations in the response are observed which suggest that multipath effects are becoming important. At ranges less than about 9 metres, evidence of a reduction in the response which is apparently due to near-field effects is observed. At ranges between 9 and 12 metres, the response varies as $1/R^4$ with only a few perturbations. A second test was performed in order to assess the effect of small changes in range on the fine structure of the response pattern. The azimuthal response pattern of the reflector was measured at ranges of 10 and 12 metres and compared. The results are presented in Figure D.19 where it can be seen that the response patterns are nearly identical. On this basis of these results, it was concluded that the optimum range at which to measure the prototype reflectors is 11 metres.

In the last test, the contributions of direct transmission between the horns and unwanted returns from the model tower and surroundings were evaluated. The conventional trihedral corner reflector was removed from the model tower and the positioner head was covered by a small section of microwave absorber. The co-polar and cross-polar responses of the background was measured in turn as the model tower was rotated in azimuth at a range of 11 metres. The results are presented in Figure D.20. The co-polar response rises above -30 dB at only a few angles and never rises above -28 dB relative to the maximum response of the prototype reflector. The cross-polar response never rises above -30 dB.

During the evaluation of the facility, several problems were noted. The gears that rotate the positioner head about a horizontal axis exhibit a small but noticeable backlash. The effect is particularly obvious when a large target such as a prototype reflector is mounted on the model tower. Since procedures for reducing the backlash require the services of a skilled machinist [6], the problem could not be corrected simply by conducting routine maintenance during the course of the measurement program. It is recommended that the problem be corrected in the near future, however.
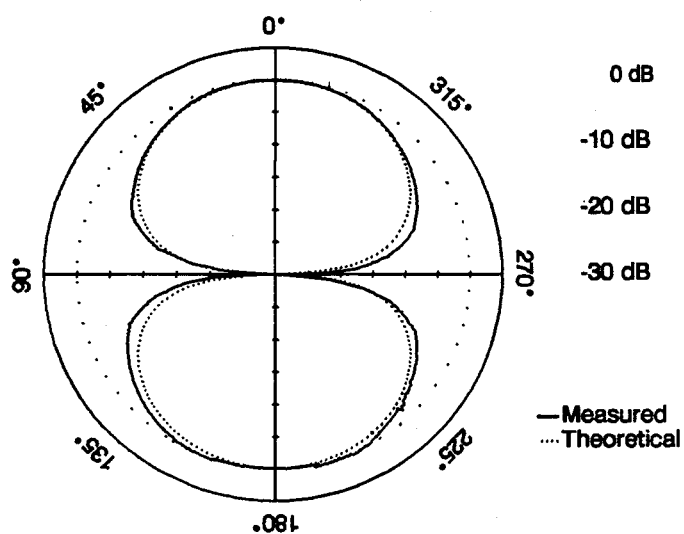
Figure D.17: Polarization response of the receiving horn at a range of 11 m.
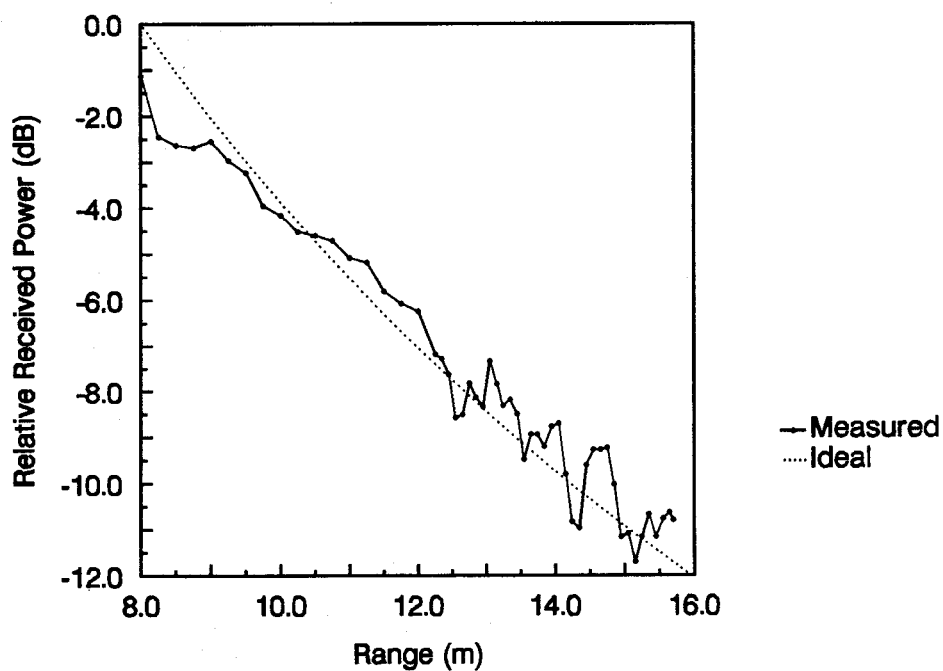

Figure D.18: Boresight response of a conventional trihedral corner reflector vs. range.
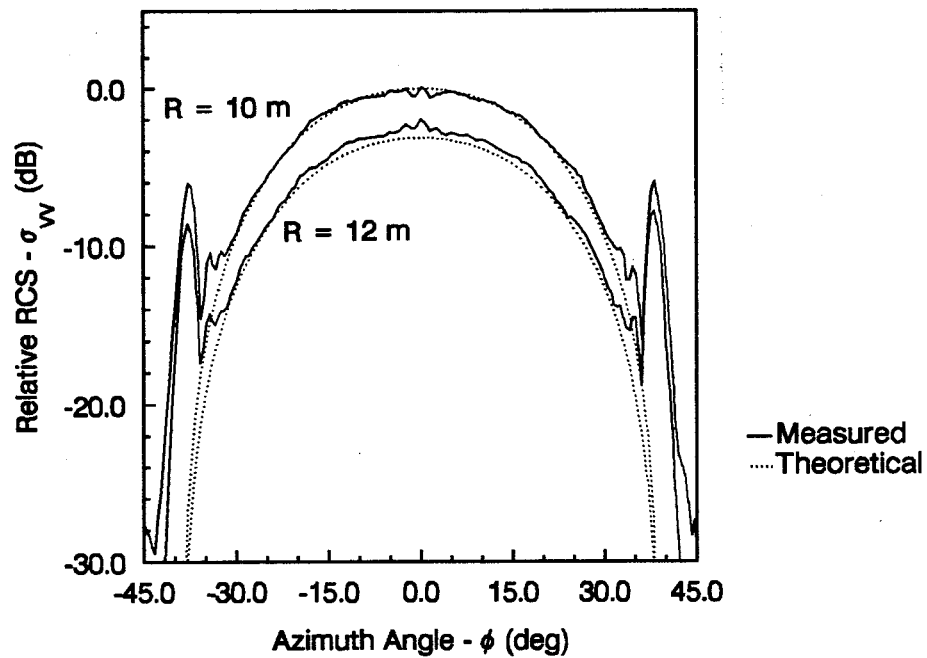
Figure D.19: Azimuthal response pattern of a conventional trihedral corner reflector at ranges of 10 and 12 m.
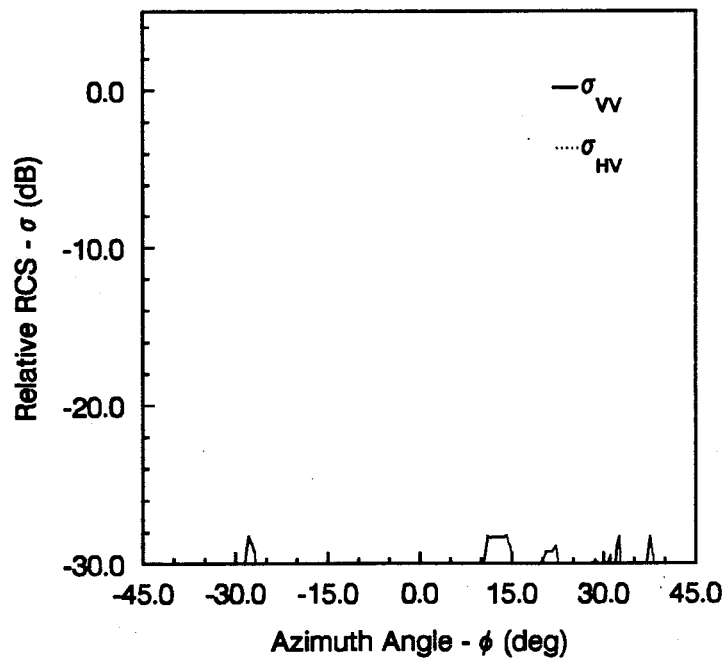

Figure D.20: Azimuthal response pattern of the model tower at a range of 11 m.

The transfer characteristic of the portable microwave receiver tends to drift noticeably after only an hour. As a result, it was necessary to recalibrate the receiver each time a new series of measurements was conducted. Since the receiver is over twenty years old and is nearing the end of its useful life, it is recommended that consideration be given to replacing it.

As noted earlier, multipath reflections were observed when the range to the target was greater than about 12 metres. It might be possible to significantly reduce multipath effects (and extend the model tower's useful range of travel) by employing either a berm or a series of radar fences to scatter the multipath ray as described by Knott [2, pp. 369–370]. It is recommended that an experimental program be conducted to assess the effectiveness of such methods in suppressing multipath effects at this antenna range

References

[1] C. G. Bachman, *Radar Targets.* Lexington, MA: D. C. Heath, 1982, pp. 109–158.

[2] E.F. Knott, J.F. Shaeffer, and M.T. Tuley, *Radar Cross Section: Its Prediction, Measurement, and Reduction.* Norwood, MA: Artech House, 1985, pp. 315–382.

[3] *Radar Cross-Section Measurements with the HP 8510 Network Analyzer.* Product Note No. 8510-2, Santa Rosa, CA: Hewlett-Packard, Apr. 1985.

[4] R.B. Dybdal, "Radar cross section measurements," *Proc. IEEE,* vol. 75, pp. 498–516, Apr. 1987.

[5] N.C. Currie, Ed., *Radar Reflectivity Measurement: Techniques and Applications,* Norwood, MA: Artech House, 1989.

[6] *Series 5800 Model Towers,* 3rd ed. Atlanta, GA: Scientific-Atlanta, Dec. 1970.

[7] *Instruction Manual for Signal Source Type 6058B.* Stevenage, UK: Marconi Instruments (Sanders Div.), 1976.

[8] *Coaxial & Waveguide Catalog and Microwave Measurement Handbook.* Palo Alto, CA: Hewlett-Packard, 1979.

[9] *Instruction Manual for VSWR Indicator and Selective Amplifier Type 6593A.* Stevenage, UK: Marconi Instruments (Sanders Div.), 1976.

[10] *Series 1710 Portable Microwave Receiver,* 2nd ed. Atlanta, GA: Scientific-Atlanta, May 1970.

[11] W. T. Slayton, *Design and Calibration of Microwave Antenna Gain Standards.* NRL Report. No. 4433, U.S. Naval Research Lab, Washington, DC, 1954.

[12] S.C. Gates and J. Becker, *Laboratory Automation using the IBM PC.* Englewood Cliffs, NJ: Prentice-Hall, 1989.

[13] B.G. Thompson and A.F. Kuckes, *IBM-PC in the Laboratory.* Cambridge: Cambridge Univ. Press, 1989.